AD-A162 691   SPECTROSCOPIC KINETIC AND DYNAMIC EXPERIMENTS ON   1/3
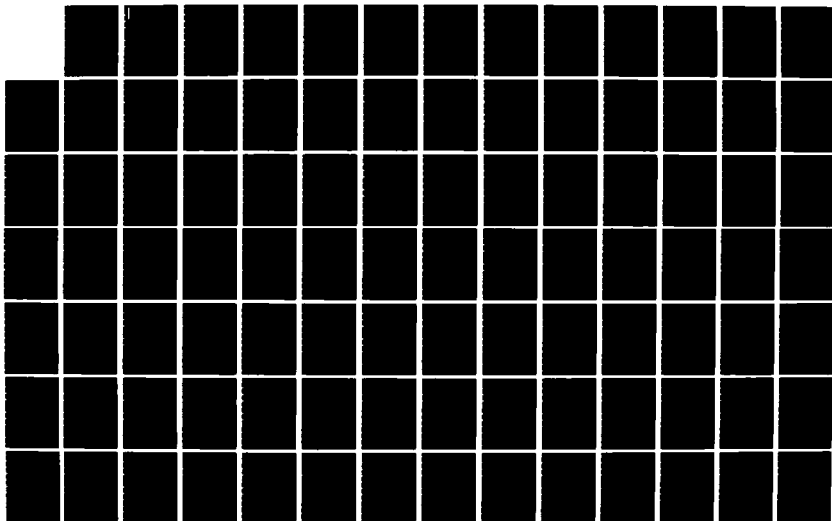   ATMOSPHERIC SPECIES(U) AIR FORCE GEOPHYSICS LAB HANSCOM
                   AFB MA   S M MILLER ET AL   21 MAR 85 AFGL-TR-85-0077
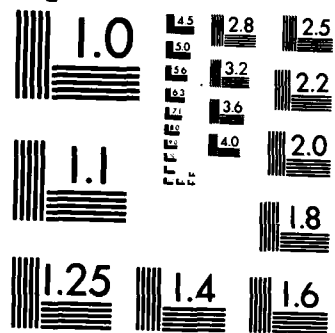
UNCLASSIFIED   F/G 4/1   NL

MICROCOPY RESOLUTION TEST CHART
NATIONAL BUREAU OF STANDARDS-1963-A

AD-A162 691

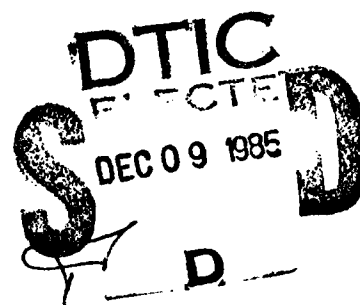# Spectroscopic, Kinetic, and Dynamic Experiments on Atmospheric Species

S. M. MILLER   J. I. STEINFELD   G. E. CALEDONIA
J. B. LURIE   W. T. RAWLINS   P. NEBOLSINE
R. A. ARMSTRONG   A. GELB   G. WEYL
I. WINKLER   L. PIPER   B. D. GREEN

21 March 1985

DTIC
ELECTE
DEC 09 1985
D

DTIC FILE COPY

INFRARED TECHNOLOGY DIVISION   PROJECT 2310

AIR FORCE GEOPHYSICS LABORATORY

HANSCOM AFB, MA 01731

85 12 6 092

"This technical report has been reviewed and is approved for publication"

FOR THE COMMANDER

ROBERT R. O'NEIL, Acting Chief
Infrared Dynamics Branch
Infrared Technology Division

RANDALL E. MURPHY, Director
Infrared Technology Division

REPORT DOCUMENTATION PAGE

1a. REPORT SECURITY CLASSIFICATION	1b. RESTRICTIVE MARKINGS
UNCLASSIFIED	A162691

2a. SECURITY CLASSIFICATION AUTHORITY	3. DISTRIBUTION/AVAILABILITY OF REPORT
	Approved for public release;
2b. DECLASSIFICATION/DOWNGRADING SCHEDULE	distribution unlimited.

4. PERFORMING ORGANIZATION REPORT NUMBER(S)	5. MONITORING ORGANIZATION REPORT NUMBER(S)
AFGL-TR-85-0077 PSRP, No. 668	

6a. NAME OF PERFORMING ORGANIZATION	6b. OFFICE SYMBOL (If applicable)	7a. NAME OF MONITORING ORGANIZATION
Air Force Geophysics Laboratory	LSI	Air Force Geophysics Laboratory

6c. ADDRESS (City, State and ZIP Code)	7b. ADDRESS (City, State and ZIP Code)
Hanscom AFB Massachusetts 01731	Hanscom AFB Massachusetts 01731

8a. NAME OF FUNDING/SPONSORING ORGANIZATION	8b. OFFICE SYMBOL (If applicable)	9. PROCUREMENT INSTRUMENT IDENTIFICATION NUMBER
Air Force Geophysics Laboratory	LSI	

8c. ADDRESS (City, State and ZIP Code)	10. SOURCE OF FUNDING NOS.			
	PROGRAM ELEMENT NO.	PROJECT NO.	TASK NO.	WORK UNIT NO.
Hanscom AFB Massachusetts 01731	61102F	2310	G4	14

11. TITLE (Include Security Classification)
Spectroscopic, Kinetic, and Dynamic Experiments on Atmospheric Species

12. PERSONAL AUTHOR(S)
S. M. Miller; J. B. Lurie; R. A. Armstrong; I. Winkler*; J. I. Steinfeld**; (over)

13a. TYPE OF REPORT	13b. TIME COVERED	14. DATE OF REPORT (Yr., Mo., Day)	15. PAGE COUNT
FINAL	FROM 1 Oct 82 TO 30 Sep 84	1985 March 21	248

16. SUPPLEMENTARY NOTATION
*Department of Chemistry, Massachusetts Institute of Technology, Cambridge, MA 02139
**Physical Sciences Inc, Research Park, Andover, MA 01810

17. COSATI CODES			18. SUBJECT TERMS (Continue on reverse if necessary and identify by block number)
FIELD	GROUP	SUB. GR.	COCHISE LINUS Nitrogen (^{4}S) Nitric Oxide
04	01		FAKIR CO_2 Emission Laser Excitation Branching Ratio
			FACELIF Nitrogen (^{2}D) Nitrogen (A state) Nitrous Oxide

19. ABSTRACT (Continue on reverse if necessary and identify by block number)
This final report contains: (Cold Chemical Infrared Simulation Experiment)

a. The results of COCHISE experiments involving the interaction of N_2 with CO, O_3(v) with N_2 and the fluorescences of NO and N_2;

b. A theoretical discussion of O_2/Ar and N_2/Ar microwave discharges;

c. Trajectory calculations involving the collisional relaxation of high vibrational-rotational states of O_3 by Ar;

d. The experimental determination of the intramolecular branching ratio of the (021) and (101) combination bands of CO_2;

e. A determination of the distribution of vibration states of NO(v) from the reaction N(^{4}S) + $O_2 \rightarrow$ NO(v) via multiphoton ionization;

f. FAKIR measurements of atomic oxygen production in the reaction between N(^{2}D) and CO_2 and the quenching of N(^{2}D) by atomic oxygen.

g. Both the visible and infrared fluorescence results from the LINUS project.

20. DISTRIBUTION/AVAILABILITY OF ABSTRACT	21. ABSTRACT SECURITY CLASSIFICATION
UNCLASSIFIED/UNLIMITED ☒ SAME AS RPT. ☐ DTIC USERS ☐	UNCLASSIFIED

22a. NAME OF RESPONSIBLE INDIVIDUAL	22b. TELEPHONE NUMBER (Include Area Code)	22c. OFFICE SYMBOL
Steven M. Miller	(617) 861-2810	AFGL/LSI

(Flowing Atmospheric Kinetic Infrared Experiment)

(Laser Infrared Nuclear Simulation)

12. Personal Author(s) (Contd)

W. T. Rawlins**; A. Gelb**; L. Piper**; G. E. Caledonia**; P. Nebolsine**;
G. Weyl**; B. D. Green**

Contents

iii

Spectroscopic, Kinetic, and Dynamic Experiments on Atmospheric Species

1. Introduction

There has been a continuing effort at AFGL during the past three years to understand processes that contribute to infrared chemiluminescence in the upper atmosphere. This effort, work unit 2310G414, includes work performed by five experimental facilities and two theoretical projects. The experimental facilities are a) COCHISE - COld CHemical Infrared Simulation Experiment, b) FAKIR experiment - Flowing Atmospheric Kinetic Infrared Experiment, c) FACELIF - Flowing Atmospheric Chemistry Experiment by Laser Induced Fluorescence, d) LINUS - Laser Infrared Nuclear Simulation, and e) FCL Experiments - Laser Induced Vibrational Spectroscopy of Atmospheric Molecules.*

COCHISE - the COCHISE facility has been used to measure the chemiluminescence of NO, N_2, CO, and O_3 from the following reactions:

$$N(^2D) + O_2 \rightarrow NO + O \tag{1}$$

$$N_2^* + CO \rightarrow N_2 + CO(v) \tag{2}$$

$$N_2 + O_3 \rightarrow N_2O(v) + O_2 \tag{3}$$

1

Of particular interest is the NO fundamental to overtone emission ratio of Reaction (1), the resulting vibrational distribution of CO in Reaction (2), and the vibrational distribution of $N_2O(v)$ in Reaction (3).

FAKIR - This facility made both spectroscopic and kinetic measurements to determine the quenching rate coefficient of Reaction (4)

$$N(^2D) + O \rightarrow N(^4S) + O \tag{4}$$

FACELIF - Utilizing multiphoton ionization, FACELIF made preliminary measurements on the production of NO via Reaction (5),

$$N_2(A) + O \rightarrow NO + N \tag{5}$$

and the vibrational distribution of NO in Reaction (6),

$$N(^4S) + O_2 \rightarrow NO(v) + O \quad . \tag{6}$$

FCL - A facility was designed, fabricated, and automated to study laser induced vibrational spectroscopy of atmospheric molecules. Both photoacoustic and fluorescence spectra of the CO_2 v_3 and $v_1 + v_3$ combination bands have been observed.

LINUS - This project entails both experimental and theoretical studies. The theoretical effort concentrates on a survey of the many physical processes occurring in the laser initiated plasma as a function of time. The experimental work examines the spatial, temporal, and spectral characteristics of radiation from the near UV to the LWIR emitted from both oxygen and nitrogen plasmas.

The first theoretical project studies the reaction dynamics of highly energetic O_3 molecules. This involves reactions of both rotationally hot, vibrationally cold ozone with Ar and vibrationally hot, rotationally cold O_3 with Ar.

The second theoretical effort examines the detailed characteristics of O_2/Ar microwave discharges.

Due to both the number and variety of experiments, each topic will be presented as a self-contained report with the appropriate contributors assigned to each. The appendix includes published articles directly related to several of the topics presented.

2. COCHISE Studies

Contents

2.1 COCHISE: Experiments

by

W. T. Rawlins
S. M. Miller

1. INTRODUCTION

Recent experiments using the COCHISE facility have investigated the kinetics and spectroscopy of potential auroral radiators in the short-wavelength (SWIR, 2-4 μm) and middle-wavelength (MWIR, 4-8 μm) infrared spectral regions. The band systems investigated include the NO fundamental and overtone bands near 5.4 and 2.7 μm, respectively, the CO fundamental band near 4.7 μm, and numerous electronic bands of N_2 between 2 and 6 μm. The NO and CO features are excited by interactions of O_2 and CO with the effluents of Ar/N_2 discharges, and the N_2 features may reflect the nature of energy-carrying metastables that are formed in such discharges. Consequently, conclusive studies of the excitation kinetics for these features require parametric investigations as functions of N_2/Ar flow conditions through the discharges. We report here the results of preliminary scoping experiments, and their implications for future measurements.

In addition, we have carried out a series of measurements to assess the potential for the formation of vibraluminescent N_2O in a chemical reaction between N_2 and vibrationally excited $O_3(v)$. We will discuss the experimental data and a preliminary analysis of the results, and will examine the potential of further experimentation along these lines.

5

In support of the on-going COCHISE studies, we have initiated theoretical investigations into the kinetics of excitation processes in microwave discharges. The ultimate goal of this effort is to predict the concentrations of energy-carrying metastable species in O_2/Ar and N_2/Ar discharges. Much of the information developed in this effort will be directly transferable to modeling of auroral excitation phenomena.

2. EXPERIMENTAL METHODS

All the experiments are performed in the standard COCHISE configuration using balanced mass flow rates of discharged and counterflow gas at ~ 0.1 g/sec. Ar is used as the diluent for the discharge gas mixture with 1-10 percent levels of N_2 or O_2. Typical discharge conditions are 1.3 Torr, 80-100 K, 50 W. The effluents of the microwave discharges interact in the low-pressure (~ 4 mTorr) reaction zone with counterflows of O_2, Ar, N_2, or mixtures of Ar and CO. The choices of discharge and counterflow constituents are dictated by the specific excitation process being investigated.

Infrared emission from the interaction zone is observed by the scanning monochromator with a typical spectral resolution of ~ 0.013 μm in first order (1-mm slits, 3-μm grating, 150 lines/mm, 0.5-m focal length). Order-sorting filters with cut-ons near 2 and 4 μm are used to isolate the 2-4 and 4-8 μm spectral regions. Spectral responsivities are determined by calibration with a 350-400 K blackbody and are typically in the range 2-5 $\times$ 10^5 V/(W cm^{-2} sr^{-1} μm^{-1}) between 2 and 8 μm.

3. RESULTS AND DISCUSSION

The experiments to be discussed here address three different but somewhat interrelated research topics: (1) fluorescence from NO(v) in the reaction of discharged N_2/Ar mixtures with O_2, and the accompanying emission from electronic states of N_2 excited in the discharges; (2) fluorescence from CO(v) excited by energy transfer from discharged Ar/N_2 mixtures, and the concomitant emission from hitherto unidentified species; and (3) emissions observed near 4-5 μm in the interaction of N_2 with discharged O_2/Ar mixtures. We discuss the results of preliminary scoping experiments and limited data analysis performed to date, as well as the definition of more detailed test matrixes for further investigations of each topic.

6

3.1 Fluorescence From NO and N_2

Previous COCHISE studies, done before the apparatus was refurbished, have addressed the kinetics and spectroscopy of vibraluminescence from the fundamental and overtone[1,2] bands of NO(v) produced in the interaction between discharged N_2/Ar mixtures and O_2. By a series of kinetic arguments, we concluded that the reaction responsible for the observed emission is[3]

$$N(^2D, \, ^2P) + O_2 \rightarrow NO(v) + O \quad . \tag{1}$$

In an attempt to measure the vibrational-state-dependent relative transition probabilities of the overtone and fundamental bands,[1] we observed, in a very limited data base, values similar to those predicted by the theory of Billingsley[4] over the range $4 \leq v' \leq 12$. This result is similar to that obtained in LABCEDE[5] for $3 \leq v' \leq 7$. However, the COCHISE results reported in Reference 1 were seriously affected by interference from neighboring emission bands; we previously identified[3] some of these bands as features of the $W^3\Delta \rightarrow B^3\pi$ system of N_2 (also known as the Wu-Benesch system). A conclusive delineation of the relative transition probabilities for levels $2 \leq v' \leq 13$ is needed for prediction of NO radiation levels at 2.7 μm in auroral events.

The improved flexibility and sensitivity of COCHISE allows us to revisit this problem to obtain conclusive results. Our approach employs: (1) improved spectral resolution (1-mm slits as opposed to 1.5-2.0 mm used earlier) to distinguish and identify the interfering radiators; (2) the use of reactive (O_2) and non-reactive (Ar, N_2) counterflows to aid in correcting the NO spectra for contributions from underlying radiators and from NO(v) formed from impurities in the discharges; and (3) a parametric study over at least an order of magnitude variation in N_2

1. Rawlins, W. T., Piper, L. G., Caledonia, G. E., and Green, B. D. (1981) Final Technical Report: COCHISE Research, Physical Sciences Inc., TR-298.

2. Kennealy, J. P., DelGreco, F. P., Caledonia, G. E., and Green, B. D. (1978) Nitric oxide chemi-excitation occurring in the reaction between metastable nitrogen atoms and oxygen molecules, J. Chem. Phys. 69:1574.

3. Rawlins, W. T., Piper, L. G., Green, B. D., Wilemski, G., Goela, J. S. and Caledonia, G. E. (1980) LABCEDE and COCHISE Analysis II, Volume I, AFGL-TR-80-0063(I) Final Report, Contract F19628-77-C-0089, Physical Sciences Inc., AD A112253.

4. Billingsley, F. P. (1976) Calculated vibration rotation intensities for NO($X^2\pi$), J. Mol. Spectr. 61:53.

5. Green, B. D., Caledonia, G. E., and Murphy, R. E. (1981) A determination of the nitric oxide Einstein coefficient ratios, J. Quant. Spectr. Radiat. Transfer. 26:215.

mole fraction in the discharge gas, to aid in identifying the background radiators and to provide supporting kinetic data on the NO precursors, that is, to distinguish between $N(^2D)$, $N(^2P)$, and excited states of N_2.

3.1.1 NO FUNDAMENTAL BAND

Spectra obtained for the highest and lowest N_2 flows, with O_2 and Ar counter-flows, are shown in Figures 1-4. The band between 5.25 and 7.0 μm is predominantly fluorescence from NO $(1 \leq v' \leq 14)$ produced from Reaction (1). Preliminary least squares analysis of the spectral distribution of Figure 1 gives relative vibrational populations consistent with those reported by Reference 3; however, Figures 3 and 4 show that there is a small but significant contribution from NO(v) formed in the discharge by impurities. We have since taken steps to reduce leakage of air into the discharge mixture, and future analysis will employ subtraction of each observed background spectrum prior to spectral fitting.
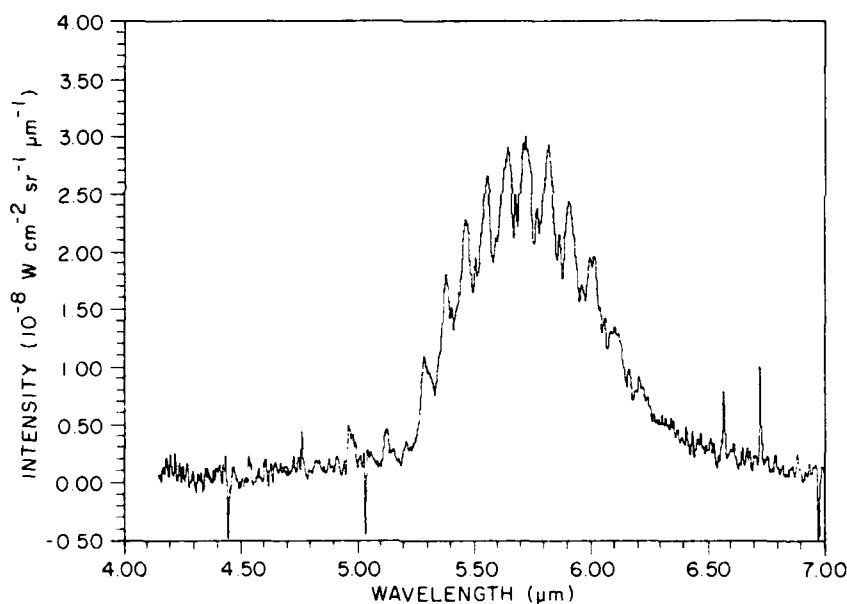
Figure 1. NO Fundamental Band, 12.1 Percent N_2 in N_2/Ar Discharge, 100 Percent O_2 Counterflow

Comparison of the intensities in Figures 1 and 2 shows that the NO(v) fluorescence intensity decreases by only about 20-30 percent when the N_2 flow rate admitted to the discharge is decreased by a factor of 13.7. This indicates that the discharge-produced precursor of NO(v) is a species whose yield from the discharge is insensitive to N_2 number density. This is characteristic of the atomic

8
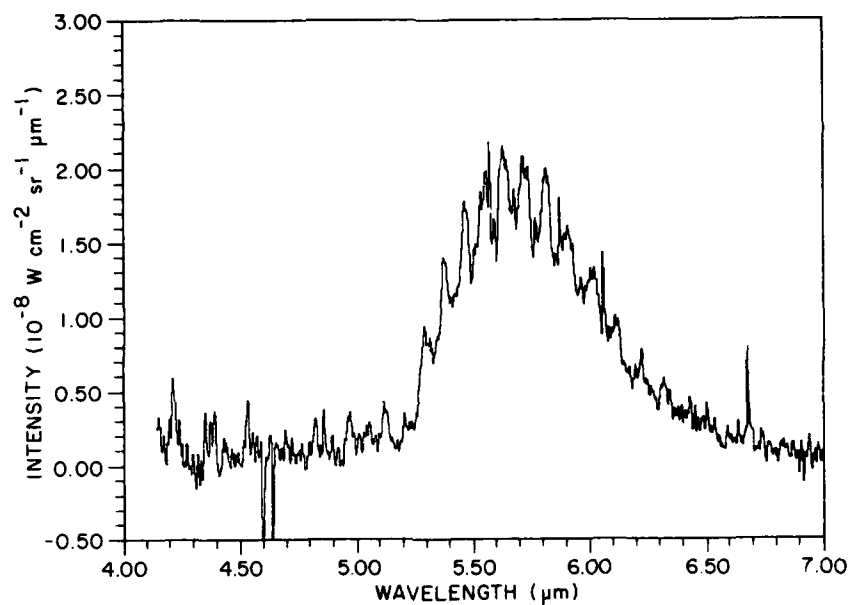
Figure 2. NO Fundamental Band, 1.04 Percent N_2 in N_2/Ar Discharge, 100 Percent O_2 Counterflow
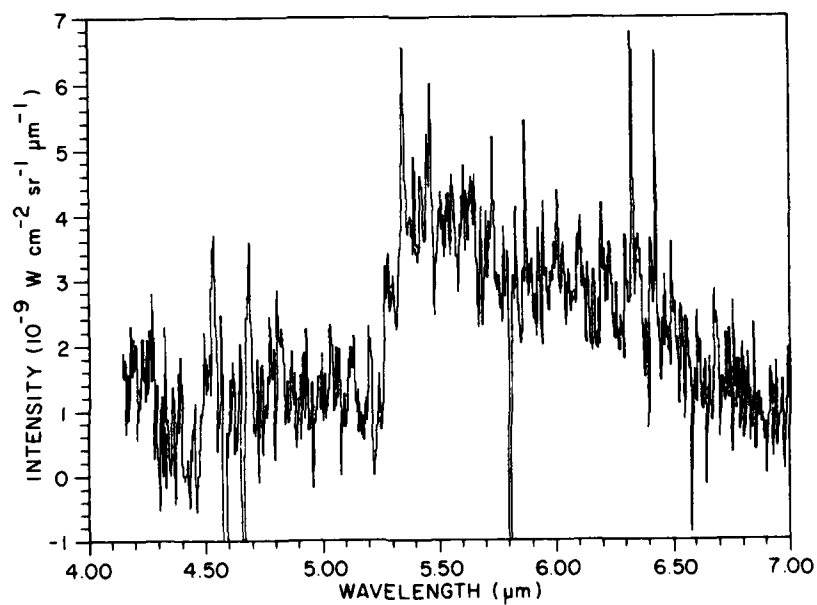
Figure 3. NO Fundamental Band, 12.1 Percent N_2 in N_2/Ar Discharge, 100 Percent Ar Counterflow

9

Figure 4. NO Fundamental Band, 1.04 Percent N_2 in N_2/Ar Discharge, 100 Percent Ar Counterflow

metastables, $N(^2D, ^2P)$, but not of excited molecular species, which show pronounced "quenching" at higher N_2 levels.[6] It remains to be seen whether contributions from $N(^2D)$ and $N(^2P)$ can be separated by this approach; detailed characterization of metastable yields from similar discharges is in progress on the FAKIR apparatus. The spectral distributions in Figures 1 and 2 exhibit only minor variations; more data are required to establish a statistical basis for these differences. At present, there is no indication for more than one excitation mechanism, in accord with the conclusions of Reference 3.

The results of Reference 3 for v' = 1 were compromised by weak, overlapping contributions from an unidentified radiator near 5.2 μm. In our present work, we are attempting to isolate and identify these bands and to correct the NO data for their presence. The interfering radiation appears in Figures 1-4 as a group of features between 4.9 and 5.3 μm. Other features near 4.2, 4.5, and 4.8 μm are also observed and exhibit kinetic behavior similar to that of the 5 μm group. These features do not appear to be related to Ar Rydberg emission observed in the

6. Piper, L. G., and Rawlins, W. T. (1983) COCHISE Atmospheric Nitrogen/Oxygen Excitation Studies: Studies on Metastable Nitrogen Atoms, Physical Sciences Inc., PSI TR-411.

absence of added N_2.[7] It is especially interesting to note that (1) the band inten-
sities depend upon N_2 flow in much the same way as the NO emission intensity,

Figure 6. NO Overtone Region, 12 Percent N_2 in N_2/Ar
Discharge, 100 Percent O_2 Counterflow

Figure 7. NO Overtone Region, 1 Percent N_2 in N_2/Ar
Discharge, 100 Percent O_2 Counterflow

13

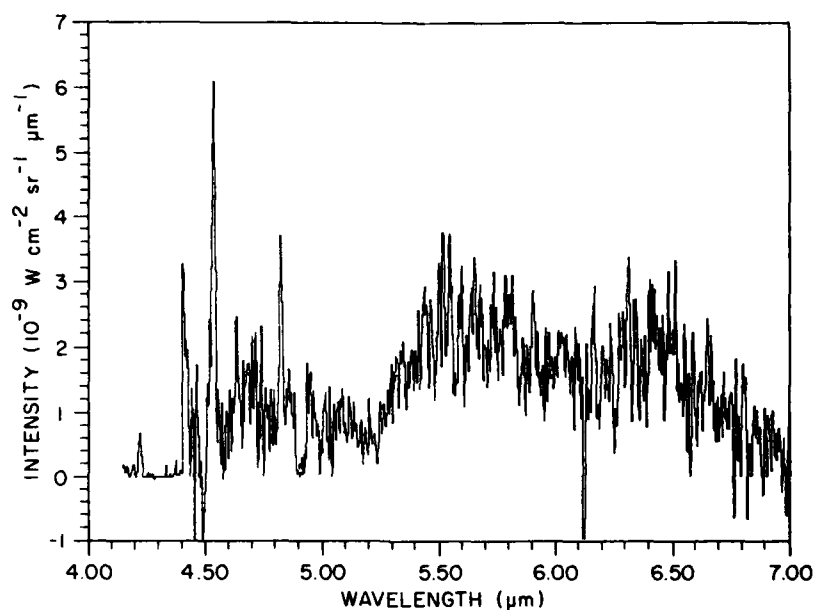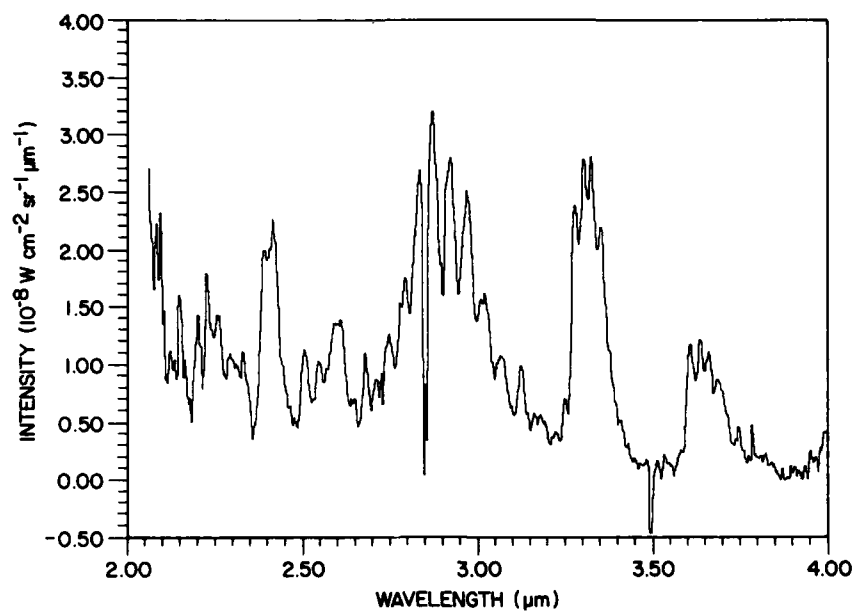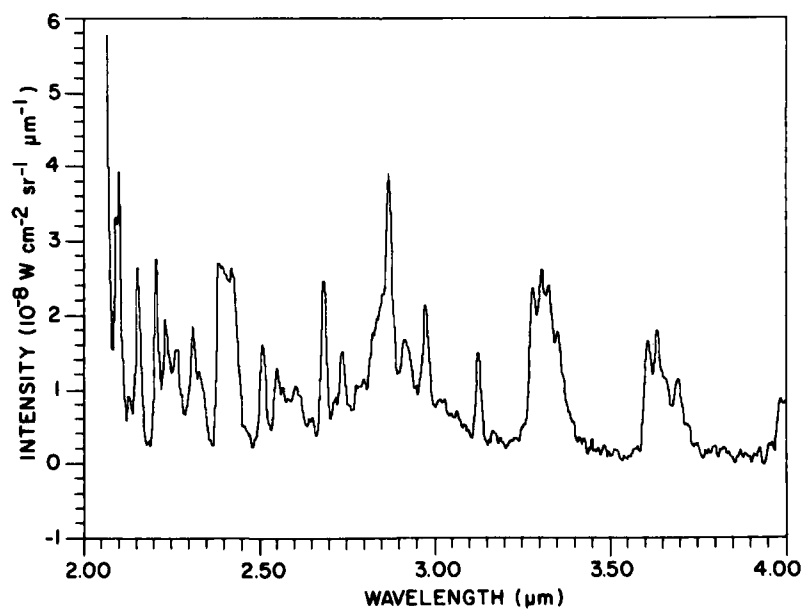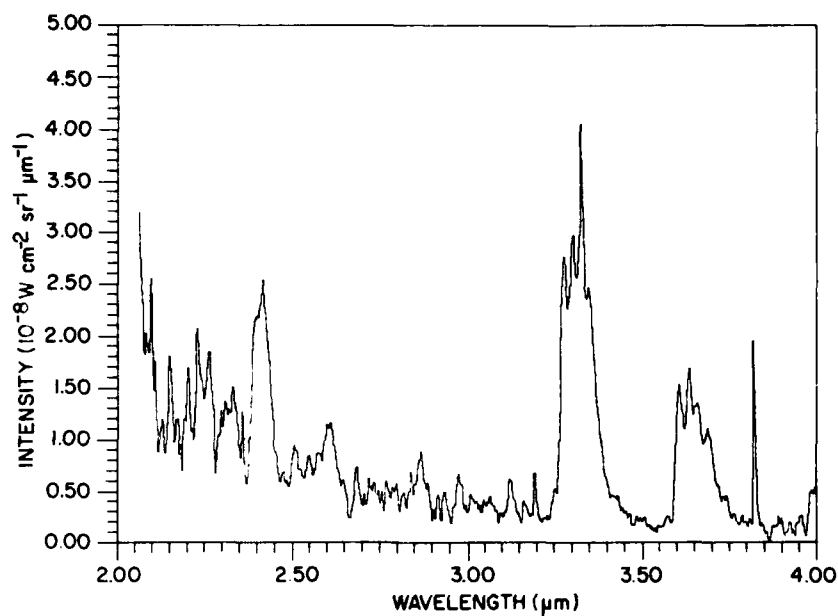Figure 8. NO Overtone Region, 12 Percent N_2 in N_2/Ar Discharge, 100 Percent Ar Counterflow

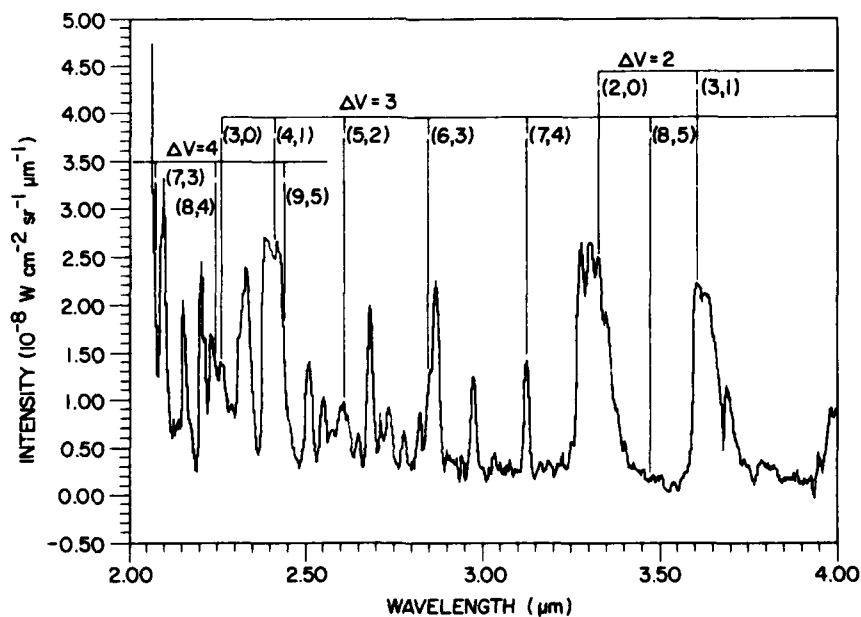Figure 9. NO Overtone Region, 1 Percent N_2 in N_2/Ar Discharge, 100 Percent Ar Counterflow. Band centers for N_2 $W(^3\Delta) \rightarrow B(^3\pi)$ (Wu-Benesch) transitions are indicated

14

in the discharge to minimize the interfering emissions, and we will correct for these features by subtracting out the background spectra.

The emission features observed between 2 and 4 μm appear to be primarily due to electronic transitions from high-lying states of N_2 that are excited in the discharge and survive the traversal into the field of view. The band intensities increase substantially when the N_2 mole fraction is decreased, suggesting discharge-related kinetic effects. Furthermore, the intensities decrease by only a factor of ~ 2 when the counterflow gas is turned off, meaning that the radiation arises from discharge-excited species that survive to reach the field of view rather than from scattered light or species excited within the field of view. Finally, the intensities of most of the features are only weakly affected by switching from Ar to O_2 counterflow, so the counterflow interaction has only a small effect on the excited state distributions.

The transitions observed here do not correspond to any known Rydberg transitions of Ar[7] or N,[8] and therefore appear to be electronic bands of N_2. While it is important to understand and remove the interference of these bands with the NO overtone band for the present experiments, these N_2 bands are worthy of study in their own right because they may be excited in the electron-disturbed upper atmosphere. These emissions could not only affect high-altitude sensors, but may also serve as diagnostics for highly energetic forms of N_2 formed in auroras. The energy carried by these metastable species will ultimately degrade to IR radiation through chemical reaction and energy transfer processes. For this reason, we have examined the spectra of Figures 6-9 to determine the feasibility of utilizing COCHISE to ivestigate the spectroscopy and kinetics of discharge-produced excited nitrogen, N_2^*. While the spectral analysis is far from complete, we are able to assign many of the features and to infer the identities of several others. Further investigations will be aided by an improved data base under conditions similar to those in Figure 9, with higher spectral resolutio. vhere possible, and with a spectral simulation/fitting analytical procedure. We summarize here the results of our first-pass inspection of the data.

The most prominent features of the spectrum are the $\Delta v = 2$ and $\Delta v = 3$ sequences of the $W^3\Delta - B^3\pi$ (Wu-Benesch) system; we have identified these bands in previous COCHISE SWIR spectra.[2] A computed spectrum of the W $\rightarrow$ B transitions, assuming unit relative vibrational state populations in the upper electronic state, is shown in Figure 10. This spectrum was computed using the best available spectroscopic data; a detailed discussion of these calculations will appear in

---

8. Biemont, E., and Grevesse, N. (1973) Infrared wavelengths and transition probabilities for atoms, $3 \leq z \leq 20$, Atomic Data and Nuclear Data Tables 12:217.
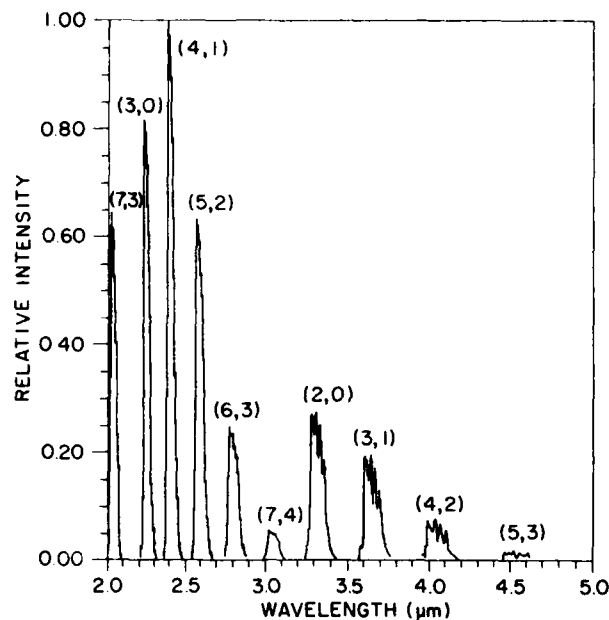
Figure 10.   Computed Band Shapes for N_2 $W^3\Delta \rightarrow B^3\pi$
Transitions, Assuming T = 80 K, $\delta\lambda$ = 0.013 μm, and
Unit Populations of the Upper States

future reports (P. F. Lewis, in preparation).   The (2,0), (3,1), and (4,2) bands
are readily identifiable between 3.3 and 4 μm.   Furthermore, the observed rela-
tive intensities suggest similar populations in the v' = 2, 3, 4 levels of the W state
for the low N_2 case.   In the Δv = 3 sequence between 2 and 3 μm, the transitions
are somewhat less prominent, but the (3,0), (4,1), and (5,2) transitions can be
identified.   However, the intensity distributions in this sequence compared to those
with the same v' in the Δv = 2 sequence are not in accord with the computed spec-
tra, perhaps due to uncertainties in the computed transition probabilities or, more
likely, to an artifact of the blackbody calibration at short wavelengths.   We will
attempt to verify the blackbody calibration in future experiments, and will con-
sider using a hotter blackbody to facilitate calibration below 2.5 μm (see next sec-
tion).   The (6,3) transition is more difficult to identify, as the 2.8 μm feature
peaks at slightly longer wavelength.   The feature near 3.1 μm corresponds well to
the expected wavelength of the (7,4) transition, but its intensity in the low N_2 case
is surprisingly large relative to those for lower v'.   The (8,5) transition near
3.5 μm is not evident.   Many of the other features in the 2-3 μm region correspond
well to expected wavelengths for transitions of the $B^3\pi$ - $A^3\Sigma$ system: (7,13),
(1,5), and (4,9) near 2.2 μm; (6,12), (0,4), and (3,8) near 2.4 μm and (5,11) near
2.7 μm.   The highest excited levels observed correspond to energies of ~8.5 eV

in the discharge-excited products. The states observed have radiative lifetimes of typically several hundred μsec, which is similar to the sum of the ~ 500 μsec cell transit time and the ~ 300 μsec residence time in the field of view. We emphasize that many of these assignments are extremely tentative and cannot be made conclusively without a detailed bandshape analysis (that is, spectral fitting) and a more consistent data base.

Many prominent transitions cannot yet be identified even tentatively, but may arise from the long-postulated $A^3\Sigma$ - $B^3\pi$ system or from electronic transitions in the singlet manifold of N_2. For example, the strong feature near 3 μm corresponds well to the (10,0) transition of the A-B system. Complete analysis of these types of spectra under various discharge and counterflow conditions would provide valuable spectroscopic data on relative transition probabilities, N_2^* excitation and energy transfer mechanisms, and vibrational and electronic redistribution processes within the B, W, and vibrationally excited A states. This information is closely related to recent observations in FAKIR of energy transfer in discharge-excited N_2/Ar mixtures.[6] Further analysis of the present data base will continue, but more definitive experiments will be conducted in the near future.

3.1.3 NO OVERTONE/FUNDAMENTAL RATIO

We have performed a first-pass least squares fitting analysis of a matched pair of NO overtone and fundamental spectra obtained at high N_2 flow. The spectra were not corrected for background radiation, nor were the computed fits optimized for rotational temperature. The results are consistent with those obtained previously,[1] namely that the Einstein coefficient ratios for each v' agree with the Billingsley[4] theory for v' > 4 but deviate significantly at lower v'. This deviation is in the direction of too much apparent radiation in the overtone band at low v', and is at least partially an artifact due to the background radiation near 2.7 μm. We will develop background correction techniques before pursuing the spectral fitting any further. Also, we will develop a more substantial data base of matched pairs of NO spectra at high N_2 flows to establish a good statistical base.

A crucially important consideration in these measurements is the accuracy of the blackbody calibration at short wavelengths. This is especially important in comparing radiation measurements at 5.4 and 2.7 μ, since the maximum blackbody temperature we can use is only 400 K. At this temperature, the short-wavelength range of the apparatus is well into the steep portion of the blackbody radiation curve; the spectral radiance of the blackbody drops by a factor of ~ 250 in going from 4 μm down to 2 μm, presenting difficulties in accurately defining the system responsivity below 2.5 μm. Furthermore, the calibration in this wavelength range will be much more sensitive to uncertainties in the blackbody temperature. The blackbody spectral radiance in W cm^{-2} sr^{-1} μm^{-1} is given by:

17

$$N_\lambda = \frac{11909}{\lambda^5} \left(e^{14388/\lambda T} - 1 \right)^{-1} \quad , \tag{2}$$

where λ is in μm. For cold blackbodies at short wavelengths, that is, for $\lambda T < 3 \times 10^3$, Eq. (2) reduces to

$$N_\lambda = \frac{11909}{\lambda^5} e^{-14388/\lambda T} \quad . \tag{3}$$

Then

$$\frac{dN_\lambda}{dT} = N_\lambda \frac{14388}{\lambda T^2} \tag{4}$$

and

$$\frac{\delta N_\lambda}{N_\lambda} = \frac{14388}{\lambda T} \frac{\delta T}{T} \quad . \tag{5}$$

We see from Eq. (5) that, for a 400 K blackbody source, the uncertainty in the absolute calibration is 18 $\delta T/T$ at 2 μm and 7.2 $\delta T/T$ at 5 μm. The relative uncertainty in ratio measurements for these two wavelengths would then be the square root of the sum of the squares or 19.4 $\delta T/T$. Thus, it is necessary to determine $\delta T/T$ to confirm the accuracy of the ratio measurements.

Values of $\delta T/T$ will be inferred from ratios of blackbody measurements at two different temperatures. The observed signal in Volts is

$$S = F(\lambda)N_\lambda \quad , \tag{6}$$

where $F(\lambda)$ is the spectral responsivity of the optical system. At a given wavelength and two temperatures $T_1 < T_2$,

$$\frac{S_2}{S_1} = \frac{e^{-14388/\lambda T_2}}{e^{-14388/\lambda T_1}} = e^{\frac{14388}{\lambda} \left(\frac{1}{T_1} - \frac{1}{T_2} \right)} \quad . \tag{7}$$

Then

$$\ln S_2/S_1 = \frac{14388}{\lambda} \frac{T_2 - T_1}{T_1 T_2} \quad . \tag{8}$$

Therefore, plots of $\ln S_2/S_1$ vs $14388/\lambda$ for blackbody scans at different nominal temperatures, for example, 400 and 350 K, will have slopes $(T_2 - T_1)/T_1 T_2$. The deviation of the observed slope from the expected one should allow an assessment of the uncertainty in T. A more detailed approach could also be employed, plotting $1/S\lambda^5$ vs $1/T$ for several different wavelengths to obtain slopes $14388/\lambda$ as described in Reference 1. However, this would require about ten blackbody scans at various temperatures, and may not be necessary if implementation of Eq. (8) provides sufficient confirmation of the calibrations.

One possible option in dealing with the $2-2.5$ μm calibration problem is to use a higher-temperature blackbody source. A commercial source capable of 800 K has been used in the past in COCHISE, but was very expensive and presented severe problems in the determination of its actual radiometric temperature.[1] This probably occurred because the epoxy attaching the thermocouple to the cavity failed at cryogenic temperatures. Conversely, the low-temperature epoxy on the present source is susceptible to failure near or above 200 F (366 K). Thus, it is not clear there is an easy solution to the problem. The major advantage is raising the blackbody temperature from 400 to 800 K lies in the 4-order-of-magnitude increase in intensity at 2 μm rather than in the factor-of-2 decrease in sensitivity to temperature uncertainties shown in Eq. (5). Increasing the intensity near 2 μm is important for defining the system responsivity near the short-wavelength cutoffs of both the 2 μm long-pass filter and the Ge optical components. However, it may be possible to achieve a satisfactory solution at 400 K merely by making some measurements at the largest possible slit width, that is, 3 mm as opposed to the usual 1 mm setting employed in calibration measurements. This will enhance the signal by a factor of 9. We will address these calibration questions in a series of COCHISE measurements in the near future.

3.2 Interaction of N_2^* With CO

The excitation of CO(v) by energy transfer from discharged N_2 has been observed for several years in COCHISE,[9] but has not been definitively studied. The interaction has been used routinely to provide a wavelength calibration; the band center of the CO($1\rightarrow0$) transition is at 2143 cm^{-1}. However, as we shall see below, the interaction is extremely complicated, and a meaningful study must explore a large parameter space.

9. Caledonia, G. E., Green, B. D., and Simons, G. A. (1977) LABCEDE and COCHISE Analysis. Volume I. Final Report, Physical Sciences Inc., PSI TR-83.

19

In the wavelength calibration measurements, fluorescence between 4.5 and 5.2 μm from vibrationally excited CO is observed in the reaction zone upon the interaction of discharged Ar/N_2 mixtures with counterflow mixtures of CO diluted in O_2, N_2, or Ar. Presumably, the v' = 1 level of CO is readily excited by rapid V-V transfer from $N_2(v)$ produced in the discharge, but the presence of higher-v' fluorescence at longer wavelengths has not been explained. In an earlier discussion,[9] multi-quantum V-V transfer from $N_2(v)$ to CO was suggested as a source of the higher levels of CO. Multi-step sequences of V-V "pumping" of CO(v' = 1) by itself or $N_2(v)$ have not yet been ruled out, but are unlikely in the near-single-collision conditions of COCHISE. Also, in the early work of Reference 9, a single spurious spectral scan showed the presence of an unusual spectral signature, which was then suggested to be due to vibrationally excited CN. We are not able to reproduce this observation under controlled conditions, at higher resolution, and with better wavelength accuracy, and have found that the original assignment was incorrect (see next paragraph). However, CN electronic fluorescence has been observed in mixtures of active N_2 and CO,[10] and we cannot yet rule out the possibility of its formation in the COCHISE experiments.

In addition to $N_2(v)$, electronically excited N_2^* and $N(^4S, ^2D, ^2P)$ can interact with CO. The N_2^* process is likely to lead to direct E-V or E-E,V energy transfer from N_2^* to CO rather than chemical reaction, owing to the "stiffness" of the two bands relative to those of NCO and to the four-center nature of the reaction to form CN and NO. (However, vibrational energy in the CO molecule could lead to a different result.) The reaction

$$N(^4S) + CO \rightarrow CN + O \tag{9}$$

is endoergic by 76.9 kcal/mol, and would thus require CO(v' > 13) to proceed at low temperatures. Similarly, the reaction

$$N(^2D) + CO \rightarrow CN + O \tag{10}$$

is endoergic by 21.9 kcal/mol and would require CO(v' > 4). It seems unlikely that such secondary processes involving CO(v) as a reaction partner would be significant under our conditions. However, $N(^2D)$ can transfer energy in an E-V process:

$$N(^2D) + CO \rightarrow N(^4S) + CO(v < 9) \quad . \tag{11}$$

---

10. Stair, A. T., Jr., Kennealy, J. P., and Murphy, R. E. (1967) A study of some inelastic collision processes using active nitrogen and carbon monoxide, J. Chim. Physique, 1:52.

This reaction proceeds with a total rate coefficient of about 2×10^{-12} cm^{-3} at room temperature. (The kinetics of quenching of N(^{2}D, ^{2}P) by CO have been studied by several previous investigators (see Reference 6), but the reported rate coefficients are in considerable disaccord. We are currently pursuing definitive measurements on the FAKIR flow reactor.) The reaction with N(^{2}P),

$$N(^2P) + CO \rightarrow CN + O \tag{12}$$

is exoergic by 5.1 kcal, but there is no adiabatic route for this process.[11] Furthermore, vibrationally excited CN cannot be formed directly unless the reactant CO is vibrationally excited. Thus, we find no direct routes for formation of CN(v) in the primary processes occurring in the reaction zone, and only a relatively slow route for possible formation of CN(v = 0), that is, Reaction (12). CN(v) fluorescence would then have to arise from secondary and tertiary processes and is therefore expected to be very weak at best. The quenching of N(^{2}P) can proceed by two branches:

$$N(^2P) + CO \rightarrow N(^2D) + CO(v < 4) \tag{13}$$

$$N(^2P) + CO \rightarrow N(^4S) + CO(v < 15) \quad . \tag{14}$$

We conclude from this discussion that the primary *interaction between discharged* N$_2$ and CO will consist of excitation of CO(v) by energy transfer from N$_2$(v), N(^{2}D), and N(^{2}P), and possibly excitation of electronically excited CO by energy transfer from N$_2$ metastables. Formation of CN and excitation of CN(v) or CN* can only occur through secondary and tertiary processes initiated by reactions of CO(v), and should not be observable in the COCHISE experiments.

The experiments discussed here were performed using discharge gas mixtures of 3-12 percent N$_2$ diluted in Ar, at reaction zone pressures of 4.5-5.0 mTorr and nominal gas temperatures of 80-100 K. The range of CO number density in the reaction zone was $2\text{-}12 \times 10^{13}$ cm^{-3}, in considerable excess over the $10^{9\text{-}10}$ cm^{-3} ranges we expect for N(^{2}D, ^{2}P). Fluorescence measurements were made in two modes of discharge operation, modulated at 23 Hz (that is, the normal mode employed in other COCHISE studies), and CW, where the fluorescence is modulated by the tuning fork chopper. Spectra for the two different modes and several combinations of N$_2$ and CO flow rates are shown in Figures 11-17.

---

11. Donovan, R. J., and Husain, D. (1970) Recent advances in the chemistry of electronically excited atoms, Chem. Rev. 70:489.
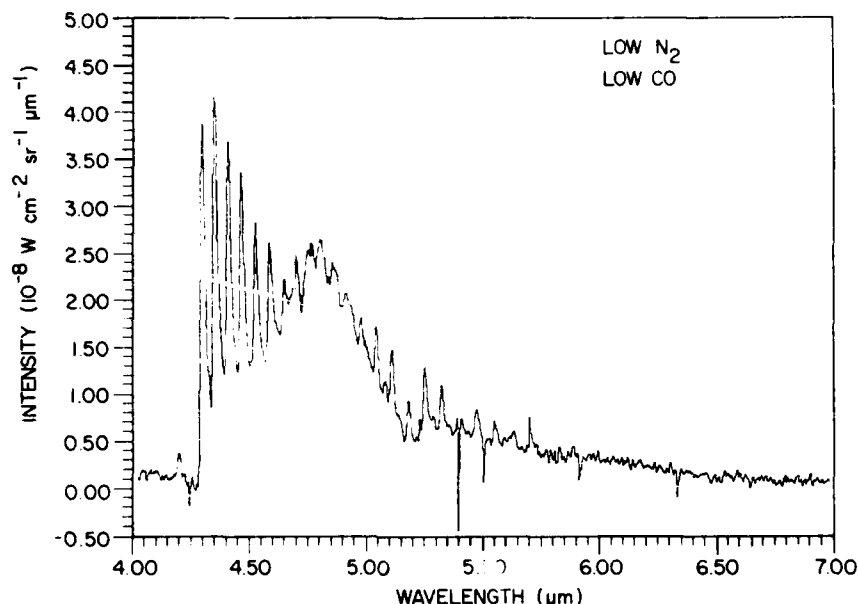
Figure 11. CO Fundamental Band Region, AC Discharges.
Discharge mixtures, 2.9 percent N_2 in Ar; Counterflow
mixture, 8.6 percent CO in Ar. $[CO] \cong 2 \times 10^{13}$ cm^{-3} in the
mixing zone. T = 80 K, P = 4.5 mTorr, $\delta\lambda$ = 0.013 μm

    The spectra obtained with the modulated (AC) discharges are shown in Figures
11-14 for combinations of high and low flow rates of N_2 and CO. Several different
spectral signatures appear in these data. The CO(v = 1) → CO(v = 0) band is prom-
inent for high N_2 flow rates (Figures 13 and 14) and can be recognized by its sharp
band center near 4.7 μm and its relatively broad R and P branches peaking near
4.6 and 4.8 μm, respectively. The resolution of the AC measurements is 0.013
μm, which is insufficient to resolve the rotational structure of CO. Fluorescence
from the higher vibrational levels of CO will extend to longer wavelengths (com-
pare with Figures 15-17), and may be responsible for the general envelope of the
spectra extending to ~5 μm. Weak fluorescence between 5.2 and 6 μm may be due
to NO formed in the discharges from trace impurities in the Ar/N_2 mixture. The
most striking feature of these spectra is the sharply structural set of features that
appear throughout. These features fall into two categories: (1) a grouping of 5-6
"lines" that lie between 4.3 and 4.6 μm, and which appear consistently in all spec-
tra; and (2) a system of transitions extending to longer wavelengths, most promin-
ent at high N_2 and low CO (Figure 13). We measured the phase differences of the
various features relative to ArI radiation scattered from the discharges. These
measurements show that the CO-related fluorescence is out of phase with the dis-
charges by 550 μsec for the 4.3 μm system, 680 μsec for the CO(1 → 0) band, and

22

Figure 12. CO Fundamental Band Region, AC Discharges. Discharge mixture, 2.9 percent N_2 in Ar; Counterflow mixture, 45.5 percent in Ar. [CO] $\cong 1.2 \times 10^{14}$ cm^{-3} in the mixing zone. Other conditions are the same as in Figure 11

~ 1000 μsec for the sharp, longer wavelength features. These values are to be compared to our estimated values of ~ 500 μsec for transit from the discharge tube outlet to the center of the reaction cell and ~ 300 μsec for the residence time in the field-of-view. Thus, the appearance of the 4.3 μm system and the CO(1 $\rightarrow$ 0) fluorescence are consistent with direct excitation within the field-of-view, but the longer wavelength features are not. These features must then arise from secondary processes, perhaps involving species that have returned to the field-of-view following collisions with the cell walls.

The sharp, line-like features between 4.7 and 6.5 μm are strongest at lower flows of CO. We have occasionally observed these features even in the absence of added CO, provided CO had previously been used as a reagent. These are essentially the same features as those that were previously thought[9] to be CN(v). Examination of these new spectra shows that the band centers of the CN ($\Delta v = 1$) transitions are ~ 10 cm^{-1} to the blue of each observed peak above 4.9 μm, but the band centers of CO($\Delta v = 1$) transitions correspond exactly with each peak. The narrowness of the features must result from an extremely low rotational temperature, which tends to collapse all the intensity into low J' transitions in the P-branch. The spectrum of Figure 13 is replotted in Figure 18; this should be compared to the computed vibrational basis functions (no population weighting) for CO
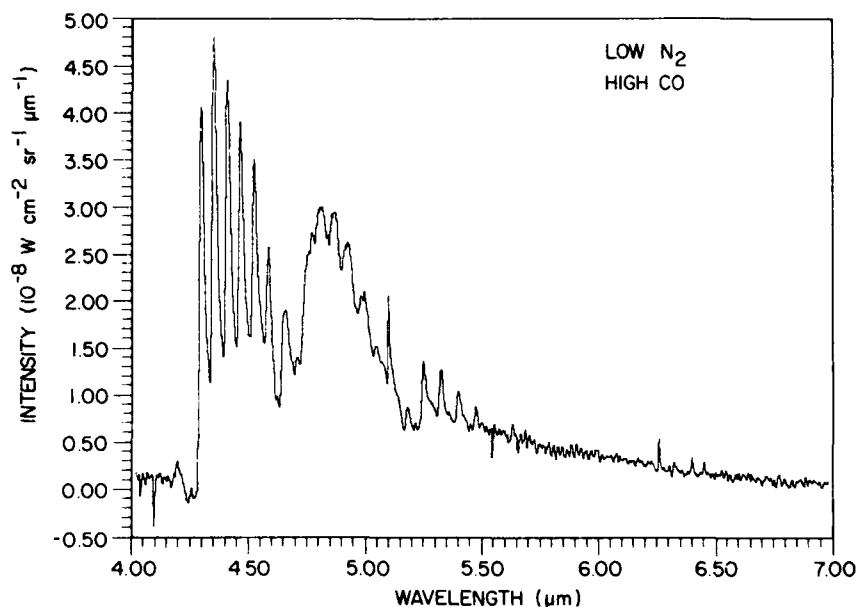
23

Figure 13. CO Fundamental Band Region, AC Discharges. Discharge mixture, 12 percent N_2 in Ar; Counterflow mixture, 8.6 percent CO in Ar. [CO] $\cong 2 \times 10^{13}$ cm^{-3} in mixing zone. Other conditions as given in Figure 11

at 5 K shown in Figure 19. The correspondence between computed and observed features is exact. We conclude that the sharp spectral features between 4.7 and 6.5 μm are due to (Δv = 1) transitions from rotationally cold CO. It seems likely that the excited CO has re-entered the field-of-view following multiple collisions with the wall and with other molecules. The observed rotational temperature appears to be < 10 K, which is somewhat colder than we might expect for the reaction cell walls (10-15 K), but may not be inconsistent in view of the difficulty of determining absolute hardware temperatures in this range. The spectrum of Figure 13 shows contributions from as high as v' = 23. This corresponds to an excitation level of ~ 5.4 eV. The excitation could arise from transfer from N_2(v) or N_2^* metastables, or from deactivation of electronically excited CO formed by N_2^*. In any case, it appears that the fluorescence results at least partially from multicollisional processes occurring outside the field-of-view and, as such, will be difficult to characterize more fully. The addition of more CO seems to diminish their relative contribution, probably because of the enhanced rate of direct excitation of CO(v). It should be noted that, due to the phase lag between the direct and indirect CO excitation spectra, it is often difficult to optimize the phase setting for the direct fluorescence. This problem can be alleviated by using the CW-discharge mode (see below).
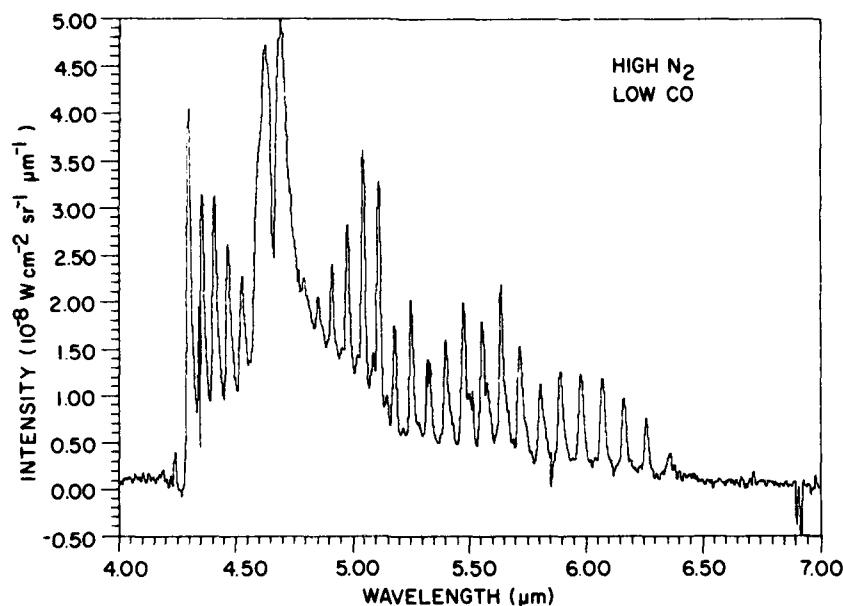
24
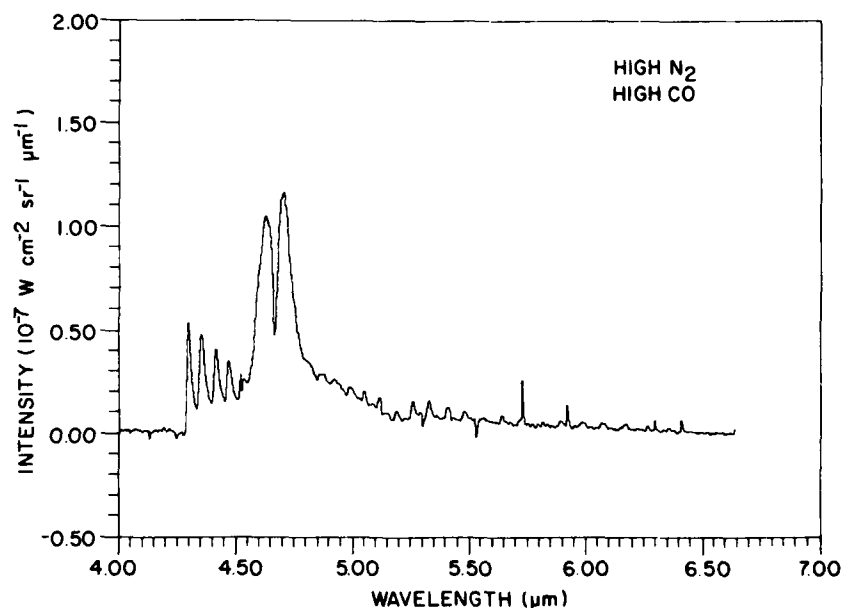
Figure 14. CO Fundamental Band Region, AC Discharges. Discharge mixture, 12 percent N_2 in Ar; Counterflow mixture, 45.5 percent CO in Ar. Other conditions as given in Figure 11

The other CO-related grouping which remains to be identified is the set of features near 4.3 μm. A high resolution scan (0.007 μm, 3.7 cm^{-1}) is plotted in frequency space in Figure 20. The features appear as five sharp-headed, red-degraded bands beginning at 2325 cm^{-1} and progressing to the red with a spacing of (29 ± 2) cm^{-1}. A sixth peak near 2180 cm^{-1} underlies the R-branch of the CO(1 → 0) band. The intensities of these peaks vary in much the same was as that of the CO($\Delta v = 1$) band with variations in CO flow. These features could be due to either vibration-rotation transitions or electronic bands of some molecule present in the reaction chamber. If they are vibration-rotation bands, the rotational temperature would have to be extremely low to account for the narrowness of the bands. If the system is treated as ($\Delta v = 1$) transitions of a diatomic molecule, the spectroscopic parameters are $\omega_e = 2354$ cm^{-1} and $\omega_e x_e = 14.5$ cm^{-1}. These values are startlingly close to those for $N_2(X^1\Sigma)$, 2358.57, and 14.324 cm^{-1}. Of course, we do not expect $N_2(v)$ to radiate, except perhaps via a collision-induced dipole in the frozen matrix on the walls, and we do not understand why such radiation would occur only in the presence of CO. We will continue to pursue that possibility, since such an observation is likely to be unique. We have thus far been unable to identify any other species with these spectroscopic properties. We have also pursued the possibility of electronic transitions of CO, using the data in Krupenie's

25

Figure 15. CO Fundamental Band Region, CW Discharges.
Nominal flow conditions: discharge, 10 percent N_2 in Ar;
counterflow, 30 percent CO in Ar. T = 80 K, P = 3.5 mTorr,
$\delta\lambda$ = 0.007 μm

monograph.[12] However, there are no clear assignments, with the possible excep-
tion of the (0,6) band of the $d^3\Delta_i \rightarrow a^3\pi$ system, which falls at 2331 cm^{-1}. We will
pursue this tack in more detail with the spectral simulation code discussed in
Section 3.1. If this system is an electronic transition, other bands corresponding
to different values of Δv should be evident at other wavelengths. We plan to sur-
vey the 2-4 μm region in future experiments. If electronic states of CO are indeed
excited by energy transfer from N_2^*, there is potential for electronic transitions
in the LWIR to occur.

Measurements with the discharges operating CW produce substantially differ-
ent results (Figures 15-17). In these measurements, the 0.007 μm resolution
allows partial resolution of the rotational structure of CO, and the rotational dis-
tributions for all vibrational levels are similar to what one would expect for the
nominal gas temperatures of 80-100 K. In this case, the entire CO spectrum ap-
pears to be the result of direct excitation. A least squares spectral analysis of
one of the spectra is depicted in Figures 21-23. The (1-0) transition is prominent,
but as many as eight or nine vibrational levels of CO can be identified. This would

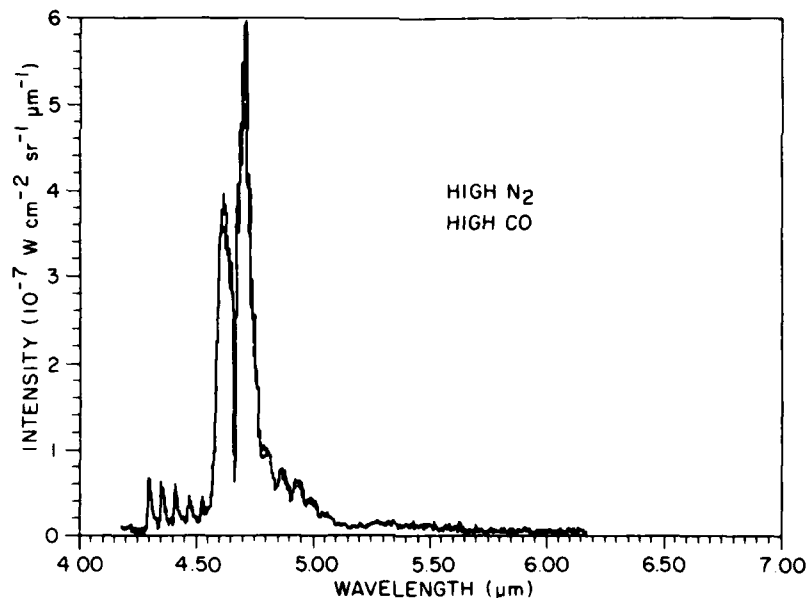12. Krupenie, P. H. (1966) The Band Spectrum of Carbon Monoxide, NSRDS-
     NBS-5.

26

Figure 16. CO Fundamental Band Region, CW Discharges. Nominal flow conditions: discharge, 10 percent N2 in Ar; counterflow, 4 percent CO in Ar. Other conditions as given in Figure 15

be consistent with excitation of CO by energy transfer from $N_2(v)$, which excites predominately $CO(v = 1)$, and from $N(^2D, ^2P)$, which could excite the higher levels. The $N_2(v)$ component is strong at higher N_2 flow, but disappears at low $N_2(v)$ in the discharge. The N^* component, however, is much less sensitive to N_2 flow, as we observed in the $NO(v)$ experiments described above.

The dependence of the intensity on CO flow rate is rather weak, but this is a consequence of the reduced metastable number density in the presence of CO. The kinetics are in steady state, according to:

$$\frac{d[CO(v)]}{dt} = k[N^*][CO] - k'[CO^*] = 0 \tag{15}$$

$$\frac{d[N^*]}{dt} = \phi_{N^*} - (k' + k[CO])[N^*] = 0 \tag{16}$$

where N^* denotes $N(^2D, ^2P)$ and/or $N_2(v)$, ϕ_{N^*} is the production rate of N^* from the discharges into the field-of-view, k is the rate coefficient for excitation of CO by N^*, and k' is the reciprocal of the residence time in the field-of-view. Combining Eqs. (15) and (16) gives
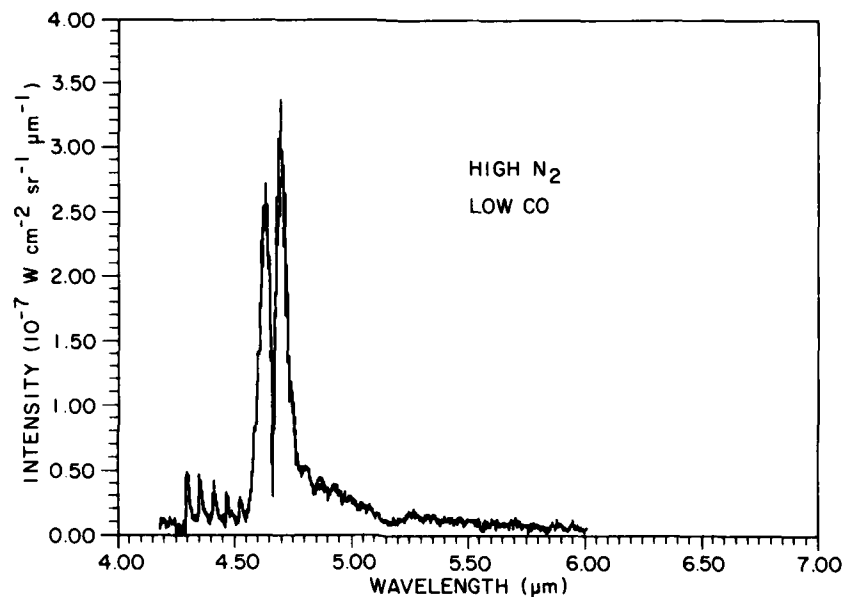
27
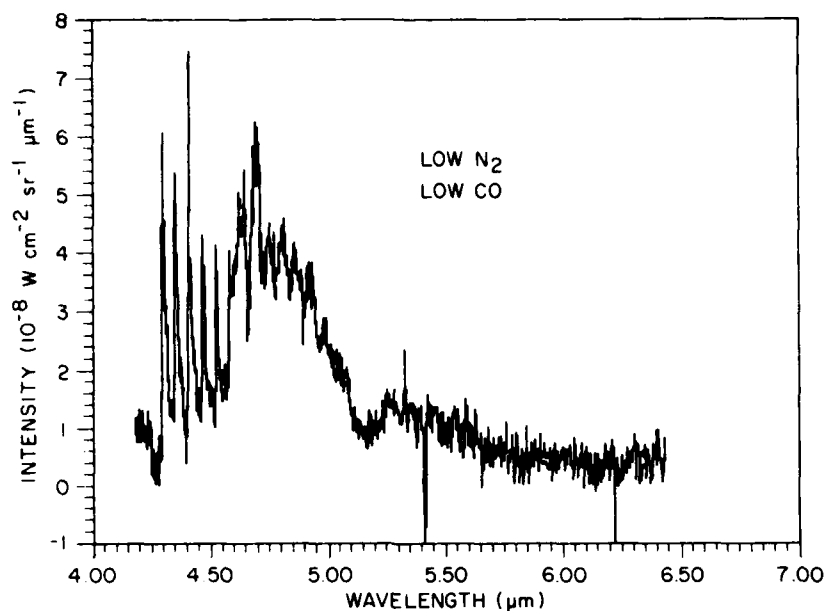
Figure 17. CO Fundamental Band Region, CW Discharges. Nominal flow conditions: discharge, 2 percent N2 in Ar; counterflow, 4 percent CO in Ar. Other conditions as given in Figure 15

$$[CO(v)] = \frac{k\phi_{N^*}[CO]}{k'(k' + k[CO])} \qquad . \qquad (17)$$

Thus, by studying the yield of CO(v) as a function of added CO, it should be possible to determine ϕ_{N^*} for a given discharge condition. Such measurements would be extremely useful as a calibration technique for other experiments, such as the NO(v) measurements.

Clearly, the CO excitation studies are in their infancy but have already raised several fascinating and important questions. Why do the AC and CW discharge methods give such disparate results? How does the rotationally cold CO(v) spectrum arise? What is the radiating species at 4.3 μm, and does it exhibit signatures in the SWIR and LWIR? Can we isolate the $N(^2D, {}^2P)$ and $N_2(v)$ mechanisms for pumping CO? Can we effectively use this reaction as a titration technique for determining $N(^2D)$ number densities? We will address these questions in future experimental studies on COCHISE, with supporting kinetic measurements on FAKIR. We must also perform a complete literature search on all aspects of the problem.

28
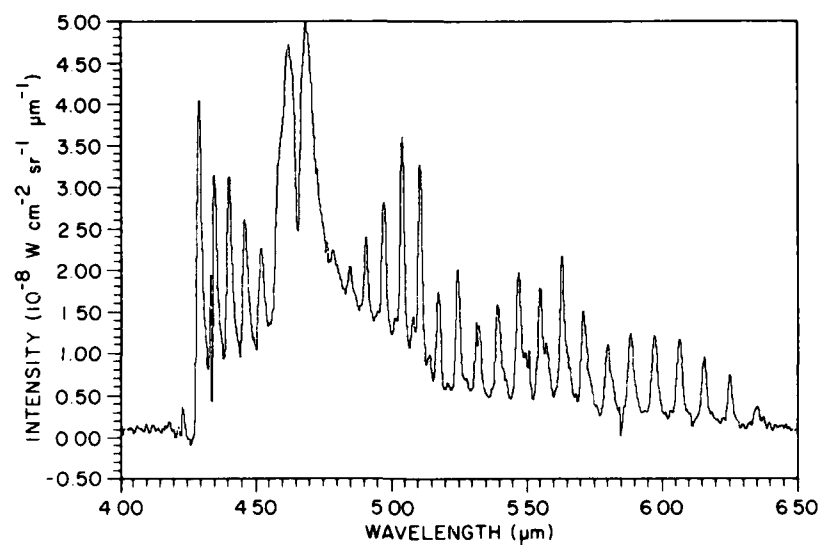
Figure 18. Spectrum of Figure 13 on Expanded Scale for Comparison With Computed Spectrum in Figure 19
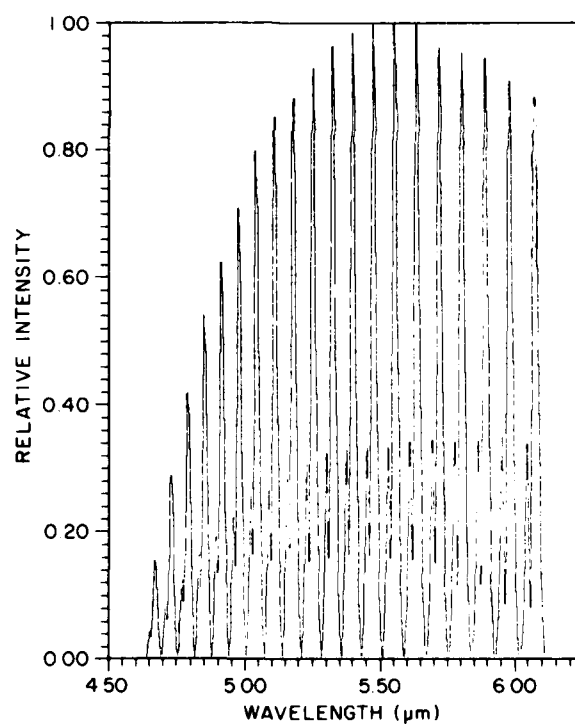
Figure 19. Computed Basis Functions of $CO(\Delta v = 1)$ Fluorescence for $T_{ROT} = 5$ K and Equal Vibrational State Populations

29
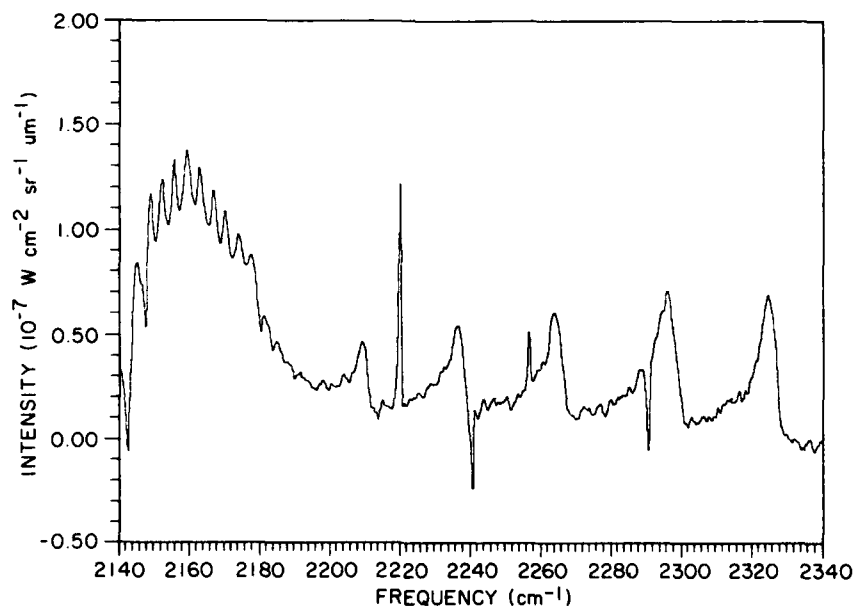
Figure 20. Frequency Spectrum of Unidentified Fluorescence Near
4.5 μm. Conditions are the same as in Figure 14, except $\delta\lambda = 0.007$
μm (~ 3.6 cm^{-1} at 4.3 μm). The CO(1, 0) band center and R branch
are at 2143 cm^{-1} and 2143-2180 cm^{-1}, respectively

3.3 Interaction of $O_3(v)$ With N_2

The chemical formation of N_2O at high altitudes is an important issue in
studies of the quiescent and auroral upper atmosphere. Numerous workers have
observed the formation of N_2O in electron-irradiated air. N_2O can be formed at
high pressures by the reaction

$$N + NO_2 \rightarrow N_2O + O \qquad ,$$
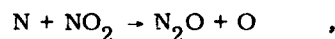
where NO_2 is formed by three-body recombination processes. However, this
route will not operate at the high altitudes characteristic of auroral and airglow
processes. N_2O formation has also been observed in low-pressure air discharges,
most notably in COCHISE and LABCEDE. Several mechanisms for its formation
at low pressure have been postulated,[13] such as the following reactions:

---

13. Zipf, E. C., and Prasad, S. S. (1980) Production of nitrous oxide in the
auroral D and E regions, Nature, 287:525; Zipf, E. C. On the formation
of nitrous oxide by the reaction between N_2 and excited OH radicals,
Nature (to be published).

30
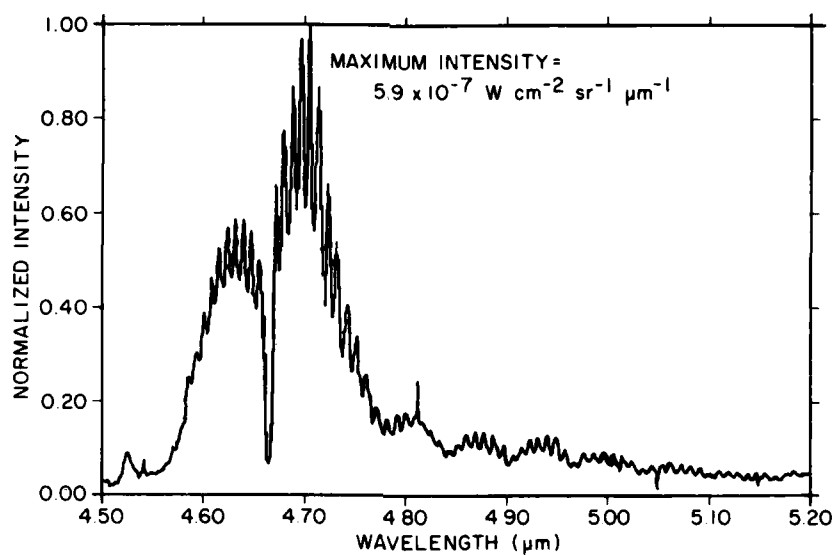
Figure 21. Experimental CO Spectrum for Comparison to Least
Squares Analysis Shown in Figure 22. Experimental conditions
are the same as those in Figure 15
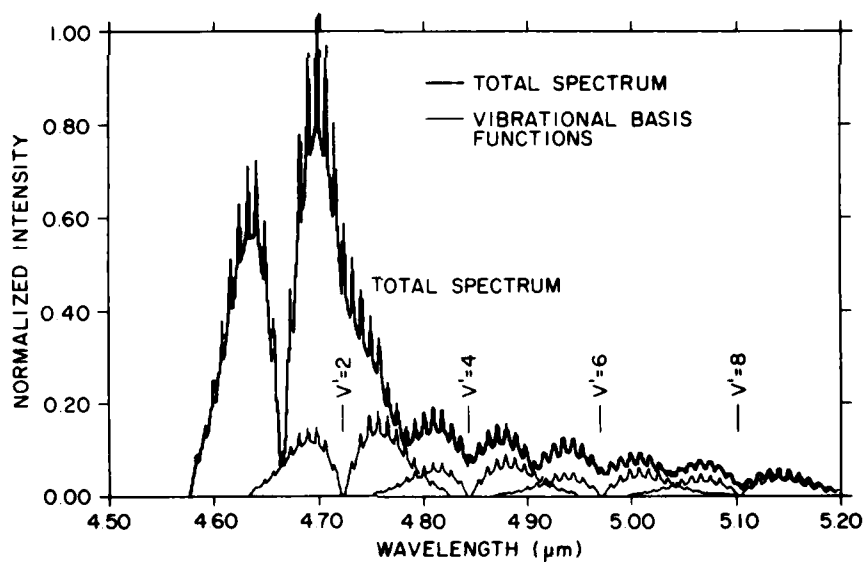
Figure 22. Computed Least Squares Spectral Fit to the Experimental CO Spectrum of Figure 21. T_{ROT} = 80K, $\delta\lambda$ = 0.007 μm
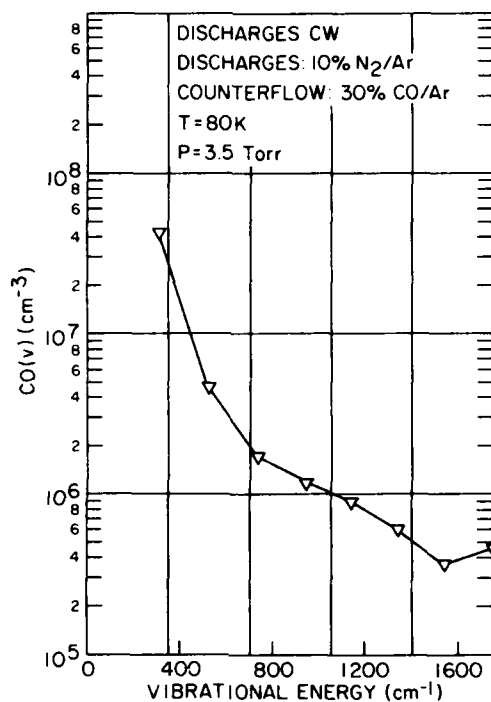
Figure 23. CO Vibrational State Number
Densities Determined From Least Squares
Analysis of Figures 21 and 22

$$N_2(A^3\Sigma) + O_2 \rightarrow N_2O + O$$

$$OH(A^2\Sigma) + N_2 \rightarrow N_2O + H \qquad .$$
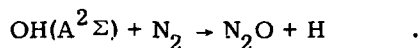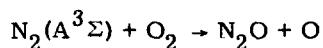
Other reactions could certainly be suggested, involving various combinations of
metastable O_2, N_2, and O_3. These reactions should be sufficiently exoergic to
form vibrationally excited N_2O, which will radiate strongly in the infrared. This
fluorescence occurs at 4.5, 7.8, and 17 μm for the ν_3, ν_1, and ν_2 bands, respect-
ively; excitation of higher levels would, of course, cause some red-shifting of
each band. By far the strongest of these bands is the ν_3 band near 4.5 μm
$(A_{001} = 258/\text{sec})$.

An interesting possible atmospheric source of $N_2O(v)$ is the reaction of N_2
with vibrationally excited O_3:

$$O_3(v) + N_2 \rightarrow N_2O(v) + O_2 \qquad . \tag{18}$$

32

In the absence of reactant vibrational energy, Reaction (18) is exoergic by 14.4 kcal/mol; each vibrational quantum of $O_3(\nu_3)$ adds about 3 kcal/mol. Thus, $O_3(v)$ carries enough energy to excite several vibrational quanta of N_2O (6.4 kcal/ mol per quantum of ν_3 excitation). Observations of $O_3(v)$ fluorescence in COCHISE[14] and in the upper atmosphere[15] show that as many as 6 ν_3 quanta of excitation in $O_3(v)$ are present at high altitudes. This would result in a maximum excitation in N_2O of $v_3 = 4$, extending the ν_3-band signature to about 4.7 μm.

We have attempted to observe Reaction (18) in COCHISE by searching for $N_2O(\nu_3)$ fluorescence in the direct interaction of discharge-produced $O_3(v)$ with counterflowing N_2. Unfortunately, in the rarefied conditions of the COCHISE reaction cell, a chemiluminescence reaction must be relatively efficient to produce easily measurable fluorescence. As will be shown below, we do not observe any $N_2O(v)$ fluorescence from Reaction (18), but the resulting upper bound on the rate coefficient is still rather large in the context of the potential atmospheric production of N_2O.

The experiments were performed by interacting a pure N_2 counterflow with discharge gas mixtures of ~ 86 $\mu mol/sec$ of O_2 and 625 $\mu mol/sec$ of Ar in each of the four discharge tubes at 1.3 Torr and 80 K. The discharges were operated in the usual AC mode. The N_2 flow rate in each injection tube was 1006 $\mu mol/sec$. The resulting total pressure in the reaction zone was ~ 4.4 mTorr. The concentration of N_2 in the reaction zone was then $\sim 3 \times 10^{14}/cm^3$.

Recent COCHISE experiments on the discharge-excited $O_3(v)$ fluorescence at 10 μm have established that the maximum $[O_3(v)]$ we can obtain from these discharges is $\sim 10^9/cm^3$, and occurs at the 12 percent O_2 condition we have employed here. The vibrational distribution under these conditions is bimodal with primary and secondary maxima at $v_3' = 1$ and $v_3' = 4$, respectively, indicating that much of the vibrational excitation may be occurring via metastable energy transfer processes. Some of the $O_3(v)$ is also clearly being formed by three-body recombination of O and O_2. The $(\nu_1 + \nu_3)$ combination states are also found to be populated under these conditions. A detailed discussion of our $O_3(v)$ results will be presented in a future report.

The results depicted in Figures 24-26 are typical of those obtained in several measurements for each of three separate COCHISE experiment cycles. The spectrum observed for an N_2 counterflow is shown in Figure 24; this is to be compared

14. Rawlins, W. T., Caledonia, G. E., and Kennealy, J. P. (1981) Observation of spectrally resolved infrared chemiluminescence from vibrationally excited O3(ν_3), J. Geophys. Res. 86:5247.

15. Green, B. D., Rawlins, W. T., and Caledonia, G. E. (1983) Atmospheric Radiation Infrared Signature Analysis, Physical Sciences Inc., PSI TR-366.
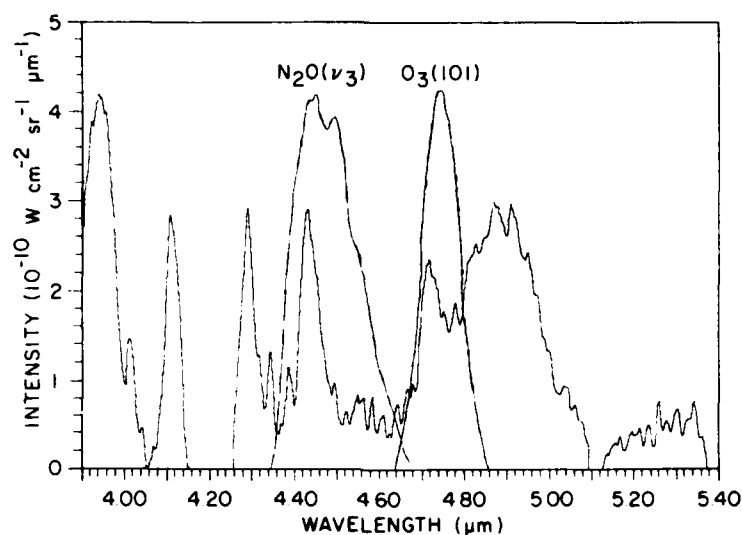
Figure 24. Spectrum of the Interaction Between $O_3(v)$ and N_2. Discharges: 86 and 625 μmol sec^{-1} of O_2 and Ar, respectively; counterflow, 1006 μmol sec^{-1} of N_2. T = 80K, P = 4.4 mTorr, $\delta\lambda$ = 0.04 μm. The expected band shapes of the $N_2O(v_3)$ and the $O_3(101)$ bands are given by the dotted curves

to spectra obtained with an unreactive Ar counterflow (Figure 25) and with an Ar counterflow and only Ar in the discharge (Figure 26). It can be seen that the sharp features between 4 and 5 μm are due to ArI Rydberg transitions, as we have described in detail elsewhere.[7] The band shapes of the N_2O (001) and $O_3(101)$ bands are also sketched in Figure 24. The N_2O band is sketched as it appears in COCHISE in AC-discharge measurements for air/Ar mixtures at the same spectral resolution (observed in recent measurements as well as reported in Reference 2). The O_3 (101 $\rightarrow$ 000) transition is sketched as computed for our experimental conditions using data from the AFGL line-parameters compilation.[16] The broad feature appearing between 4.6 and 5.1 μm is undoubtedly the $(v_1 + v_3)$ band of O_3, with most of the radiation arising from vibrationally excited "hot" bands. The phase settings were locked into this feature for the measurements. The fluorescence peaks at ~ 4.9 μm or 2041 cm^{-1}. This corresponds within 1 cm^{-1} to the band center of the 102 $\rightarrow$ 001 transition. In the 10 μm $O_3(v)$ fluorescence measurements, the (102) state is observed to be the most strongly populated combination state under these discharge conditions, so the present observations are consistent with the v_3-band data.

16. McClatchey, R. A., Benedict, W. S., Clough, S. A., Burch, D. E., Calfee, R. E., Fox, K., Rothman, L. S., and Garing, J. S. (1973) AFCRL Atmospheric Absorption Line Parameters Compilation, AFCRL-TR-73-0096, AD A762904.

34
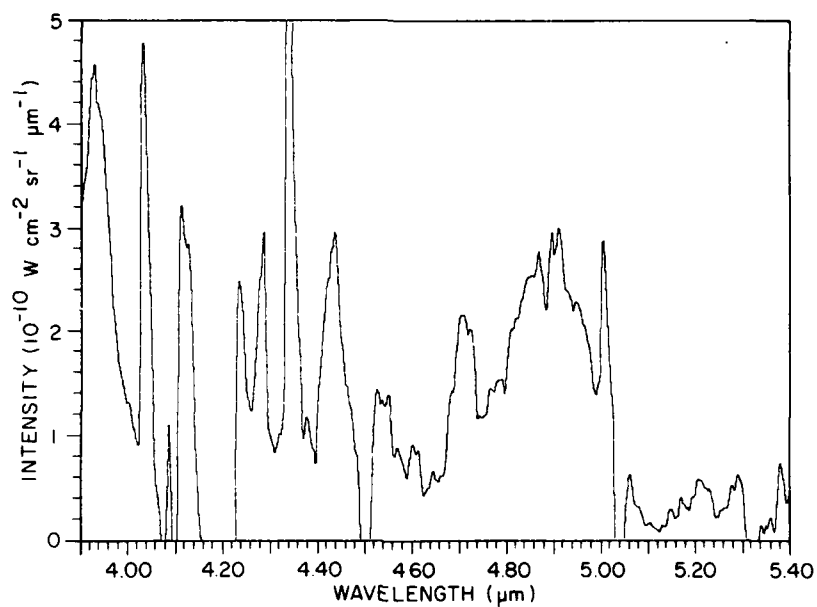
Figure 25. Spectrum of the Interaction Between O₃(v) and Ar. Conditions are the same as in Figure 24 except counterflow is 100 percent Ar
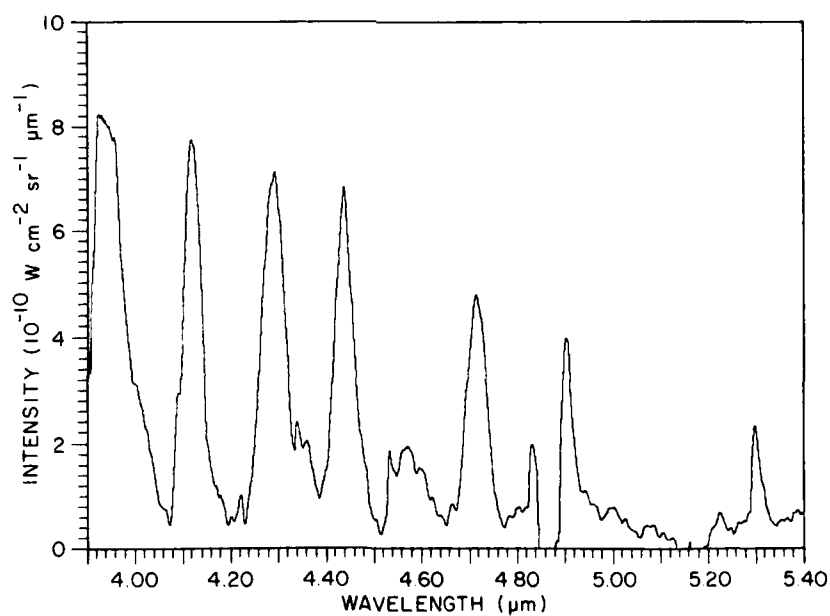
Figure 26. Spectrum Observed When Only Ar is Admitted to Both the Discharge and Counterflow Sides. Other conditions are the same as in Figure 24

35

Fluorescence from N_2O should occur near 4.5 μm, with possible hot bands extending to the energetic limit near 4.8 μm. There is evidence of a broad emission feature between 4.4 and 4.7 μm underlying the Ar lines. However, this also appears in the Ar counterflow case, so it is not likely to be due to N_2O. The emission could be due to weak, unresolved Ar lines, or possibly to strong OI Rydberg transitions which are predicted to occur at these wavelengths.[8] There is no evidence of $N_2O(v)$ formation from Reaction (18).

This negative observation places an upper bound on the rate coefficient for $N_2O(v)$ formation from Reaction (18). From comparison of the spectra with N_2 and Ar counterflows (Figures 24 and 25), the $N_2O(v)$ fluorescence at 4.5 μm is less than 3×10^{-11} W cm^{-2} sr^{-1} μm^{-1}. For a bandwidth of 0.2 μm, this transforms to 3.4×10^7 photons cm^{-3} sec^{-1} or

$$[N_2O(v)] < 1.3 \times 10^5 \text{ cm}^{-3} \quad .$$

In the steady-state conditions of the reaction zone, we have

$$[N_2O(v)] = \frac{k_{18}[O_3(v)][N_2]}{k'} \quad , \tag{19}$$

where k_{18} is the rate coefficient for Reaction (18) and k' is the inverse of the residence time in the field-of-view. For the typical conditions $[O_3(v)] \sim 10^9/\text{cm}^3$, $[N_2] = 2.6 \times 10^{14}/\text{cm}^3$, and $(k')^{-1} \sim 300$ μsec, we obtain

$$k_{18} < 2 \times 10^{-15} \text{ cm}^3/\text{sec} \quad .$$

It must be stressed that this upper bound pertains only to the formation of vibrationally excited N_2O, not to formation of ground state N_2O which, of course, cannot be observed in COCHISE. However, for lack of better information, it is consistent with our experience with vibraluminescent processes to assume that the reaction to form $N_2O(v = 0)$ will be kinetically similar to that forming vibrationally excited N_2O.

The upper bound obtained in COCHISE is still too large to rule out significant atmospheric and auroral production of $N_2O(v)$ by Reaction (18). In the quiescent atmosphere, values of $[O_3(v)]$ are typically in the $10^5/\text{cm}^3$ range near 80-100 km and range up to as high as $10^6/\text{cm}^3$ at 70 km in the daytime.[15] We would then predict upper bounds to the $N_2O(v)$ production rate of $\sim 10^6/\text{cm}^3$ sec at 70 km (daytime) and $\sim 10^{4-5}/\text{cm}^3$ sec at 90 km (day or night). These are very large production rates for these altitudes, being comparable to the excitation rates of $O_3(v)$ by recombination and earthshine absorption.[15] By comparison, Zipf and Prasad,[13]

36

using an incorrect description of the kinetics of $N_2(A^3\Sigma^+)$, predicted auroral pro-
duction rates for total N_2O from the postulated reaction of $N_2(A)$ with O_2 to be of
order $10^3/cm^3$ sec near 100 km. Since the chemical lifetime of N_2O at high alti-
tudes is quite long,[13] only a very small production rate is required to produce
significant quantities of total N_2O. Thus, the present COCHISE measurements do
not give a sufficiently definitive answer to the question of atmospheric production
of N_2O.

We can see from this analysis that, because of the rarefied conditions of the
reaction volume, COCHISE experiments on direct excitation of $N_2O(v)$ may be ex-
traordinarily sensitive but cannot provide definitive results for the upper atmo-
sphere unless the reaction in question proceeds with a significant reaction proba-
bility, that is, at least 10^{-5}. However, as alluded to above, we have been able to
observe $N_2O(v)$ fluorescence excited in low-pressure, discharged mixtures of N_2,
O_2, and Ar. This intriguing observation offers another, albeit less direct, avenue
for studying $N_2O(v)$ formation in electron-disturbed air. In the higher pressures
and longer contact times available in the discharge tubes, slower processes can
occur that would not otherwise be observed in the reaction chamber. The princi-
pal difficulty with such experiments lies in the conclusive identification of the
species and reactions responsible for the observed product formation. However,
at this stage of the N_2O problem, we do not even know whether the key reactants
are metastables of N_2 or of O_2, and a discharge experiment can address this most
fundamental point. We know from discharged N_2/Ar experiments that $N(^2D, ^2P)$
yields decrease only slightly at low N_2 levels, while $N_2(v)$ yields are large at high
N_2 and yields of the high-lying metastables of N_2 are largest at low N_2. Similarly,
from discharged O_2/Ar experiments, we have documented the variation of $O_3(v)$,
$O_2(v)$, and metastable O_2 with O_2 flow into the discharges. In addition, we are
developing kinetic models for the excitation of O_2, N_2, and Ar in the COCHISE dis-
charges (see Appendixes A and B). Thus, a systematic kinetic study of $O_2/N_2/Ar$
discharges in which N_2 and O_2 are independently varied should allow us to deduce
the relative importance of several discharge-excited species in the formation of
$N_2O(v)$.

4. CONCLUSIONS: FURTHER STUDIES

We have reviewed a recently acquired, preliminary data base on chemiexcita-
tion of NO(v), CO(v), and $N_2O(v)$. Examination of these data has suggested a great
deal of further experimentation needed to address the various problem areas as
well as to provide the final data base. They are:

(1) NO fundamental/overtone measurements

    (a) Fundamental band: more exhaustive data on N_2 variations; more detailed characterization of unknown 5 μm bands for spectral subtraction (use lower resolution, compare to spectral simulations); correct for impurity NO(v).

    (b) Overtone band: use highest possible N_2 flows, subtract N_2^* background; obtain at least five matched overtone and fundamental spectra, all at the same conditions, for good statistics.

    (c) Blackbody calibration: test with two-temperature ratio method; extend to shorter wavelengths by using wider slits, no filter.

(2) N_2^* SWIR fluorescence

    (a) Obtain more data at low N_2 flow rate, use highest possible resolution.

    (b) Analyze by spectral simulation/fitting.

    (c) Examine state redistribution as function of discharge conditions, relate to FAKIR observations.

    (d) Potential for measurements of transition branching ratios.

(3) Excitation of CO

    (a) Unidentified bands: survey shorter wavelengths for related transitions; use spectral simulations; search literature for possible radiators and related kinetics.

    (b) CO(v) excitation mechanisms: direct comparison of AC and CW discharge experiments; more extensive study of N_2, CO dependencies; temperature dependence; recalibrate flowmeter for CO (potential titration for $[N(^2D)]$).

(4) Formation of $N_2O(v)$: examine 4.5 μm signature as function of N_2 and O_2 flows in $N_2/O_2/Ar$ discharges; shorten discharge tubes to cut down interference from ArI lines.

The most straightforward project to complete is the NO fundamental/overtone study, and we plan to pursue that in the next series of COCHISE experiments. We also hope to complete the CO excitation studies in the next few months, but this will depend upon the success of the next stage of measurements.

References

1. Rawlins, W. T., Piper, L. G., Caledonia, G. E., and Green, B. D. (1981) *Final Technical Report: COCHISE Research*, Physical Sciences, Inc., PSI TR-298.

2. Kennealy, J. P., DelGreco, F. P., Caledonia, G. E., and Green, B. D. (1978) Nitric oxide chemi-excitation occurring in the reaction between metastable nitrogen atoms and oxygen molecules, *J. Chem. Phys.* 69:1574.

3. Rawlins, W. T., Piper, L. G., Green, B. D., Wilemski, G., Goela, J. S., and Caledonia, G. E. (1980) *LABCEDE and COCHISE Analysis II, Volume 1,* AFGL-TR-80-0063(I), AD A112253, Final Report, Contract F19628-77-C-0089, Physical Sciences Inc., PSI TR-298.

4. Billingsley, F. P. (1976) Calculated vibration rotation intensities for NO(X$^2\pi$), *J. Mol. Spectr.* 61:53.

5. Green, B. D., Caledonia, G. E., and Murphy, R. E. (1981) A determination of the nitric oxide Einstein coefficient ratios, *J. Quant. Spectry. Radiat. Transfer.* 26:215.

6. Piper, L. G., and Rawlins, W. T. (1983) *COCHISE Atmospheric Nitrogen/Oxygen Excitation Studies: Studies on Metastable Nitrogen Atoms,* Physical Sciences Inc., PSI TR-411.

7. Rawlins, W. T., and Gelb, A. (1983) *COCHISE Atmospheric Nitrogen/Oxygen Excitation Studies: COCHISE Observations of Ar Rydberg Emission From 2 to 16 μm,* Physical Sciences Inc., PSI TR-383.

8. Biemont, E., and Grevesse, N. (1973) Infrared wavelengths and transition probabilities for atoms, $3 \le z \le 20$, *Atomic Data and Nuclear Data Tables* 12:217.

9. Caledonia, G. E., Green, B. D., and Simons, G. A. (1977) *LABCEDE and COCHISE Analysis. Volume 1.* Final Report, Physical Sciences Inc., PSI TR-83.

10. Stair, A. T., Jr., Kennealy, J. P., and Murphy, R. E. (1967) A study of some inelastic collision processes using active nitrogen and carbon monoxide, J. Chim. Physique, 1:52.

11. Donovan, R. J., and Husain, D. (1970) Recent advances in the chemistry of electronically excited atoms, Chem. Rev. 70:489.

12. Krupenie, P. H. (1966) The Band Spectrum of Carbon Monoxide, NSRDS-NBS-5.

13. Zipf, E. C., and Prasad, S. S. (1980) Production of nitrous oxide in the auroral D and E regions, Nature, 287:525; Zipf, E. C. On the formation of nitrous oxide by the reaction between N_2 and excited OH radicals, Nature (to be published).

14. Rawlins, W. T., Caledonia, G. E., and Kennealy, J. P. (1981) Observation of spectrally resolved infrared chemiluminescence from vibrationally excited $O_3(\nu_3)$, J. Geophys. Res. 86:5247.

15. Green, B. D., Rawlins, W. T., and Caledonia, G. E. (1983) Atmospheric Radiation Infrared Signature Analysis, Physical Sciences Inc., PSI TR-366.

16. McClatchey, R. A., Benedict, W. S., Clough, S. A., Burch, D. E., Calfee, R. E., Fox, K., Rothman, L. S., and Garing, J. S. (1973) AFCRL Atmospheric Absorption Line Parameters Compilation, AFCRL-TR-73-0096, AD A762904.

Contents

2.2 COCHISE: Microwave Discharge Theory

by

G. E. Caledonia

1. INTRODUCTION

Most infrared fluorescence measurements in the COCHISE facility use O_2/Ar and N_2/Ar microwave discharges as sources for the precursors to the observed infrared radiation. In these discharges, the excitation conditions can vary significantly with gas composition, pressure, and applied power, giving rise to different levels of atoms and metastables entering the reaction cell. Detailed understanding of the dynamics of these discharges is generally not available in the literature. We discuss here the basic operating conditions of the microwave discharge, and present calculations of its physical properties. These characteristics are essential input for subsequent kinetic modeling of excitation processes in microwave discharges, which will be discussed in a future report.

We present here predictions for excitation rates in O_2/Ar microwave discharges which are an update to those presented in Reference 1. The update includes some scale corrections to the O_2 cross section base as well as incorporation of cross sections for O atom excitation, ozone dissociation, and ionization of argon metastable states.

1. Rawlins, W. T., Piper, L. G., Gelb, A., Lucht, R. A., and Caledonia, G. E. (1983) <u>COCHISE Research</u>, Physical Sciences Inc., PSI TR-349.

We have used a computer model that solves the Boltzmann transport equation to evaluate the excitation rates characteristic of the O_2/Ar discharges used in the COCHISE ozone studies. Discharge characteristics were predicted for various O_2/Ar mixtures as a function of E/N (electric field per unit length normalized by total number density). The inputs to these calculations are the electron-energy-dependent cross sections for the inelastic processes occurring in the discharge, while the outputs include discharge characteristics such as characteristic electron energy and drift velocity as well as excitation rate constants. The calculational techniques are straightforward and well understood (see for example Reference 2).

The predictions are, of course, only as accurate as the cross sections employed. For argon, all the cross sections are well known with the exception of those for electronic excitation. We have characterized electronic excitation with two processes representing s state excitation with an energy loss of 11.6 eV and p state excitation with an energy loss of 13.1 eV. The respective recommended cross sections are tabulated in Table 1. Note that these are meant to be aggregate cross sections and include the effect of excitation to other states such as the [1]P levels. These latter states, although optically allowed, will be radiatively trapped, and will behave similarly to the metastables. These cross sections were used with the more standardly accepted cross sections for momentum transfer and ionization for Ar[2,3] to predict the transport properties of argon discharges.

Table 1. Electronic Excitation Cross Sections for Ar

Ar(3P-4S)		Ar(3P-4P)	
E, eV	$\sigma \times 10^{16}$, cm^2	E, eV	$\sigma \times 10^{16}$, cm^2
0	0	0	0
11.58	0		
12	0.017		
13	0.065	13.1	0
14	0.12	14	0.10
15	0.17	15	0.21
17.5	0.28	17.5	0.49
20	0.38	20	0.77
25	0.42	25	1.00
30	0.46	30	1.12
40	0.45	40	1.36
100	0.40	100	1.06

2. Frost, L. S., and Phelps, A. V. (1964) Momentum transfer cross sections for slow electrons in He, Ar, Kr and Xe from transport coefficients, Phys. Rev. 136:A1538.

3. Kieffer, L. J. (1973) A Compilation of Electron Collision Cross Section Data for Modeling Gas Discharge Lasers, JILA Information Center Report 13.

The discharge properties of argon have been the subject of numerous measurements.[4] The transport properties are integral measurements of the electron energy distribution. Therefore, a necessary, but not sufficient, criterion for the validation of any set of excitation cross sections is that they can be used to predict these properties successfully. A comparison between data and prediction is given in Table 2, where the data is representative of that presented in Reference 4. Comparisons are provided for drift velocity, characteristic energy, and ionization coefficient. As can be seen, the comparison is reasonably good. The cross sections could have been fine-tuned to provide a better comparison but such an effort was not warranted for the present study.

Table 2. Transport Properties in Ar Discharges

$E/N \times 10^{16}$, V cm^2	$W \times 10^{-6}$, cm/sec		ε_K, eV		$\alpha/N \times 10^{19}$, cm^2	
	Exp.	Theory	Exp.	Theory	Exp.	Theory
1.	~1.03	1.03	7.8	7.66	0.0	0
2.	1.83	2.0	7.8	7.75	0.35	0.17
3.	2.6	2.9	8.0	7.94	1.6	1.9
4.	~3.5	3.7	8.0	8.1	6.8	6.8
5.	~4.2	4.5	8.0	8.24	16	15

The cross section data base O_2 discussed extensively by Phelps and coworkers[5-7] has been used. These cross sections provided reasonable agreement with O_2 discharge data and limited measurements of O_2 metastable state excitation rates.[5,6] The processes considered include momentum transfer, rotational and vibrational excitation, electronic excitation of several states, dissociation, dissociative attachment, and ionization. Several of the key cross sections are tabulated in Table 3.

Several excitation processes involving O and O_3 have also been included in the analysis. These species have been treated as traces and thus do not affect the discharge electron energy distribution. Electron impact excitation of $O(^3P)$ to $O(^1D)$ and $O(^1S)$ has been specified by the cross sections recommended by Jackman

4. Dutton, J. (1975) A survey of electron swarm data, J. Phys. and Chem. Ref. Data 4:577.

5. Lawton, S. A., and Phelps, A. V. (1978) Excitation of the $b^1\Sigma g^+$ state of O_2 by low energy electrons, J. Chem. Phys. 69:1055.

6. Tachibana, K., and Phelps, A. V. (1981) Excitation of the O_2 $(a^1\Delta g)$ state by low energy electrons, J. Chem. Phys. 75:3315.

7. Phelps, A. V. (1982) Private Communication.

Table 3. Selected Excitation Cross Sections for O_2

$O_2(^3\Sigma) \rightarrow O_2(^1\Delta)$		$O_2(^3\Sigma) - O_2(^1\Sigma)$		$O_2(^3\Sigma) \rightarrow 2O(^3P)$	
E, eV	$\sigma \times 10^{17}$, cm^2	E, eV	$\sigma \times 10^{17}$, cm^2	E, eV	$\sigma \times 10^{17}$, cm^2
0.0	0.0	0.0	0.0	0.0	0.0
0.977	0.0	1.627	0.0	6.0	0.0
1.5	0.058	2.0	0.026	7.0	1.5
2.0	0.153	3.0	0.097	7.8	2.3
3.0	0.380	3.5	0.133	9.0	2.3
3.5	0.490	4.0	0.149	10.0	2.1
4.0	0.570	5.0	0.182	12.0	1.65
5.0	0.740	5.69	0.194	15.0	1.05
5.62	0.825	6.54	0.194	17.0	0.65
5.91	0.862	7.34	0.191	20.0	0.475
6.19	0.888	8.41	0.183	45.0	0.19
6.53	0.908	9.26	0.174	100.0	0.0
6.99	0.914	10.0	0.160		
7.61	0.891	13.0	0.131		
7.89	0.863	14.9	0.117		
8.96	0.768	17.0	0.103		
10.04	0.679	19.4	0.092		
13.0	0.527	20.7	0.086		
15.1	0.455	22.5	0.080		
17.5	0.387	24.0	0.072		
20.5	0.324	28.0	0.061		
24.9	0.256	35.1	0.047		
30.9	0.196	41.9	0.034		
41.0	0.137	45.1	0.031		
45.0	0.120	100.0	0.0		
100.0	0.0				

et al., [8] and dissociation of O_3 by the analysis of Keto. [9] The latter treatment is theoretical with no experimental validation. These cross sections are shown in Figure 1.

8. Jackman, C. H., Garvey, R. H., and Green, A. E. S. (1977) Electron impact on atmospheric gases I. Updated cross sections, J. Geophys. Res. 82:5081.

9. Keto, J. W. (1981) Electron beam excited mixtures of O_2 in argon, II, electron distributions and excitation rates, J. Chem. Phys. 74:4445.
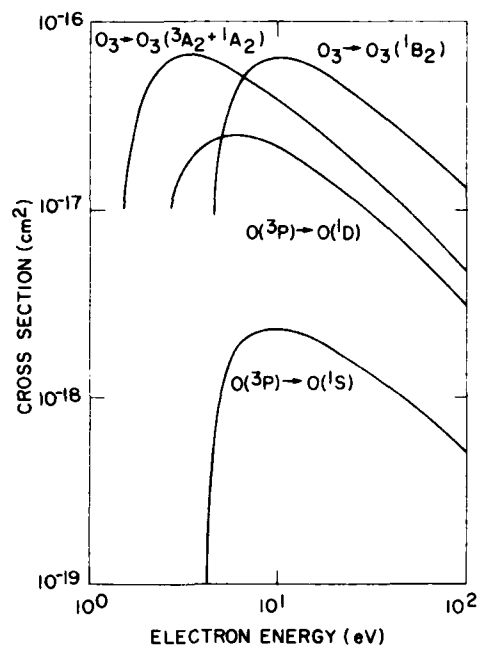
Figure 1. Electron Impact Excitation
Cross Sections. The excited states of
O_3 are dissociative

Similarly, electron impact ionization of the Ar(4S, 4P) states have also been incorporated. These cross sections, shown in Figure 2, have been taken from the theoretical treatment in Reference 10. The cross sections for Ar(4S) have been validated experimentally. Ar metastables were only treated as a trace in the calculations.

These cross sections have been used to calculate discharge properties and excitation/de-excitation rate constants of various O_2/Ar mixtures as a function of E/N. Such predictions are shown in Figures 3-10. The excitation rate constants for Ar metastables are displayed in Figure 3. They can be seen to fall off at higher O_2 mole fractions where the lower energy O_2 excitation processes dominate the electron energy distribution functions. There appears to be only one measurement of metastable excitation rates in argon discharges[11] and these values fall approximately a factor of 2 below those shown in Figure 3 at low O_2. We have

10. Bretagne, J., Godart, J., and Puech, V. (1982) Low-energy electron distribution in an electron-beam-generated argon plasma, J. Phys. D 15:2205.

11. Bozin, J. V., Urosevic, V. V., and Petrovic, A. Lj (1983) Experimental investigation of excitation of argon metastables by an electron swarm in argon nitrogen gas mixtures, Z. Phys. A: Atoms & Nuclei 312:439.
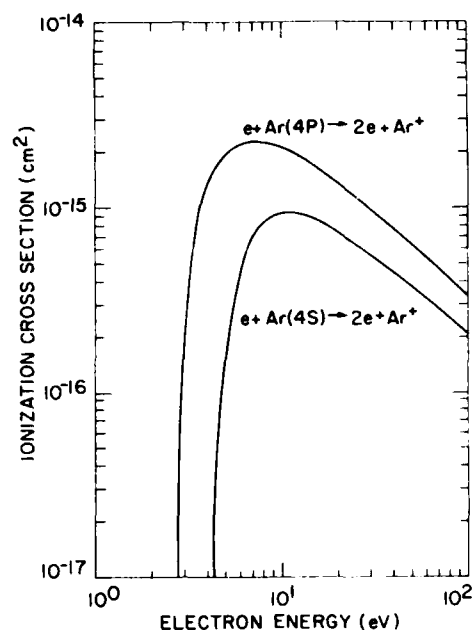
Figure 2.   Electron Impact Ionization
Cross Sections for Argon Metastable
States
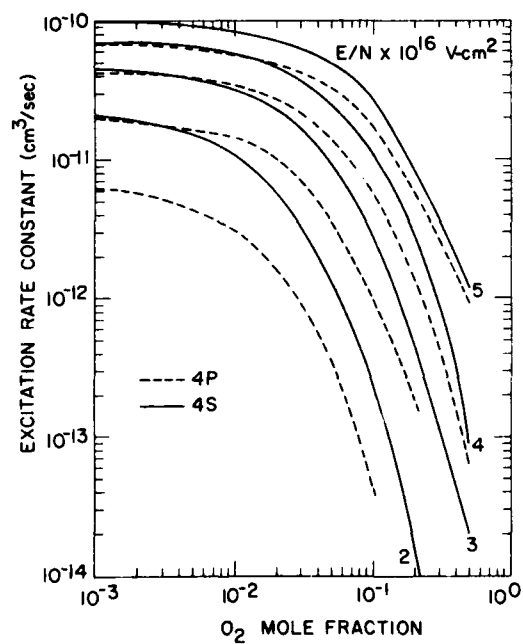
Figure 3.   Argon Electronic State Excita-
tion Rate Constants for Microwave Excited
O_2/Ar Mixtures

46
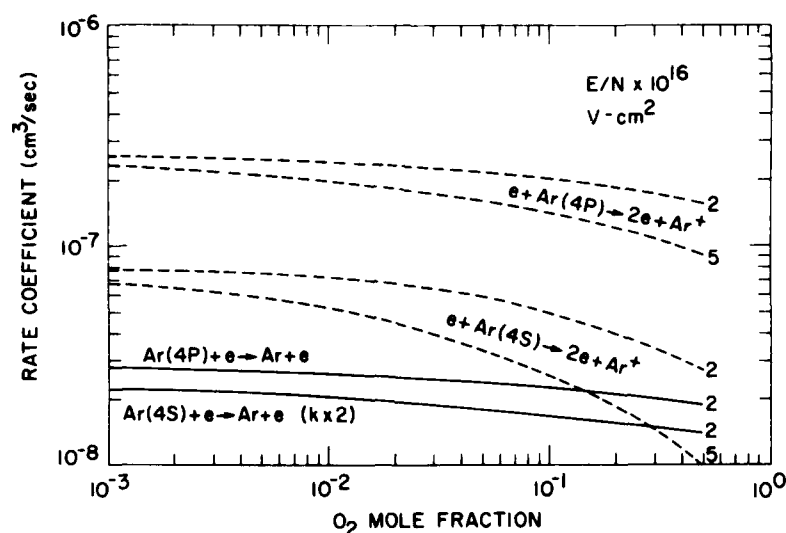
Figure 4. Argon Metastable State Ionization and De-Excitation
Rate Constants in Microwave Excited Ar/O_2 Mixtures

decided not to adjust the cross sections given the uncertainty in the measured rate
constants. Predicted argon metastable electron impact ionization and de-excita-
tion (that is, superelastic collisions) rates are shown in Figure 4. Note that these
rate constants are quite large, reflecting the high characteristic energies of the
discharge, and these processes can ultimately limit the concentration of argon
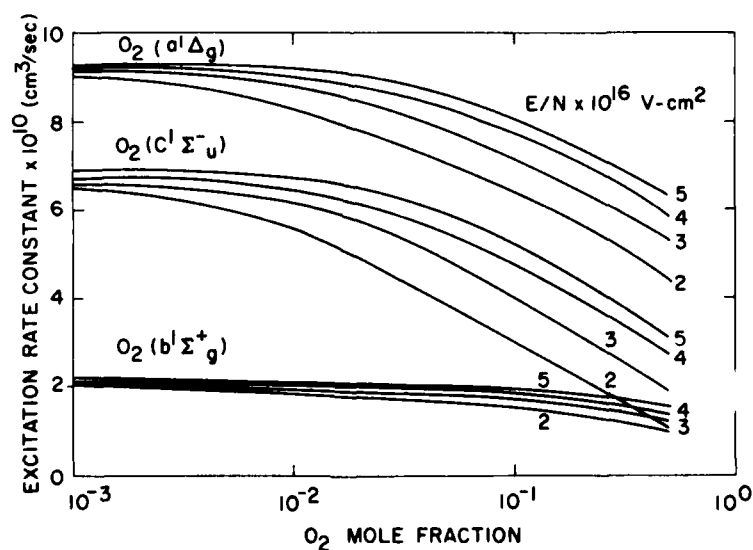
Figure 5. Rate Constants for Electron Impact Excitation of
Ground O_2 to Several Metastable States for Microwave Ex-
cited O_2/Ar Mixtures

47
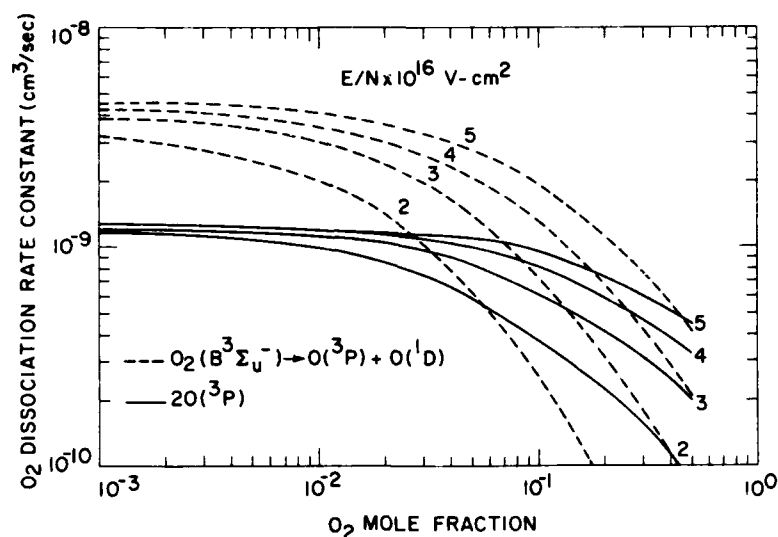
Figure 6. Predicted Rate Constants for O_2 Dissociation in Microwave Excited O_2/Ar Discharges

metastables in the discharge. Similar predictions for the O_2 metastable $a^1\Delta$, $b^1\Sigma$, and $c^1\Sigma$ are shown in Figure 5. These states are found to have significant excitation rates over the full range of discharge parameters. The rate constants for electron impact dissociation of O_2 are shown in Figure 6. Two processes are shown: (a) The excitation of continuum states leading to $2O(^3P)$ atoms; and (b) excitation of the $B^3\Sigma$ state, which we have assumed leads to formation of $O(^1D)$ + $O(^3P)$ with unit efficiency. Once again both processes exhibit high rate constants.

Rate constants for excitation of the $v = 1$ and $v = 2$ vibrational levels of O_2 are shown in Figure 7. Only results for the direct excitation process (4.5 eV) are shown. The rate constants for the lower energy resonant states could not be calculated accurately because of the coarseness of the energy mesh used in the calculations (0.2 eV). Given the large characteristic energies of the electron distribution (see Figure 8) it is anticipated that resonant excitation will be less important than direct excitation.

The predicted rate constants for electron impact excitation of $O(^3P)$ to $O(^1D)$ and $O(^1S)$ and for electron impact dissociation of O_3 are shown in Figures 9 and 10, respectively. The rate constant for excitation of $O(^1D)$ is an order of magnitude larger than that for $O(^1S)$ as would be expected from the cross sections shown in Figure 1. Dissociation of O_3 is very effective, reflecting its weak bond strength and the availability of low-lying dissociative states.

Superelastic de-excitation rate coefficients have also been calculated for the electronic states of O and O_2 considered. In general, these are large for states with low ($\sim$ 1 eV) excitation energies, such as, vibration, $O_2(^1\Delta, \ ^1\Sigma)$ and $O(^1D)$;

48
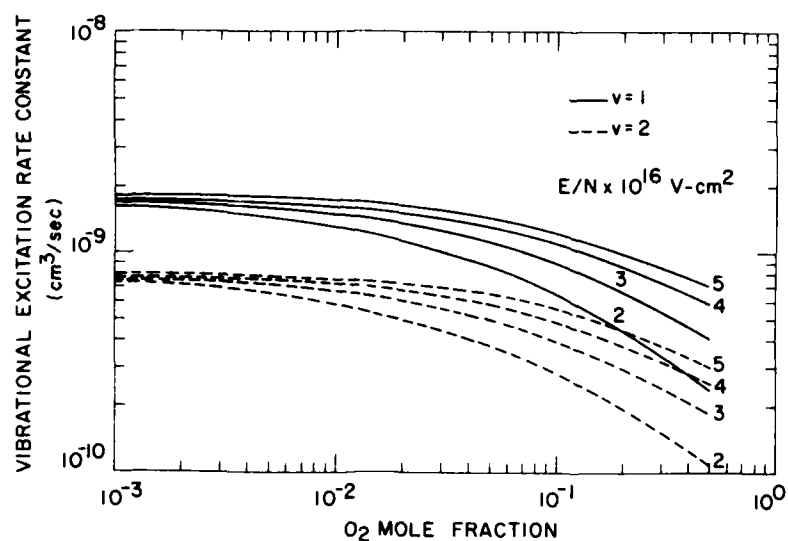
Figure 7. Predicted Rate Constants for Direct Excitation of Vibrational Levels v = 1 and 2 of O_2 in Microwave Excited Mixtures of O_2/Ar

Figure 8. Predicted Characteristic Energies in Microwave Excited Mixtures of O_2/Ar

Figure 9. Predicted Rate Constants for Electron Impact Excitation of $O(^3P)$ to $O(^1D)$, $O(^1S)$ in Microwave Excited O_2/Ar Mixtures

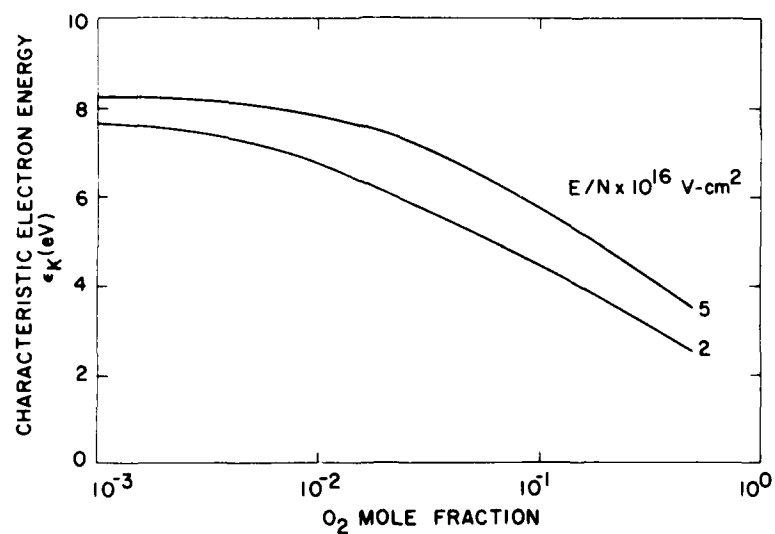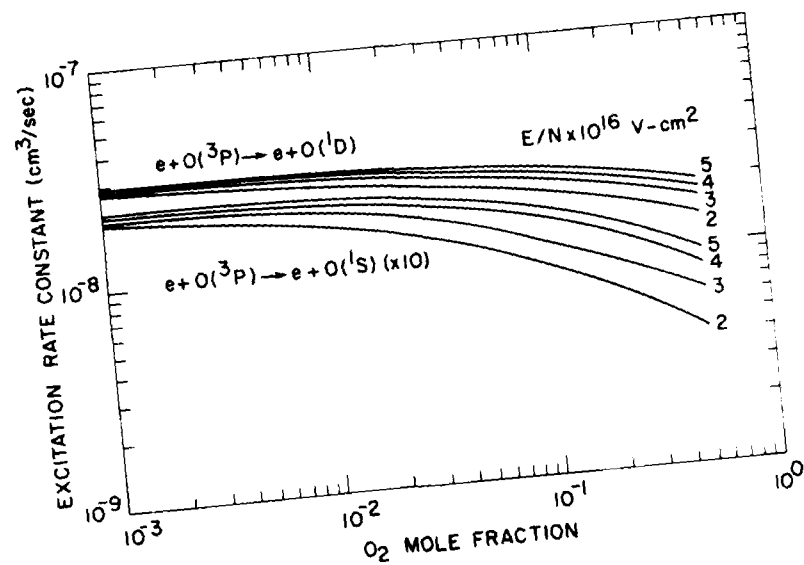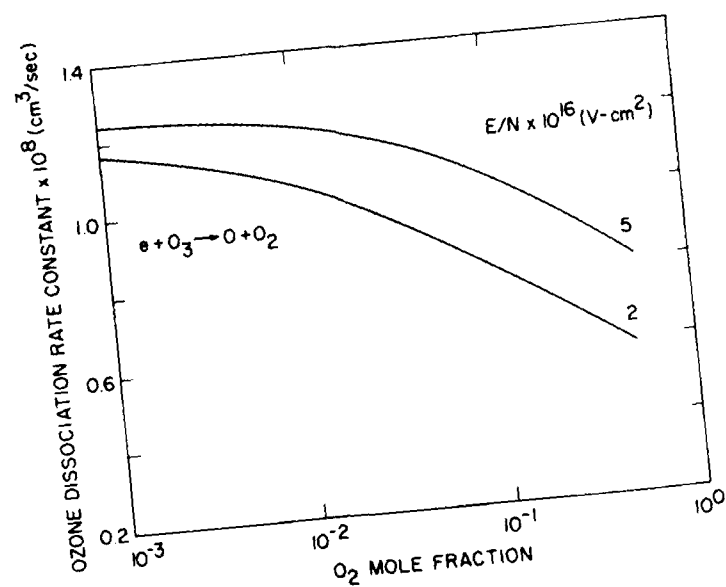Figure 10. Predicted Rate Constant for Electron Impact Dissociation of O_3 in Microwave Excited O_2/Ar Mixtures

50

the excitation and de-excitation rate constants are of the same order of magnitude, reflecting the high characteristic electron energy in the discharge. For high-lying electronic states, the de-excitation rates can be several orders of magnitude larger than the excitation rates.

It must be noted that these predictions should not be considered to be exact. Indeed, at these high characteristic energies the adequacy of the first order expansion of the transport equation is in question. Furthermore, superelastic collisions have not been accounted for and it has been assumed that the O and O_3 concentrations are traces relative to those for O_2. If the latter assumption is valid, and given the accuracy of the cross sections, we expect the rate constants to be accurate to within a factor of 2.

2. ANALYSIS

When a low pressure (0.1 - 10 Torr) DC glow discharge is struck between cathode and anode a rich axially structured light pattern is observed between the plates characterized by a number of regions with distinct optical and electrical properties.[12] Much of this structure is specific to the cathode and anode regions, however a relatively uniform region, called the positive column, fills the major part of the discharge.

The use of high-frequency electrodeless discharges eliminates the complications of anode and cathode regions and provides a relatively uniform glow which resembles the positive column of an equivalent DC discharge.[13] The excitation mechanism is, of course, distinct in the AC discharge, inasmuch as the electrons gain energy through collisions with neutral molecules as they oscillate with the field. These collisions disturb the phase relationship (90° in vacuum) between field and electrons, allowing energy transfer between the two, as well as promoting a modest energy transfer between electrons and neutrals. The electrons continue to gain energy in this manner until a balance is struck between energy gain from the field and energy loss through inelastic collisions with neutrals. It can readily be shown[13, 14] that an AC discharge with electric field E_o is equivalent to a DC discharge of effective field E_e defined by

---

12. Cobine, J. D. (1958) Gaseous Conductors, Dover Publications, New York, pp. 205-289.

13. Kaufman, F. (1969) The Production of Atoms and Simple Radicals in Glow Discharges, American Chemical Society, pp. 29-47.

14. Brown, S. C. (1956) Breakdown in cases: Alternating and high frequency fields, in Encyclopedia of Physics, Vol. XXII Gas Discharges II, S. Flugge, (Ed.), Springer-Verlag, Berlin, pp. 531-575.

$$E_e = E_o \left(\frac{\nu^2}{\nu^2 + \omega^2} \right)^{1/2} \qquad ,$$

where ν is the collision frequency for momentum transfer and $\omega = 2\pi f$, where f is the field frequency (2.5 GHz for COCHISE).

Definition of the appropriate field strength is not so obvious. Such discharges are diffusion dominated and thus operating conditions are determined by a balance between diffusive losses and volume ionization. Specifically the steady operating condition depends upon gas, pressure, and discharge diameter. The defining equation for electron density may be written as

$$d^2n/dr^2 + \frac{1}{r} \, dn/dr + \frac{Z}{D_a} \, n = 0 \qquad , \qquad (1)$$

where cylindrical geometry and a constant volume ionization rate has been assumed. Here n is electron density, Z is the number of ionizing collisions per second, per electron, and D_a is the ambipolar diffusion coefficient. Equation (1) has the solution

$$n_v = n_o J_o (r \sqrt{Z/D_a}) \qquad , \qquad (2)$$

where J_o is a Bessel function of order zero and the solution is only valid to the first zero of the function, which occurs when

$$r = R = 2.405 \sqrt{D_a/Z} \qquad , \qquad (3)$$

where R is the tube radius. Thus

$$Z = 5.8 \, D_a/R^2 \qquad . \qquad (4)$$

Now in a discharge the electron temperature T_e will be much higher than the ion temperature T_i (which will be at the heavy temperature T) and it can be shown that

$$D_a \approx D_+ \, T_e/T_i \qquad (5)$$

The classical approach[12] to characterize the discharge is to assume a Maxwellian electron distribution and a kinetic ionization rate of the form

$$Z = A \sqrt{T_e} \, e^{-I/T_e} \qquad , \qquad (6)$$

where I is the ionization potential for the gas. In this case Eq. (4) becomes a transcendental equation that can be solved for T_e. Typical solutions are given in Cobine[12] where it is found that for gases such as Ar and N_2 and COCHISE conditions of R = 0.5 cm, p ~ 1 Torr the electron temperature is ~ 1.5 eV. Unfortunately, although this approximation appears reasonable for N_2, it is quite poor for Ar. This apparently happens because the large Ramsauer minimum in the electron/argon collision cross-section drives the electron energy to a very non-Maxwellian distribution.

Fortunately there are measured values available for the ionization rate and electron diffusion coefficient over mobility (~ T_e) for gases such as N_2 and Ar as a function of E/N (field strength/number density). Typical measured results are provided in Table 4 (see review in Reference 4). Listed in order are E/N, ionization coefficient, drift velocity, characteristic energy (D/μ), and ionization rate. As can be seen, the properties of Ar and N_2 are quite different.

Table 4. Selected Discharge Properties of N_2/Ar

Gas	$E/N \times 10^{16}$ $(V\ cm^2)$	α/N (cm^2)	$W \times 10^{-6}$ (cm/sec)	ε (eV)	Z/N (cm^3/sec)
Ar	2.0	3.0×10^{-20}	1.7	~ 8.0	5.1×10^{-14}
	3.0	2.5×10^{-19}	2.5		6.3×10^{-13}
	4.0	6.8×10^{-19}	3.3		2.2×10^{-12}
	5.0	1.6×10^{-18}	4.0		6.4×10^{-12}
	7.0	4.0×10^{-18}	5.0	~ 8.0	2.0×10^{-11}
	10.0	9.5×10^{-18}	7.4		7.0×10^{-11}
	20.0	3.4×10^{-17}	14.0		4.8×10^{-10}
N_2	8.5	1.8×10^{-20}	9.5	1.7	1.7×10^{-13}
	10.0	7.0×10^{-20}	10.5		7.4×10^{-13}
	15.0	$\sim 1.0 \times 10^{-18}$	14.0	~ 2.7	1.4×10^{-11}
	20.0	5.0×10^{-18}	19.5		9.8×10^{-11}

Equation (4) can be evaluated using the data in Table 4. One can rewrite D_+ in terms of the atmospheric diffusion coefficient as

$$D_+ \approx D_{+o} \frac{N_o}{N} \qquad (7)$$

where N_o is 2.67×10^{19} cm^{-3}. At 273 K values of D of 0.15 and 0.17 cm^2/sec are appropriate for neutral Ar and N_2 respectively (values for ionic species will

typically be one-third smaller). The COCHISE discharges are nominally at
$T = 80$ K, however some ion heating will occur, and the number-density-normal-
ized values at 273 K are probably appropriate to within a factor of 2. Thus Eq.
(4) becomes

$$Z/N \approx \frac{10^{21}}{N^2} T_e(eV) \qquad . \qquad (8)$$

Evaluations of Eq. (4) for total number densities of 10^{16} and 10^{17} cm^{-3} are pro-
vided in Table 5. We note that nitrogen requires slightly higher E/N's than argon
although the characteristic energies are considerably lower. These values of
E/N are required to make detailed rate predictions. Recall that E is the effective
field rather than the real AC field.

Table 5. Predicted Operating Conditions for COCHISE Discharges

Gas	N (cm^{-3})	Z/N (cm^3/sec)	T_e (eV)	E/N (V cm^2)	E (V/cm)
Ar	10^{17}	8.0×10^{-13}	8.0	3.2	32
	10^{16}	8.0×10^{-11}	8.0	10.0	10
N_2	10^{17}	1.8×10^{-13}	1.8	9.0	90
	10^{16}	2.8×10^{-11}	2.8	16.0	16

As pointed out earlier, the high characteristic energies in Ar result from the
Ramsauer minimum in the electron-collision cross-section, which causes argon
to be nearly transparent to low energy electrons. This cross-section behavior
provides for very non-Maxwellian electron energy distributions in argon micro-
wave discharges. An example of a predicted electron energy distribution in argon
at an E/N of 2×10^{-16} V cm^2 is shown in Figure 11. The characteristic energy of
this distribution is 7.6 eV. This prediction is contrasted in the figure with Max-
wellian distributions at electron temperatures of 1.5 and 7.4 eV. We note that
below ~ 10 eV the Ar distribution is similar to that of the 7.5 eV Maxwellian and
then falls off precipitously at higher energies. Interestingly enough, the predicted
Ar distribution crosses the 1.5 eV Maxwell distribution at ~ 15.8 eV, the ioniza-
tion potential for argon. The latter distribution would actually exhibit a larger
ionization rate.

We note that the power supplied by the field is just

$$P = N N_e e W E/N V \qquad , \qquad (9)$$

where V is the volume of the discharge. The COCHISE discharge has a length of 17.5 cm and radius of 0.5 cm for a volume of $\sim 14 \text{ cm}^3$, and provides a total power of 50 W. Thus,

$$N_e = 2.2 \times 10^{19}/(N \text{ E/N W}) \qquad . \qquad (10)$$

For example for an N of 10^{17}, $E/N = 3 \times 10^{-16}$, $W = 2.9 \times 10^6$ cm/sec we find,

$$N_e = 2.5 \times 10^{11}/\text{cm}^3 \qquad . \qquad (11)$$

Note that Eq. (9) assumes 100 percent conversion efficiency of electrical power to the gas. This appears to be appropriate for a properly tuned cavity.
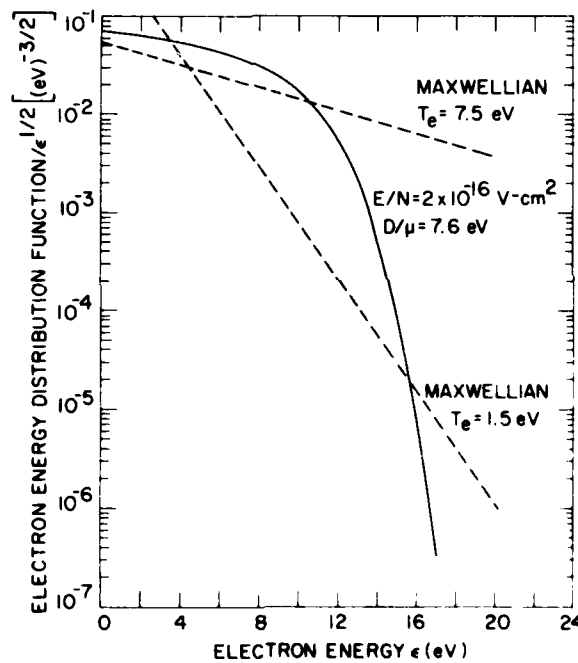
Figure 11. Predicted Electron Energy Distribution in Argon

55

3. CONCLUSIONS

Examination of the physics of microwave discharges in Ar diluent gives the unexpected result that characteristic electron energies are near 8 eV rather than the ~ 2 eV that has been generally accepted in the literature. This latter value appears only for undiluted diatomic gases. This result has significant ramifications for Ar/O_2 and Ar/N_2 mixtures, since the higher electron temperature can cause considerable enhancement in ionization, dissociation, and excitation rates. Kinetic modeling of discharge excitation in Ar/O_2 mixtures is now in progress.

References

1. Rawlins, W. T., Piper, L. G., Gelb, A., Lucht, R. A., and Caledonia G. E. (1983) COCHISE Research, Physical Sciences, Inc., PSI TR-349.

2. Frost, L. S., and Phelps, A. V. (1964) Momentum transfer cross sections for slow electrons in He, Ar, Kr and Xe from transport coefficients, Phys. Rev. 136:A1538.

3. Kieffer, L. J. (1973) A Compilation of Electron Collision Cross Section Data for Modeling Gas Discharge Lasers, JILA Information Center Report 13.

4. Dutton, J. (1975) A survey of electron swarm data, J. Phys. and Chem. Ref. Data 4:577.

5. Lawton, S. A., and Phelps, A. V. (1978) Excitation of the $b^1\Sigma g^+$ state of O_2 by low energy electrons, J. Chem. Phys. 69:1055.

6. Tachibana, K., and Phelps, A. V. (1981) Excitation of the O_2 $(a^1\Delta g)$ state by low energy electrons, J. Chem. Phys. 75:3315.

7. Phelps, A. V. (1982) Private Communication.

8. Jackman, C. H. Garvey, R. H., and Green A. E. S. (1977) Electron impact on atmospheric gases I. Updated cross sections, J. Geophys. Res. 82: 5081.

9. Keto, J. W. (1981) Electron beam excited mixtures of O_2 in argon, II, electron distributions and excitation rates, J. Chem. Phys. 74:4445.

10. Bretagne, J., Godart, J., and Puech, V. (1982) Low-energy electron distribution in an electron-beam-generated argon plasma, J. Phys. D 15:2205.

11. Bozin, J. V., Urosevic, V. V., and Petrovic, Z. Lj (1983) Experimental investigation of excitation of argon metastables by an electron swarm in argon nitrogen gas mixtures, Z. Phys. A: Atoms & Nuclei 312:349.

12. Cobine, J. D. (1958) Gaseous Conductors, Dover Publications, New York, pp. 205-289.

13. Kaufman, F. (1969) The Production of Atoms and Simple Radicals in Glow Discharges, American Chemical Society, pp. 29-4".

14. Brown, S. C. (1956) Breakdown in cases: Alternating and high frequency fields, in Encyclopedia of Physics, Vol. XXII Gas Discharges II, S. Flugge, (Ed.), Springer-Verlag, Berlin, pp. 531-575.

Contents

2.3 COCHISE: Trajectory Calculations

by

A. Gelb
W. T. Rawlins

1. INTRODUCTION

Ozone has long been known to be an important infrared radiator in the lower thermosphere and upper mesosphere.[1,2] A significant level of understanding of the ratiation-producing mechanisms for this species has developed from recent high-altitude in situ measurements[3-7] and kinetic modeling of the quiescent and disturbed upper atmosphere.[8,9] This work has been well supported by a variety of laboratory studies of the relevant production and loss processes. However, the modeling efforts have identified crucial problems in the kinetic schemes, and these problems are difficult to solve unambiguously by experiment. For example, for infrared emission from $O_3(\nu_3)$, the nascent vibrational distribution formed in $O-O_2$ recombination

---

Because of the large number of references cited above, they will not be listed here. See References, page 78.

$$O + O_2 + M \rightarrow O_3 (v') + M$$
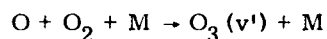
and its subsequent collisional relaxation

$$O_3 (v') + M \rightarrow O_3 (v'') + M$$
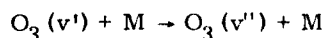
need to be characterized in detail.

Although experimental studies of this and other reactions are ongoing, particularly in research groups at the Air Force Geophysics Laboratory, Massachusetts Institute of Technology, and Physical Sciences Inc., these reactions are extremely difficult to study unambiguously in the laboratory. The difficulties arise from the requirements to produce large but uncontaminated fluxes of atomic oxygen, to form and/or detect very low levels of state-specific reactants and products using sophisticated infrared and ultraviolet fluorescence techniques, and to isolate collisional cascade effects. Furthermore, the eventual results of such experiments need to be interpreted and validated in terms of fundamental concepts of reaction dynamics. Thus, it is important that the laboratory work, as well as continued atmospheric modeling, be supported by detailed theoretical efforts aimed at increasing our understanding of how these reactions occur. We now summarize the salient features of the O_3 problem from the viewpoint of modeling the high-altitude chemistry of O_3.[9, 10]

In the quiescent upper atmosphere, $O_3(v)$ containing more than one quantum of vibrational energy is thought to be formed by three-body recombination of O and O_2. This occurs over a narrow altitude range with a maximum rate near 80 km. The production rate by recombination is negligible above 110 km, and below 70 km at night, but may persist to lower altitudes during the daytime. The principal collision partners in this altitude region are N_2, O_2, and O. Collisional deactivation of $O_3(v)$ by N_2 and O_2 is important below 90 km, and O may be an important collision partner between 90 and 110 km under certain conditions. The rate coefficients of these processes for the higher vibrational levels are totally unknown. In particular, the possibility of O-atom encounters that are reactive,

$$O + O_3 \dagger \rightarrow O_2 + O_2$$
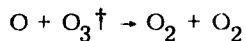
offers the potential for an odd-oxygen loss mechanism that has not been considered in atmospheric photochemical models.

---

10. Green, B. D., Rawlins, W. T., and Caledonia, G. E. (1982) High Altitude Radiation Signatures, Physical Sciences Inc., PSI TR-296.

The principal laboratory investigations of high-altitude $O_3(v)$ chemistry have been performed on the COCHISE facility at AFGL.[11,12] These experiments are performed at 80-150 K, with Ar as the principal third body and O as a dominant relaxation partner, and yield a lower bond to the "nascent" vibrational distribution formed in recombination. By contrast, the atmospheric temperature near the mesopause (100 km) is about 200 K, and the major collision partners are N_2, O_2, and O. A major objective of the theoretical effort discussed here is to verify the supposition that the experiments performed in COCHISE indeed provide a useful representation of the high-altitude chemistry despite these differences. The growing data base now emerging from the COCHISE experiments will provide valuable benchmarks with which the theoretical results can be compared.

The results to be presented here are the initial results from a project designed to investigate several aspects of the reaction dynamics of complex energy transfer processes that are important in high altitude infrared fluorescence mechanisms. Our present work is focused on a theoretical description of the O_3 system. This system offers a unique opportunity to examine the closely coupled dynamics of recombination and collisional deactivation, a topic that has been addressed previously only for relatively simple atom-atom systems (see below). The basic technical approach is to perform classical trajectory calculations for the deactivation of quasi-bound O_2-O by selected collision partners; several methods will be used to define the initial O_2-O orbiting complexes and the required potential surfaces.

Work thus far has treated collisional relaxation of high vibrational-rotational states of ozone by Ar. In particular, we have examined energy transfer as a function of ozone vibrational-rotational excitation and relative translational energy. Ab initio calculations of the ozone potential energy surface at extended configurations have been performed (see Appendix A) and also preliminary calculations on multicollisional relaxation of excited ozone. Before presenting our results to date, some details and background of the computational approaches will be presented. Finally we outline the next steps in this project.

11. Rawlins, W. T., Caledonia, G. E., and Kennealy, J. P. (1981) Observation of spectrally resolved infrared chemiluminescence from vibrationally excited $O_3(v_3)$, J. Geophys. Res. 86:5247.

12. Rawlins, W. T., and Armstrong, R. A. (1982) COCHISE Observations of O_3 Formed by Three-Body Recombination of O and O_2, AFGL-TR-82-0273, AD A123153.

2. THEORETICAL METHODS

2.1 Introduction

The present program is a theoretical study of the dynamics of ozone recombination. Our goal is to predict nascent vibrational and rotational distributions for recombined ozone and to compute relaxational rates of the newly formed molecules. These calculations will provide a basis for the theoretical prediction of radiation from recombined ozone in the upper atmosphere. Our approach is to use classical and semi-classical trajectory methods to compute the outcome of the collision of unbound O_2-O complexes with third body partners such as atomic oxygen and argon.

The recombination of ozone by collision with oxygen atoms is assumed to occur by the following sequence of reactions:

$$O_2 + O \rightarrow O_3^* \tag{1}$$

$$O_3^* + O \rightarrow O_3(v) + O \qquad . \tag{2}$$

In Reaction (1) an oxygen atom and molecule collide to form an unbound or quasi-bound ozone molecule. This complex is unstable and reverts to O_2 and O unless stabilized by collision. In Reaction (2) the quasibound O_3^* collides to form rotationally vibrationally excited ozone. The excess (above the dissociation limit) energy of O_3^* is removed by collision with the incident oxygen atom. Initially, we will adopt Reactions (1) and (2) as the sole mechanism for ozone recombination. Other mechanisms involving collision with O_2 or N_2 as the stabilizing third body, or complexes formed from O_2-O_2 collisions colliding with oxygen atoms, can be addressed at a later time. We will also consider laboratory situations such as the COCHISE experiment in which Ar is the likely collision partner. A similar recombination mechanism is assumed. In the upper atmosphere, however, oxygen atoms are a major species, and it is possible that reactions (1) and (2) describe an important mechanism for the formation of ground-state ozone.

Some discussion has been made with regard to ozone recombination via ozone triplet states. We will not address that issue here directly. Estimates will be made for models of ozone excited states within a single potential surface treatment. Our initial effort will not include the possibility of curve crossings or radiation from recombined triplet states of ozone. The complexities of such an extension would be beyond the scope of our initial study.

2.2 Classical Trajectory Studies of Ozone Recombination

The use of classical trajectories to study chemical reactions dates back to the work of Eyring and Polanyi.[13] However, until the advent of large computers in the late 1950s, classical trajectory studies were quite restricted. The first large scale Monte Carlo trajectory calculations were done by Bunker[14] and Karplus, Porter, and Sharma.[15] Since then, classical trajectory techniques have been widely applied to the study of many chemical processes including three-body exchange reactions, unimolecular decomposition reactions, and energy transfer processes.[16, 17]

Relatively little work using classical trajectory techniques has been done to address molecular recombination dynamics. Shui[18] used Keck's variational phase space technique[19] to calculate $H + H + H \rightarrow H_2 + H$ rates. Burns and coworkers[20-25] have calculated recombination rates for halogen atoms by rare gas atoms. They examined the relative contributions from the radical molecule complex mechanism

$$X + M = XM$$

$$XM + X \rightarrow X_2 + M$$
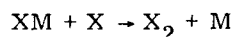
and the energy transfer mechanism

$$X + X = X_2^*$$

$$X_2^* + M = X_2 + M \qquad .$$
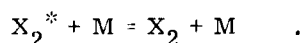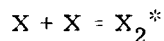
Correction factors for subsequent collisional dissociation of the nascent molecules have been computed by using classical trajectories to solve the Boltzmann equation.[26] This correction factor is quite large (0.6 - 0.8) for halogen atom recombination[23] with inert gas third-body colliders.

The appeal of the classical trajectory technique is its relative computational tractability. Accurate quantum mechanical calculations of polyatomic recombination are not possible on even the fastest computers. Experience has shown that classical trajectory calculations are accurate in cases when tunneling and interference phenomena are not important. This indeed should be the case in ozone recombination.

Because of the large number of references cited above, they will not be listed here. See References, page 78.

2.3 Classical Trajectory Methodology

The calculation of classical trajectories consists of three tasks: (1) selection of initial conditions, (2) integration of Hamilton's equations of motion, and (3) final state analysis. Several reviews have described each of these tasks in considerable detail. The reader is referred especially to the reviews by Bunker,[16] and Porter and Raff.[27] Only points specific to the present calculations will be discussed here.

2.3.1 COORDINATE SYSTEM

We use a four-body coordinate system with the origin fixed at the center of mass. A convenient coordinate system for integration of Hamilton's equations of motion is defined by the relations:

$$\bar{q}_i = \bar{r}_i - \bar{r}_4$$

$$i = 1, \ 2, \ 3$$

$$\bar{p}_i = m_i \dot{\bar{r}}_i \quad ,$$

where $\bar{r}_i$ are the coordinates of the four particles relative to the center of mass and are defined by the relations

$$\sum_{i=1}^{4} m_i \bar{r}_i = 0$$

$$\sum_{i=1}^{4} m_i \dot{\bar{r}}_i = 0 \quad .$$

In the $\bar{q}_i$ coordinate system the Hamiltonian H becomes

$$H = 1/m_4 \sum_{i=1}^{3} (m_i + m_4) \bar{p}_i^2 / 2m_i + 1/m_4 \sum_{i>j} \bar{p}_i \cdot \bar{p}_j + U \quad .$$

where U is the potential energy function. Hamilton's equations are written as

---

27. Porter, R. N., and Raff, L. M. (1976) Classical trajectory methods in molecular collisions, in Dynamics of Molecular Collisions Part B, W. H. Miller, Ed., Plenum Press, New York.

$$\dot{\overline{q}}_i = \frac{\partial H}{\partial p_i} = \frac{m_i + m_4}{m_i m_4} \, \overline{p}_i + \frac{1}{m_4} \, (\overline{p}_{j \neq i} + \overline{p}_{k \neq j \neq i})$$

and

$$\dot{\overline{p}}_i = \frac{\partial H}{\partial \overline{q}_i} = -\frac{\partial U}{\partial \overline{q}_i} \quad .$$

2.3.2 METHOD OF INTEGRATION

The numerical integrations were performed using a fourth order fixed step size Runge-Kutta integrator for the first five integration points. Subsequent points were computed using a fixed step size, fourth order Adams-Moulton integrator.

Computed trajectories were checked for numerical accuracy by back integration of selected trajectories and observation of conservation of energy and angular momentum. Total energy was usually constant to a few parts in 10^6. Angular momentum components were conserved to better than 1-2 parts in 10^6. The integrations were performed using 60 bit CDC single precision arithmetic. Most calculations were performed on the Cyber 175 computer at the Air Force Geophysics Laboratory.

2.3.3 POTENTIAL SURFACE

For collisions of Ar with O_3 we use the Varandas-Murrell potential surface.[28] The ozone portion of this potential was derived using available spectroscopic data by Murrell et al.[28, 29]

The potential function is written as

$$U = V_{Ar-O_3} + V_{O_3} \quad ,$$

where V_{Ar-O_3} is the potential function for the Ar-O_3 interaction and V_{O_3} is the potential function for ozone. V_{Ar-O_3} is given by a sum of pairwise Ar-O Lennard-Jones 6-12 potentials between the Ar atom and each oxygen atom, that is,

28. Varandas, A. J. C., and Murrell, J. N. (1982) Dynamics of the $^{18}O + {}^{16}O_2$ (v = 0) exchange reaction on a new potential energy surface for a ground state ozone, Chem. Phys. Lett. 88:1.

29. Carter, S., Mills, I. M., Murrell, J. N., and Varandas, A. (1982) Analytical potentials for triatomic molecules IX. The prediction of anharmonic force constants from potential energy surfaces based on harmonic force fields and dissociation energies for SO_2 and O_3, J. C. Molec. Phys. 45:1053.

$$V_{ArO_3} = \sum_{i=1}^{3} 4\varepsilon_{ArO} \left[\left(\frac{\sigma}{|\bar{q}_i|} \right)^{12} - \left(\frac{\sigma}{|\bar{q}_i|} \right)^{6} \right] \quad .$$

The ozone interaction, V_{O_3}, is written as a function of the oxygen interatomic distances, r_1, r_2, and r_3, defined by

$$\bar{r}_1 = \bar{q}_1 - \bar{q}_2$$

$$\bar{r}_2 = \bar{q}_2 - \bar{q}_3$$

$$\bar{r}_3 = \bar{q}_1 - \bar{q}_3$$

and is given by

$$V_{O_3} = [P(r_1 r_2 r_3) + G(r_1 r_2 r_3)][1 - \tanh 2.2Q_1]$$

$$+ V_{O_2}(r_1) + V_{O_2}(r_2) + V_{O_2}(r_3) \quad ,$$

where

$$V_{O_2}(r) = C_1[1 + C_2(r - C_3)] \ e^{-C_4(r - C_3)} \quad ,$$

$$Q_1 = C_{12}[(r_1 - C_{13}) + (r_2 - C_{13}) + (r_3 - C_{13})] \quad ,$$

$$Q_2 = C_{14}[(r_2 - C_{13}) - (r_e - C_{13})] \quad .$$

$$Q_3 = C_{15}(r_1 - C_{13}) + C_{16}(r_2 - C_{13}) + C_{17}(r_3 - C_{13}) \quad ,$$

$$P = C_5 + C_6 Q_1 + C_7 Q_1^2 + C_8(Q_2^2 + Q_3^2) + C_9 Q_1(Q_2^2 + Q_3^2)$$

$$+ C_{10}(Q_3^3 - 3Q_2^2 Q_3) + C_{11}(Q_2^2 Q_3^2)^2 \quad ,$$

$$G = g_1(1 + g_3 Q_1) g_P^5 \ e^{-g_4(Q_2^2 + Q_3^2)}$$

and

$$g_p = g_3 + \sum_{\substack{i=1 \\ i \neq j \\ i=h}}^{3} [(r_i^2 - r_j^2 - r_h^2)/2r_j r_h] \quad .$$

66

3. CLASSICAL TRAJECTORY CALCULATIONS

3.1 Test Matrix

The first effort in this project was devoted to a systematic study of energy relaxation of highly vibrationally rotationally excited ozone by collision with argon. Calculations were performed at fixed Ar-O_3 relative translational energy. Translational energies of 0.5, 1.0, 2.0, and 4.0 kcal/mol were considered (corresponding to average kinetic energies for temperatures of 250, 500, 1000, and 2000 K). Ozone molecular energies of 25, 20, 15, and 10 kcal/mol were used for each translational energy. (The ozone dissociation energy on this potential surface is approximately 26 kcal/mol from the well minimum). For each ozone internal energy the molecular angular momentum was varied between 0 and a value for which almost all the molecular energy was in rotation. For calculations at fixed ozone angular momentum, impact parameters were chosen randomly with a maximum value of 4Å. Calculations were done in batches of 500-1000 (usually 750) for each set of translational energy, molecular energy, and molecular angular momentum. Approximately 80,000 trajectories were computed for this effort.

Calculations were also performed at fixed total molecular energy with different partitionings of molecular energy (set equal to 25 kcal/mol) between rotation and vibration. Initial vibrational energy was equal to 0, 12.5, and 25 kcal/mol. Each calculation was done for a relative translational energy of 2 kcal/mol and fixed impact parameter. Impact parameters were varied between 0 and 4Å in steps of 0.5Å. Batches of (usually 1000) trajectories were computed for each set of initial conditions. About 27,000 trajectories were computed for these initial conditions.

Initial multiple collision simulations of vibrationally rotationally excited ozone have also been begun. These calculations provide an approximate description of the temporal behavior, that is, relaxation, of ozone in a bath of argon. The relaxation of ensembles of 60 ozone molecules by 250 sequential collisions with argon has been computed. Two cases were treated, each with initial total molecular energy equal to 15 kcal/mol. The two batches differed by the amount of angular momentum in the initial molecules. The relative translational energy for each collision in the sequence was fixed at a value of 2.388 kcal/mol corresponding to an approximate bath temperature of 597 K. Some calculations have also been performed for relaxation and dissociation of highly excited ozone with 25 kcal/mol initial vibrational energy.

3.2 Results and Discussion

In the first part of this effort we have examined energy transfer from highly excited ozone by collision with argon as a function of molecular angular momentum. The focus has been to examine the effect on energy transfer of partitioning of the total molecular internal energy between rotation and vibration. The primary quantity of interest is the mean energy transferred in a collisional event, $\langle \Delta E \rangle$. This quantity is computed by suitably averaging over an ensemble of trajectories with randomly chosen initial conditions. Computed values of $\langle \Delta E \rangle$ vs initial ozone angular momentum are shown in Figures 1-4, for total ozone internal energies of 25, 20, 15, and 10 kcal/mol respectively. For each initial ozone internal energy, relative translational energies of 0.5, 1.0, 2.0, and 4.0 kcal/mol were considered. Molecular angular momentum was varied from zero (non-rotating molecule) to a value such that almost all the internal energy was present as rotational energy. Molecular angular momentum is plotted in units of 16 ℏ for convenience. The significance of these initial calculations to the relaxation of nascent recombined ozone molecules will be discussed briefly later.

Figure 1. Average Energy Transferred per Collision, $\langle \Delta E \rangle$, Between Ozone and Argon as a Function of Initial Ozone Molecular Angular Momemtum, J_{mol}, for Relative Translational Energies of 0.5, 1.0, 2.0, and 4.0 kcal/mol. Initial ozone molecular energy is equal to 25 kcal/mol

Figure 2. Average Energy Transferred per Collision,
$\langle\Delta E\rangle$, Between Ozone and Argon as a Function of Initial
Ozone Molecular Angular Momentum, J_{mol}, for Rela-
tive Translational Energies of 0.5, 1.0, 2.0, and 4.0
kcal/mol. Initial ozone molecular energy equal to
20 kcal/mol

Figure 3. Average Energy Transferred per Collision,
$\langle\Delta E\rangle$, Between Ozone and Argon as a Function of Initial
Ozone Molecular Angular Momentum, J_{mol}, for Rela-
tive Translational Energies of 0.5, 1.0, 2.0, and 4.0
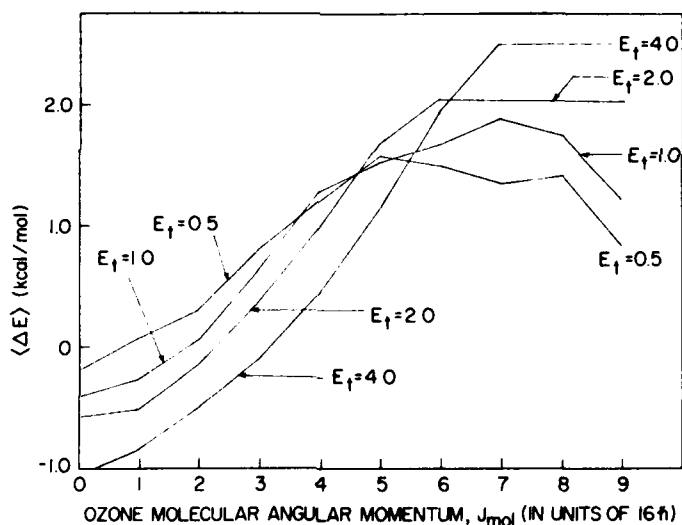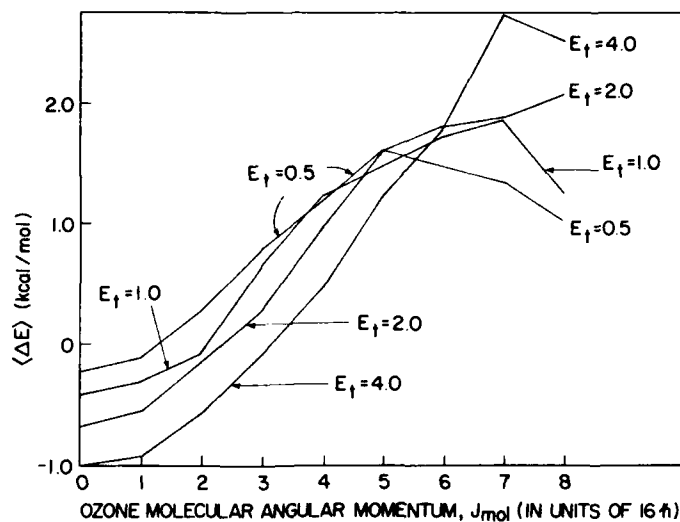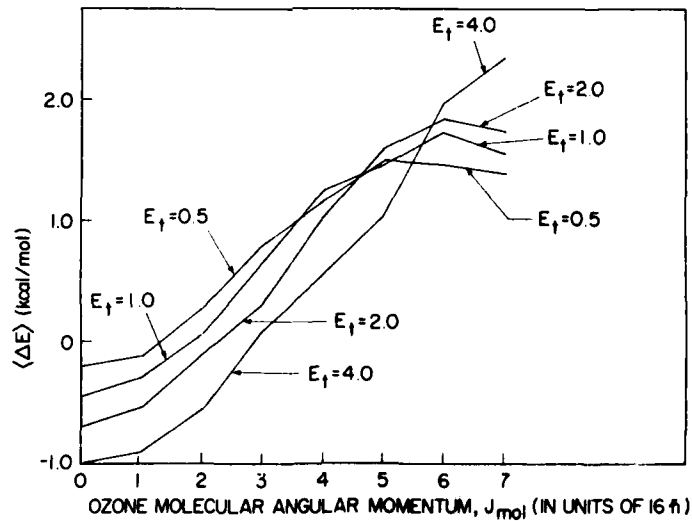kcal/mol. Initial ozone molecular energy equal to
15 kcal/mol

69
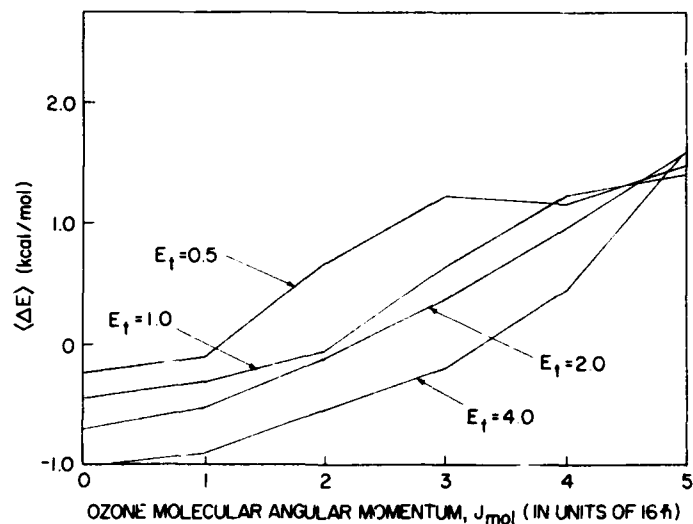
Figure 4. Average Energy Transferred per Collision,
$\langle \Delta E \rangle$. Between Ozone and Argon as a Function of Initial
Ozone Molecular Angular Momemtum, J_{mol}, for Rela-
tive Translational Energies of 0.5, 1.0, 2.0, and 4.0
kcal/mol. Initial ozone molecular energy equal to
10 kcal/mol

We discuss first the results for collisions with ozone with 25 kcal/mol inter-
nal excitation. The adiabatic dissociation energy of ozone via the reaction

$$O_3 \rightarrow O_2 + O$$
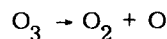
requires slightly more than 26 kcal/mol (from the well bottom, neglecting zero
point energy). Thus in this case we are considering energy transfer from mole-
cules excited to within 1 kcal/mol of their dissociation limit. The computed
values of $\langle \Delta E \rangle$ are displayed in Figure 1. Two points are immediately obvious
and noteworthy. First, despite the high internal energy, molecules with low an-
gular momentum gain energy per collision. This occurs for all relative transla-
tional energies. This gain in energy is correlated with a transfer of relative
orbital angular momentum into molecular angular momentum. Second, as the
molecular angular momentum is increased the energy transfer is reversed and
the ozone molecules lose energy per collision. The results indicate that transfer
of energy to ozone by collision occurs most readily by transfer into rotational
energy. The implication of this for relaxation of newly recombined ozone is that
despite high vibrational excitation, relaxation occurs when substantial angular
momentum is available. Low angular momentum molecules will gain energy and
have a high probability of redissociation.

70

We note also the dependence of energy transfer on relative translational energy. At zero initial ozone angular momentum the average energy transferred per collision, $\langle\Delta E\rangle$, decreases with increasing translational energy, that is, the amount of energy transferred into the molecule increases with increasing translational energy. Thus for the range of translational energy considered here, which corresponds to a translational temperature range of 250-2000 K, the net effect of collisions with non-rotating ozone is to pump energy into the molecule and the magnitude of the energy transferred increases with the available translational energy.

As the initial ozone angular momentum is increased the sign of the energy transfer begins to change and energy transfer from the molecule occurs. Energy transfer from the molecule as a function of molecular angular momentum occurs first for the lowest translational energy, 0.5 kcal/mol. Thus at intermediate values of molecular angular momentum the average energy transfer varies inversely with relative translational energy. As the molecular angular momentum is increased further the dependence of the energy transferred on translational energy changes again. At high values of initial molecular angular momentum $\langle\Delta E\rangle$ again increases with increasing translational energy. This transition occurs for the translational energies considered when a large fraction of the 25 kcal/mol is available as rotational energy. (Note however that at internal energies of 25 kcal/mol a strict separation of rotational and vibrational energy is not feasible.)

At low initial angular momentum the impinging Ar atom sees a cold rotational mode and transfers energy into it. As mentioned, the vibrational motion is highly energetic but does not couple readily to the atom translation. Thus the net effect is energy transfer into the molecule. At intermediate values of molecular angular momentum the rotational mode and translational energy are balanced so that they do not exchange energy. Energy exchange between vibration and translation does not occur readily and the net effect is that the average energy passes through zero for each translational energy. As expected, this occurs at higher values of molecular angular momentum for higher translational energies. At high values of molecular angular momentum the impinging atom sees a hot rotational mode which readily loses energy to translation and thus the net effect of collisions is that the molecule loses energy. If molecular angular momentum could be increased indefinitely, its characteristic time scale would become too short to effectively couple with translation and a decrease in energy transfer is expected.

The computed values of $\langle\Delta E\rangle$ for ozone internal energies of 20, 15, and 10 kcal/mol are shown in Figures 2, 3, and 4 respectively. These results are extraordinarily similar to those for internally excited ozone of 25 kcal/mol. This

71

result is in accordance with the fact that energy transfer occurs primarily between translational and rotational modes. At the lower vibrational energies this should be even more true due to the shorter timescale of vibrational motion as one goes down into the potential well.

Selected calculations have been performed for $\langle \Delta E \rangle$ as a function of impact parameter. Three cases for ozone with (initially) 25 kcal/mol internal energy have been computed: (1) all internal energy in vibration, (2) the internal energy (arbitrarily) divided equally between vibration and rotation, and (3) all internal energy as rotation. The calculations are for relative translational energy of 2 kcal/mol. The results are displayed in Figure 5.
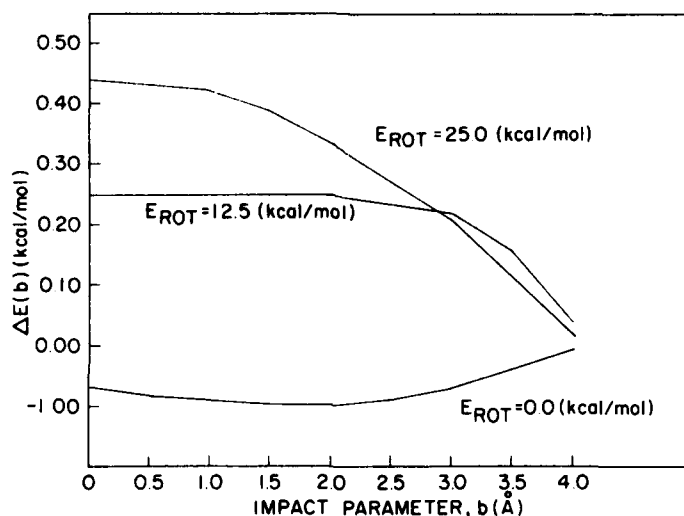
Figure 5. Average Energy Transferred per Collision, $\Delta E(b)$, Between Ozone and Argon as a Function of Impact Parameter for Initial Ozone Rotational Energy Equal to 0, 12.5, and 25 kcal/mol. Total initial ozone molecular energy is equal to 25 kcal/mol

For the non-rotating case ($E_{ROT} = 0$) the energy transfer is negative at all impact parameters, that is, energy is pumped into the molecule. This shows that the net negative values discussed earlier that were averaged over impact parameters had no positive energy transfer range. The magnitude of the energy transfer increases initially due to the increasing orbital angular momentum of the relative translational motion. At large impact parameters the energy transfer decreases rapidly due to the fairly rapid drop-off of the potential with inter-molecular distance. For the case when all the initial triatom energy is in rotation, very large average energy transfers are computed. In this case the average energy transfer decreases monotonically with increasing impact parameters. The

case of equally divided initial rotational and vibrational energy resembles the $E_{VIB} = 0$ case. Here the magnitude of energy transferred per collision is somewhat reduced due to the lesser amount of rotational energy.

It is also of interest to examine the distribution of energy transfers per collision. Distributions of magnitudes of energy transfers are shown in Figure 6 for initial molecular excitation of 25 kcal/mol, and translational energy of 2 kcal/mol for two values of initial angular momentum: 31 and 125 $\hbar$. As before, positive values of energy transfer signify energy is lost from the molecule while for negative values the molecule gains energy in a collision. As seen in both Figures 6 and 7 most collisional encounters lead to small energy transfers due to the fairly large maximum impact parameter of 4Å used in the calculations. For the lower value of molecular angular momentum there are very few encounters in which more than 1-2 kcal/mole is transferred out of the molecule. Hence, as previously mentioned, the net collisional transfer is into the ozone molecule despite its initial high vibrational-rotational excitation. For higher molecular angular momentum the result is quite different. The average energy transfer is from the molecule to relative translational motion. Additionally there are a substantial number of large energy transfer collisions. The total cross section for energy transfers greater than 10 kcal/mol is computed to be 2.4 Å^2. It is clear that the presence of large molecular angular momentum qualitatively changes the energy transfer.

Figure 6. Relative Frequency of Energy Transfers, ΔE, in Argon-Ozone Collisions at Initial Relative Translational Energy of 2 kcal/mol, Ozone Molecular Energy of 25 kcal/mol, and Initial Molecular Angular Momentum Equal to 31 $\hbar$
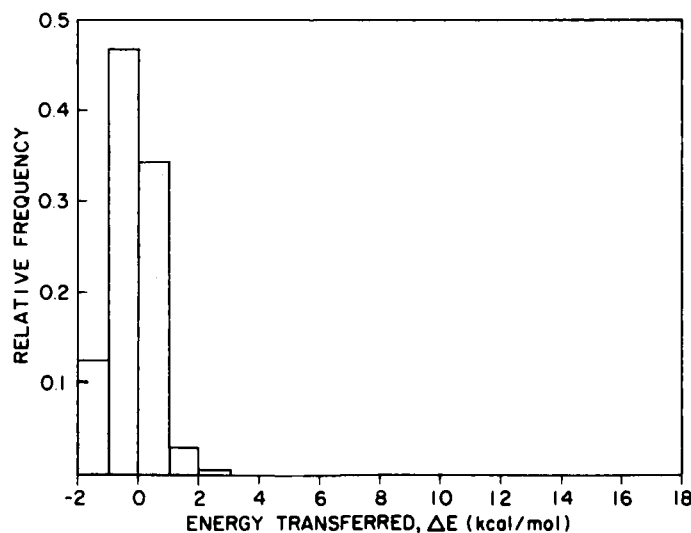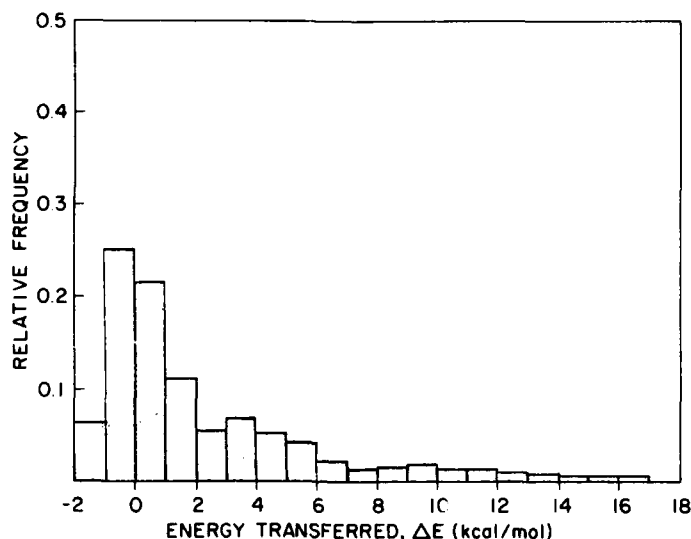
Figure 7. Relative Frequency of Energy Transfers, ΔE, in Argon-Ozone Collisions at Initial Relative Translational Energy of 2 kcal/mol, Ozone Molecular Energy of 25 kcal/mol, and Initial Molecular Angular Momentum Equal to 125 $\hbar$

Multiple collision calculations were performed to simulate the relaxation of excited ozone in a bath of argon. Two cases were treated in this preliminary effort; (1) molecules initially with excited 15 kcal/mol with angular momentum equal to 16 $\hbar$ and (2) molecules excited 15 kcal/mol with angular momentum equal to 63 $\hbar$. The average molecular energy vs collision is plotted in Figure 8 for both cases. A fixed value of the relative translational energy equal to 2.3 kcal/mol was chosen.

The effect of initial molecular angular momentum is readily seen. Initially the low angular momentum molecules gain energy as angular momentum is built up by collisions. On the other hand, the higher angular momentum molecules undergo a rapid energy loss initially associated with a loss in average molecular angular momentum. The difference in behavior between the two ensembles is highly transitory. After approximately 50 collisions the characteristic relaxation behaviors of both ensembles become identical. This behavior, however, has serious implications for the early relaxation of recombined molecules formed very close to the dissociation limit. For molecules with low angular momentum, energy will be pumped into the molecule as angular momentum is increased by collisions. This will lead to dissociation for some molecules. However, molecules formed with high angular momentum will lose energy and should have a substantially lower probability of dissociation.

74
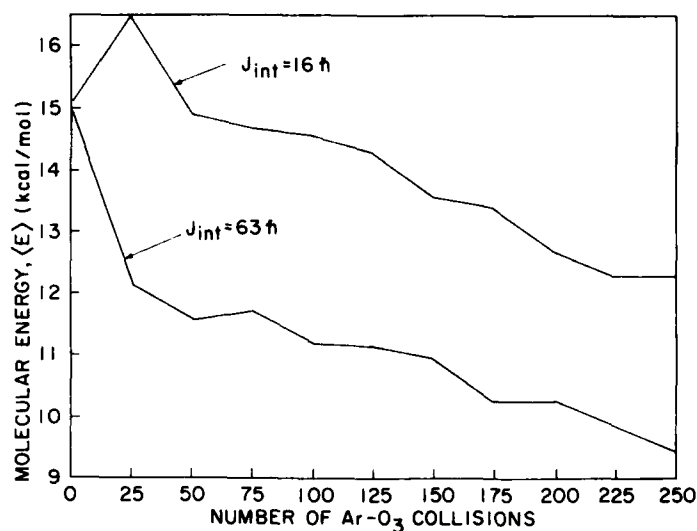
Figure 8. Average Molecular Internal Energy of an Ensemble of Ozone Molecules as a Function of Number of Collisions with Argon Atoms. The results for two ozone ensemble initial conditions are shown: (1) total ozone energy equal to 15 kcal/mol and initial ozone angular momentum, J_{int}, equal to 16 $\hbar$, and (2) total ozone energy equal to 15 kcal/mol and J_{int} - 63 $\hbar$. Relative translational energy is equal to 2.3 kcal/mol in both cases

Preliminary calculations of the relaxation of 25 kcal/mol vibrationally excited ozone (with zero angular momentum) show that on the order of one-third of the molecules are dissociated after 25 collisions. Dissociation, curiously, is a very low probability single collision event. Approximately 10,000 trajectories were computed in which the total energy exceeded the ozone dissociation energy. However only one trajectory was observed to lead to dissociation. The multicollisional calculations imply that dissociation is quite important for very highly excited molecules and makes a very significant contribution to the computed rates of recombination and relaxation. These early calculations would seem to establish the need for describing nonequilibrium effects in any realistic description of ozone recombination.

3.3 Implication for COCHISE and High Altitude Processes

In the COCHISE apparatus, radiation is measured from recombined ozone. The measurements are made after the nascent molecules have undergone between 10^2 and 10^4 collisions. Analysis of the measured spectra indicates vibrational states above the sixth quantum level are not detected. The conclusion of the present study is that the COCHISE measurements are from ensembles of recombined

75

ozone that have undergone substantial molecular relaxation and thus do not directly reflect the nascent distribution of very highly excited ozone vibrational states.

It is important to compare the conditions of the COCHISE experiment and high altitude processes. At 100 km collision frequencies are about 3/msec. Radiative lifetimes from highly excited vibrational states of ozone are predicted to be 20 msec. Thus on the average, 50 collisions occur before radiation is emitted. The calculations presented here imply that substantial relaxation of very highly excited molecular states could occur on this time scale. Thus the radiation emitted from recombined ozone at these altitudes could reflect a partially relaxed distribution of molecular states.

To compare the degree of relaxation in the COCHISE experiments to that in the upper atmosphere we first note that it is expected that the rate of collisional relaxation of uppermost ozone states should be faster than that of lower states. Two factors should make this true: (1) very highly excited states may be depleted both by energy loss and by energy gain via dissociation, and (2) for lower states, the energy gap between states increases and coupling between rotational and vibrational modes decreases. Our tentative conclusion is that the very uppermost states are relaxed in both the COCHISE apparatus and at 100 km altitude. Substantially more relaxation occurs in the COCHISE experiments. However, this additional effect should be considerably less dramatic due to the slower relaxation of less excited atates.

3.4 Future Work

The goal of this project is to develop a theoretical description of ozone recombination dynamics to aid in the interpretation of available data. Thus far we have developed the computational machinery for this effort and have completed a systematic study of energy relaxation of vibrationally rotationally excited ozone by collision with argon atoms. We have started to examine the time evolution of excited ozone in a thermal bath of argon atoms. When this is completed, our future efforts will become more specifically directed towards recombination simulation studies.

The first step will be characterization of unbound O_3 complexes. Two approaches will be used: (1) a classical trajectory search for long-lived O_3^* formed by O_2-O collisions and (2) a semiclassical calculation of resonance states[30-32] above the dissociation limit (by D. Noid and M. Koszykowski). Collision rates (one-way fluxes) will then be calculated for stabilization of O_3^* by argon atoms

---

References 30 to 32 will not be listed here. See References, page 78.

and ensembles of nascent recombined ozone will be generated. The relaxation of the nascent ensembles will be studied using multicollision calculations. The results of these calculations should provide a valuable insight into the experimental data. In addition to the $Ar-O_3$ system we shall begin work on the $O-O_3$ system.

A potential surface for $O-O_3$ interactions will be generated using the available O_3 surface and ab initio quantum mechanical calculations (by D. Noid and M. Koszykowski). The recombination dynamics and relaxation of this system will then be studied using the techniques established for the $Ar-O_3$ system.

References

1. Stair, Jr., A. T., Ulwick, J. C., Baker, D. J., Wyatt, C. L., and Baker, K. C. (1974) Altitude profiles of infrared radiance of O_3(9.6 μm) and CO_2 (15 μm), Geophys. Res. Lett. 1(No. 3):117.

2. Stair, Jr., A. T., Ulwick, J. C., Baker, K. D., and Baker, D. J. (1975) Rocketborne observations of infrared emissions in the auroral region, in Atmospheres of the Earth and the Planets, B. M. McCormack, Ed., D. Reidel, Dordrecht-Holland, pp. 335-346.

3. Stair, Jr., A. T., Pritchard, J., Coleman, I., Bohne, C., Williamson, W., Rogers, J., and Rawlins, W. T. (1983) The rocketborne cryogenic (10 K) high resolution interferometer spectrometer flight-HIRIS: atmospheric and auroral infrared emission spectra, Appl. Opt. 22:1056.

4. Rawlins, W T., Caledonia, G. E., Gibson, J. J., and Stair, Jr., A. T. (1981) Infrared emission from NO(Δv = 1) in an aurora: spectral analysis and kinetic interpretation of HIRIS measurements, J. Geophys. Res. 86:1313.

5. Rawlins, W. T., Caledonia, G. E., Gibson, J. J., and Stair, Jr., A. T. (1985) HIRIS rocketborne spectra of infrared fluorescence in the O_3 (ν_3) band near 100 km, J. Geophys. Res., 90:2896-2904.

6. Nadile, R. M., Stair, Jr., A. T., Wheeler, N. B., Frodsham, D. G., Wyatt, C. L., Baker, D. J., and Grieder, W. F. (1978) SPIRE-Spectral Infrared Rocket Experiment (Preliminary Results), AFGL-TR-78-0107, AD A058504.

7. Green, B. D., Rawlins, W. T., and Nadile, R. M. (1985) Diurnal variability of vibrationally excited ozone in the mesosphere, J. Geophys. Res. (to be submitted).

8. Caledonia, G. E., and Kennealy, J. P. (1982) NO infrared radiation in the upper atmosphere, Planet Space Sci. 30:1043.

9. Rawlins, W. T. (1985) Chemistry of vibrationally excited ozone in the upper atmosphere, J. Geophys. Res. (to be submitted).

10. Green, B. D., Rawlins, W. T., and Caledonia, G. E. (1982) *High Altitude Radiation Signatures*, Physical Sciences Inc., PSI TR-296.

11. Rawlins, W. T., Caledonia, G. E., and Kennealy, J. P. (1981) Observation of spectrally resolved infrared chemiluminescence from vibrationally excited O_3 (ν_3), *J. Geophys. Res.* 86:5247.

12. Rawlins, W. T., and Armstrong, R. A. (1982) *COCHISE Observations of O_3 Formed by Three-Body Recombination of O and O_2*, AFGL-TR-82-0273, AD A123153.

13. Eyring, H., and Polanyi, J. (1931) Monte Carlo calculation of triatomic disassociation rates I, *Z. Phys. Chem.* B12:279.

14. Bunker, D. L. (1962) Dynamics of reactive collisions: the H & H_2 exchange reaction, *J. Chem. Phys.* 37:393.

15. Karplus, M., Porter, R. N., and Sharma, R. D. (1964) *J. Chem. Phys.* 40:2033.

16. Bunker, D. L. (1971) Classical trajectory methods, *Meth. Comp. Phys.* 10:287.

17. Porter, R. N. (1974) Classical trajectory methods in molecular collisions, *Am. Rev. Phys. Chem.* 25:317.

18. Shui, V. H. (1973) Thermal dissociation and recombination of hydrogen according to the reactions $H_2 + H = H + H + H$, *J. Chem. Phys.* 58:4068; and earlier references.

19. Keck, J. C. (1972) Monte Carlo trajectory calculations of atomic and molecular excitation in thermal systems, *Advanc. At. Mol. Phys.* 8:39.

20. Clarke, A. G., and Burns, G. (1971) Trajectory studies of atomic recombination reactions, *J. Chem. Phys.* 55:4717.

21. Clarke, A. G., and Burns, G. (1972) Trajectory studies of atomic recombination reactions II. the energy transfer mechanism and non-equilibrium effects, *J. Chem. Phys.* 56:4636.

22. Clarke, A. G., and Burns, G. (1973) Trajectory studies of atomic recombination reactions III. energy transfer in bromine-inert gas systems, *J. Chem. Phys.* 58:1908.

23. Wong, W. H., and Burns, G. (1973) Trajectory studies of atomic recombination reaction IV. recombination of iodine atoms, *J. Chem. Phys.* 58:4454.

24. Chang, D. T., and Burns, G. (1976) Trajectory studies of atomic recombination reactions VII. recombination of I and Br atoms, *Can. J. Chem.* 54:1535.

25. Burns, G., and Young, A. W. (1980) Trajectory study of atomic recombination reactions VIV. the energy transfer mechanism, *J. Chem. Phys.* 72:3630.

26. Gelb, A., Kapral, R., and Burns, G. (1972) Nonequilibrium effects in atomic recombination reactions, *J. Chem. Phys.* 56:4631.

27. Porter, R. N., and Raff, L. M. (1976) Classical trajectory methods in molecular collisions, in *Dynamics of Molecular Collisions Part B*, W. H. Miller, Ed., Plenum Press, New York.

28. Varandas, A. J. C., and Murrell, J. N. (1982) Dynamics of the $^{18}O + ^{16}O_2$ (v = 0) exchange reaction on a new potential energy surface for a ground state ozone, *Chem. Phys. Lett.* 88:1.

79

29. Carter, S., Mills, I. M., Murrell, J. N., and Varandas, A. (1982) Analytical potentials for triatomic molecules IX. The prediction of anharmonic force constants from potential energy surfaces based on harmonic force fields and dissociation energies for SO_2 and O_3, J. C. Molec. Phys. 45:1053.

30. Marcus, R. A. (1973) Semiclassical theory for collisions involving complexes (compound state resonances) and for bound states, Fara. Disc. Chem. Soc. 55:34 and reference therein.

31. Noid, D. W., and Marcus, R. A. (1975) Semiclassical calculation of bound states in a multidimensional system. Use of Poincare's surface of section, J. Chem. Phys. 62:2119.

32. Noid, D. W., and Marcus, R. A. (1977) Semiclassical calculation of bound states in a multidimensional system for nearly 1:1 degenerate systems, J. Chem. Phys. 67:559.

Appendix 2.3A:
Quantum Chemical Calculations on O$_3$

by

D. Noid and M. Koszykowski

The ultimate goal of this project is a theoretical description of O-O$_3$ recombination dynamics. A prerequisite for such calculations is a reasonably accurate representation of the O$_3$-O potential energy surface. To this end, ab initio quantum mechanical calculations are to be done at Sandia National Laboratories. As a first step in this effort we computed energies at selected configurations on the ozone potential surface. The results of these calculations will be used for evaluating the currently used Murrell et al ozone potential surface and for re-parameterizing that surface if necessary. The results of the ozone potential surface calculation techniques and results are presented below.

Studies have shown that the calculation of spectroscopic properties and collision cross sections are frequently very sensitive to changes in the shape of the potential energy surface used for the calculations. No complete quantum chemically calculated surfaces exist for this system, primarily since calculations on three- or four-heavy-atom systems are prohibitively computer intensive. A carefully constructed surface of O$_3$ does not exist but was fit with a heavy reliance on existing experimental data. To test this surface and possibly improve the parameters we have performed a series of quantum chemistry calculations on O$_3$ that sample various regions of the surface, especially at extended internuclear separations.

There are numerous approximations one can employ in these quantum chemical calculations. We will briefly discuss three types of calculations: (1) Hartree-Fock (HF), (2) Configuration-Interaction (CI), and (3) Many Body Perturbation Theory (MBPT), and list the considerations that led us to use MBPT.

81

Hartree-Fock calculations are the simplest method we will discuss and also form the starting basis for the other two methods. We write the wavefunction ψ_o as a determinant of one electron spin orbitals χ_i

$$\psi_o = (n!)^{-1/2} \det(\chi_1 \ldots \chi_n) \qquad,$$

where n is the number of electrons and the χ are electron functions which are a product of space and spin. In the linear combination of atomic orbitals approximation, the χ_i are expanded in terms of N functions ϕ_j

$$\chi_i = \sum_{1=i}^{N} C_{ij}\phi_j$$

and in our case the ϕ_j are Gaussian approximations to Slater orbitals centered on the atoms. We now solve for the C_{ij} by minimizing the expectation value of the total energy variationally

$$E = \int \ldots \int \psi_o^* H \psi_o \, d\tau \qquad,$$

where H is the non-relativistic, non-magnetic Born-Oppenheimer Hamiltonian. *This gives us the Hartree-Fock energy and wavefunction.* In effect we have solved the equation for each electron in the average field of the (n-1) remaining electrons. Electrons, however, respond to each other via Coulomb's law instantaneously, that is, *the electrons do not move in an averaged field but are correlated.* This correlation energy between the pairs of electrons is neglected in the Hartree-Fock treatment and is defined as

$$E_\rho = E_{exact} - E_{HF} \qquad.$$

The self-consistent field (SCF) or Hartree-Fock energy is generally good for evaluating the overall surface topology and is excellent for calculations of equilibrium geometries. However as the bond displacements increase the correlation energy increases and a correlation correction must be made to adequately describe the long-range interactions.

The most common method of calculating the correlation energy is commonly referred to as the *Configuration Interaction (CI)* method. The SCF wavefunction contains n orbitals $(\chi_1 \ldots \chi_n)$ that are occupied and (N-n) orbitals $(\chi_{n+1} \ldots \chi_n)$ that are virtual or unoccupied. An obvious way to go beyond the HF calculation is to *variationally determine the total energy* by including wave functions with different configurations, that is, each new configuration replaces an occupied orbital

82

from the SCF wavefunction with a virtual orbital. A common method of classifying configurations is by examining the total number of orbitals in the wave function that differ from the SCF reference wavefunction. We write the CI wavefunction as

$$\psi_{CI} = C_o \psi_o + \sum_i C_i \phi_i^S + \sum_j C_j \phi_j^D + \ldots$$

where a single excitation function, ϕ_i^S, differs from the SCF reference χ_o by one orbital and the double excitation function ϕ_j^D by two, and so on. The CI coefficients, C_i, are then determined variationally to yield the lowest possible total energy. In the limit of a complete basis set ($N \to \infty$) and where all possible substitutions are included in ψ_{CI}, the variational energy approaches the correct non-relativistic Born-Oppenheimer results. Errors arise from a truncation of the functions used to determine the SCF reference wavefunction and from the truncation of the excitation functions series in ψ_{CI}. The reference wavefunction ψ_o will typically be the same for a CI or Many Body Perturbation Theory (MBPT) calculation, however, for a molecule even as small as water, ψ_{CI} becomes a function of a very large number of basis functions. Because of this one must truncate the expansion and eliminate unimportant configurations. In general one can show that

$$\langle \psi_o | H | \phi^T \rangle = \langle \psi_o | H | \psi^Q \rangle = 0)$$

In words, the matrix elements between the reference wavefunctions and triple and quadruple excitations is zero. Thus to first order, only single and double excitations contribute. Because of this, many CI calculations attempt to include all single and double excitations in the expressions for ψ_{CI}. To go beyond this, generally more than one reference wavefunction is used.

In MBPT we will again begin with the SCF wavefunction (ψ_o) as our reference and attempt to account for E_c, the correlation energy. The concept of substitution or excitation functions described in the above section on CI calculations will carry over to the MBPT calculations. In MBPT one can write the wavefunction, ψ_p, as

$$\psi_p = e^T | \phi \rangle$$

where T is an excitation operator defined as

$$T = T_S + T_D + T_T + T_Q \ldots$$

83

where S, D, T, and Q refer to Single, Double, Triple, and Quadruple substitutions respectively. One can write T_n, in general, where n refers to the number of excitations as

$$T_n = \frac{1}{n!} \sum_{\ell, a} t_\ell^a x_a^+ \cdots x_\ell \quad ,$$

where the sum over a represents excited orbitals and ℓ occupied orbitals. The total energy is now given by

$$E_{MBPT} = \langle \phi_o | He^T | \phi_o \rangle \quad .$$

To evaluate E_{MBPT}, the t_ℓ^a from above must be determined. An equivalent expression that makes the perturbation expansion clearer is

$$E_{MBPT} = \sum_{K=0}^{\infty} \langle \phi_o | H [E_o - H_o)^{-1} H]^k | \phi_o \rangle \quad ,$$

where the sum is over only so called linked diagrams, H_o has eigenfunctions ϕ_o, and the expansion potential $V = H - H_o$, the perturbation. The k = 0 term gives the reference energy and for k > 0 correlation corrections are included. In practice the MBPT total energy is calculated by truncating the T operator expansion and projecting $He^{Tn} | \phi_o \rangle$ onto the appropriate n-space. This leads to a set of nonlinear coupled equations for the t_ℓ^a coefficients which correspond to the CI expansion coefficients. The equations are solved iteratively and E_{MBPT} evaluated. In practice T_4 is an upper limit that corresponds to quadruple substitutions. The series is an oscillatory convergent sum, which in practice has proven to be at least as accurate as E_{CI} with single and double excitations included.

The best possible method to use would be a full CI (all possible configurations) with a complete basis set. However, since the number of configurations is proportional to $\langle n |^\ell$, where n is the number of basis functions and ℓ is the level of excitation, it would be prohibitive to even include all single and double excitations. This truncation causes the loss of size consistency. Size consistency implies that the energy calculated for A and B far apart is the sum of the energy calculated for A and B separately. In a size extensive calculation the energy is proportional to the size of the system. These properties are very important if one wishes to compute correct relative energies on a potential energy surface. MBPT, on the other hand, is guaranteed to have the correct size-dependence because the expansions contain only the so-called linked diagrams. In addition,

84

because of the computational efficiency of MBPT, calculations can be performed up to fourth order in the perturbation expansion and include single, double, triple, and quadruple excitations in the calculation of the correlation energy. For these reasons we have chosen to use MBPT in our investigation of the potential energy surface of O_3.

All calculations reported here were performed with a split valence plus polarization basis set, the so-called 6-31G** basis. This adequately spans the s, p space of occupied O_3 orbitals and includes one set of polirization orbitals or d-functions. Test calculations without any polarization functions proved to be totally inadequate. Adding additional polarization functions or f-orbitals does not significantly alter the relative energies but does tremendously increase the computation time making it impractical to do a survey of the surface with this basis set. In Table A1 we compare six different calculations at various geometries where one bond distance and the O_3 bond angle were varied. The energies listed refer to Hartree-Fock (HF), second order perturbation theory (MP2), third order (MP3), and fourth order (MP4) with various types of substitutions accounted for. The dipole moment has also been listed for possible spectroscopic use in future dynamics calculations. From this comparison we see that MP4 (SDTQ) is significantly better than the lower levels and all further calculations will be done at this level. In addition we note that while the total energy is changing from level to level the overall shape of the surface the atoms move on is converging rapidly. In Table A2 we list MP4 (SDTQ) energies and the dipole for a number of additional geometries. Next, the relative shape of the MP4 (SDTQ) points should be compared to the existing surface to determine if additional regions are important or if the existing surface can be improved.

85

Table A1. Computed Ozone Total Born-Oppenheimer Energies and Molecular Dipole Moment (Energy in Hartrees)

R1(Å)	θ (degs)	HF	MP2	MP3	MP4 (DQ)	MP4 (SDQ)	MP4 (SDTQ)	DIPOLE (a.u.)
1.204	119.015	-224.2614	-224.8491	-224.8200	-224.8230	-224.8349	-224.8677	0.826
1.004	119.015	-224.1670	-224.6961	-224.6850	-224.6878	-224.6978	-224.7198	1.804
1.104	119.015	-224.2440	-224.8040	-224.7842	-224.7871	-224.7976	-224.8246	1.173
1.304	119.015	-224.2521	-224.8548	-224.8110	-224.8236	-224.8402	-224.8781	1.095
1.404	119.015	-224.2352	-224.8275	-224.7979	-224.8032	-224.8257	-224.8631	1.653
1.504	119.015	-224.2212	-224.7862	-224.7685	-224.7764	-224.7975	-224.8283	1.994
1.604	119.015	-224.2121	-224.7534	-224.7440	-224.7534	-224.7706	-224.7960	1.998
1.704	119.015	-224.2063	-224.7211	-224.7264	-224.7364	-224.7510	-224.7735	1.808
1.804	119.015	-224.2024	-224.7154	-224.7139	-224.7242	-224.7369	-224.7575	1.549
1.904	119.015	-224.1995	-224.7039	-224.7048	-224.7152	-224.7265	-224.7457	1.286
1.204	115.015	-224.2599	-224.8475	-224.8191	-224.8219	-224.8334	-224.8660	0.916
1.204	117.015	-224.2611	-224.8487	-224.8199	-224.8228	-224.8346	-224.8672	0.871
1.204	113.015	-224.2579	-224.8455	-224.8174	-224.8201	-224.8314	-224.8638	0.959
1.204	111.015	-224.2551	-224.8425	-224.8148	-224.8173	-224.8285	-224.8608	1.002
1.204	109.015	-224.2512	-224.8985	-224.8113	-224.8131	-224.8246	-224.8567	1.044
1.204	121.015	-224.2611	-224.8487	-224.8193	-224.8225	-224.8345	-224.8675	0.780
1.204	123.015	-224.2601	-224.8475	-224.8180	-224.8213	-224.8335	-224.8665	0.734
1.204	125.015	-224.2584	-224.8457	-224.8160	-224.8194	-224.8317	-224.8649	0.687
1.204	127.015	-224.2562	-224.8433	-224.8134	-224.8169	-224.8294	-224.8626	0.640
1.204	129.015	-224.2534	-224.8402	-224.8102	-224.8138	-224.8275	-224.8597	0.592
1.204	132.015	-224.2482	-224.8345	-224.8045	-224.8082	-224.8211	-224.8544	0.522
1.204	135.015	-224.2421	-224.8277	-224.7977	-224.8015	-224.8146	-224.8479	0.451
1.204	140.015	-224.2298	-224.8138	-224.7843	-224.7881	-224.8014	-224.8347	0.337

Table A2. Ozone Born-Oppenheimer Energies and Dipole
Moment for Several Extended Molecular Configurations
[MP4 (SDTQ) Level of Calculation]

R1 (Å)	R2 (Å)	θ (degs)	E (hartrees)	Dipole (a. u.)
1.204	1.204	140.015	-224.8347	0.3372
1.1043	1.1043	119.0154	-224.7780	0.9289
1.0043	1.1043	119.0154	-224.6679	1.2584
1.3043	1.1043	119.0154	-224.8362	1.6999
1.4043	1.1043	119.0154	-224.8222	2.1678
1.5043	1.1043	119.0154	-224.7942	2.3591
1.1043	1.7043	119.0154	-224.7483	2.0423
1.0043	1.0043	119.0154	-224.5503	0.9932
1.0043	1.3043	119.0154	-224.7351	2.3437
1.0043	1.4043	119.0154	-224.7268	2.7145
.0043	1.5043	119.0154	-224.7068	2.8204
1.0043	1.6043	119.0154	-224.6863	2.7042
1.0043	1.7043	119.0154	-224.6682	2.4645
1.3043	1.4043	119.0154	-224.8778	1.0913
1.3043	1.5043	119.0154	-224.8400	1.6440
1.3043	1.3043	119.0154	-224.8890	0.6968
1.3043	1.6043	119.0154	-224.8004	1.7915
1.3043	1.7043	119.0154	-224.7739	1.6685
1.4043	1.4043	119.0154	-224.8753	0.5650
1.0543	1.2043	119.0154	-224.7827	1.4712
1.1543	1.2043	119.0154	-224.8515	0.9385
1.2543	1.2043	119.0154	-224.8761	0.8866
1.3543	1.2043	119.0154	-224.8740	1.3748
1.0543	1.1043	119.0154	-224.7367	1.1297
1.1543	1.1043	119.0154	-224.8069	0.9874
1.2543	1.1043	119.0154	-224.8339	1.4255
1.3543	1.1043	119.0154	-224.8320	1.9587
1.3543	1.1543	119.0154	-224.8579	1.6675
1.2543	1.1543	119.0154	-224.8603	1.1290
1.1543	1.1543	119.0154	-224.8347	0.8816
1.0543	1.1543	119.0154	-224.7639	1.2175

Contents
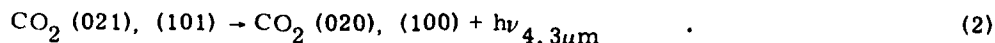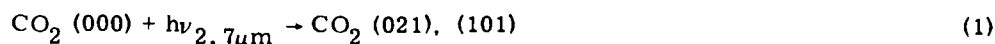
3. FCL Experiment

by

S. M. Miller

1. INTRODUCTION

Several field experiments such as ICECAP, HIRIS, and SPIRE[1,2] have observed radiation in the 4.0 to 4.5 μm band under both quiescent and aurorally excited conditions in the upper atmosphere. A strong candidate at 4.3 μm is the ν_3 asymmetric stretch mode of CO_2. The excitation process has been proposed to be direct solar pumping of CO_2 into the V, V_3 and $V_2 V_3$ combination bands with subsequent radiative decay to the V_1 and V_2 bands as described in Eqs. (1) and (2),

$$CO_2 \ (000) + h\nu_{2.7\mu m} \rightarrow CO_2 \ (021), \ (101) \tag{1}$$

$$CO_2 \ (021), \ (101) \rightarrow CO_2 \ (020), \ (100) + h\nu_{4.3\mu m} \tag{2}$$

Under aurorally excited conditions the 4.3 μm radiation is probably due to energy transfer from excited nitrogen to CO_2, as described in Eqs. (3) and (4),

1. Kumer, J. B. (1975) Atmospheres of Earth and Planets, D. Reidel Publishing Company, pp. 347-358.

2. Stair, A. T., et al (1975) Rocketborne observations of atmospheric infrared emissions in the auroral region, Atmospheres of the Earth and Planets, D. Reidel Publishing Company, pp. 335-346.
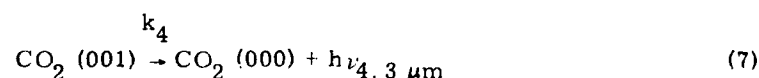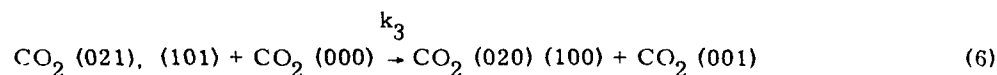
$$N_2^* + CO_2 \rightarrow N_2 + CO_2 \ (001) \tag{3}$$

$$CO_2 \ (001) \rightarrow CO_2 \ (000) + h\nu_{4.3\mu m} \tag{4}$$

The amount of 4.3 μm produced due to Eqs. (1) and (2) depends critically upon the branching ratio of the combination bands (021) and (101). J. B. Kumer and T. C. James[3] have calculated that solar pumped CO_2 will result in 4.3 μm radiation with 95 percent probability and re-emission at 2.7 μm via the process in Eq. (5) will occur with a 5 percent probability,

$$CO_2 \ (021), \ (101) \rightarrow CO_2 \ (000) + h\nu_{2.7, 2.77 \ \mu m} \tag{5}$$
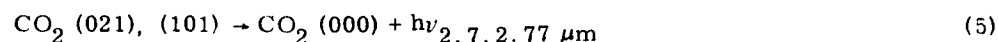
This branching ratio along with collisional effects will be measured in this laboratory experiment.

In addition to the processes described in Eqs. (1), (2), and (5) one must consider collisional processes. Although there is not a sufficient number density of CO_2 molecules in the upper atmosphere for collisions to be of importance, these processes provide specific constraints on laboratory experiments. Processes 6 and 7 compete directly with both

$$CO_2 \ (021), \ (101) + CO_2 \ (000) \xrightarrow{k_3} CO_2 \ (020) \ (100) + CO_2 \ (001) \tag{6}$$

$$CO_2 \ (001) \xrightarrow{k_4} CO_2 \ (000) + h\nu_{4.3 \ \mu m} \tag{7}$$

Processes 2 and 5. Finzi and Moore[4] have measured k_3 and determined it to be 1.3×10^{-10} cm^3/mol-sec. This reduces the effective lifetime of the combination bands to 0.25 μsec/Torr CO_2. Thus requiring one to work at CO_2 pressures below 50 μm in order to observe sufficient fluorescence from Processes 2 and 5 to measure the appropriate branching ratio.

3. Kumer, J. B., and James, T. C. (1979) Fluorescence Experiment and Auroral Data Evaluation to Improve Prediction of Nuclear Atmospheric Infrared Background, DNA 4906F.

4. Finzi, I., and Moore, C. B. (1975) Relaxation of CO_2 (10°1), CO_2 (021) and N_2O (101) vibrational levels by near resonant V → V energy transfer, J. Chem. Phys. 63(No. 6).

2. PROCEDURE

The experimental approach will be to utilize a CW laser at 2.7 μm and an interferometer with sufficient resolution to distinguish between radiation from Process 2 and Process 7. This contrasts with T. C. James[5] and C. B. Moore's approach utilizing a pulsed coherent source of photons at 2.7 μm and thus relying on intensities and lifetimes to make the proper distinctions.

There are several advantages to the CW approach. The most significant of these are:

(1) The FCL emits coherent radiation with the very narrow linewidth of 1 MHz = 5×10^{-5} cm. This guarantees the laser line will be narrower than the CO_2 absorption line at 2.7 μm at pressures in the micron regime. Up-conversion by optical paramagnetic oscillation (OPO) creates laser line widths of > 0.1 cm. This is 10 to 1000 times the CO_2 linewidth as a function of the CO_2 pressure. This indicates that the CW beam is more effectively utilized.

(2) The FCL laser frequency is stable to 20 MHz over a period of an hour, allowing slower scans and larger integration times than the significantly less stable pulsed systems utilizing OPO.

(3) The problems associated with pulse to pulse repeatability are avoided with a CW laser system.

(4) The CW nature of the FCL also allows the use of an interferometer to distinguish directly between the intramolecular transition at 4.3 μm and the collisionally relaxed fluorescence at 4.26 μm.

(5) The pulsed experiments are inherently limited by their ability to saturate the transitions of interest. This places an upper limit on the signal to noise ratio they can achieve. The CW experiment never approaches saturation. Thus there is a tradeoff between the pulsed system's ability to discriminate in time against noise to CW system's ability to discriminate in frequency.

(6) Kumer and James used a cold gas filter between their fluorescence cell and detector. This was to absorb any radiation due to (001) → (000) transitions resulting from intermolecular VV energy transfer. Unfortunately they did not take into consideration either diffusion of the CO_2 molecules before emission or the resulting re-emission of V_3 radiation. Steven Adler-Golden[6] has modeled this behavior and has shown that a short cold gas filter is not very efficient at eliminating all V_3 radiation between the fluorescence cell and the detector.

---

5. James, T. C. (1976) Laboratory Investigation of Infrared Fluorescence of CO_2, DNA 4238F.

6. Adler-Golden, S. M. (1983) Transport of CO_2 4.3 μm Radiation: Effects of Trapping, Re-Emission and Diffusion, SSI-TR-36.

To avoid this potential problem, we will use a Michelson interferometer to spectrally resolve the $001 \rightarrow 000$ transition from the $101 \rightarrow 1000$ transition 26 cm^{-1} to the red. This will allow us to obtain all the information in each scan necessary to ratio both the intramolecular to intermolecular influenced radiation and the 2.7 to 4.3 μm fluorescence branching ratio.

3. EXPERIMENTAL FEATURES

The Burleigh FCL-20 laser used in these experiments is in good operating order after a major rebuild/upgrade by Burleigh Instruments. It presently has the additional adjustment of the cavity end mirror which is necessary to run the laser in the single mode configuration.

Without the intracavity etalon, the output consists of a single longitudinal mode and a corresponding spacial hole burning mode. These modes are separated by 1.5 GHz (0.05 cm^{-1}). The intracavity etalon permits only one mode, with a linewidth of 1 MHz, to oscillate. Although this FCL has been successfully run in single mode, there are several problems that limit the utility of this configuration. The foremost is the limited tunability available while remaining in single mode ($<$ 100 MHz without elaborate computer control). This eliminates the ability to take excitation spectra by scanning the laser over the tunable range of the crystal. Furthermore, it becomes very difficult to place the laser at any specified wavelength due to the large number of iterations necessary to obtain single mode operation. Possibly with the help of the wavemeter presently under construction, this single mode operation will become more useful.

The mode separation of 1.5 GHz is great enough so that only one CO_2 rotational line is excited at a time, thus multi-mode interference is not a major problem.

As presently configured, the FCL laser emits 25 mW of 2.640 μm laser light when pumped by 1 W of 647 μm laser light from a Spectra Physics model 171 krypton ion laser. The highest power level produced to date is 90 mW at 2.640 μm when pumped with 1.75 W of 647 μm laser light. Under these conditions crystal No. 2 (F_8(II):KCl) is tunable from 2.5 to 3.1 μm at 10 dB. This allows efficient pumping of both the (021) and (101) combination bands in CO_2.

To determine the laser wavelength precisely, two approaches have been taken. First, an absorption cell was constructed with a sensitive microphone installed. This allows one to monitor the nonradiative decay of CO_2 vibrational bands by means of photoacoustic spectroscopy. The rotational structure of the CO_2 (021) band was measured this way and is shown in Figure 1. By tuning the laser to a particular rotational line, one is assured of light absorption by CO_2 in a separate

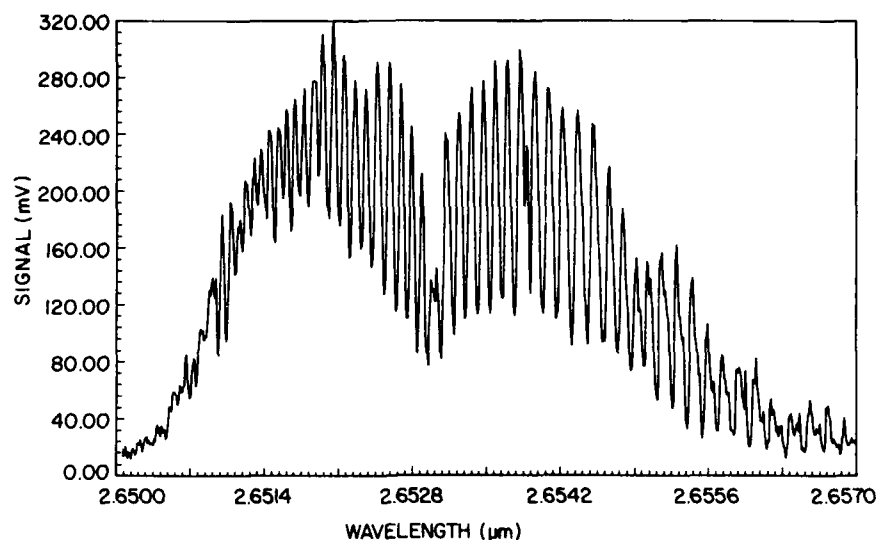Figure 1. Photoacoustic Spectrum of the (021) Vibrational Band of CO_2

fluorescence cell. This establishes the laser wavelength within 0.1 cm^{-1}, limited by the relatively slow response of the microphone. This resolution is adequate to measure CO_2 fluorescence at 4.3 μm but totally inadequate to operate the FCL in a single mode configuration. To increase this resolution significantly, we are constructing a wavemeter. This wavemeter is of the Michelson interferometer type, utilizing two corner reflectors mounted on an air bearing slide. The fringes of a stabilized HeNe laser are counted as a reference and ratioed to the number of FCL light fringes counted during that same time period. Knowing the HeNe frequency to 1 MHz allows the FCL wavelength to be determined routinely to within 3×10^{-3} cm^{-1} from the measured fringe ratio. This can be extended to 3×10^{-4} cm^{-1} (1 part in 10^7 or 50 MHz) by utilizing electronic signal processing or by slowing the data rate from one wavelength reading per second to one wavelength reading per 10 sec. This high resolution will be sufficient for all foreseeable future experiments.

The F center laser and related apparatus has been automated using a Hewlett Packard model 6942A data acquisition system utilizing a HP9836CS computer as a controller. This system presently controls three phases of operation; wavelength control of the F center laser, data collection, and data display.

The FCL wavelength can be scanned from 0.015 to 1000 Å/sec using a pulse output from the 6942A to a stepper motor translator. The translator in turn sends the stepper motor the proper phase sequence of current to produce a single step. The accuracy of the stepper motor's position increases the ability to reproduce spectral scans.

Software is presently being written to extend this simple wavelength scanning to include FCL frequency stabilization. As described above, this will be accomplished initially using a photoacoustic detection system and ultimately utilizing a wavemeter. In the first method the laser will be tuned to the peak of an absorption line. The computer will then include a periodic dither to the stepper motor, essentially searching for the nearest peak. This should extend the laser frequency stability to hours albeit only within ± 0.10 cm^{-1}. The second method will not depend upon an absorption peak, only on readings made by the wavemeter. This feedback will control the cavity length by modulating the rear cavity mirror. This will have the potential of keeping the laser stable to $<$ 1 GHz over a period of hours.

Data is recorded from the lockin amplifier or boxcar integrator through an analog multiplexer and A/D converter and temporally stored in the memory of the 6942A multiprogrammer. When a scan is finished the data is transferred to an array in the controller. The analog multiplexer allows several signals to be monitored during the experiment, such as laser power, photoacoustic cell output, and the fluorescence signal. The A/D converter can run up to 25 kHz. This allows one to average over many samples for each data point and the 6942A memory permits the data to be collected without the necessity of elaborate computer communication.

Once in the controller the data can be scaled and plotted on the computer screen with the appropriate units and labels. This spectrum can be expanded in the X or Y direction to examine any spectral details. Finally the spectrum is stored on disc and plotted on an HP7475A plotter for hard copy.

4. RESULTS AND FUTURE EXPERIMENTS

Future software developments will include the ability to plot multiple spectra simultaneously, perform mathematical operations on data arrays, and data transfer from the HP9836 to the VAX for further data analysis.

The experimental configuration used to observe CO_2 fluorescence at 4.3 μm when excited at 2.7 μm is shown in Figure 2. The FCL is tuned to a relatively strong VJ transition in the 021 band of CO_2 and focused into a cell containing 1 Torr of CO_2 and 50 Torr of Ar. The fluorescence is observed by a SBRC photovoltaic InSb detector through a 4.3 μm bandpass filter. The InSb signal is amplified by a SBRC model 220 preamp and processed by a PAR model 124A lockin. The output of the lockin is simultaneously sent to a chart recorder and the data acquisition system described above. When the FCL is scanned through the 021 band, the resulting excitation spectrum observed is shown in Figure 3.
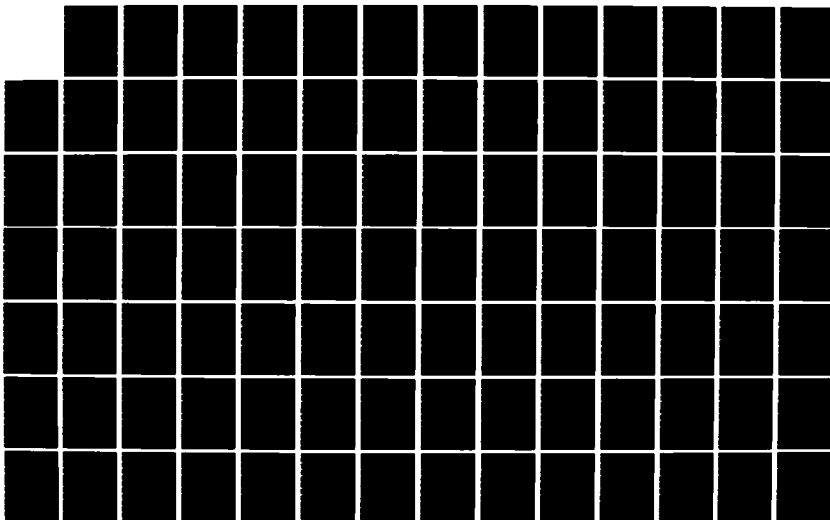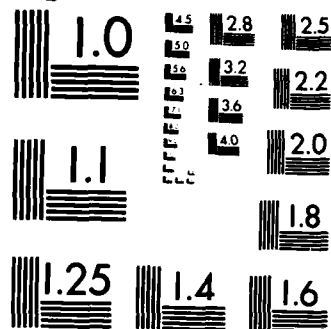
94

MICROCOPY RESOLUTION TEST CHART
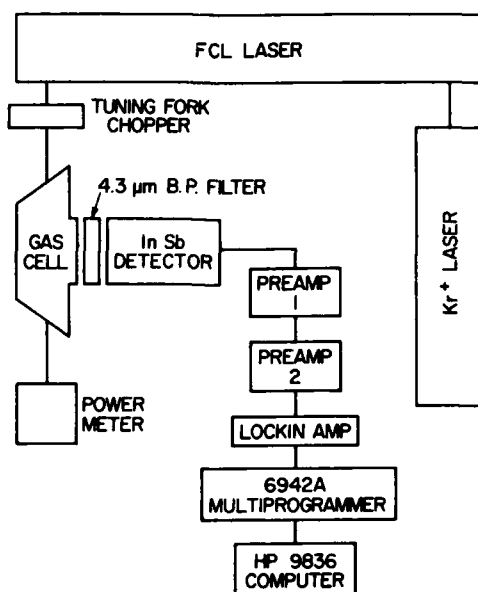
NATIONAL BUREAU OF STANDARDS-1963-A

Figure 2. Experimental Setup
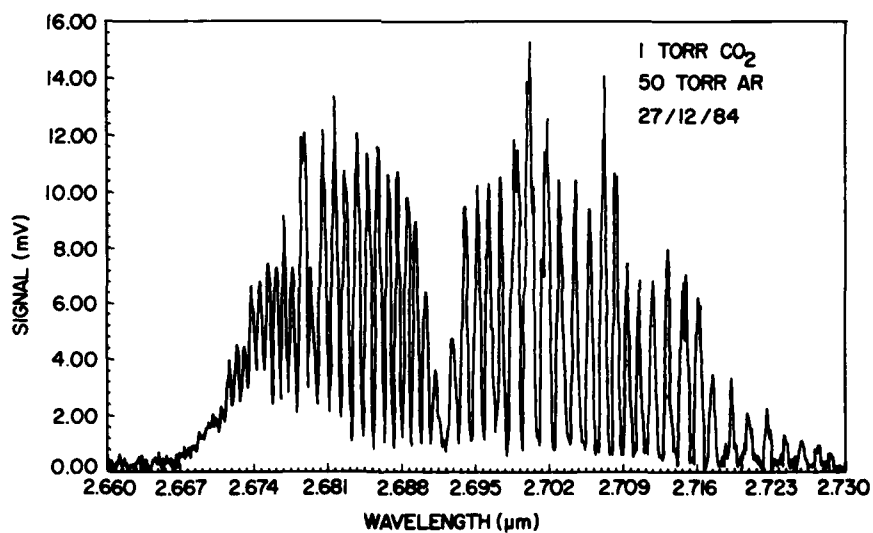for CO_2 Fluorescence Studies

Figure 3. Fluorescence Excitation Spectrum of $(00n\nu_3)$ Vibrational
Band of CO_2

The remaining measurements to be made are:

(1) Obtaining a signal with a signal to noise ratio of 10:1 or better at a CO_2 partial pressure of $100\,\mu$m or less. This is the regime where the intermolecular relaxation resulting in $001 \rightarrow 000$ transitions should be reduced sufficiently to observe the intramolecular $021 \rightarrow 020$ radiative transition.

(2) A reduction of light scattering in the fluorescence cell in order to observe $021 \rightarrow 000$ fluorescence directly. This will be accomplished by exciting CO_2 into high rotational levels of the 021 band and observing fluorescence from the lower rotational levels.

(3) Frequency stabilize the FCL to remain on a single rotational line for 20-60 min. This can be done by stabilizing the Kr^+ power, evaculating the FCL tuning arm and letting everything stabilize over a period of several hours.

(4) Finally, an interferometer will be installed and fluorescence light will be spectrally resolved. This will allow measurements of spectral intensities at 2.7, 4.26, and 4.3 μm, which, along with the measurements of instrument response, will permit the calculation of the appropriate inter- and intra-molecular branching ratios of the CO_2 combination bands 021 and 101.

References

1. Kumer, J. B. (1975) Atmospheres of Earth and Planets, D. Reidel Publishing Company, pp. 347-358.

2. Stair, A. T., et al (1975) Rocketborne observations of atmospheric infrared emissions in the auroral region, Atmospheres of the Earth and Planets, D. Reidel Publishing Company, pp. 335-346.

3. Kumer, J. B., and James, T. C. (1979) Fluorescence Experiment and Auroral Data Evaluation to Improve Prediction of Nuclear Atmospheric Infrared Background, DNA 4906F.

4. Finzi, I., and Moore, C. B. (1975) Relaxation of CO_2 (10°1), CO_2 (021) and N_2O (101) vibrational levels by near resonant V → V energy transfer, J. Chem. Phys. 63(No. 6).

5. James, T. C. (1976) Laboratory Investigation of Infrared Fluorescence of CO_2, DNA 4238F.

6. Adler-Golden, S. M. (1983) Transport of CO_2 4.3 μm Radiation: Effects of Trapping, Re-Emission and Diffusion, SSI-TR-36.
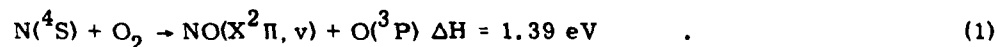
Contents

4. FACELIF Experiments

by

I. Winkler
J. Steinfeld
S. Miller

1. INTRODUCTION

The overall rate of the reaction of ground state nitrogen atoms, $N(^4S)$, with molecular oxygen is slow[1] at room temperature, $k_1 = 9 \times 10^{-17}$ cm^3/sec:

$$N(^4S) + O_2 \rightarrow NO(X^2\Pi, v) + O(^3P) \quad \Delta H = 1.39 \text{ eV} \qquad . \qquad (1)$$

Vibrational state specific rates for Reaction (1) have been determined by analysis[2,3] of low-resolution infrared chemiluminescence data for v = 2 - 7. These measurements indicate that about 20 percent of the product NO molecules are

1. Baluch, D., Drysdale, D., Horne, D., and Lloyd, A. (1973) Evaluated Kinetic Data for High Temperature Reactions, II, Butterworths, London.

2. Whitson, M., Darnton, L., and McNeal, R. (1976) Vibrational energy distribution in the NO produced by the reaction of $N(^4S)$ with O_2, Chem. Phys. Lett. 41:552.

3. Rahbee, A., and Gibson, J. (1981) Rate constants for formation of NO in vibrational levels v = 2 through v = 7 from the reaction $N(^4S)$ with O_2, J. Chem. Phys. 74:5143.

formed with v = 2 or greater. Recently, this system was investigated[4] using laser-induced fluorescence detection of the NO product. The LIF technique permitted interrogation of the v = 0, 1 levels, and 38 percent of the product NO molecules were reported to be formed in v = 2 or higher levels. The reported distributions are shown in Table 1.

Table 1. $N(^4S) + O_2 \rightarrow NO(v) + O$

Comparison of Other Work:
Vibrational Distributions of NO(v) from $N(^4S) + O_2$

Source:	Herm et al [Ref. 4]		Whitson et al [Ref. 2]	Rahbee and Gibson [Ref. 3]
Detection Method:	Laser-Induced Fluorescence		$\Delta v = 2$ Chemiluminescence	$\Delta v = 2$ Chemiluminescence
v	% (v)	f*(v)	f*(v)	f*(v)
0	57.8	1.52	---	---
1	4.21	0.11	---	---
2	5.71	0.15	0.24 - 0.23	0.30 ± 0.07
3	6.89	0.18	0.16 - 0.13	0.31 ± 0.05
4	5.83	0.15	0.25 - 0.26	0.18 ± 0.02
5	6.46	0.17	0.23 - 0.24	0.13 ± 0.02
6	6.63	0.17	0.07 - 0.08	0.04 ± 0.01
7	6.48	0.17	0.05 - 0.06	0.03 ± 0.01

Note: The quantity $f^*(v) \equiv k(v)/\sum_{v=2}^{7} k(v)$ is used to facilitate intercomparison of data in this table and in Table 4. Where data for v = 0 and 1 are also available, both percent (v) [total = 100 percent] and f*(v) are given.

The present work, utilizing two-photon ionization detection for NO(v), was undertaken to address the discrepancy among the previous reports and to develop the laser ionization (LI) technique for use as a quantitative probe. The results will be shown in Table 2.

---

4. Herm, R., Sullivan, B., and Whitson, M. (1983) Nitric oxide vibrational excitation from the $N(^4S) + O_2$ reaction, J. Chem. Phys. 79:2221.

Table 2. $N(^4S) + O_2 \rightarrow NO(v) + O$
Summary of LI Detection Results in This Work

Run #	1	2	3	4	5	% v	f*(v)
v = 0	74.7	78.6	72.7	69.2	68.7	72.8 ± 4.1	3.47 ± 0.19
1	5.0	5.1	6.6	6.5	8.3	6.3 ± 1.3	0.30 ± 0.06
2	6.5	5.8	6.9	7.6	7.9	6.9 ± 0.8	0.33 ± 0.04
3	2.5	2.4	3.5	4.2	3.7	3.3 ± 0.8	0.16 ± 0.04
4	5.9	3.3	4.4	5.4	5.4	4.9 ± 1.0	0.23 ± 0.05
5	2.4	1.9	3.0	3.3	2.6	2.6 ± 0.5	0.12 ± 0.02
6	2.1	2.2	2.1	3.2	2.5	2.4 ± 0.5	0.11 ± 0.02
7	0.9	0.7	0.8	0.7	0.8	0.8 ± 0.08	0.04 ± 0.01

Note: For definition of f*(v), see footnote to Table 1.

2. KINETIC ANALYSIS

The primary loss mechanism for NO in the flow reactor is

$$N(^4S) + NO \rightarrow N_2 + O \qquad . \tag{2}$$

The rate constant[5] for Reaction (2) is 2.2×10^{-11} cm^3/sec. The dependence of k_2 on the vibrational energy of the NO molecule is not known; however, due to the exoergicity of Reaction (2) it has been assumed to be v independent.[2] NO may, therefore, be treated as a steady-state intermediate in the net reaction
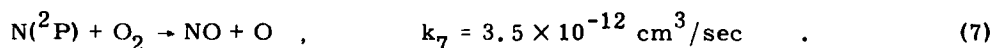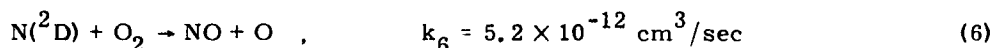
$$2N(^4S) + O_2 \rightarrow N_2 + 2O(^3P) \tag{3}$$

and

$$[NO]_{ss} = (k_1/k_2)[O_2] \tag{4}$$

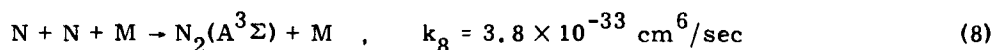gives the steady-state concentration of NO in the flow reactor. The mean residence time of an NO molecule is given by

$$\bar{\tau}_r = 1/[N(^4S)] \, k_2 \tag{5}$$

---

5. Phillips, L., and Schiff, H. (1962) Mass spectrometric studies of atom reactions. I. Reactions in the atomic nitrogen - ozone system, J. Chem. Phys. 36:1509.
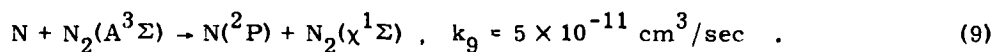
the reciprocal of the pseudo-first order loss rate constant, and is approximately 7 msec under the present flow conditions. Since the transit time from the microwave discharge to the LI detection region is long compared to the NO residence time, atomic nitrogen metastable species, $N(^2D)$ and $N(^2P)$, formed in the discharge, are lost by diffusion to the walls. At 1 Torr He in a 5-cm diameter flow tube, the lifetime[6] of $N(^2D)$ with respect to loss at the walls is 2.2 msec. Reactions (6) and (7), therefore, make a negligible contribution to the observed NO(v).

$$N(^2D) + O_2 \rightarrow NO + O \quad, \qquad k_6 = 5.2 \times 10^{-12} \text{ cm}^3/\text{sec} \qquad (6)$$

$$N(^2P) + O_2 \rightarrow NO + O \quad, \qquad k_7 = 3.5 \times 10^{-12} \text{ cm}^3/\text{sec} \qquad . \qquad (7)$$

At high $N(^4S)$ concentrations, however, a steady-state concentration of $N(^2P)$ can be established by reactions

$$N + N + M \rightarrow N_2(A^3\Sigma) + M \quad, \qquad k_8 = 3.8 \times 10^{-33} \text{ cm}^6/\text{sec} \qquad (8)$$

and

$$N + N_2(A^3\Sigma) \rightarrow N(^2P) + N_2(X^1\Sigma) \quad, \qquad k_9 = 5 \times 10^{-11} \text{ cm}^3/\text{sec} \quad . \qquad (9)$$

This steady-state concentration is given by

$$[N(^2P)]_{ss} = \frac{k_8 k_9 [M] \, [N]^3}{\{k_7[O_2] + k_w(P)\} \, \{k_9[N] + k_{11}[O_2] + k_w(A)\}} \quad, \qquad (10)$$

where $k_w(P)$ and $k_w(A)$ are the wall loss rate constants for $N(^2P)$ and $N_2(A^3\Sigma)$ respectively, and the major vibrational relaxation processes are

$$NO(v) + O_2 \rightarrow NO(v-1) + O_2 \qquad (11)$$

and

$$NO(v_i) + O \rightarrow NO(v < v_i) + O \qquad . \qquad (12)$$

The rate constant, k_{12}, is dependent on the NO vibrational energy and varies[7] linearly with v from $2.2 - 3.1 \times 10^{-14}$ cm^3/sec for v = 1 to $5.1 - 7.7 \times 10^{-13}$ cm^3/sec for v = 6. Using the $k_{12}(v)$ values from Reference 7, the reciprocal

6. Lin, C., and Kaufman, F. (1971) Reactions of metastable nitrogen atoms, J. Chem. Phys. 3760.

7. Green, B., Caledonia, G., Murphy, R., and Robert, F. (1982) The vibrational relaxation of NO(v = 1-7) by O_2, J. Chem. Phys. 76:2441.

102

pseudo-first order vibrational quenching rate constants equal the residence time of NO at O_2 concentrations 2×10^{15} cm^3 and 2×10^{14}/cm^3, for $v = 2$ and $v = 6$, respectively. Effects of the vibrational cascade relaxation have been ignored. This result is consistent with the NO(v)-O_2 dependence data shown in Figures 1 and 2. As expected, the $v = 2$ data are linear throughout the range of O_2 concentration while the $v = 6$ data begin to exhibit curvature at $[O_2] \approx 6 \times 10^{14}$/cm^3.
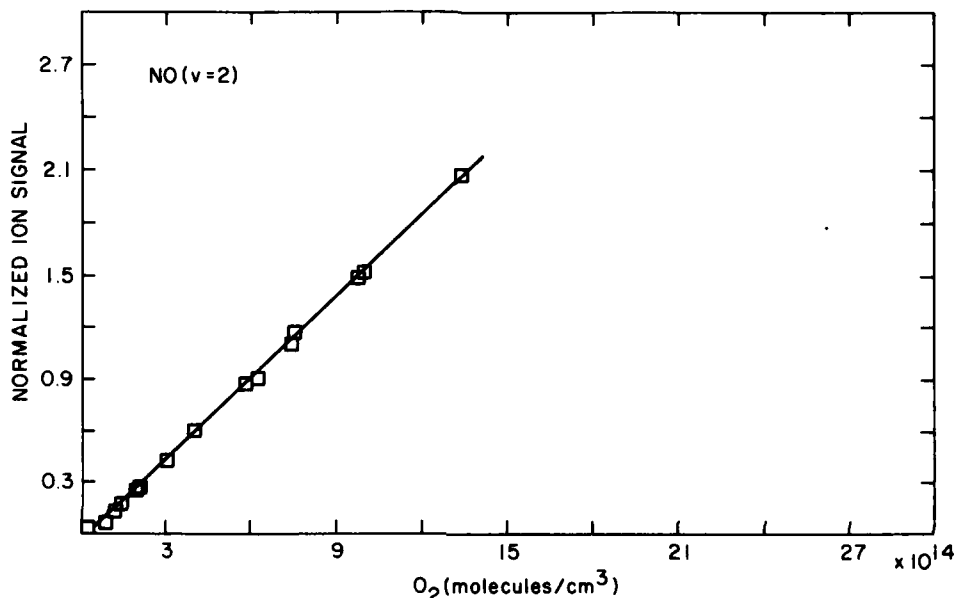
Figure 1. NO(v = 2) LI Signal vs O_2 Density

Atomic oxygen is formed by the slow net Reaction (3) and $[O] \ll [N]$ at the time of the LI probe. The rate constant for Reaction (13) is known only for $v = 1$, $k_{13}(v = 1) = 6.5 \times 10^{-11}$ cm^3/sec.[8] Since $k_{13}(v = 1) \approx 3k_2$, vibrational relaxation of NO(v) by O atoms is unimportant unless a multi-quantum relaxation mechanism is active and k_{13} increases for higher v.

The effect of atomic nitrogen reactions on the nascent NO distribution from Reaction (1) is not known. Reaction (2) has generally been assumed to be v independent and the process

$$N + NO(v_i) \rightarrow N + NO(v < v_i) \tag{13}$$

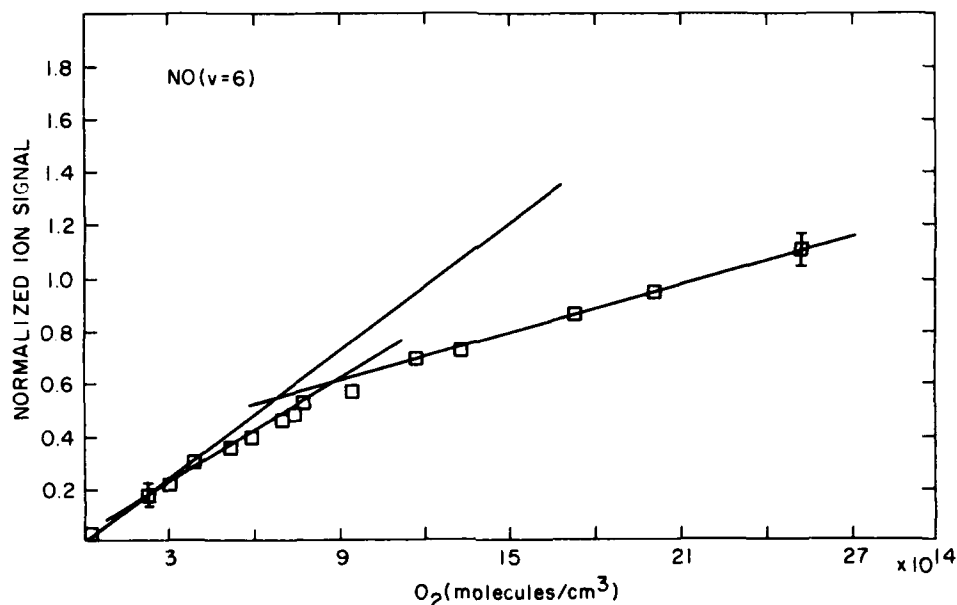8. Fernando, R., and Smith, I. (1979) Vibrational relaxation of NO by atomic oxygen, Chem. Phys. Lett. 66:218.

Figure 2. NO(v = 6) LI Signal vs O_2 Density

has not been examined. It has been pointed out[4] that since Reactions (13), (1), and (2) are first-order in N atom, the role of Reaction (13) cannot be determined by simple variation of the flow reactor parameters.

3. DEPENDENCE OF NO SIGNAL ON O_2 PRESSURE

The flow reactor system with LI probe has been described in previous reports. A diagram of the apparatus and experimental parameters are given as Figure 3 and Table 3, respectively. For these measurements, the gases passed through cold traps before entry into the flowtube. Titanium and copper gettering furnaces have been installed on the helium and nitrogen supplies; these have minimized the NO background. The N atom concentration was not measured, but N atoms are expected to comprise about 1 percent of the total nitrogen in a dilute N_2/He mixture after passage through a 2450 MHz discharge. The LI probe was tuned to the P_{11} bandhead feature of the transitions listed in Table 3. The linearity of the photoion signal with respect to NO concentration was checked by measuring the thermally populated NO(v = 1) P_{11} bandhead intensity versus NO concentration. These data are shown in Figure 4. Then, the signal intensity vs the O_2 concentration was measured, for v = 0, 1, 2, and 6. These data are shown as Figures 1 and 2 and 5 and 6 and provide support for the kinetic model described in the preceding section.
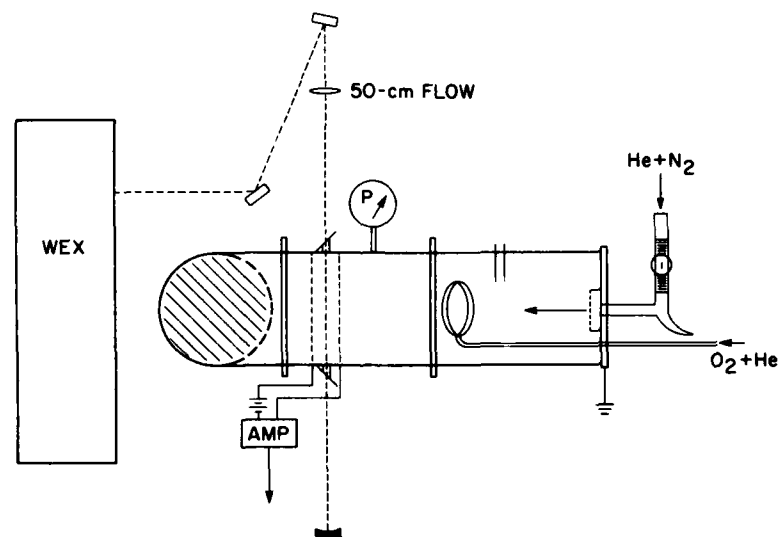
104

Figure 3. Schematic of LI Experimental Apparatus

Table 3. $N + O_2 \rightarrow NO + O$

Experimental Conditions

Pressure: 1.0 Torr

Flow Speed: 550 cm/sec

He: 3.5×10^{16} molecules/cm^3

N$_2$: 4.0×10^{14} molecules/cm^3

O$_2$: nominal 5×10^{14} molecules/cm^3 (~ 15 mTorr)

MPI signal was measured for NO(v) vs O$_2$ concentration.

v'	v''	For $^2\Pi_{1/2}$ Bandhead
0	0	226.3 nm
1	1	223.9 nm
2	2	221.6 nm
1	6	280.1 nm

O$_2$ injected at 10 msec

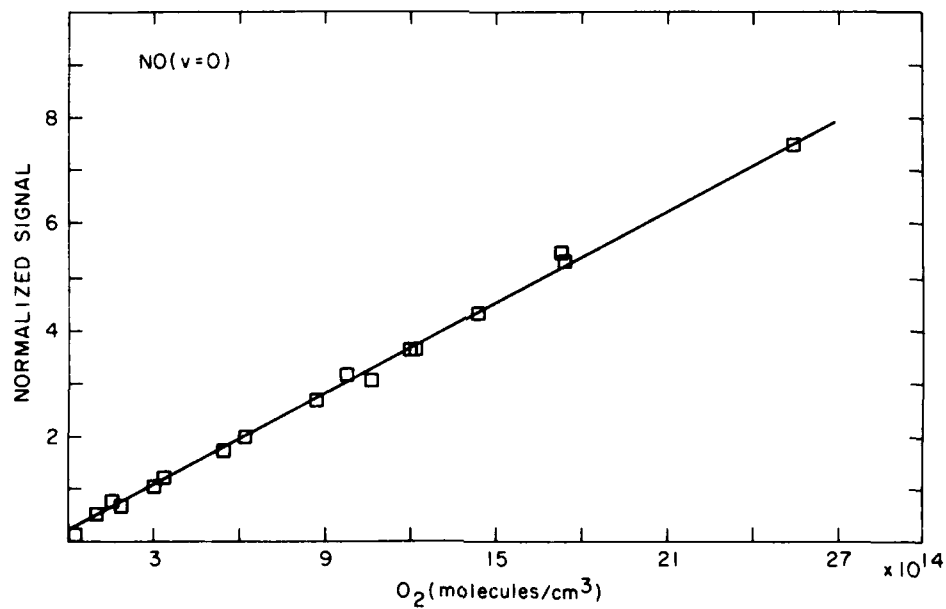Laser probe at 40 msec from O$_2$
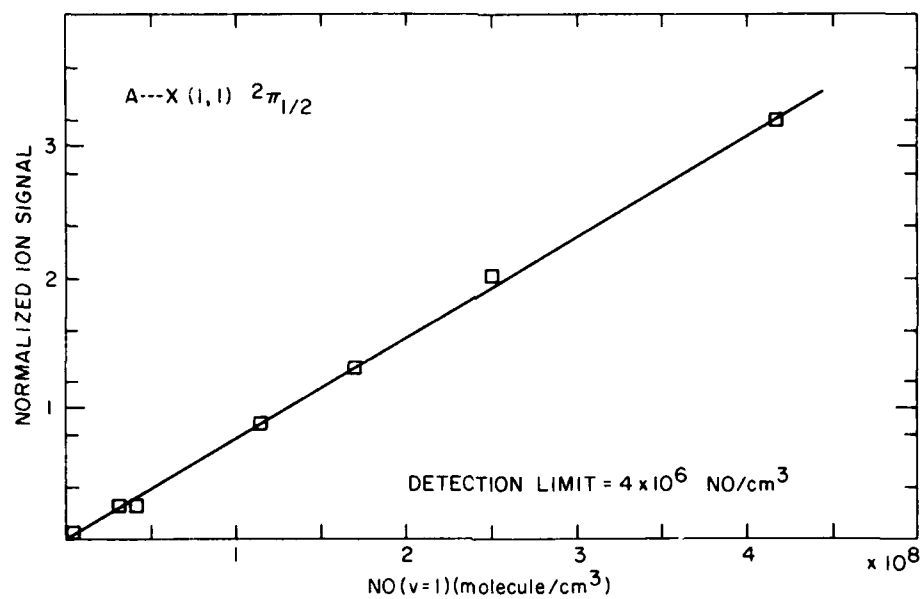
Figure 4.   LI Calibration Curve for NO(v = 1)

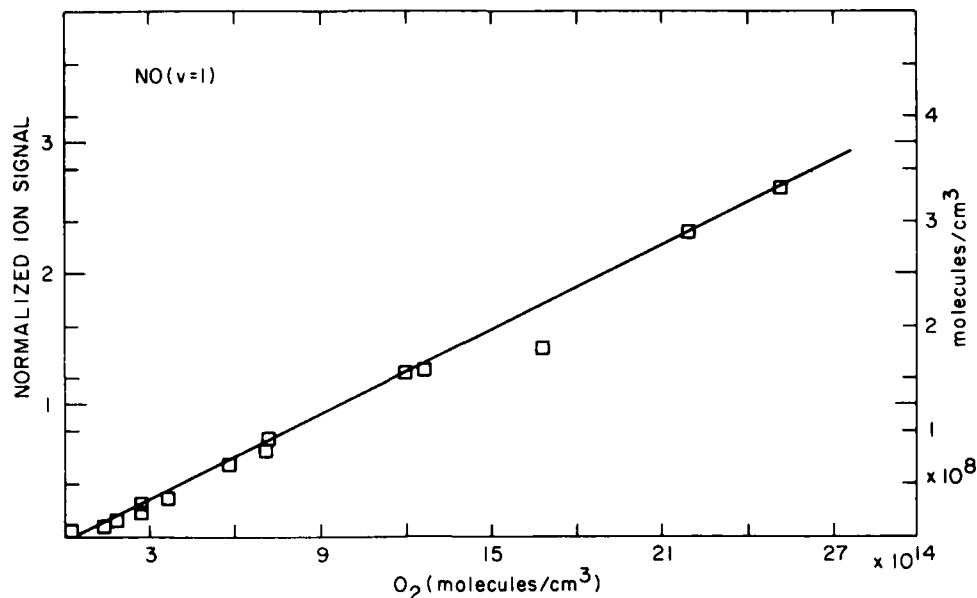Figure 5.   NO(v = 0) LI Signal vs O_2 Density

Figure 6. NO(v = 1) LI Signal vs O_2 Density

4. PHOTOIONIZATION DETECTION

Since its initial construction[9] the FACELIF facility has been modified to allow
LI detection of reactant and product species. This mode of detection eliminates
the problems associated with laser induced fluorescence (LIF), namely, back-
ground due to scattered light and afterglow emission, and fluorescence quenching.
In addition, LI is approximately ten times more sensitive than LIF.

The modifications include installation of two Ni wire grid electrodes oriented
perpendicular to the flow, a third wire grid approximately 1 cm in front of the
discharge tube, rotatable Brewster's angle window mounts, and a current to volt-
age amplifier mounted directly on the photoionization cell. (See Figure 3.)

Spectra are obtained by focusing the tunable output from the Quanta Ray laser
system between the Ni grid electrodes that are biased at 45 V. The ion signals
collected by the electrodes are amplified by the current to voltage amplifier
($\times 10^{10}$) and fed into a boxcar integrator. Mounting the preamp directly on the

9. Piper, L. (1982) FACELIF design concepts, in R. A. Armstrong et al,
   Atmospheric Chemiluminescence, COCHISE and Related Experiments,
   AFGL-TR-82-0305, AD A130546, pp. 77-104.

photoionization cell minimizes the microphonic pickup and the grounded wire
electrode located near the discharge prevents the charged species generated in
the discharge from entering the flow tube.

The rotatable window mounts are approximately 15 cm shorter than the original LIF sidearms. This permits greater flexibility in the choice of focusing optics and since the mounts are rotatable, changes in laser beam polarization can also be compensated. The system can be changed back to LIF detection by simply replacing the rotatable window mounts with baffle arm window mounts, and installing a phototube on one of the ports on the sample cell.

5. DEPENDENCE OF NO SIGNAL ON LASER POWER

The relative vibrational populations of NO are measured by comparing the intensities of the two-photon ionization signals that arise from molecules in states $X^2\Pi$ ($v = 0$) through $X^2\Pi$ ($v = 7$). Absorption of the first photon takes the molecules in $X^2\Pi$ (v) to an accessible vibrational state in the $A^2\Sigma^+$ manifold; the second photon ionizes the molecule. (See Figure 7.) Since the signal strength depends on the laser power, and the power varies over the wavelengths needed to measure the population distribution, the ion signal must be normalized to the laser power. In a two-photon transition the dependence of the signal on the laser power may be linear, quadratic, or intermediate between the two. Table 4 summarizes the power dependences that have been observed. [10-13] To determine the power dependence under the experimental conditions of this work, the ion signal was measured as a function of laser power with and without a focusing lens.

Log-log plots of the NO ion signal vs laser power are shown in Figure 8. The data for the upper plot were obtained by focusing the 226.7-nm output of the laser into the photoionization cell with a 25 cm focal length lens, then attenuating the

10. Mallard, W. G., Miller, J. H., and Smyth, K. C. (1982) Resonantly enhanced two-photon ionization of NO in an atmospheric flame, J. Chem. Phys. 76:3843.

11. Asscher, M., Guthrie, W. L., Lin, T. H., and Somorjai, G. A. (1982) Vibrational and rotational energy distribution of NO scattered from the PT (III) crystal surface: detection by two-photon ionization, Phys. Rev. Lett. 49:76.

12. Sudb, Aa. S., and Loy, M. M. T. (1982) Measurement of absolute state to state rate constants for collision-induced transitions between spin-orbit and rotation states of NO ($X^2\Pi$, $V = 2$), J. Chem. Phys. 76:3646.

13. Goldstein, N., Greenblatt, G. D., and Wiesenfeld, J. R. (1982) Observation by laser ionization spectroscopy of vibrationally excited nitric oxide following $O(^1D) + N_2 \rightarrow 2NO$, Chem. Phys. Lett. 96:410.

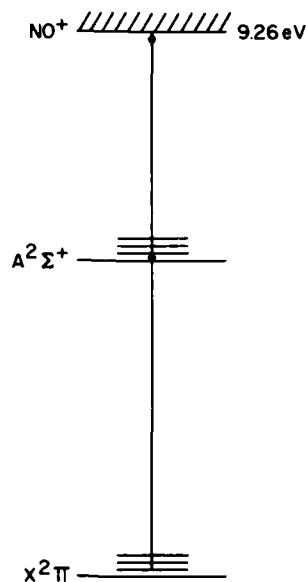Figure 7. Two-Photon Ion-
ization of NO via $A^2\Sigma^+$

beam using quartz plates. The signal from the $P_{22} + Q_{12}$ bandhead of the γ(0, 0)
band was recorded as the laser power was attenuated. The slope of 1.03 indicates
the signal is linearly dependent on the laser power (to within the ~ 10 percent un-
certainty) since $S = \sigma I^n$, where S is the ion signal, σ the absorption cross section,
I the laser intensity, and n the order of non-linearity. The high correlation,
R = 0.9946, is consistent with this conclusion. The data plotted on the lower
graph result when the 25 cm lens is removed. The slope of 1.29 indicates a
power dependence intermediate between quadratic and linear, which probably re-
sults from the pulse-to-pulse fluctuations in laser power. The lower correlation,
R = 0.9747, is consistent with the intermediate power dependence.

Further evidence that the system can be forced into a linear power dependence
is provided by the two-photon laser ionization spectra of the NO A $\leftarrow$ X(0, 0) band
shown in Figure 9. The spectra on the right were calculated with (upper spectrum)
and without (lower spectrum) the appropriate Hönl-London factors, and therefore
illustrate the spectral differences that may be expected when the A $\leftarrow$ X transition
is saturated (linear power dependence). The relative intensity of the P_{12} and
$P_{22} + Q_{12}$ bandheads is the most prominent difference between them. The spectra
shown on the left are those traced without (upper spectra) and with (lower spectra)
the 25 cm focal length lens. When comparing the spectrum measured under un-
focused conditions to that measured under focused conditions, we see the same
qualitative change in the relative bandhead intensity as when comparing the upper

Table 4. Comparison With Other Work

| Reference	Mallard et al[10]	Asscher et al[11]	Sudbo and Loy[12]	Goldstein et al[13]	Winkler et al
Bands Studied	$\gamma(0,7)$, $\gamma(1,8)$, $\gamma(0,6)$, $\gamma(1,7)$, $\gamma(0,5)$, $\gamma(1,6)$, $\gamma(0,4)$, $\gamma(1,5)$, $\gamma(0,3)$	$\gamma(0,0)$, $\gamma(0,1)$	$\gamma(2,2)$	$\gamma(1,1)$, $(2,2)$, $(3,3)$, $(7,8)$, $(6,7)$, $(5,6)$, $(10,12)$, $(9,11)$, $(8,10)$, $(0,5)$, $(2,8)$, $(1,7)$, $(5,12)$, $(4,11)$	$\gamma(0,0)$, $(1,1)$, $(2,2)$, $(3,3)$
Laser Power	100 μJ/pulse	40-800 μJ/pulse	"a few μJ"/pulse	not reported	140-400 μJ/pulse
Beam Cross-sectional Area	4.9×10^4 cm^3	not reported	not reported	not reported	not reported
Laser Band Width (FWHM)	.011-.14 nm (Dye Fundamental)	~ 2 cm^4	~ 0.4 cm^4	not reported	~ 1.5 cm^4
Focal Length of Focusing Lens	15 cm	125 cm	20 cm	15 cm	25 cm
NO Number Density	3.2×10^{14} cm^4	$> 3.22 \times 10^7$ cm^4	$\sim 10^{19}$ cm^4	not reported	$\sim 5 \times 10^8$ cm^4
NO Source	Atmospheric pressure H_2/air/N_2O flame	Supersonic beam scattered off Pt(III)	Static gas cell	$O(^1D_2) + N_2O \rightarrow 2NO$ (Flowing gas)	$N(^4S) + O_2 \rightarrow NO + O$ (Flow reactor)
Comments on Power Dependence	"The dependence of the signal on laser power, while steeper than linear, cannot be viewed as a reliable check on the model due to poor laser beam quality."	"The NO ion signal was found to be linearly dependent on laser energy in the range 40-800 μJ/pulse."	"We checked independently that a square law dependence of the two photon ionization signal on the UV pulse energy was obeyed on the average. Pulse to pulse fluctuations in the temporal structure of the UV pulses give rise to single pulse deviations from the square law dependence."	"Use of an unfocused beam results in the observation of an intensity dependence which is quadratic in the laser power, while use of a focused beam results in the laser dependence expected under conditions of saturation."	When the laser beam is unfocused, the NO ion signal has a laser power dependence intermediate between linear and quadratic. When the beam is focused, a linear power dependence is observed.
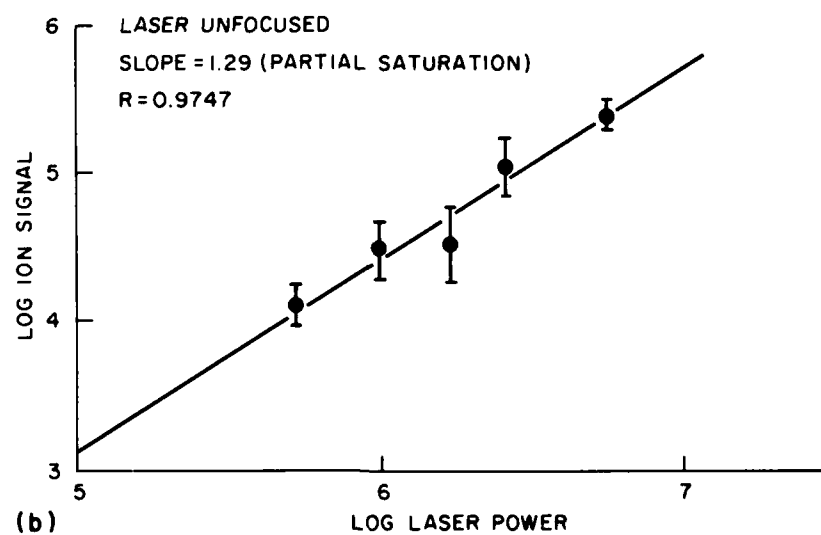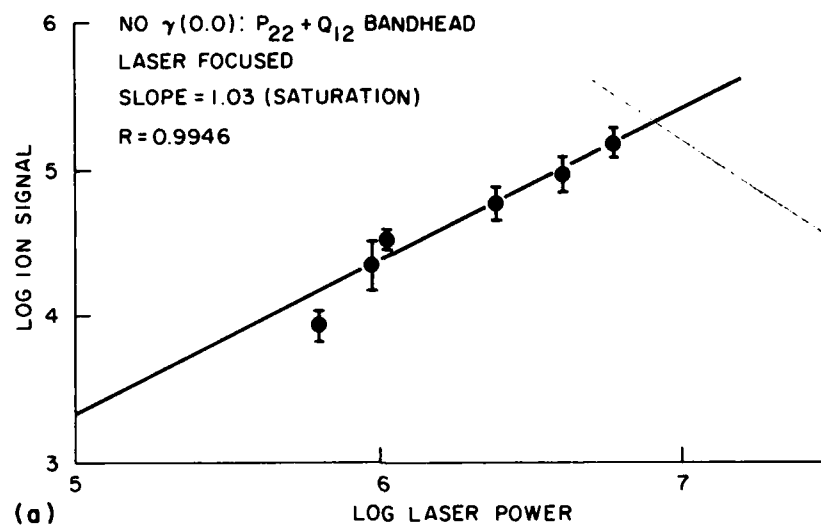
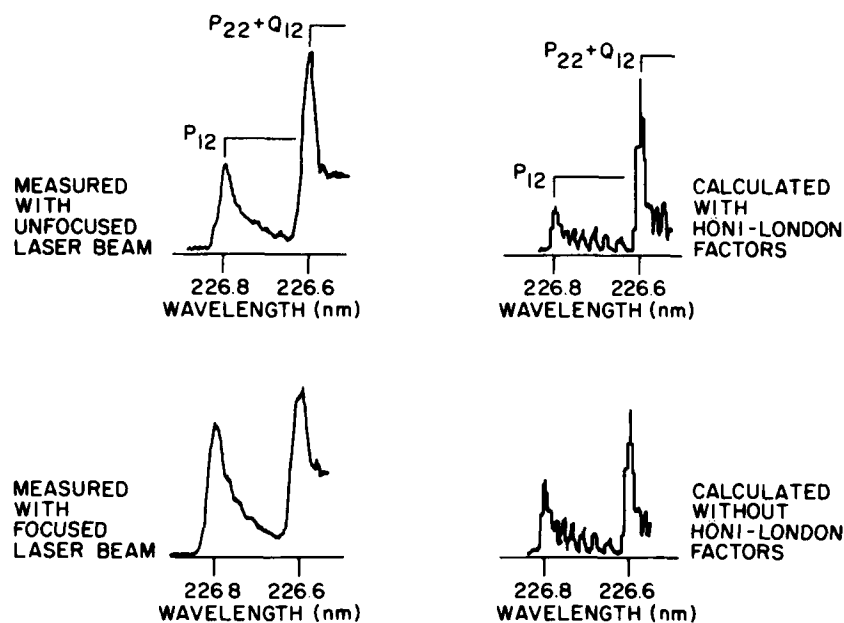Figure 8. Ion Signal vs Laser Power (Log-Log Plot)

111

Figure 9. Dependence of $\gamma(0, 0)$ Rotational Structure on Laser Power

calculated spectrum to the lower. These data also indicate that the intensities of the spectra measured with the focused laser beam are linearly dependent on laser power. The lack of quantitative agreement between calculated and measured spectra results from differences in the actual line widths and those used in the calculation. It should also be noted that the linearly normalized ion signal shows no change when the laser is attenuated by up to 30 percent. Similar measurements have been made on the other seven γ bands used to measure populations. In all cases a linear power dependence was achieved by focusing the beam.

Operating in a power regime in which the $A \leftarrow X$ transition is saturated eliminates the need for line strength factors in the data analysis. However, under these conditions the dependence of the ionization probability on the particular intermediate $[A^2\Sigma^+(v)]$ state must be considered, that is, the probability of ionizing an NO molecule in $A^2\Sigma^+(v = 1)$ may be different from that for $A^2\Sigma^+(v = 2)$, etc. The propensity rule[14] governing this process is based on the Franck-Condon principle and requires that $\Delta v = 0$, where Δv is the difference in vibrational quantum of the NO $A^2\Sigma^+$ molecule and the $NO^+ X^1\Sigma^+$ ion. If the ionizing photon has more energy than needed to prepare an $NO^+ X^1\Sigma^+(v)$ ion from an NO $A^2\Sigma^+(v)$ molecule,

14. White, M. G., Seaver, M., Chupka, W. A., and Colson, S. D. (1982) Observation of Rydberg ($C^2\Pi$)-valence ($B^2\Pi$) interactions in NO by multi-photon photoelectron spectroscopy, Phys. Rev. Lett. 49:28.

112

the excess energy is taken up by the departing electron. This is the case even if there is enough energy available to reach a higher vibrational state in the ion. Non-Franck-Condon behavior in NO has been reported[15] but is not expected to be important in this work.

The ionization probabilities of NO $A^2\Sigma^+(v)$ are not known. We assume they are approximately equal under our experimental conditions since the propensity rules are expected to hold. Some support for this assumption is provided by two observations. First, the population of NO $X^2\Pi(v = 6)$ was measured via two different intermediate states; $A^2\Sigma^+(v \approx 0)$ and $A^2\Sigma^+(v = 1)$. The results agreed to within 20 percent. Second, no distortion of the γ-band rotational structure is observed when two different vibrational states of the ion are reached within the energy region of the band.

If the $A^2\Sigma^+(v)$ ionization probabilities are not equal, the population distribution measured by the two-photon ionization technique will require correction when the ionization probabilities become available.

6. MEASUREMENT OF VIBRATIONAL POPULATIONS

The γ-band spectra needed to measure populations have been obtained. These bands, including $\gamma(0, 0)$, $\gamma(1, 1)$, $\gamma(2, 2)$, $\gamma(3, 3)$, $\gamma(3, 4)$, $\gamma(0, 5)$, $\gamma(1, 6)$, and $\gamma(1, 7)$, will be used to check the synthesized spectra necessary for data reduction. Experimental spectra of the first four bands are shown in Figure 10.

The relative populations are obtained by tracing each band in the region of the P_{11} bandhead. This feature was chosen because it is usually the strongest feature in the spectrum and can be unambiguously identified. The flow conditions used are similar to those in Table 3. The oxygen pressure used falls on the linear part of the NO vs $[O_2]$ curves which, according to the kinetic model discussed earlier, indicates the distribution is unrelaxed. All spectra are scanned under the same flow conditions and the entire measurement is made in one day. The results of five such measurements are given in Table 2. Although the data are quite reproducible they are uncorrected for spectral differences among the γ-bands and for NO background signal. The background may account for as much as 30 percent of the total $v = 0$ signal, less for the higher vibrational states. Therefore, the actual distribution is probably more weighted towards the higher states than the results shown in Table 2 would indicate. Additional measurements to purify feed gases, particularly elimination of residual O_2 in the helium and nitrogen passing through the discharge region, should eliminate most of this background. These measurements are currently in progress.

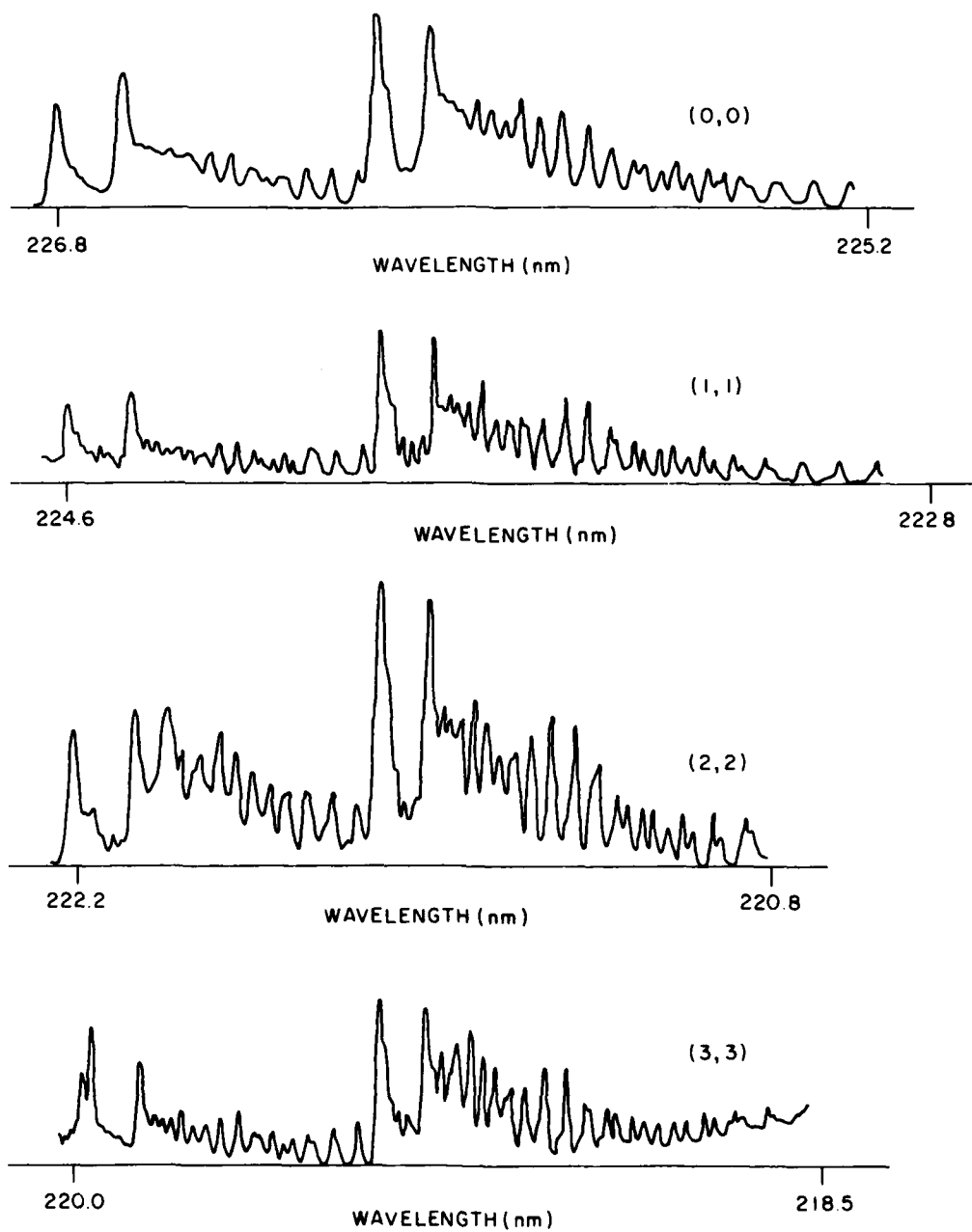15. White, M. G. (1984) Private Communication.

Figure 10. MPI Spectra for $\gamma(0,0)$, $\gamma(1,1)$, $\gamma(2,2)$, and $\gamma(3,3)$ Bands of NO

114

References

1. Baluch, D., Drysdale, D., Horne, D., and Lloyd, A. (1973) Evaluated Kinetic Data for High Temperature Reactions, II, Butterworths, London.

2. Whitson, M., Darnton, L., and McNeal, R. (1976) Vibrational energy distribution in the NO produced by the reaction of $N(^4S)$ with O_2, Chem. Phys. Lett. 41:552.

3. Rahbee, A., and Gibson, J. (1981) Rate constants for formation of NO in vibrational levels $v = 2$ through $v = 7$ from the reaction $N(^4S)$ with O_2, J. Chem. Phys. 74:5143.

4. Herm, R., Sullivan, B., and Whitson, M. (1983) Nitric oxide vibrational excitation from the $N(^4S) + O_2$ reaction, J. Chem. Phys. 79:2221.

5. Phillips, L., and Schiff, H. (1962) Mass spectrometric studies of atom reactions. I. Reactions in the atomic nitrogen - ozone system, J. Chem. Phys. 36:1509.

6. Lin, C., and Kaufman, F. (1971) Reactions of metastable nitrogen atoms, J. Chem. Phys. 3760.

7. Green, B., Caledonia, G., Murphy, R., and Robert, F. (1982) The vibrational relaxation of $NO(v = 1-7)$ by O_2, J. Chem. Phys. 76:2441.

8. Fernando, R., and Smith, I. (1979) Vibrational relaxation of NO by atomic oxygen, Chem. Phys. Lett. 66:218.

9. Piper, L. (1982) FACELIF design concepts, in R. A. Armstrong et al, Atmospheric Chemiluminescence, COCHISE and Related Experiments, AFGL-TR-82-0305, AD A130546, pp. 77-104.

10. Mallard, W. G., Miller, J. H., and Smyth, K. C. (1982) Resonantly enhanced two-photon ionization of NO in an atmospheric flame, J. Chem. Phys. 76:3843.

11. Asscher, M., Guthrie, W. L., Lin, T. H., and Somorjai, G. A. (1982) Vibrational and rotational energy distribution of NO scattered from the PT (III) crystal surface: detection by two-photon ionization, Phys. Rev. Lett. 49:76.

12. Sudb, Aa. S., and Loy, M. M. T. (1982) Measurement of absolute state to state rate constants for collision-induced transitions between spin-orbit and rotation states of NO ($X^2\Pi$, V = 2), J. Chem. Phys. 76:3646.

13. Goldstein, N., Greenblatt, G. D., and Wiesenfeld, J. R. (1982) Observation by laser ionization spectroscopy of vibrationally excited nitric oxide following $O(^1D) + N_2 \rightarrow 2NO$, Chem. Phys. Lett. 96:410.

14. White, M. G., Seaver, M., Chupka, W. A., and Colson, S. D. (1982) Observation of Rydberg ($C^2\Pi$)-valence ($B^2\Pi$) interactions in NO by multiphoton photoelectron spectroscopy, Phys. Rev. Lett. 49:28.

15. White, M. G. (1984) Private Communication.

Contents

5. FAKIR Experiments

by

L. Piper
W. T. Rawlins

1. INTRODUCTION

Metastable nitrogen atoms, N(^{2}D, ^{2}P), play an important role in the chemistry of disturbed atmospheres. N(^{2}D), through its reaction with molecular oxygen,

$$N(^2D) + O_2 \rightarrow NO(v) + O \quad , \tag{1}$$

is an important precursor for producing vibrationally excited nitric oxide in the upper atmosphere. Both the rate coefficient[1] for removal of N(^{2}D) by O_2 and the relative distribution of NO(v > 1) produced from Reaction (1) are fairly well established.[2] What is not known is the absolute rate coefficient for producing NO(v) from the reaction, that is, the branching fraction into v = 0.

1. Iannuzzi, M. P., and Kaufman, F. (1980) Rates of some reactions of N(^{2}D and ^{2}P) near 300 K, J. Chem. Phys. 73:4701.

2. Kennealy, J. P., DelGreco, F. P., Caledonia, G. E., and Green, B. D. (1978) Nitric oxide chemi-excitation occurring in the reaction between meta-stable nitrogen atoms and oxygen molecules, J. Chem. Phys. 69:1574.

In addition to understanding fully the product side of Reaction (1) one must also understand whether or not $N(^2D)$ is quenched significantly by atomic oxygen before the total importance of Reaction (1) in producing vibrationally excited nitric oxide in the upper atmosphere can be assessed.[3] Two laboratory measurements[1,4] seem to indicate that the rate coefficient for Reaction (2),

$$N(^2D) + O \rightarrow N(^4S) + O \qquad (2)$$

is about 2×10^{-12} cm^3 molecule^{-1} sec^{-1}. Aeronomic predictions, however, favor a much lower value, and because both the laboratory measurements were plagued with various uncertainties, this issue is far from settled.

We have begun to do some experiments on the FAKIR apparatus to try to address the above two issues. One approach to the issue of the absolute rate coefficients for NO(v) formation from Reaction (1) would be to repeat the classic COCHISE measurement on the NO(v) distribution from Reaction (1), with a simultaneous measurement of the absolute $N(^2D)$ number density in the reaction volume. Several years ago[5] we designed a VUV absorption lamp to be fit into COCHISE that would measure $N(^2D)$ number densities. We have recently begun to try to measure the yield of atomic oxygen from Reactions (3) plus (4)

$$N(^2D) + CO_2 \rightarrow CO + NO \qquad (3)$$

$$N(^4S) + NO \rightarrow O + N_2 \qquad . \qquad (4)$$

By comparing these yields with absorption measurements of $N(^2D)$ number densities, we hope to obtain an absolute calibration of the VUV resonance lamp. Some of our previous publications have detailed the necessity for establishing absolute calibrations of VUV resonance lamps that use microwave discharge excitation.[5]

We have also begun a series of experiments aimed at determining the rate coefficient for Reaction (2). Our preliminary results are in rough accord with the previous laboratory measurements, but need significant further refinement. Our basic approach is to try as many different sources of atomic oxygen as possible,

---

3. Caledonia, G. E., and Kennealy, J. P. (1982) NO infrared radiation in the upper atmosphere, Planet Space Sci. 30:1043.

4. Davenport, J. E., Slanger, T. G., and Black, G. (1976) The quenching of $N(^2D)$ by $O(^3P)$, J. Geophys. Res. 81:12.

5. Rawlins, W. T., and Piper, L. G. (1981) Effects of excitation mechanism on linewidth parameters of conventional vacuum ultraviolet (VUV) discharge line sources, Proc. Soc. Photo.-Opt. Instrum. Eng. 279:58.

hoping to obtain congruent results from all, and thereby demonstrate that difficult-to-detect species that may accompany some of the sources, such as $O_2(a^1\Delta)$, are not a factor in the measurements.

The following sections describe the apparatus, discuss the lamp absorption measurements, and give results of some preliminary measurements using a resonance fluorescence technique, of $N(^2D)$ quenching-rate coefficients by several quenchers including atomic oxygen.

2. EXPERIMENTAL ARRANGEMENTS AND PROCEDURES

The apparatus is a modification of one we have used previously in a number of other studies.[6-9] It consists of a 2-in. flow tube pumped by a Leybold-Heraeus Roots blower/forepump combination capable of producing linear velocities up to 5×10^3 cm/sec at pressures of 1 Torr. The flow-tube design is modular (see Figure 1), with separate source, reaction, and detection sections that clamp together with O-ring joints. The detection region is a rectangular stainless-steel block bored out internally to a 2-in. circular cross section and coated with Teflon® (Dupont Poly TFE #852-201) to retard surface recombination of atoms.[10] The surface was primed with black primer prior to the Teflon® coating to reduce scattered light inside the block. Two sets of viewing positions consisting of four circular ports each on the four faces of the block are separated by a distance of 7.5 cm. The circular ports, all of which contain MgF_2 windows, accommodate vacuum ultraviolet resonance lamps, VUV and visible monochromator interfaces, laser delivery side-arms, and a spatially filtered photomultiplier/interference filter combination.

The upstream observation position is fitted with two microwave-discharge resonance lamps placed normal to each other, and a 0.2 m vacuum ultraviolet monochromator (Minuteman 302 VM) diametrically opposite one of the resonance

6. Piper, L. G., Caledonia, G. E., and Kennealy, J. P. (1981) Rate constants for deactivation of $N_2(A)v' = 0$, by O_2, J. Chem. Phys. 74:2888.

7. Piper, L. G., Caledonia, G. E., and Kennealy, J. P. (1981) Rate constants for deactivation of $N_2(A^3\Sigma_u^+, v' = 0, 1)$ by O, J. Chem. Phys. 75:2847.

8. Piper, L. G. (1982) The excitation of $O(^1S)$ in the reaction between $N_2(A^3\Sigma_u^+)$ and $O(^3P)$, J. Chem. Phys. 77:2373.

9. Piper, L. G., Clyne, Michael A. A., and Monkhouse, P. (1982) Electronic energy transfer between metastable argon atoms and ground-state oxygen atoms, J. Chem. Soc., Faraday Trans. 278:1373.

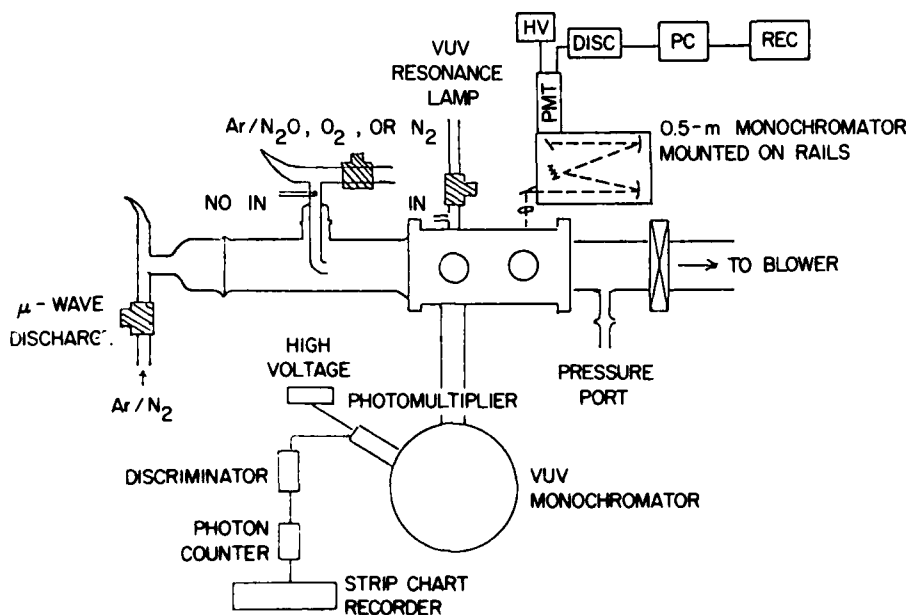10. Berg, H. C., and Kleppner, D. (1962) Storage technique for atomic hydrogen, Rev. Sci. Instr. 33:248.

Figure 1. Apparatus for $N^*(^2D, {}^2P)$ Studies

lamps. The lamp viewed by the monochromator is used in absorption studies, while the lamp normal to the monochromator's optical axis is used to excite resonance fluorescence of atomic species formed in the flow reactor. The lamps and the monochromator are separated from the flow tube by 25 mm diameter MgF_2 windows that have a short wavelength cutoff of 115 nm. In addition, a MgF_2 lens in the optical train of the monochromator collects light from the flow tube.

Figure 2 is a schematic showing the resonance lamps and detection cell. The lamps are constructed from 13 mm (o. d.), medium-wall Pyrex® tubing. He or Ar flows through each lamp at rates of ~150 μmol/sec and total pressures of ~1.5 Torr. The discharge plasmas are excited by Evenson[11] cavities powered by 2.45 GHz supplies (Raytheon PGM-10) operating at a power of about 20 W for the absorption lamp and 50 W for the resonance-fluorescence lamp. The gas flow enters the lamp near the window and passes from front to back. This procedure inhibits the buildup of pockets of absorbing atoms between the emitting region and the exit window. Occasionally, controlled amounts of air are added to the lamp to enhance nitrogen emissions, but usually the impurity level of N_2 (a few ppm) in the He and Ar bath gases is sufficient to give intense but optically thin multiplets

11. Fehsenfeld, F. C., Evenson, K. M., and Broida, H. A. (1965) Microwave discharge cavities operating at 2450 MHz, Rev. Sci. Instr. 36:294.
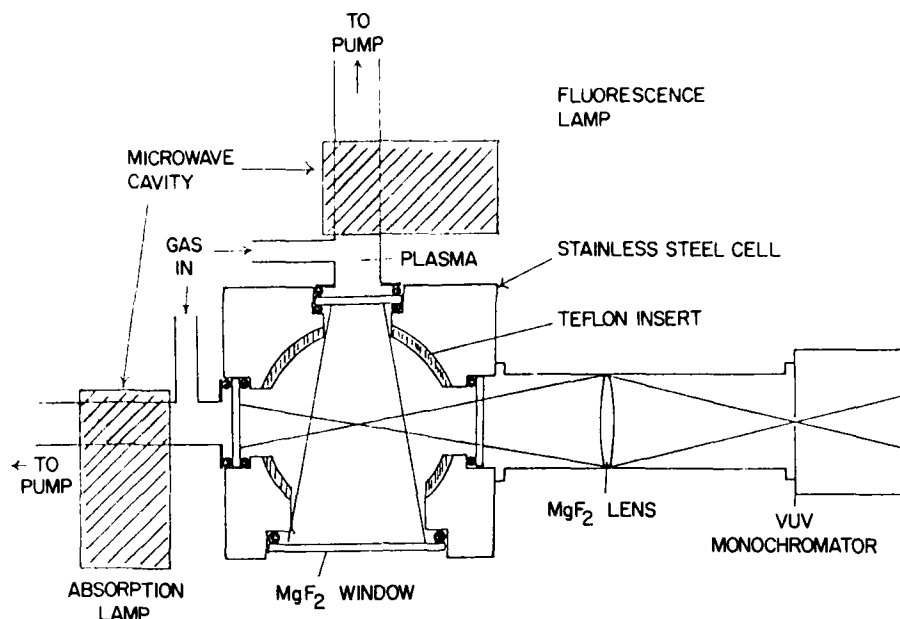
Figure 2. Cross Sectional View of the Absorption/Fluorescence Cell Show-ing the Placement of the Lamps. The direction of the flow in the reactor is perpendicular to the figure

at 149 and 174 nm. The absence of self-absorption is determined spectrally by confirming that the observed intra-multiplet line ratios are consistent with those predicted from spin-orbit sum rules.[12] Instability in the emission intensity, due to long-term variations in the lamp cooling rate and thereby in the steady-state operating temperature of the lamp (typically 500-600 K), is minimized by regulat-ing the flow of cooling air to the cavity.

Atomic nitrogen metastables are made in the flow tube by discharging mix-tures of nitrogen and either argon or helium in a McCarroll[13] cavity powered by another Raytheon 2.45 GHz supply. Molecular nitrogen is moderately efficient at quenching the atomic metastables ($k_{N(2D) + N2} = 1.6 \times 10^{-14}$ cm^3 molecule^{-1} sec^{-1}),[12, 14] so that the best metastable yields come from fairly dilute mixtures of N_2 in Ar or He, typically < 1 percent N_2.

12. Lin, C., and Kaufman, F. (1971) Reactions of metastable nitrogen atoms, J. Chem. Phys. 55.

13. McCarroll, B. (1970) An improved microwave discharge cavity for 2450 MHz, Rev. Sci. Instr. 41:279.

14. Husain, D., Mitra, S. K., and Young, A. N. (1974) Kinetic study of elec-tronically excited nitrogen atoms, $N(2^2D_J, 2^2P_J)$, by attenuation of atomic resonance radiation in the vacuum ultra-violet, J. Chem. Soc., Faraday II 70:1721.

Quenchers or titration reagents are injected into the flow tube through a moveable injector. We have installed this moveable injector to use in kinetic studies. The moveable injector consists of a 0.25 in. diameter length of stainless steel with a teflon loop epoxied into its downstream end. The loop is slightly more than an inch in diameter and is set on the stainless steel tube so that it is concentric with the flow reactor. A number of small holes have been drilled around both the inside and outside of the loop to allow reagent gas to escape into the gas stream, and the quality of mixing was checked by observing the air afterglow when NO was added through the loop injector to a flow containing O atoms. The 0.25 in. stainless tube slides along the bottom of the flow reactor, and exits it through a Swagelok fitting in the end flange of the flow reactor. The Swagelok fitting has been slightly modified for this purpose by boring it out completely to accept the tube, using a double O-ring seal in place of the front ferrule, and reversing the rear ferrule. The zero of the scale relating the distance between the injector and the detection region was calibrated by measuring the point at which the scattered light from the resonance-fluorescence lamp suddenly increased as the injector was moved into the detection region. Atomic oxygen for quenching measurements is made upstream in one of the hook injectors by discharging Ar/N_2O or Ar/O_2 mixtures. NO formation from the Ar/N_2O discharge is eliminated by using large flows of argon (~ 600 μmoles/sec) and relatively high discharge powers (~ 70 W). We have characterized this source of atomic oxygen in a previous report. [15]

Mass-flow meters monitor the flow rates of argon or helium and nitrogen, rotameters measure those of quenching reagents and of argon through the O-atom discharge, and measurements of the rate of increase in pressure with time in a calibrated volume determines the flow rate of nitric oxide that was needed to calibrate an O-atom resonance lamp and to measure O-atom yields from the Ar/O_2 or Ar/N_2O reagent discharges. All flow meters were calibrated by measuring rates of increase of pressure with time into 6.5 or 12 l flasks, using appropriate differential pressures transducers (Validyne DP-15), which had themselves been calibrated with silicon oil or mercury manometers. Typically the flow rates from argon or helium, nitrogen, and quencher were 2000-5000, 50, and 0-120 μmole/sec, respectively. The total pressure was generally 1-3 Torr, and the flow velocity was 1000-3500 cm/sec.

The argon or helium and the nitrogen flow through molecular-sieve traps to remove water and carbon dioxide prior to entry into the flow reactor, while the argon through the injector flowed straight from the cylinder. Most experiments

15. Piper, L. G., Rawlins, W. T., and Armstrong, R. A. (1983) O-Atom Yields from Microwave Discharges in N_2O/Ar Mixtures, AFGL-TR-83-0031, AD A130429.

used quenchers, N_2O, CO_2, or O_2, straight from their cylinders without further purification.

Nitric oxide was purified by flowing it slowly at atmospheric pressure and room temperature through an Ascarite trap, then through a trap immersed in a liquid nitrogen/methanol slush bath (175 K). It was stored in a 5-l bulb. Final nitric oxide purification involved several freeze, pump, thaw cycles of the gas in the storage bulb. The Ascarite trap previously had been baked overnight under vacuum.

Some spectral observations were made in the visible/near UV using a 0.5 m monochromator equipped with a thermoelectrically cooled photomultiplier having an S-20 response. A photon-counting rate meter monitored the output of the photomultiplier. VUV observations also employed the photon-counting rate meter, or in some cases, a scaler counted individual photons. Since the dark count of the VUV solar blind PMT was about 0.4 Hz, count rates well below 10 Hz could be determined with reasonable precision. When pulse counting, the procedure generally was to average 4-10 sets of 10 second counts.

Atomic-oxygen number densities produced from Reactions (3) plus (4) in the lamp calibration experiments were measured using resonance absorption at 130 nm. The absorption diagnostic was calibrated by adding NO to excess N and then equating the O produced with NO consumed. This diagnostic lacks sensitivity to be used accurately at O-atom number densities above 10^{13} atoms/cm^3, which are required for measurements of Reaction (2). For those experiments atomic oxygen number densities were determined by measuring the intensity of the O/NO air afterglow when known amounts of NO were added to the reactor with the main Ar (or He)/N_2 discharge turned off.[7,15-17] The filtered photomultiplier at the second observation position detected this light. We have described elsewhere in great detail how we calibrate and use this diagnostic to monitor O-atom number densities.[7,15-17]

The operation of the apparatus has been improved by incorporation of a computerized data-acquisition and analysis system. The system employs an IBM PC interfaced to a Data Translation DT 2801A A/D board using a software package developed by Laboratory Technologies Corporation. An extremely competent student worked out a series of analysis schemes based upon the popular Lotus 1-2-3 business software. This system now allows us to take and analyze data more efficiently, and in addition will allow us to do spectral fitting. This will be needed during the

16. Kaufman, F. (1958) The air afterglow and its use in the study of some reactions of atomic oxygen, Proc. Roy. Soc. (London) A 247:123.

17. Kaufman, F. (1973) The air afterglow revisited, Chemiluminescence and Bioluminescence, M. J. Cormier, D. M. Hercules, and J. Lee, Eds., pp. 83-100.

next year's effort, and would have been nearly impossible without the computer-
ized data-acquisition system. We will discuss spectral fitting in more detail later.

3. RESULTS

3.1 Production of Atomic Oxygen in the Reaction Between $N(^2D)$ and CO_2

The basic concept behind these measurements is straightforward: to relate
the atomic oxygen produced in Reactions (3) plus (4) to measurements of the $N(^2D)$
fractional absorption, to determine an effective temperature for the emission line
in the $N(^2D)$ lamp. The data are complicated to interpret, however, because even
in the absence of added O_2, $N(^2D)$ is removed from the system by diffusion to the
reactor walls. The $N(^2D)$ absorption measurements, therefore, determine the
$N(^2D)$ number density at the observation point, whereas the atomic oxygen meas-
urements relate to $N(^2D)$ number densities between the injector and the observa-
tion position. Atomic oxygen is essentially unperturbed by collisions with reactor
walls. We have modeled the reaction system to analyze our data and thereby
correct for the diffusive losses of $N(^2D)$.

The differential equation for the loss of $N(^2D)$ in the reactor is

$$\frac{\bar{v}\, d[N(^2D)]}{dz} = -0.62\left\{\frac{D_o}{\Lambda^2 P} + k_3[CO_2]\right\}[N(^2D)] \quad , \tag{5}$$

where

  D_o is the diffusion coefficient of $N(^2D)$ in Ar or He buffer,
  Λ is the characteristic diffusion length $(r/2.405)^2$,
  z is the distance from the injector to the detector,
  $\bar{v}$ is the bulk flow velocity, and the factor 0.62 corrects for the coupling
     of a radial density gradient in $N(^2D)$ with a radial velocity profile.

Because the added CO_2 is in great excess compared to the $N(^2D)$ in the reactor,
pseudo first-order conditions prevail and Equation (5) has the solution

$$[N(^2D)] = [N(^2D)]^{\circ} \exp\left\{-0.62\left(\frac{D_o}{\Lambda^2 P} + k_3[CO_2]\right)z/\bar{v}\right\} \quad . \tag{6}$$

The differential equation for the production of atomic oxygen in Reactions (3) plus
(4) is

$$\frac{d[O]}{dt} = k_3[CO_2]\,[N(^2D)] \quad . \tag{7}$$

The formation of O from $N(^4S)$ and CO_2 is negligibly small under our conditions,[18] as is the loss of O in wall recombination.[19] Using Eq. (6) for $[N(^2D)]$ we can solve Eq. (7) to get

$$[O] = \frac{[N(^2D)]^\circ}{1 + k_D/k_3[CO_2]} \left(1 - \exp\{-0.62\,(k_D + k_3\,[CO_2])\,z/\bar{v}\} \right) \quad , \qquad (8)$$

where

$$k_D = \frac{D_o}{\Lambda^2 P} \quad .$$

We can use Eq. (6) in the absence of added CO_2 to determine $[N(^2D)]^\circ$ at the injector in terms of the number density at the detector, $[N(^2D)]^\circ$ obs. The ratio of $[O]/[N(^2D)]^\circ$ obs is then

$$\frac{[O]}{[N(^2D)]^\circ \text{obs}} = \frac{e^{0.62\,k_D z/\bar{v}}}{1 + k_D/k_3[CO_2]} \left(1 - \exp\{-0.62(k_D + k_3[CO_2])z/\bar{v}\} \right) \quad . \qquad (9)$$

We wrote a computer program to generate values of the ratio $[O]/[N(^2D)]^\circ$ obs as a function of $[CO_2]$ for the various sets of experimental conditions in our reactor and using $D_o(Ar) = 240 \text{ cm}^2 \text{ sec}^{-1} \text{ Torr}^{-1}$,[13] $D_o(He) = 750 \text{ cm}^2 \text{ sec}^{-1} \text{ Torr}^{-1}$,[12] and $k_3 = 3.6 \times 10^{-13} \text{ cm}^3 \text{ molecules}^{-1} \text{ sec}^{-1}$ (see below). Figure 3 compares model predictions with observations for two cases.

The absolute $N(^2D)$ number density at the detector is given by the ratio of the measured atomic-oxygen number densities to the ratio $[O]/[N(^2D)]^\circ$ obs calculated from Eq. (9). This absolute $[N(^2D)]^\circ$ obs can then be compared to various lamp models to extract an effective temperature for the $N(^2D)$ absorption multiplet.

Relative metastable nitrogen number densities are given by the relation $[N(^2D)]_{rel} = \ln(1/(1-A))$, where A is the fractional absorption of the 149 nm resonance multiplet. This expression is a Beer's law analogue that we have shown previously to apply to our conditions.[17] The results of the fitting indicate that $[N(^2D)]_{rel} = 1.0$ corresponds to absolute number densities of 6.5 and 9×10^{12} atoms cm^{-3} for runs in helium and argon buffer respectively. These data translate to effective lamp temperatures of 6000 and 13,000 K determined from runs in helium and argon buffer respectively.

18. Rawlins, W. T., and Kaufman, F. (1976) The reaction of CO_2 with active nitrogen, J. Chem. Phys. 64:1128.
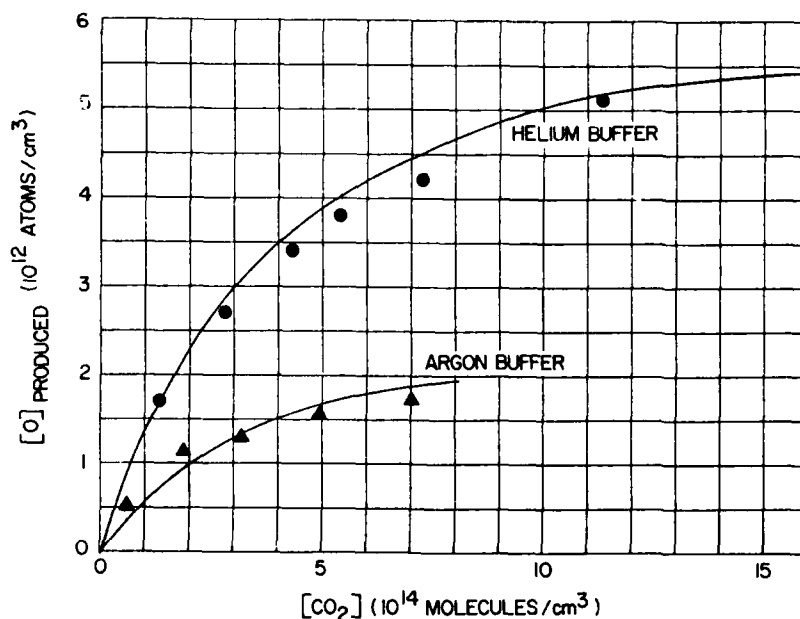19. Kaufman, F. (1961) Reactions of oxygen atoms, Prog. React. Kinet. I:1.

Figure 3. The Production of Atomic Oxygen From Excited
Nitrogen Plus CO_2. The lines through the data points are
from the kinetic model described by Eq. (9)

We have several good reasons to believe that the temperature in the resonance
lamp using a helium buffer is actually more like the 500-600 K ambient tempera-
ture in the discharge.[5] If the lamp temperature is as suspected, then the experi-
mental data imply that roughly 2.7 and 3.7 atoms of oxygen are produced per atom
of $N(^2D)$ consumed in the helium and argon buffer experiments respectively. The
only way that excess oxygen atoms can be produced is for there to be other energy
carriers in the discharged Ar/N_2 or He/N_2 mixtures. Figures 4 and 5 show that
this is undoubtedly the case. These figures show spectra of the nitrogen first-
positive bands downstream from an Ar/N_2 discharge. The spectral distribution
in Figure 4 is what one expects to see when the first-positive emission is produced
by nitrogen-atom recombination. Figure 5, which was taken at a much shorter
delay time between the discharge and the observation region, shows a much differ-
ent spectral distribution.

This spectrum was taken 9 msec downstream of the discharge, so the emis-
sion cannot result from $N_2(B^3\Pi_g)$ excited in the discharge and then carried down-
stream because the $N_2(B)$ state has a lifetime of only about 8 μsec. Thus the
spectrum must be excited by some metastable energy carrier in the gas flow that
can be collisionally converted to $N_2(B)$. The metastable species in question is not
$N_2(A^3\Sigma_u^+)$ because the ground-state atomic-nitrogen number density is so great as

126
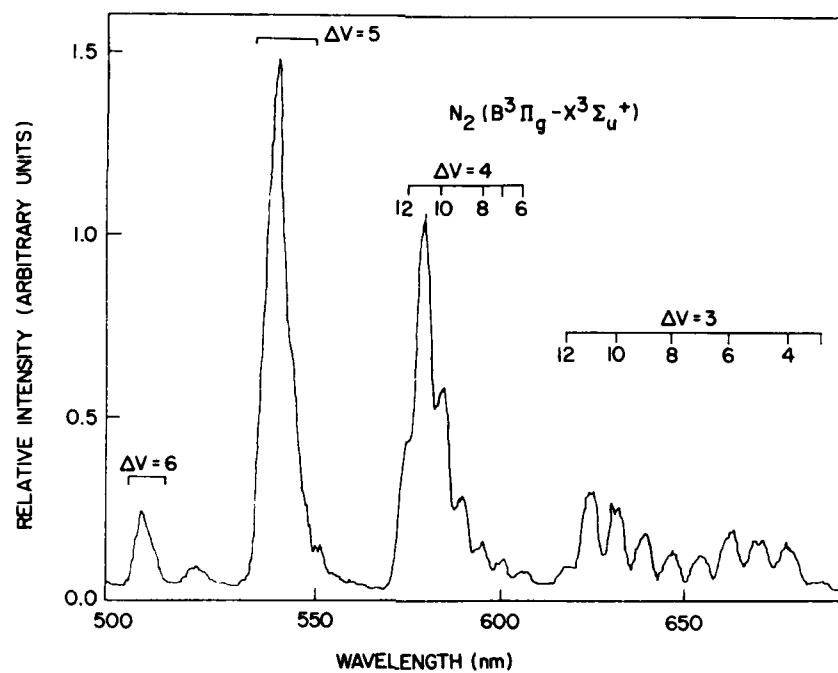
Figure 4. Nitrogen First-Positive Emission, $N(B^3\Pi_g - A^3\Sigma_u^+)$, Excited by N-atom Recombination
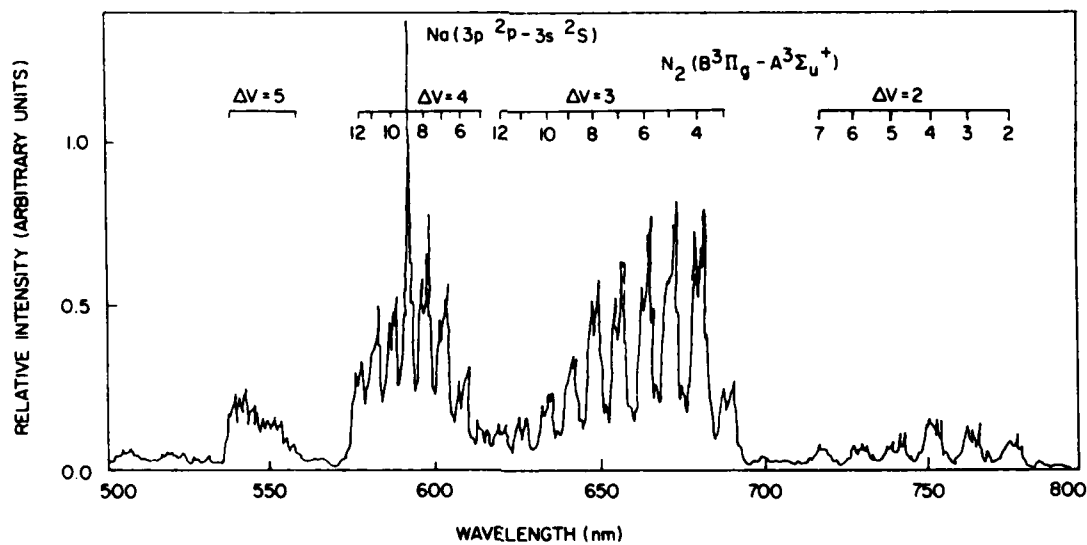

Figure 5. Visible Spectrum 9 msec Downstream From an Ar/N_2 Discharge $\chi_{N_2} = 0.02$

127

to quench $N_2(A)$ to an insignificant level in the 9 msec transit time from the discharge to the observation region.[20] The identity of this $N_2(B)$ precursor could have important atmospheric implications and should be pursued further.

Three other experiments also show there must be additional energy carriers in the discharge effluent. Two runs in argon buffer with only one-third of the transit time from the discharge to the injector as compared to the other argon runs gave a value of 14×10^{12} atoms cm^{-3} for unit $(N(^2D))$ relative while one run in which some CO was added to the discharge effluent upstream from the injector gave a value of 1.75×10^{12} atoms cm^{-3} for unit relative $N(^2D)$ number density. These experiments indicate that the precursor state is relaxed either by longer contact time with argon or else by wall collisions as evidenced by the great differences in the argon runs with a long flow time to the injector compared to the runs with a short flow time. In addition, the precursor state is quenched efficiently by carbon monoxide, but lacks sufficient energy to dissociate it. Some further experiments with the pre-quenched discharge effluent are needed to get good quantitative results on the portion of O from Reaction (1), but our CO run indicates that the yield of O per $N(^2D)$ consumed is unity, and that the temperature of the helium lamp is indeed 500-600 K.

3.2 Kinetic Measurements

The rate coefficient is determined from measurements of the change in the natural log of the metastable nitrogen number density as a function of number density of added quenching reagent:

$$\Gamma = \frac{- d\ell n[N(^2D)]}{d[Q]} = k_Q z/\bar{v} \qquad . \qquad (10)$$

The desired rate coefficient is obtained from the slope of Γ vs z/v where the Γ's were determined at a variety of values of z but with other conditions constant. Figures 6 - 9 illustrate this procedure for measurements on O_2 and CO. Table 1 summarizes the results to date.

The metastable-nitrogen studies used a resonance fluorescence technique to monitor the atomic-nitrogen-metastable number density in the reactor. At sufficiently low number densities, the metastable-nitrogen number density is directly proportional to the intensity of the observed resonance fluorescence (see Figure 10). The two metastable nitrogen atoms, $N(^2D)$ and $N(^2P)$, have a common upper state

20. Meyer, J. A., Setser, D. W., and Stedman, D. H. (1970) Energy transfer reactions of $N_2(A\,^3\Sigma_u{}^+)$. II. quenching and emission by oxygen and nitrogen atoms, J. Phys. Chem. 74:2238.
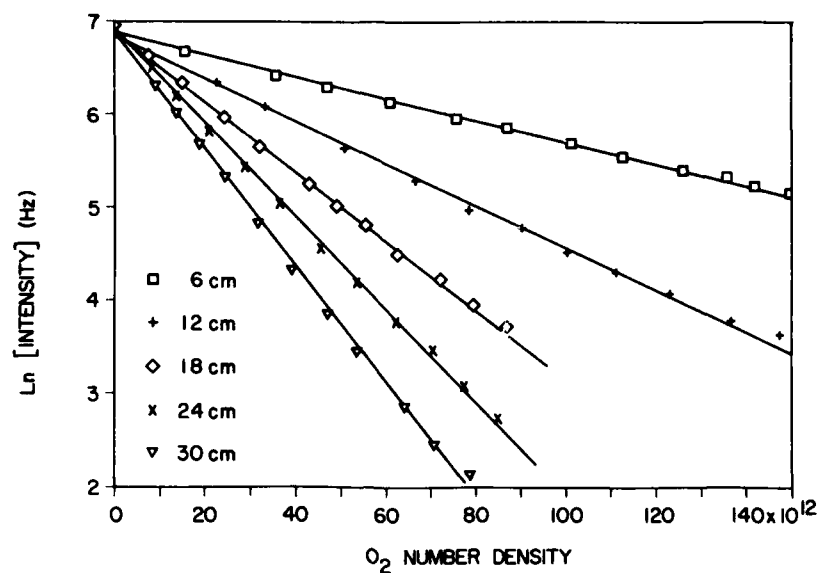
Figure 6. Decay of the Log of $[N(^2D)]$ as a Function of $[O_2]$ at Five Different Reaction Distances
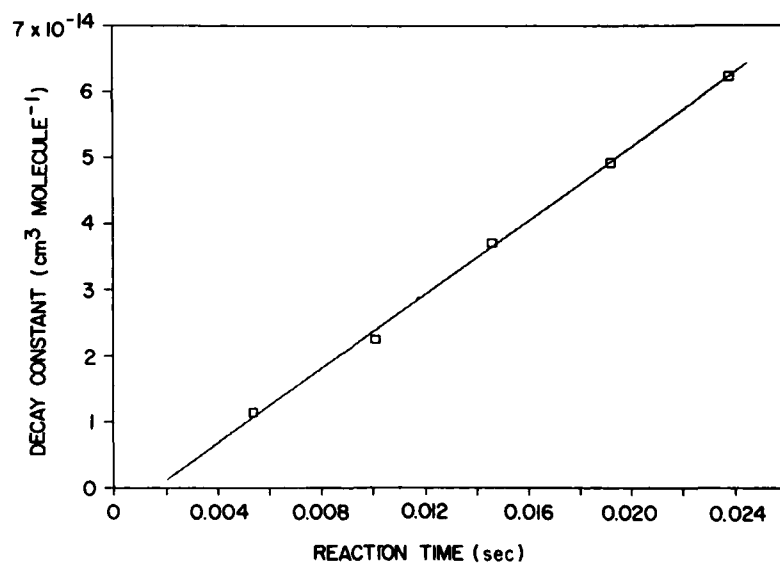

Figure 7. Variation in Decay Constant With Reaction Time for the $N(^2D) + O_2$ Reaction. The ordinates of the data points are determined from the slopes of the lines in Figure 6
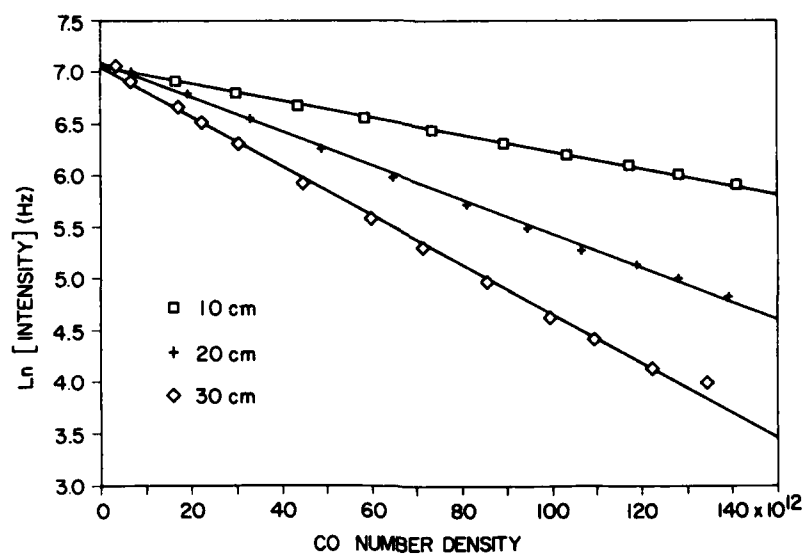
129

Figure 8.   Decay of the Log of [N(^{2}D)] With [CO] for
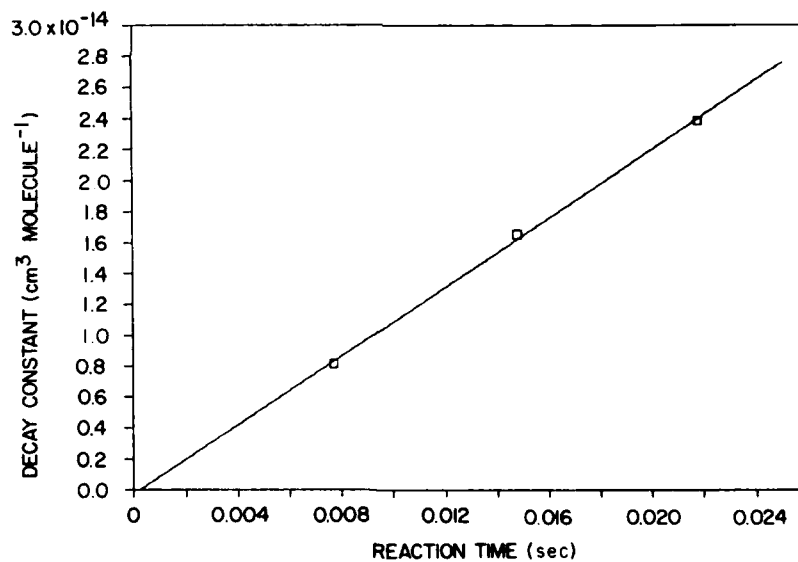Different Reaction Times

Figure 9.   Variation in Decay Constant Γ With Reaction Time
for the N(^{2}D) + CO Reaction.   The data points are derived
from Figure 8

130

Table 1. Preliminary Rate Coefficients

N(^{2}D) Quenching		
Molecule	Value	Reference
CO_2	3.6×10^{-13}	FAKIR
	$(1.8 \pm 0.2) \times 10^{-13}$	Husain, Mitra, Young[14]
	$(5 \pm 2) \times 10^{-13}$	Lin and Kaufman[12]
	6×10^{-13}	Black, Slanger, Young[21]
	6.8×10^{-13}	Fell, Rivas, McFadden[22]
N_2O	2.3×10^{-12}	FAKIR
	1.6×10^{-12}	Husain, Mitra, Young[14]
	$(3.5 \pm 1.2) \times 10^{-12}$	Lin and Kaufman[12]
	3×10^{-12}	Black, Slanger, Young[21]
	3.1×10^{-12}	Fell, Rivas, McFadden[22]
O_2	$(4.7 \pm 0.4) \times 10^{-12}$	FAKIR
	5.2×10^{-12}	Husain, Mitra, Young[14]
	$(6 \pm 2) \times 10^{-12}$	Lin and Kaufman[12]
	7.4×10^{-12}	Black, Slanger, and Wood[23]
	6.1×10^{-12}	Fell, Rivas, McFadden[22]
CO	$(1.7 \pm 0.4) \times 10^{-12}$	FAKIR
	$(2.1 \pm 0.2) \times 10^{-12}$	Husain, Mitra, Young[14]
N_2	4×10^{-14}	FAKIR
	1.5×10^{-14}	Husain, Mitra, Young[14]
	1.6×10^{-14}	Lin and Kaufman[12]
H_2	$(3 \pm 1) \times 10^{-12}$	FAKIR
	$(2.1 \pm 0.3) \times 10^{-12}$	Husain, Mitra, Young[14]
	5×10^{-12}	Black, Slanger, Young[23]
	$(3.5 \pm 1) \times 10^{-12}$	Fells, Rivas, McFadden[22]

21. Black, G., Slanger, T. G., St. John, G. A., and Young, R. A. (1969) Vacuum-UV photolysis of N_2O, 4, deactivation of N(^{2}D), J. Chem. Phys. 51:116.

22. Fell, B., Rivas, I. V., and McFadden, D. L. (1981) Kinetic study of electronically metastable nitrogen atoms, N(2 ^{2}D_J), by electron spin resonance absorption, J. Phys. Chem. 85:224.

23. Slanger, T. G., Wood, B. J., and Black, G. (1971) Temperature coefficients for N(^{2}D) quenching by O_2 and N_2O, J. Geophys. Res. 76:8430.

Table 1. Preliminary Rate Coefficients (Contd)

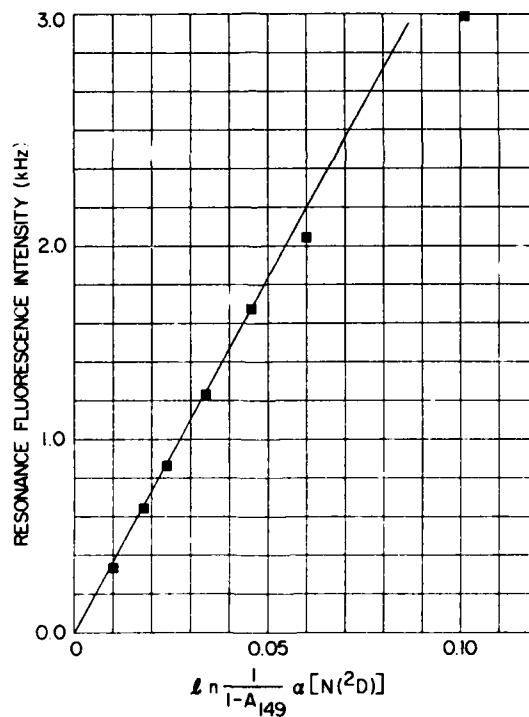| $N(^2P)$ Quenching		
Molecule	Value	Reference
CO_2	7×10^{-15} 1.1×10^{-15}	FAKIR Husain, Mitra, Young[14]
N_2O	7×10^{-14} $(5 \pm 2) \times 10^{-14}$	FAKIR Husain, Mitra, Young[14]
Ar	2×10^{-15} 7×10^{-16} 4×10^{-16}	FAKIR Lin and Kaufman[12] Ianuzzi and Kaufman[1]

Figure 10. Variation in $N(^2D)$ Resonance Fluorescence Intensity at 174 nm as a Function of Relative $N(^2D)$ Number Density. Ar buffer; 250-μm slits

for their resonance lines so that one of the lines must be filtered from the lamp to discriminate between the two levels. A laser reflector centered at about 175 nm on a MgF_2 substrate discriminates moderately well against the 174 nm line that is absorbed by $N(^2P)$ while passing the 149 nm multiplet, which is absorbed by $N(^2D)$. We found that commercially available reflectors were imperfect, however, giving a transmission ratio, T_{149}/T_{174} of about 8:1. Some further discrimination that enhances resonance fluorescence from $N(^2D)$ pumping over that from $N(^2P)$ pumping results from a greater intensity in the 149 nm multiplet, a slightly larger oscillator strength for 149 nm absorption, and by the fact that $N(^2D)$ outnumbers $N(^2P)$. Absorption measurements on the ratio of $[N(^2D)]$ to $[N(^2P)]$ showed a variation of greater than 7:1 in argon to as little as 2.5:1 in helium. The fraction of the initial resonance fluorescence observed in argon that could be attributed to $N(^2P)$ pumped by leakage through the lamp filter was only about 1 percent, but was as much as 3-5 percent in helium buffer. This leakage causes severe problems in getting reliable kinetic data because the $N(^2P)$ is much less readily quenched than is $N(^2D)$--by one to two orders of magnitude--so that after only one e-fold in measured resonance-fluorescence decay, as much as 15 percent of the residual resonance-fluorescence signal comes from unquenched $N(^2P)$. Thus, decay plots in helium can become severely non-linear over less than an order of magnitude decay. Such non-linearity is unacceptable for obtaining reliable quenching measurements. One would like two orders of magnitude of linear decay if possible, and given the low background counts in the system, several orders of magnitude in resonance fluorescence decay as a function of added quencher is certainly attainable.

We tried a non-linear least-squares fit to the decay plots using the sum of two exponential decays, one relating to $N(^2D)$ and the other to $N(^2P)$. Adequate fits were possible only in cases in which the decays were carried out to very high quencher additions where all of the resonance fluorescence signal could be attributed solely to $N(^2P)$ pumping. In those cases, however, hand fits were equally good. Such a case is shown in Figure 11, which shows the decay in the resonance fluorescence signal as a function of added N_2O for two runs in helium buffer, one in which only N_2O was added through the injector, and another in which a flow of argon, comprising about 12-14 percent of the total flow, was added through the injector along with the N_2O. The two interesting points to notice about the data with the large argon flow are that the initial signal in the absence of N_2O addition is much larger than the initial signal without the added argon, and that the data with the added argon decay to a much lower residual $N(^2P)$ resonance-fluorescence intensity. The initial signal is larger because the addition of the argon slows down the loss of metastable nitrogen by diffusion to the walls. The lower $N(^2P)$ plateau
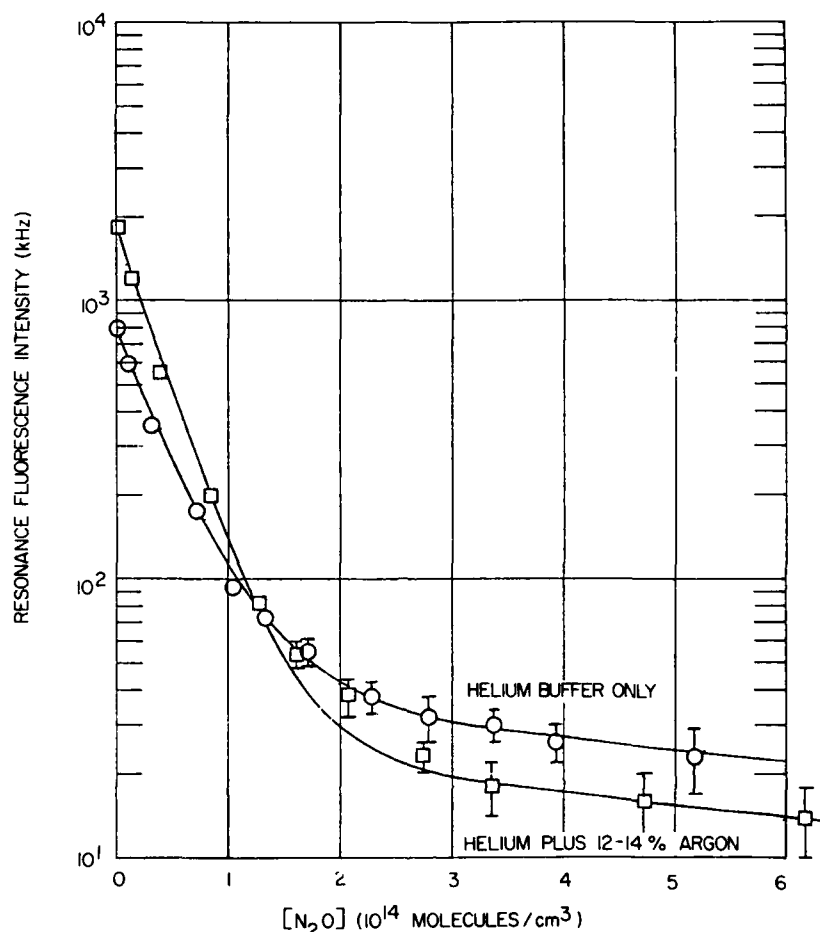
133

Figure 11. The Quenching of N(^{2}D, ^{2}P) by N$_2$O in Helium Buffer
With and Without the Addition of 12-14 Percent Argon

results because argon is a more efficient quencher of N(^{2}P) than it is of N(^{2}D). We
estimate from these and some other data that N(^{2}P) is quenched by argon with a
rate coefficient of about 2×10^{-15} cm^3 molecule^{-1} sec^{-1}.

The effect of adding small amounts of a heavier gas to slow diffusive losses in
helium were also evident in comparing changes in N(^{2}D) number density measured
in absorption as a function of the amount of N$_2$ added to the reactor. With helium
buffer, increasing the molecular nitrogen from 0.5 to 5 percent of the total flow
attenuated the metastable-nitrogen-atom number density only slightly (< 7 percent),
whereas similar increases in N$_2$ in an argon buffer dropped the metastable nitro-
gen atom number density by more than 70 percent. The molecular nitrogen
quenches the N(^{2}D) reasonably efficiently; our data suggest a quenching rate coef-
ficient of $(4 \pm 1) \times 10^{-14}$ cm^3 molecule^{-1} sec^{-1}, but in helium this more rapid

134

quenching by higher number densities of N_2 is offset by the slowing of diffusive losses with higher N_2 mole fractions in the reactor.

Our preliminary results on the quenching of $N(^2D)$ by N_2O, CO_2, and O_2, obtained from initial slopes of decays of plots like Figure 11, result in values of 2.3×10^{-12}, 3.6×10^{-13}, and 4×10^{-12} cm^3 $molecule^{-1}$ sec^{-1} respectively. These data have not encompassed an adequate variation in mixing distance, so that some further measurements are in order to obtain definitive values. However, they are in reasonable accord with the literature as shown in Table 1. Accurate values will be forthcoming with the addition of the moveable injector. The CO_2 measurement is critical to the analysis of the O-atom production studies, while the N_2O and O_2 values are critical to the analysis of the O-atom quenching measurements to be reported below.

The data for which decays extended to sufficiently high quencher number density so as to eliminate all resonance fluorescence from $N(^2D)$ should give rate coefficients for quenching $N(^2P)$. Our measurements give values of 7×10^{-15} and 1.2×10^{-13} cm^3 $molecule^{-1}$ sec^{-1} for quenching by CO_2 and N_2O respectively. Better data on $N(^2P)$ quenching can be obtained by monitoring that state directly in fluorescence at 346.6 nm. Under certain conditions this emission appears strongly in our reactor.

3.3 The Quenching of $N(^2D)$ by Atomic Oxygen

Two preliminary measurements on the quenching of $N(^2D)$ by atomic oxygen were made by comparing the differences in the $N(^2D)$ attenuation as a function of added quencher in the presence and absence of a microwave discharge to dissociate the reagent gases. Figure 12 displays results taken using N_2O as the reagent gas. Clearly, discharging the gas reduces the $N(^2D)$ attenuation, showing that atomic oxygen is less efficient than N_2O in quenching $N(^2D)$.

With the discharge off the equation governing the resonance fluorescence intensity is:

$$\ln I_{off} = \ln I_o - \{k_D + k_{N_2O}(N_2O)\} z/\bar{v} \qquad , \qquad (11)$$

and with the discharge on, the equation is

$$\ln I_{on} = \ln I_o - \{k_D + k_O[O] + k_{O_2}[O_2]\} z/\bar{v} \qquad . \qquad (12)$$

We tried to measure the efflux of undissociated N_2O from the discharge by monitoring the attenuation of the 129.6 nm Xe resonance line as N_2O was added to the discharge. Our measurements indicated no N_2O exited the discharge, thus
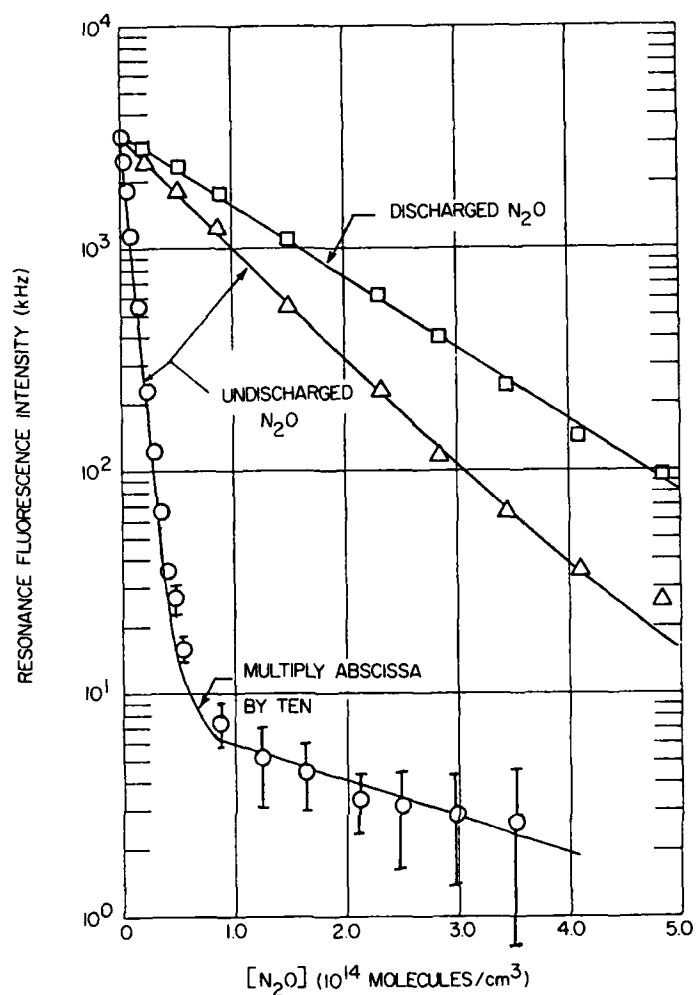
135

Figure 12. Variation in Resonance Fluorescence Intensity of $N(^2D, ^2P)$ as a Function of Added N_2O for Both Discharged and Undischarged N_2O

implying that the N_2O was completely dissociated and that any discrepancy between O produced and N_2O consumed must be the result of O-atom recombination to produce O_2, some of which may well be in the $a^1\Delta$ state. With the discharge on, the number density of atomic oxygen is

$$[O] = \alpha[N_2O]^\circ \qquad (13)$$

and that for molecular oxygen is

$$[O_2] = \frac{1 - \alpha}{2} [N_2O]^\circ \qquad , \qquad (14)$$

136

where α is calculated from the ratio of the measured atomic-oxygen number density to the N_2O number density with the discharge off. Using these above two relations in Eq. (12) and combining with Eq. (11) gives the working equation for our data analysis

$$\ln \frac{I_{on}}{I_{off}} = \{k_{N_2O} - \alpha k_O - \frac{1}{2} \, \overline{}^{\alpha} \, k_{O_2}\} [N_2O]^{\bullet} \, z/\overline{v} \qquad . \qquad (15)$$

For experiments with discharged O_2 the analysis equation is

$$\ln \frac{I_{on}}{I_{off}} = \{k_{O_2} - 2k_O\} \, \alpha [O_2]^{\circ} \, z/\overline{v} \qquad , \qquad (16)$$

where in this case α is defined as the fractional O_2 dissociation or

$$\alpha = \frac{[O_2] - [O_2]_o}{[O_2]_o} = \frac{[O]}{2[O_2]_o} \qquad . \qquad (17)$$

Figure 13 shows a plot of the data according to Eq. (15) for the experiments with discharged N_2O, while Figure 14 shows the results of the experiment with discharged O_2. The two sets of data give O-atom quenching rate coefficients of 0.5 and 1×10^{-12} cm^3 molecule^{-1} sec^{-1} for the N_2O and O_2 experiments respectively. The fractional dissociations in both experiments were not particularly impressive ($\approx$ 30 percent). We hope to boost the fractional dissociations and thereby enhance the O-atom number densities relative to the molecular discharge products. We also plan some experiments in which atomic oxygen is made by titrating excess N in the upstream part of the injector with NO. This latter approach produced O free from other reactive species if recombination in the injector is avoided. It cannot produce such large number densities of atomic oxygen as the other two techniques, however, thus making decay measurements more tenuous.

Our preliminary measurements indicate a rate coefficient for Reaction (2) which is marginally smaller than previous laboratory measurements, but further, more precise data are required before a definitive conclusion can be reached.

In addition to the kinetic measurements, we have implemented a spectral-fitting code,[24] which allows us to determine relative vibrational populations of electronically excited emitting species by making a least-squares fit between the

24. Lewis, P., and Green, B. D. (1984) Computation of Electronic Spectra of Diatomic Molecules, Physical Sciences Inc., PSI TR-413.
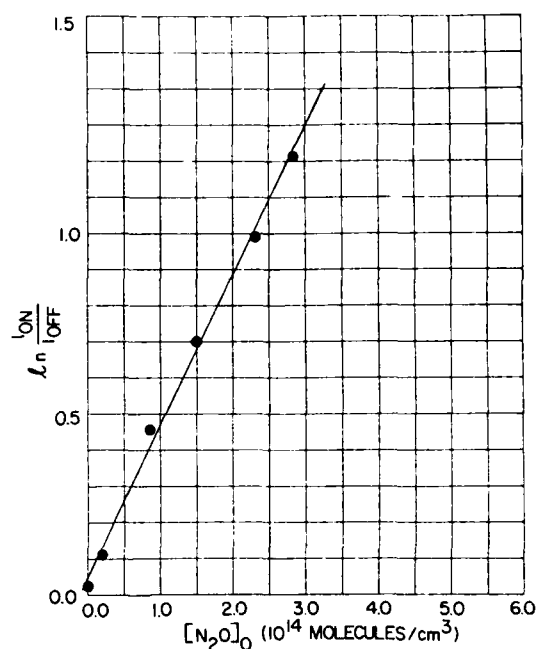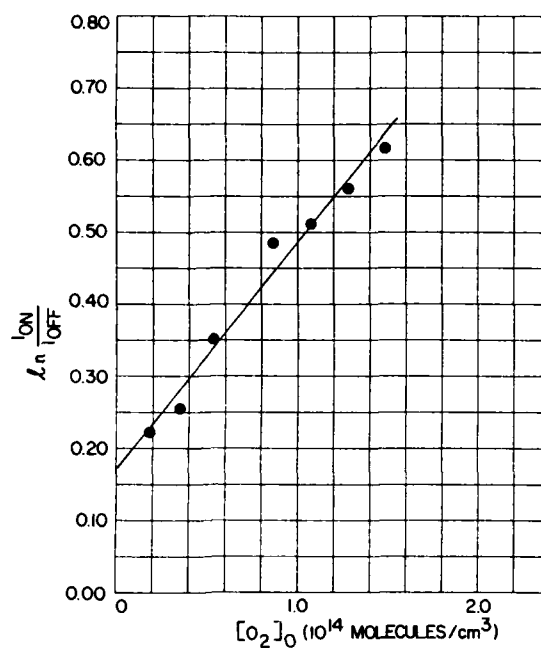
Figure 13. Variation in the Log of the Ratio of $N(^2D)$ Resonance Fluorescence Intensity in the Presence of Microwave Discharged N_2O to that in the Presence of Undischarged N_2O

data and a computed synthetic spectrum. This code, which was developed for use on other contracts, is a modified version of a code originally developed by NASA/Ames personnel (Cosmic Program #ARC-10221), and was adapted for analysis of the electronic band systems observed in FAKIR. Figure 15 compares the spectrum of the Vegard-Kaplan bands (N_2 $A^3\Sigma_u^+ - X^1\Sigma_g^+$) with the best-fit synthetic spectrum. Clearly the fit is very good. In addition to emission from vibrational levels 0-2 of the N_2 Vegard-Kaplan systems, the spectral fitting had to include emission from the NO γ-bands (NO A $^2\Sigma^+ - X^2\Pi$, v' = 0, 1) and the OH(A 2 $^+ - X^2$) system produced in the energy transfer from $N_2(A)$ to trace impurities NO and OH in the flow, and the nitrogen second-positive bands (N_2 C $^3\Pi_u - B^3\Pi_g$, v' = 0-4) produced in $N_2(A)$ energy pooling. We will expand upon this fitting capability to map out completely the $N_2(A)$ in subsequent months. In addition, we will use this capability to investigate the nitrogen first-positive (N_2 $B^3\Pi_g - X$ $^3\Pi_u^+$) excitation as seen far downstream from an Ar/N_2 discharge.

138

Figure 14. Variation in the Log of the Ratio
of the N(^{2}D) Resonance Fluorescence Intensity
in the Presence of Microwave Discharged O_2
to that in the Presence of Undischarged O_2 as
a Function of Initial Molecular Oxygen Number
Density

4. CONCLUSIONS

We have reported preliminary measurements on the yield of atomic oxygen
from the reaction of N(^{2}D) with CO_2 and quenching rate coefficients of N(^{2}D) by a
number of species including atomic oxygen. Our results indicate a large number
density of energetic species in addition to N(^{2}D), which also produce atomic oxy-
gen when they interact with CO_2. These species appear to be quenched more effi-
ciently by carbon monoxide than is N(^{2}D).

Our quenching measurements are comparable to other measurements in the
literature, although our rate coefficient for quenching N(^{2}D) by atomic oxygen is
about half that previously reported. Definitive measurements of these processes
are now in progress.
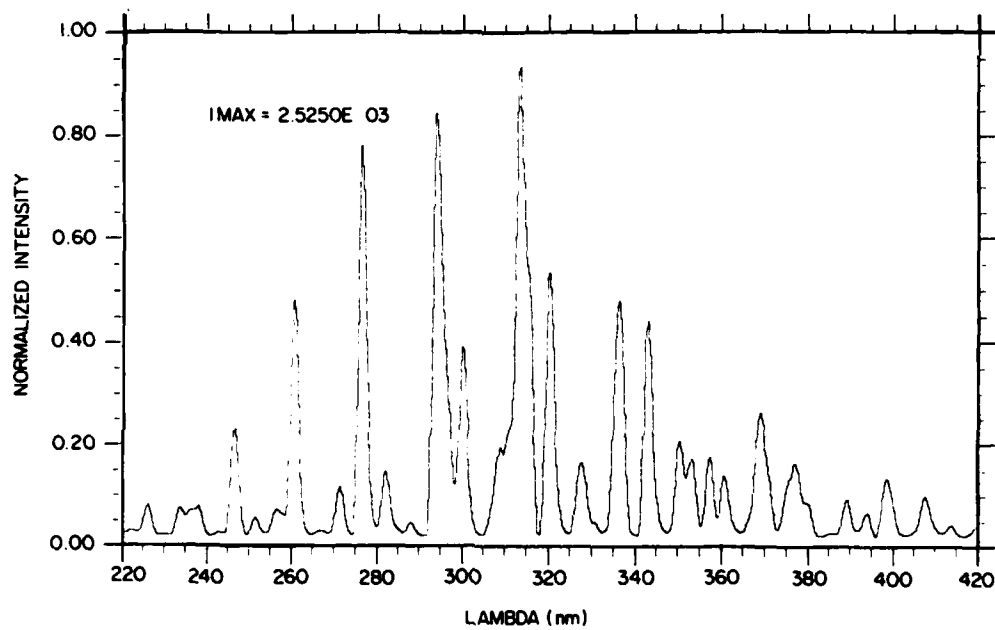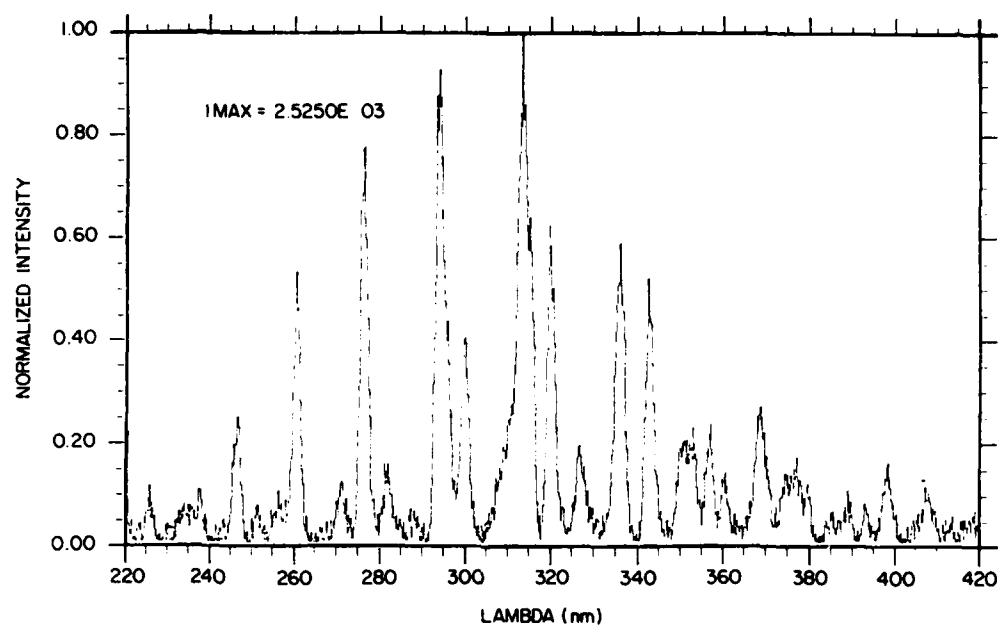
Figure 15. Experimental (Top) and Computed (Bottom) Spectrum of the Vegard-Kaplan Bands

140

References

1. Iannuzzi, M. P., and Kaufman, F. (1980) Rates of some reactions of $N(^2D$ and $^2P)$ near 300 K, J. Chem. Phys. 73:4701.

2. Kennealy, J. P., DelGreco, F. P., Caledonia, G. E., and Green, B. D. (1978) Nitric oxide chemi-excitation occurring in the reaction between meta-stable nitrogen atoms and oxygen molecules, J. Chem. Phys. 69:1574.

3. Caledonia, G. E., and Kennealy, J. P. (1982) NO infrared radiation in the upper atmosphere, Planet Space Sci. 30:1043.

4. Davenport, J. E., Slanger, T. G., and Black, G. (1976) The quenching of $N(^2D)$ by $O(^3P)$, J. Geophys. Res. 81:12.

5. Rawlins, W. T., and Piper, L. G. (1981) Effects of excitation mechanism on linewidth parameters of conventional vacuum ultraviolet (VUV) discharge line sources, Proc. Soc. Photo.-Opt. Instrum. Eng. 279:58.

6. Piper, L. G., Caledonia, G. E., and Kennealy, J. P. (1981) Rate constants for deactivation of $N_2(A)v' = 0$, by O_2, J. Chem. Phys. 74:2888.

7. Piper, L. G., Caledonia, G. E., and Kennealy, J. P. (1981) Rate constants for deactivation of $N_2(A\ ^3\Sigma_u^+, v' = 0, 1)$ by O, J. Chem. Phys. 75:2847.

8. Piper, L. G. (1982) The excitation of $O(^1S)$ in the reaction between $N_2(A\ ^3\Sigma_u^+)$ and $O(^3P)$, J. Chem. Phys. 77:2373.

9. Piper, L. G., Clyne, Michael A. A., and Monkhouse, P. (1982) Electronic energy transfer between metastable argon atoms and ground-state oxygen atoms, J. Chem. Soc., Faraday Trans. 278:1373.

10. Berg, H. C., and Kleppner, D. (1962) Storage technique for atomic hydrogen, Rev. Sci. Instr. 33:248.

11. Fehsenfeld, F. C., Evenson, K. M., and Broida, H. A. (1965) Microwave discharge cavities operating at 2450 MHz, Rev. Sci. Instr. 36:294.

12. Lin, C., and Kaufman, F. (1971) Reactions of metastable nitrogen atoms, J. Chem. Phys. 55.

13. McCarroll, B. (1970) An improved microwave discharge cavity for 2450 MHz, Rev. Sci. Instr. 41:279.

14. Husain, D., Mitra, S. K., and Young, A. N. (1974) Kinetic study of electronically excited nitrogen atoms, $N(2^2D_J, 2^2P_J)$, by attenuation of atomic resonance radiation in the vacuum ultra-violet, J. Chem. Soc., Faraday II 70:1721.

15. Piper, L. G., Rawlins, W. T., and Armstrong, R. A. (1983) O-Atom Yields from Microwave Discharges in N_2O/Ar Mixtures, AFGL-TR-83-0031, AD A130429.

16. Kaufman, F. (1958) The air afterglow and its use in the study of some reactions of atomic oxygen, Proc. Roy. Soc. (London) A 247:123.

17. Kaufman, F. (1973) The air afterglow revisited, Chemiluminescence and Bioluminescence, M. J. Cormier, D. M. Hercules, and J. Lee, Eds., pp. 83-100.

18. Rawlins, W. T., and Kaufman, F. (1976) The reaction of CO_2 with active nitrogen, J. Chem. Phys. 64:1128.

19. Kaufman, F. (1961) Reactions of oxygen atoms, Prog. React. Kinet. I:1.

20. Meyer, J. A., Setser, D. W., and Stedman, D. H. (1970) Energy transfer reactions of $N_2(A\,^3\Sigma_u^+)$. II. quenching and emission by oxygen and nitrogen atoms, J. Phys. Chem. 74:2238.

21. Black, G., Slanger, T. G., St. John, G. A., and Young, R. A. (1969) Vacuum-UV photolysis of N_2O, 4, deactivation of $N(^2D)$, J. Chem. Phys. 51:116.

22. Fell, B., Rivas, I. V., and McFadden, D. L. (1981) Kinetic study of electronically metastable nitrogen atoms, $N(2\,^2D_J)$, by electron spin resonance absorption, J. Phys. Chem. 85:224.

23. Slanger, T. G., Wood, B. J., and Black, G. (1971) Temperature coefficients for $N(^2D)$ quenching by O_2 and N_2O, J. Geophys. Res. 76:8430.

24. Lewis, P., and Green, B. D. (1984) Computation of Electronic Spectra of Diatomic Molecules, Physical Sciences Inc., PSI TR-413.

6. LINUS Studies

Contents

6.1 LINUS: Visible Experiments

by

P. Nebolsine
G. Weyl
B. D. Green

1. INTRODUCTION

Physical Sciences Inc. is supporting the LINUS (Laser Initiated Nuclear Sim-
ulation) experiments being performed at AFGL. The LINUS experiments measure
the radiative properties of a plasma created by a Q-switched Nd^{3+}-YAG laser.
Broadband emission, spectral features, and temporal history have been measured.
The emphasis of the PSI effort has been in applying existing models to a laser-pro-
duced plasma to further understand the phenomena. The efforts have included
spectroscopy studies, an experiment definition task to measure the radial temper-
ature profile, and hydrodynamics to model the temperature-density field. Since
PSI was involved in the initial scoping LINUS experiments, we have included an
assessment of those results in an effort to more fully understand them.

Figure 1 shows the generic experimental arrangement. A Q-switched Quanta Ray Nd^{3+}-YAG laser is used in an unstable resonator configuration. The output beam is an annulus of 1.06 μm radiation with a pulse duration of approximately 10 nsec and a full beam divergence of 0.5 mrad. After numerous beam directing optical elements, the laser beam is focused by a lens (focal length ~ 6 cm) into a test cell. The test cell is vacuum tight and can be filled with the desired gas to the desired pressure. Most experiments have been performed from 3 to 125 Torr. The test cell has windows perpendicular to the laser beam to allow for observation and also a rear window that is used to monitor the transmitted laser energy. No detectable absorption of the laser energy is observed at the low pressures even though a breakdown exists.
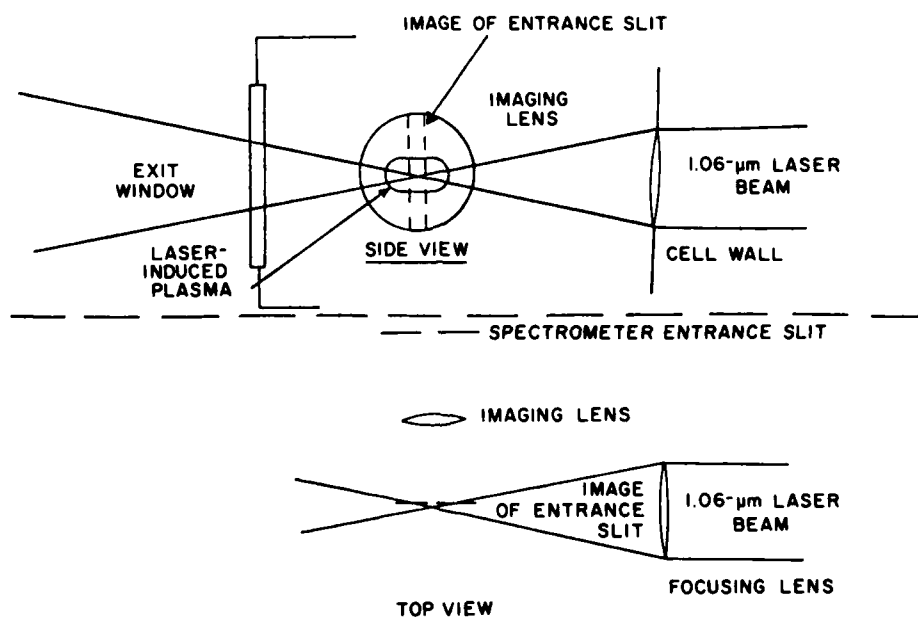
Figure 1. Schematic of Experiment

A spectrometer has been the principal diagnostic instrument. It has been used in zero order for broadband measurements and in first order for spectroscopic measurements. A Spex spectrometer (0.5 m focal length, f/8.6) was used with a CaF_2 collecting lens providing a nominal 1:1 magnification. The entrance slit is narrow compared to the spark length and the entrance slit height is comparable to the spark diameter.

Section 2 of this chapter is devoted to an examination of the data collected by Roy Lucht in 1981.[1] Section 3 discusses experiments that can be performed to obtain more information to characterize the spark. Section 4 is devoted to blast wave analysis of a laser-produced spark and Section 5 is a short data analysis of data taken by John Swanton measuring broadband optical emission from the spark.[2]

2. REVIEW AND ANALYSIS OF SCOPING EXPERIMENTS

Roy Lucht obtained data using the apparatus outlined in the introduction. Breakdown thresholds as a function of pressure were measured for N_2, Ar, and O_2; Figure 2 is the compilation of the data.[1] Both breakdown data and spectra were taken for these gases. The monochromator was operated with a 35 μm wide
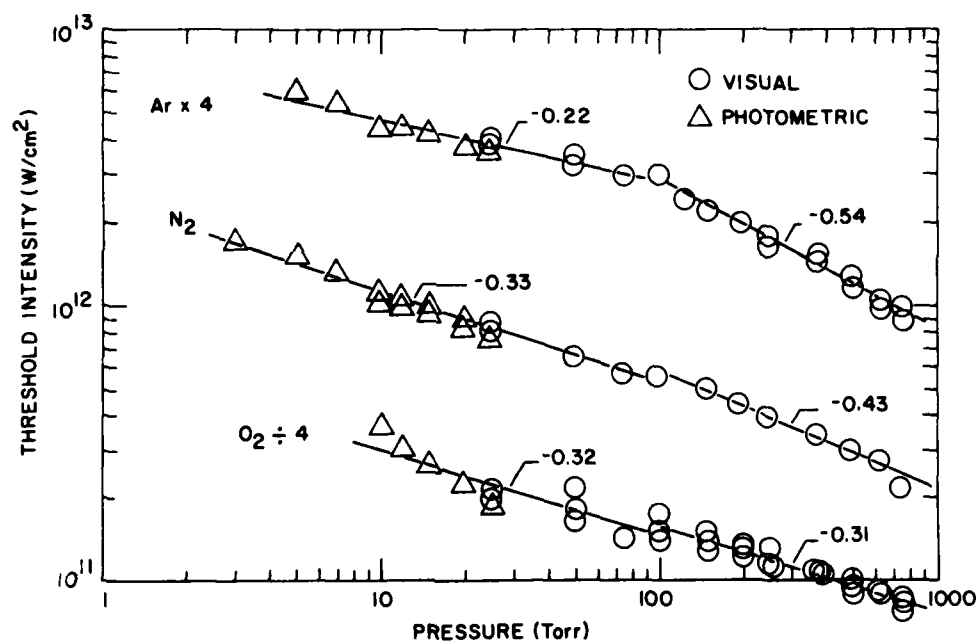
Figure 2. Apparent Breakdown Thresholds for Ar, N_2, and O_2. Pressure exponents obtained from least squares fits (solid lines) for $p \geq 100$ Torr and $p \lesssim 100$ Torr are indicated

1. Lucht, R., Unpublished.
2. Swanton, J., Unpublished.

entrance slit, which is small compared to luminous length of the plasma. A box-car integrator was used for the spectral measurements. The time gate was adjusted to be 200 nsec and most of the emitted light within the field-of-view was collected. Line spectra were observed and radiating species were identified. At 125 Torr, pressure continuum radiation was observed in addition to the line radiation. Other data were taken by fixing the wavelength of the monochromator and shifting a 5 nsec gate from the initiation of the laser pulse. Figure 3 is a typical trace for spectral lines of N^+, N^{++}, and N^{+++}. The peak emission appears to to occur substantially after the laser pulse is off. Since the boxcar does not give an origin of time, the precise sequencing of the emission of one line to another and to the laser pulse is unknown. The temporal sequence of the peaks in the radiation of N^{+++}, N^{++}, and N^+ is compatible with cooling of the plasma with time. Because the field-of-view of the monochromator is small compared to the spark dimension, the time profile may not be accurate for the entire N^{+++}, N^{++}, and N^+ radiation from the spark. The decay times from observed lines are on the order of 1 to 20 times the lifetime of a specific transition.
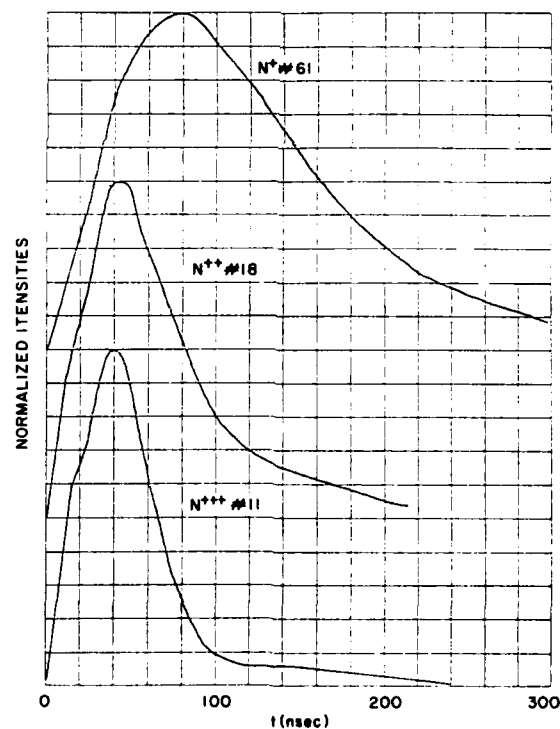

Figure 3. Line Profiles Using 10 Torr N_2 and 2.9×10^{12} W/cm^2

148

Using this apparatus, color temperature measurements were made using at least six lines from a radiating species. Color temperatures of 18,000 to 28,000 K were observed using a time gate of 200 nsec. Because the temperature predicted by blast wave theory varies strongly within the spark, the color temperature can only be used as a gross indication of the plasma conditions.

The techniques and data will now be examined. This discussion should be considered to be instructive in designing better experiments rather than criticizing the scoping experiments that were performed.

Much of the breakdown data in the literature is qualitative because it is difficult to quantitatively measure breakdown. In a colloquial sense, it is one of those "you know" events. At high pressure (for example, 1 atm) there is no question whether or not there is breakdown because the transition is so abrupt from no visible plasma to a highly ionized absorbing plasma. Potential definitions of breakdown include:

    (1) visible flash
        (a) detection by eye
        (b) detection by a photo-detector
    (2) specific amount of radiation
        (a) independent of pressure
        (b) normalized by pressure
    (3) specific percentage of ionization.

Eye observation of a breakdown is the definition used by a number of investigators. A measurement of the degree of ionization is the preferred definition of breakdown. Unfortunately such a measurement is not trivial, hence radiation is typically used as a measure of breakdown. A broadband measurement of radiation normalized to the ambient density can provide a reasonable definition for experiments. This definition approximately specifies an equal amount of ionization to determine a breakdown threshold.

To take high quality breakdown data, the only parameters that should be varied are the laser beam irradiance and gas pressure. Also the repetition rate of the laser (in our case 10 Hz) should be low enough that residual ionization from previous pulses is not a factor in determining the breakdown threshold. (This should be carefully checked for each gas.) The purity of the gas is also an issue. Particulates and trace impurities can lower the breakdown threshold.

Roy Lucht acquired scoping data by varying the flash-lamp pump energy to vary the laser output energy. This process of controlling the laser output energy also varied the laser's near field irradiance. This could have also varied the fluence distribution (peak fluence and/or irradiance) at focus. Operating the laser at fixed output conditions and using a variable attenuator to vary the irradiance in the focal plane is the preferred technique. The irradiance distribution in the focal

149

plane can be determined by using a long focal length lens to obtain spatial extent of reasonable size. (If no lens is used, the laser beam would have to propagate 200 m to have the observation plane be in the far field.) Using a lens with a focal length of 30 m is probably a reasonable compromise between distance, fluence, and spatial extent.

The irradiance fluence distribution can be determined by scanning a detector in the focal plane. An unaberrated unstable resonator beam in the far field looks similar to the Airy pattern. However, the dark rings are not quite in the same location and less energy is within the first dark ring than for a uniformly illuminated aperture. Such measurements of the laser beam parameters will allow both a peak and average laser beam fluence to be calculated. The deduced fluence distribution can be scaled for the lens used in the experiment as long as aberrations are not important. Spherical aberration will limit the fluence level as the focal length of the focusing lens is reduced. The minimum focal length without significant spherical aberration and the use of multiple lenses or an aspheric lens so that data at higher irradiances can be taken will be discussed in the next section.

The data shown in Figure 2 show a weak dependence on pressure. Some of this dependence may be due to the changing beam divergence with output power. The use of an attenuator to change the laser beam irradiance in the cell, without changing the spot size, will provide a capability to take well characterized breakdown data.

3. SUGGESTED EXPERIMENTS

Experiments to characterize the laser breakdown process include:

3.1 Breakdown Data

Higher quality breakdown data can be taken by using a more accurately characterized laser beam and a quantitative definition for breakdown. The technique to scan fluence distribution in the focal plane of a long focal length lens was discussed in Section 2. The temporal pulse shape of the laser pulse needs to be measured. The addition of the line narrowing feature in the laser will prevent spontaneous mode-locking. (Spontaneous mode-locking will generate high intensity fluctuations of the laser pulse that make data interpretation more difficult.) Shorter focal length lenses than used to date will allow higher laser beam irradiances at the focus, permitting breakdown below 1 Torr to be studied.

Figure 4 shows the breakdown data for N_2 obtained by Roy Lucht and also the maximum irradiances that can be obtained using one, two, and three lenses. The irradiance limit was calculated knowing the laser energy and spot size, and
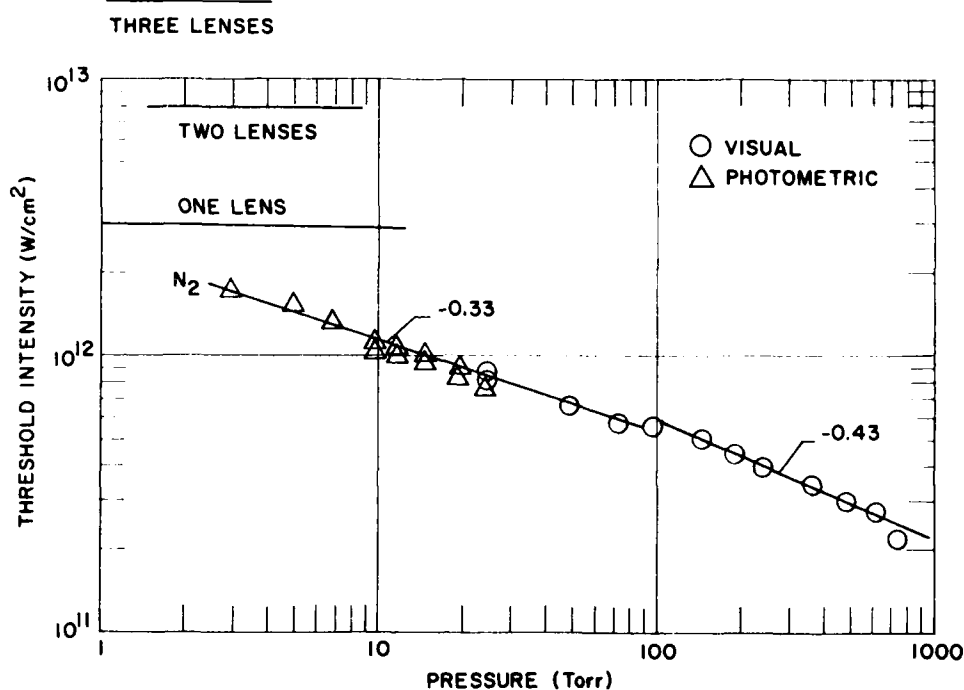
150

THREE LENSES

Figure 4. Breakdown Threshold for N_2 and Maximum Intensities for 1, 2, and 3 Lenses

choosing a focal length so that the aberrated spot size would be two-thirds the beam divergence spot size. Breakdowns for pressures below 1 Torr can be studied with shorter than 6 cm focal length lenses. The practical alternative to multiple lenses to reduce spherical aberration is to use an aspheric lens. Aspheric lenses are commercially available with short focal lengths and low f/numbers.

The use of attenuators to vary only the peak irradiance but not the irradiance distribution is advocated. Care must be taken to utilize a nonaberrating attenuator. Fresnel reflections are an established technique to vary the energy in a laser beam without affecting the distribution of energy.[3]

3. Nichols, D. B., and Hall, R. B. (1980) Laser-beam attenuation for spatial profiling of small focal spot, Rev. Sci. Instr. 51:1131.

3.2 Optical Characterization of the Spark

3.2.1 NO SPECTRAL RESOLUTION OR SPATIAL RESOLUTION

A pyroelectric detector can be used to measure the total optical radiation from the plasma. Pyroelectric detectors are rather insensitive ($\sim 10^{-6}$ A/W responsivity) but do have very broad wavelength coverage from the VUV to LWIR. This measurement would provide a lower bound on the energy deposited in the gas by the YAG laser beam. Care must be taken not to have this measurement corrupted by scattered 1.06-μm light from the laser or flash lamp. With baffling of the detector and a proper background it should be straightforward to obtain good measurements. Given the detector's responsivity and the anticipated signal strengths, probably only a measurement of radiant energy in units of J/sr is possible.

The ratio of radiated energy to laser energy is a measure of the efficiency of depositing laser energy. A discussion of the relationship of radiated energy in a finite bandpass to laser energy as a function of gas pressure is presented in Section 5.

Finite bandwidth detectors such as photomultiplier tubes and other high quantum efficiency detectors can be used to measure the temporal emission of the spark.

3.2.2 SPECTRAL RESOLUTION/NO SPATIAL RESOLUTION

The measurement would be of $P_\lambda(t)$ in units of W/sr-μm, that is, radiant power per steradian per unit bandwidth. To perform this measurement, the total spark needs to be imaged into the entrance slit. Using 10 μm as a nominal entrance slit width, an image reduction of 200:1 is appropriate to collect all the visible light. With such an image reduction the f/number of the collecting optics will be very high (~ 2000) when matching the f/8.6 optics of the spectrometer.

Measurements can be either time-resolved or time-integrated to provide spectral information. Measuring as a function of pressure will provide data for pressure-dependent effects. Roy Lucht's data gave an indication that first and second maxima existed for these laser sparks. Because the field-of-view was limited (~ 35 μm compared to the spark length of ~ 500 μm), only a rough comparison to phenomena pertinent to the whole spark can be made. Changing the field-of-view to include the whole spark will allow observations for first and second maximum.

The measurements will provide data for the time evolution of the radiation from specific species. Figure 3 is an example of past work with a limited field-of-view. Similar measurements should be performed when observing the whole spark. It is expected that the radiation from the most highly ionized species would

152

decay sooner than the singly ionized or neutral atoms because of the cooling of the spark.

Even though the temperature is not expected to be uniform within the spark, a color temperature could be computed by measuring the ratio of intensities from different radiating lines of a specific species. The plasma is optically thin (see Section 3.2.4.3) so that radiation will be observed from all the radiating species.

These measurements will provide additional information on the optical radiation loss mechanism of the spark. For example, continuum radiation as well as line radiation was observed at 125 Torr. The measurements will allow the computation of the amount of energy lost from the spark from specific lines and also continuum emission.

3.2.3 SPATIAL RESOLUTION/NO SPECTRAL RESOLUTION

The laser energy is deposited in the spark in a volume determined by the outline of the laser beam. The absorbed laser energy raises the pressure of the ambient gas and the gas expands. Blast wave theory can be applied to estimate the energy deposition, rate of expansion and shock temperatures, and cooling rates. Blast wave theory gives a power law dependence for the shock front position vs time. The shock front can be measured by the presence of the luminous front for strong shocks and Schlieren photography for weaker shocks. Section 4 will be devoted to a discussion of blast wave physics and its application to this problem.

3.2.4 SPECTRAL AND SPATIAL RESOLUTION

Spatial resolution of the measurements would be fine compared to any dimension of the spark. These measurements would provide radiometric information in units of W/cm^2 sr μm for time-resolved measurements or J/cm^2 sr μm for time-integrated measurements. If the spark is optically thin, then an Abel inversion can be used to obtain local values. For example, the local radiant emission in units of W/cm^3 sr μm would be obtained. This data can be analyzed assuming local thermodynamic equilibrium to deduce a temperature of an emitting species. These results can provide information on the thermal profile within the spark. Blast wave theory for a spherical expansion (see Section 4) predicts a very strong radial dependence, that is,

$$T(r) \sim T_o \left(\frac{r_o}{r} \right)^{3/\gamma - 1} \qquad r < r_o \qquad , \qquad (1)$$

where T_o is the temperature at shock location r_o and r is the radius within r_o. We note that the central core of the spark will be much hotter than the outside region. Once the gas is shock heated, it expands isentropically, dropping its temperature and pressure. Two types of gas will exist: (1) gas directly heated by the laser

pulse, and (2) gas shock-heated by the laser-heated gas. The spatial and temporally resolved measurements will be able to resolve the properties of these two differently heated gases. We will now discuss the measurement to deduce a local temperature.

We wish to calculate line emission from a hot $(15,000 < T < 30,000$ K) plasma and find the optimum spectral bandwidth for temperature measurements using line radiation from the plasma.

3.2.4.1 Line Intensities

Consider a small volume element containing N_u atoms in some excited (u) state, that are radiating to some lower (l) state. The power emitted per unit time in 4π sr is

$$P = N_u h \nu A_{ul} \qquad , \qquad (2)$$

where A_{ul} is the Einstein A coefficient $(\sec^{-1})$ for the transition and is tabulated in Reference 4. The power radiated per unit volume is given by

$$\rho = \frac{ph\nu}{kT} \frac{c_\alpha g_u e^{-\varepsilon_u/kT}}{Z_\alpha} A_{ul} \qquad (3)$$

where p = pressure, C_α = concentration of species α, Z_α = partition function of species α(N, N^+, N^{++}, etc.), and g_u = degeneracy of upper state. We show in Figures 5 and 6 the molar concentrations of N_2, N, N^+, and N^{++} as a function of temperature for pressures P = 10 and 1000 Torr. These were obtained by solving (on a hand calculator) the simultaneous Saha equation for N_2, N^+, N^{++}, and N. These concentrations were defined such that $2C_{N2} + C_N^+ + C_N^{++} = 1$. To account for the dilution due to the electron concentration, we must divide the concentration of Figures 5 and 6 by $(1 + C_N^+ + 2C_N^{++})$.

The partition functions of interest are given in Table 1.

Table 1. Partition Functions $Z\alpha$

SPECIES	N	N^+	N^{++}
T = 300 K	4		6
T = 30,000 K	10	11.35	6.8

---

4. Wiese, W., Smith, M., and Glennon, B. (1966) Atomic Transition Probabilities, Vol. 1, National Bureau of Standards, NSROS-NBS4.
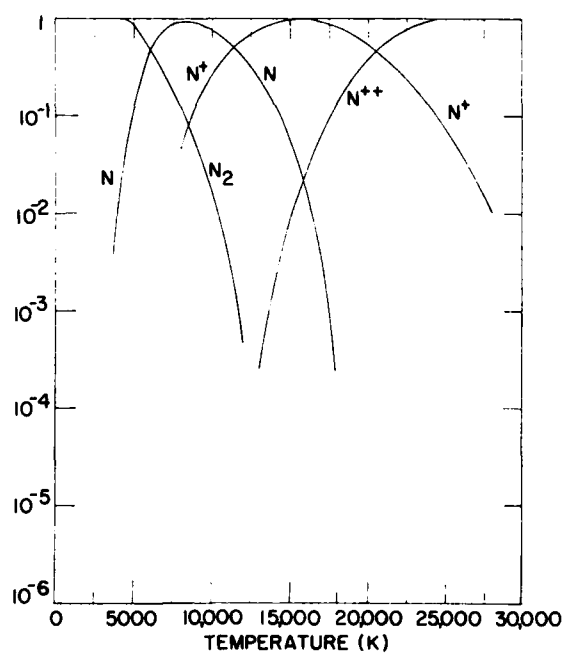
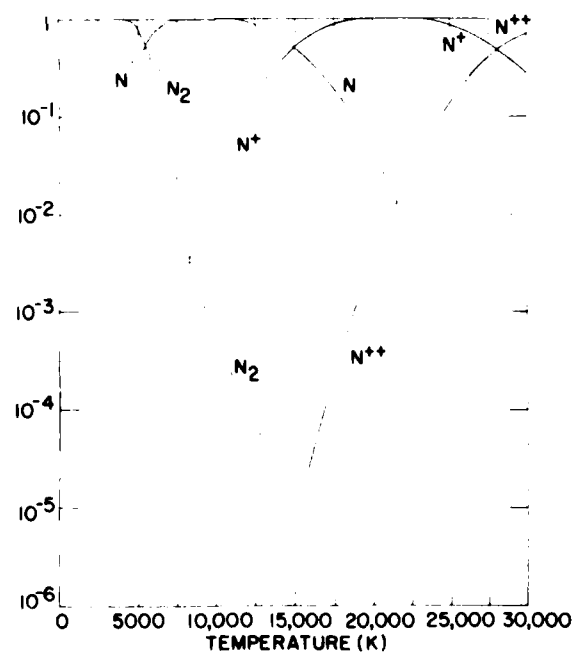Figure 5. Concentration of Nitrogen Species
at 10 Torr

Figure 6. Concentration of Nitrogen Species
at 1000 Torr

155

The only species whose partition function variation with temperature has to be considered is N. However, the concentration of nitrogen atoms above 15,000 K is negligible, and we will not be concerned with nitrogen lines.

We now calculate the radiation from a line plasma that enters the slit of the spectrometer, with the optical system shown in Figure 7. The magnification at the slit is $f_2/f_1 = (10/25)$ and the solid angle subtended by the line plasma is $\Delta\Omega = (\pi d^2/4\ell_1^2)$ where d = diameter of lens and ℓ_1 = distance from lens to the plasma. f_1 and f_2 are the f numbers associated with the collection lens shown in Figure 7. The amount of radiation entering the slit during the measurement time Δt is given by

$$E = (P\Delta t)(A'\ell\,\Delta\,\Omega) \qquad , \qquad (4)$$

where P is given by Eq. (3) and $A'\ell$ is the volume of the radiating element imaged onto the slit. We are interested in determining the energy incident on individual detectors in the detector array of the optical multi-channel analyzer (OMA). This array is two dimensional, one dimension giving the spectral resolution; the other dimension, perpendicular to the image of the slit in the plane of the detector array, gives spatial resolution at each wavelength. We also assume that the magnification of the spectrometer is unity. In this case the effective area of the slit imaged onto the detector is $(f_2/f_1)^2 A' = \delta h$, where δ = slit width and h = detector dimension parallel to slit. If the radius of the plasma that is radiating is r, we have, for the central rays (those passing through the axis of the plasma)
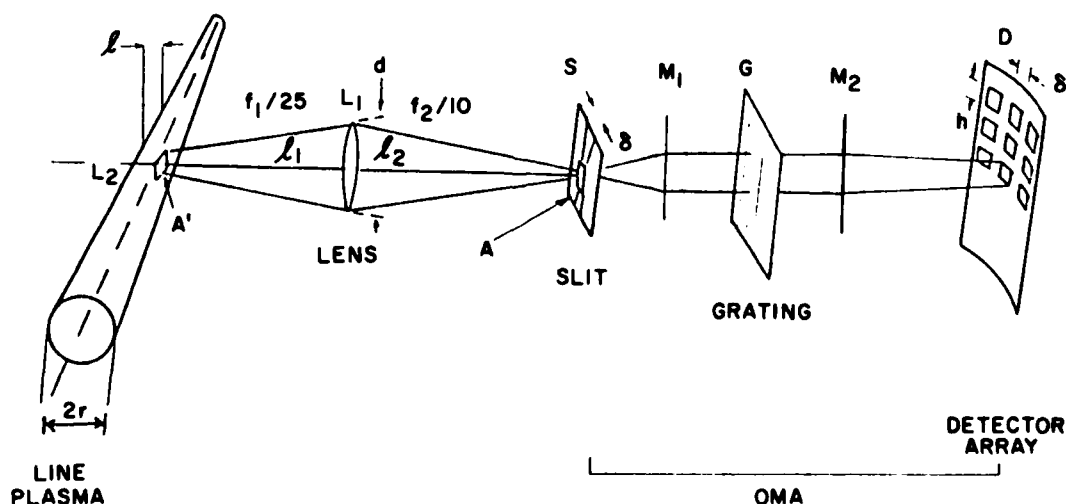

Figure 7. Schematic of Optical System and OMA

156

$$A'\ell = (\delta h) \times (f_1/f_2)^2 \times 2r = 2rh\delta(f_1/f_2)^2 \quad . \tag{5}$$

The number of photon counts on the detector is given by

$$N = \frac{E}{h\nu} = \frac{\pi}{2} \frac{\delta h}{f_1^2} r \frac{p}{kT} \frac{C_\alpha e^{-\varepsilon_u/kT} g_u}{Z_\alpha} \Delta t A_{u\ell} \quad . \tag{6}$$

We will now present results under the specific conditions $\delta = h = 25~\mu m$, $T = 25,000$ K, $f_1 = 25$

$$N = 3 \times 10^5 \frac{C_\alpha e^{-\varepsilon_u/kT}}{Z_\alpha} A_{u\ell} \Delta t p(\text{Torr}) \quad .$$

We will be concerned with measurement times Δt of the order of 50 nsec and pressure $p \approx 10$ Torr. Typical values of $A_{u\ell}$ for visible transition are $\sim 10^8/\text{sec}$ so that we will have $N \cong (3 \times 10^5) \times (10^8 \times 50 \times 10^{-9}) \times 10 \times X_{\alpha u} \cong 10^7 X_{\alpha u}$, where $X_{\alpha u} > 10^{-7}$ in order that more than one photon be incident on the (central) detector in one measurement interval.

We show in Table 2 calculations for specific lines of N^+ and N^{++} that are the most intense in the band 3000-7000 $\overset{\circ}{A}$. We consider the two temperatures $T = 17,000$ K and $T = 30,000$ K.

Table 2. Transition Parameters for N^+ and N^{++}

	Transition $\overset{\circ}{A}$	ε_u (cm^{-1})	g_u	$A_{u\ell}$ (10^8/sec)	T = 17,000 K		T = 30,000 K	
					$X_{\alpha u}$	N	$X_{\alpha u}$	N
N^+	4040.9	211332	27	2.64	2^{-8}	0.8	1.6^{-7}	6.3
	4239.4	211053	21	2.04	1.5^{-8}	0.5	1.3^{-7}	4.1
	4630.54	170667	5	0.84	1.7^{-7}	2.2	2^{-7}	2.6
	5001.4	186572	7	1.08	2.5^{-8}	0.4	1^{-7}	1.6
	5005.14	186653	9	1.22	3^{-8}	0.5	1.3^{-7}	2.4
	5179.5	223787	11	1.02	5.5^{-10}	0.008	1.1^{-8}	0.17
	5679.56	166579	7	0.56	2.2^{-7}	2	3.4^{-7}	2.9
N^{++}	4097.3	245102	4	0.96	x	x	1.6^{-6}	2.3
	4514.9	304857	8	0.8	x	x	1.5^{-7}	2.12

From Table 2 we see that the temperature can be measured using lines of N^+ over the temperature range 17,000-30,000 K, but one has to span the spectral range 4239 to 5001 Å. There are three energy levels that can be used for N^+: 211,000, 186,000, and 166,000 cm^{-1}. Temperature measurements using the two lines of N^{++} at 4097 and 4515 Å can be used only for the highest temperatures.

3.2.4.2 Line Widths

A line width is determined by the dominant of the three broadening mechanisms: (1) lifetime of upper state; (2) Doppler broadening; and (3) collision or Stark broadening. Due to the high temperature and electron densities of the present study, mechanisms 2 and 3 dominate. Stark broadening parameters can be found in Table 4-5 of the book by Griem.[5] The line width $\Delta\lambda$ (in Å) is, following Griem, given by (n_e: electron concentration in cm^{-3}).

$$\Delta\lambda = W(T) \left(\frac{n_e}{10^{16}}\right) \qquad (7)$$

As a typical example, consider the line at 4630 Å, for which, at 10,000 K where the nitrogen is dissociated and partially ionized, $W = 6.4 \times 10^{-3}$. We calculate an electron density at T = 20,000 K, where the nitrogen is singly ionized, p = 10 Torr of 2.8×10^{15} cm^{-3}, so that $\Delta\lambda$ (λ = 4630 Å) = 2×10^{-3} Å.

Consider now Doppler broadening at the same temperature

$$\frac{\Delta\lambda}{\lambda} = \frac{\Delta\nu}{\nu} = \frac{U_{th}}{c} = \frac{4.5 \times 10^5}{3 \times 10^{10}} = 1.5 \times 10^{-5} \quad \text{or} \quad \frac{\Delta\nu}{\nu} = 3.6 \times 10^{-7} \frac{T}{M} \quad ,$$

where U_{th} is the thermal velocity. This gives a line width, for the same line, $\Delta\lambda = 7 \times 10^{-2}$ Å. Since each detector is expected to span approximately a few tenths of an angstrom, we would expect no line overlaps to occur between detectors due to the finite line widths. The 0.5 m Spex monochromator with a 1200 line/mm grating has a dispersion of 0.4 Å/picture element. An entrance slit of 10 μm will give 0.6 resolution and the line width will not be resolved.

3.2.4.3 Optical Density of Plasma

The formulas that we have used neglected stimulated emission and are strictly valid only for a plasma that is quite optically thin. Knowing the line widths, we can easily calculate the optical density of the plasma by comparing $2r\rho(\lambda)$ with the black body expression for the power. The black body intensity is given by

---

Griem, H. (1964) <u>Plasma Spectroscopy</u>, McGraw Hill, New York.

$$I = \frac{2h\nu^3}{c^2} \frac{1}{(e^{h\nu/kT} - 1)} \qquad . \tag{8}$$

The intensity at the center of a given line is given by:

$$\frac{2r\rho}{\Delta\nu} \approx \frac{2rph\nu}{kT} \frac{C_\alpha g_u e^{-\varepsilon_u/lT}}{Z_\alpha \Delta\nu} A_{ue} \qquad . \tag{9}$$

For the line at 4630.5 $\overset{\circ}{A}$ and T = 17,000 K, we find that $(2rP/I\Delta\nu) = 3 \times 10^{-4}$, that is, the plasma is quite optically thin, even at the line center. The emission will be optically thin for all lines of the observed species.

4. BLAST WAVE THEORY

The N^{+++}-YAG/laser pulse deposits energy in the gas during the laser pulse duration of approximately 10 nsec. The gas expands due to the pressure rise and entrains gas as it expands. When the laser induced shock wave is strong, then blast wave theory is applicable. In its usual form, blast wave theory does not have any loss mechanisms, assumes a constant ratio of specific heats (γ), thermal equilibrium and continuum fluid mechanics.

Blast wave theory was originally developed for instantaneous release of energy and then was extended to a power-law time-dependence of energy release.[6] In all cases the energy is released into zero mass at a point, in a line, or in a plane. Hence, the temperature goes to infinity at the origin.

The general formulas for the shock radius as a function of time for both an instantaneous deposition of energy and power law deposition are:[6]

$$r_s = Kt^n \qquad , \tag{10}$$

where

$$n = \frac{2+\beta}{3+\alpha} \quad \text{and} \quad K = \left(\frac{W_\alpha a_o^2}{p_o n^2 J_o}\right)^{1/\alpha+3} \tag{11}$$

and

6. Zel'dovich, Ya. B., and Raizer, Yu. P. (1966) Physics of Shock Waves and High Temperature Hydrodynamic Phenomena, Academic Press, New York.

159

$$E_\alpha = W_\alpha t^\beta \qquad , \qquad (12)$$

where $\beta = 0$ for instantaneous and $\beta = 1$ for constant input power and E_α = energy input/unit area ($\alpha = 0$), $= \frac{1}{2\pi}$ energy input/unit length ($\alpha = 1$), $= \frac{1}{4\pi}$ energy input ($\alpha = 2$). a_0 = ambient sound speed and p_0 is the ambient pressure.

Geometry	Dimensionality	α	J_0 ($\beta=0$)
Plane	1 Dimensional	0	1.67
Line	2 Dimensional	1	0.88
Point	3 Dimensional	2	0.60

Once the shock front position is determined, the pressure behind the shock is determined by:

$$P_s = \frac{2}{\gamma + 1} \rho_0 \left(\frac{dr}{dt} \right)^2 \qquad . \qquad (13)$$

The similarity profiles of pressure, particle velocity, density and temperature are determined by computation. Figure 8 is an example of these profiles for $\gamma = 1.23$ and instantaneous release of energy at a point.[6] The pressure drops to about one-half the shock pressure for $0 \leq r \leq 0.8 \, r_s$, the density drops nearly to zero and the temperature asymptotes to a very high temperature (ideally infinity) with $r \to 0$.

The characteristic amount of energy deposited by the laser pulse will now be computed for an f/6 laser beam. The energy will be computed by first looking at the degree of ionization from Figures 5 and 6 and the fact that a color temperature of $\sim 28,000$ K was determined by Roy Lucht.[1] We see that most of the nitrogen will be doubly ionized. To compute the energy per nitrogen molecule we add the energy to dissociate N_2 (10 eV) + twice the ionization potential [2(14 eV)] + twice the ionization potential of N^+ [2(25 eV)] + six times the heat capacity at 30,000 K [$\sim 6(2.5$ eV)] $= \frac{103 \text{ eV}}{N_2 \text{ molecule}}$. We multiply this energy/molecule by the number of molecules/cm^3 times the breakdown volume. At 10 Torr the ambient number density is 3×10^{17}/cm^3 and the volume is computed from optics.

The volume in which there is breakdown will now be estimated. Figure 9 shows the energy contours for a diffraction limited beam from a uniformly illuminated aperture. The ordinate is scaled to the distance from the focal plane [$U = \frac{\pi}{2\lambda} (D/f)^2 Z$]. The abscissa is scaled radially from the optical axis $\frac{\pi}{2} \frac{D}{f} \cdot R$). The position of the node of the Airy Disk is annotated as well as the radius for a 0.24 mrad half angle beam divergence of the Quanta Ray laser. (This
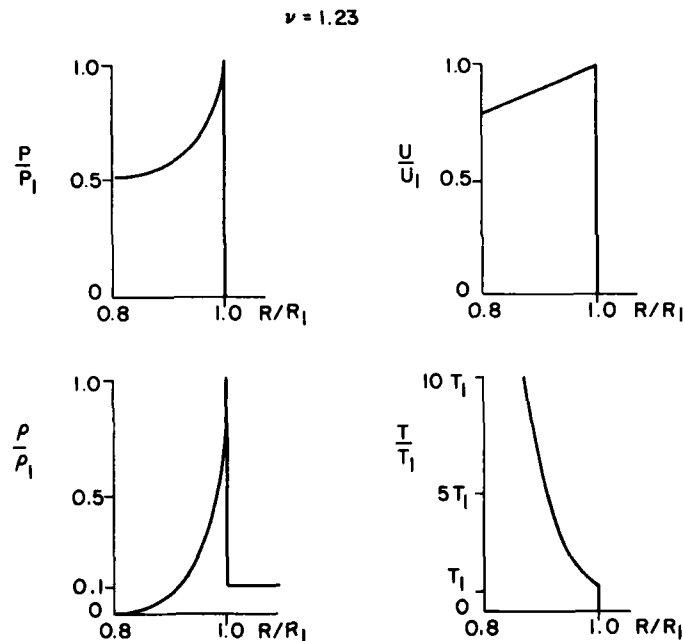
160

$\nu = 1.23$

Figure 8. Spherical Blast Wave Profiles

is the beam divergence specified by the manufacturer of the laser). The third line provided for reference is the geometrical shadow line. The minimum deposition volume is the volume bounded by the beam divergence (V = 7.8) and the intersection with the geometrical shadow (U = 7.8). However, because the beam divergence is not likely to be measured for the greatest extent of the laser beam but some nominal extent, we will use the intersection of the V = 7.8 and the 50 percent contour (U = 12.5, which is $Z \sim \pm 290$ μm). The deposition volume is thus $2 \times (290$ μm$)(\pi)(14$ $\mu)^2 = 3.5 \times 10^{-7}$ cm^3. Combining the 103 eV molecule, 3×10^{17} molecules/cm^3 and V = 3.5×10^{-7} cm^3, we obtain a deposition energy of 2×10^{-6} J. We will now provide a number of figures that plot blast wave results for this case of 2×10^{-6} J energy deposition.

4.1 3-D Expansion - Instantaneous Energy Deposition

Figure 10 is a plot of the shock radius as a function of time. The radius increases as $t^{2/5}$. This computation yields a radius of 100 μm at 10 nsec after energy deposition. This is a dimension considerably larger than the 14 μm beam radius computed from the laser beam divergence and focal length. Later in this section we will discuss the comparison to depositing the energy in 10 nsec.

Figure 11 is a plot of the shock pressure vs time, where p $\propto t^{-6/5}$. It will take over 1 μsec for the shock pressure to relax to ambient pressure.

161
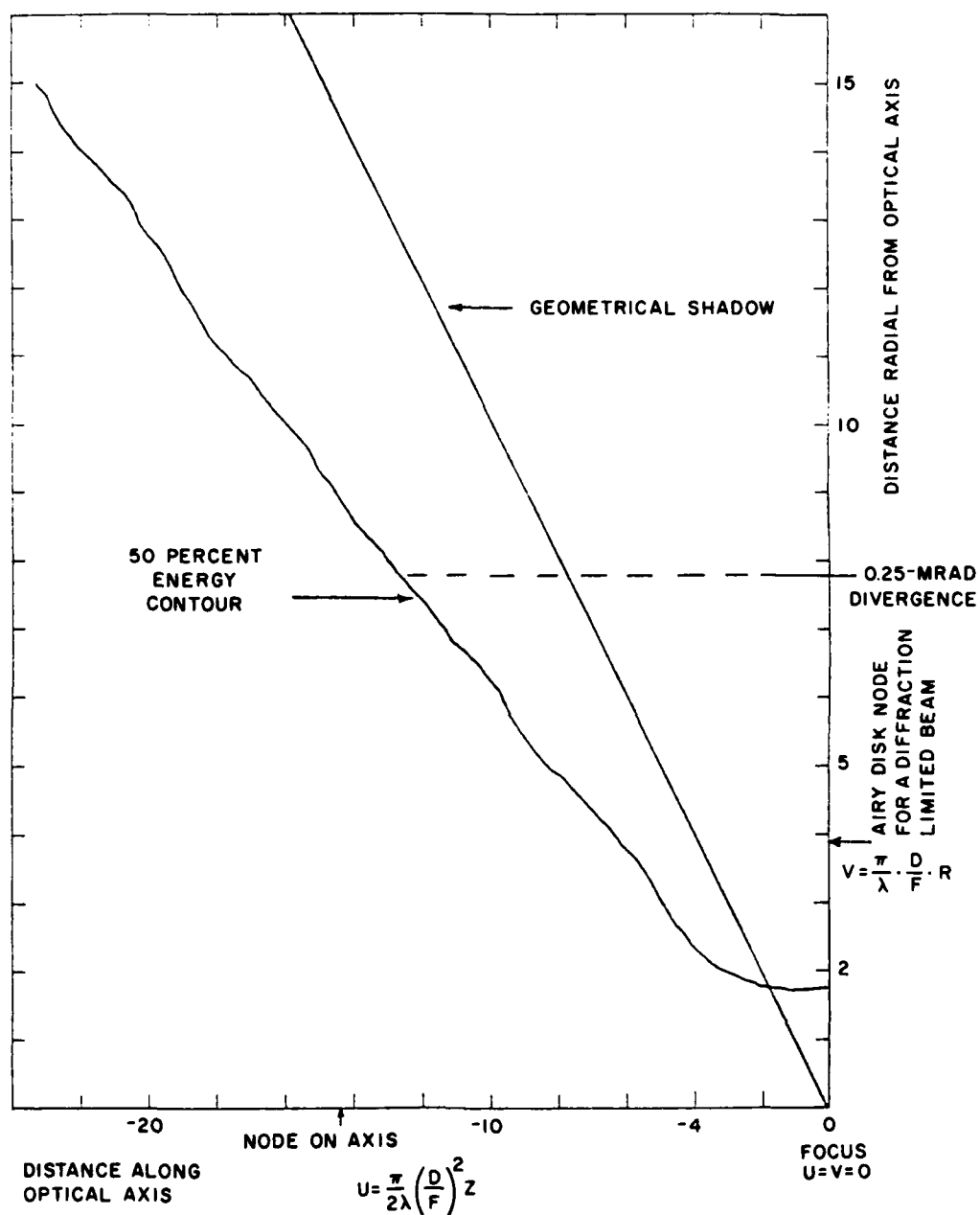
Figure 9. Deposition Contour Around Focus

162
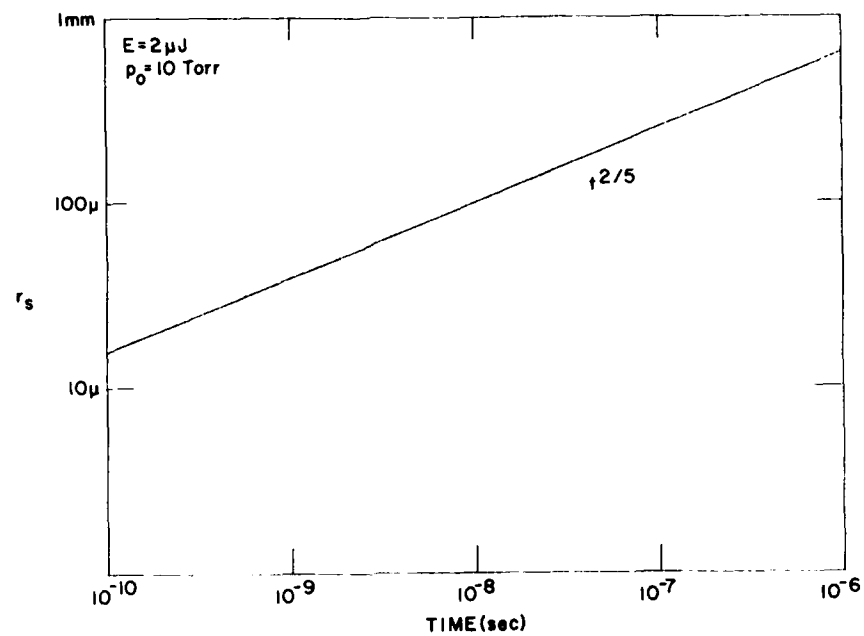
Figure 10. Shock Wave Position vs Time
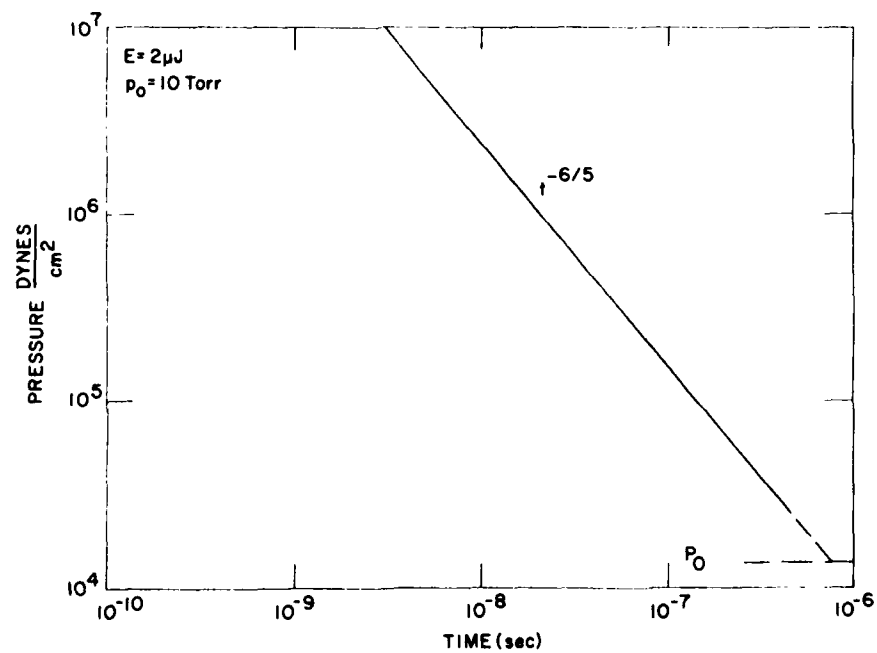
Figure 11. Pressure vs Time

163

Figures 12 and 13 provide temperature information. Figure 12 is the temperature at the shock front vs time. The temperature jump is due to the shock heating. Figure 13 is the temperature of the shock where it occurs in radius. For example, when the shock has expanded to 200 μm, the temperature at the shock is 1200 K.
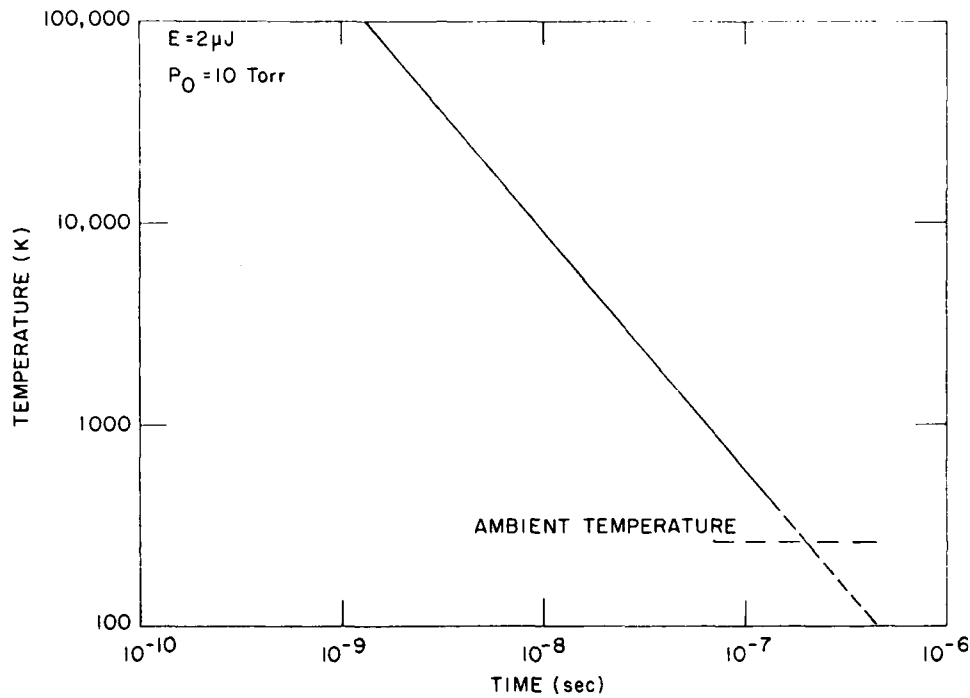

Figure 12. Temperature Behind Shock vs Time

The temperature profile within the shock is a very rapidly rising temperature as $r \to 0$. The functional form is:

$$T \sim T_o \left(\frac{r_s}{r}\right)^{3/\gamma - 1} \tag{14}$$

so for $\gamma = 1.4$,

$$T \sim T_o \left(\frac{r_s}{r}\right)^{7.5} \qquad .$$

Profiles are shown in Figure 14 for $r_s = 100$ μm and 210 μm, which occur at 10 nsec and 65 nsec. A γ of 1.4 is chosen as representative.

164
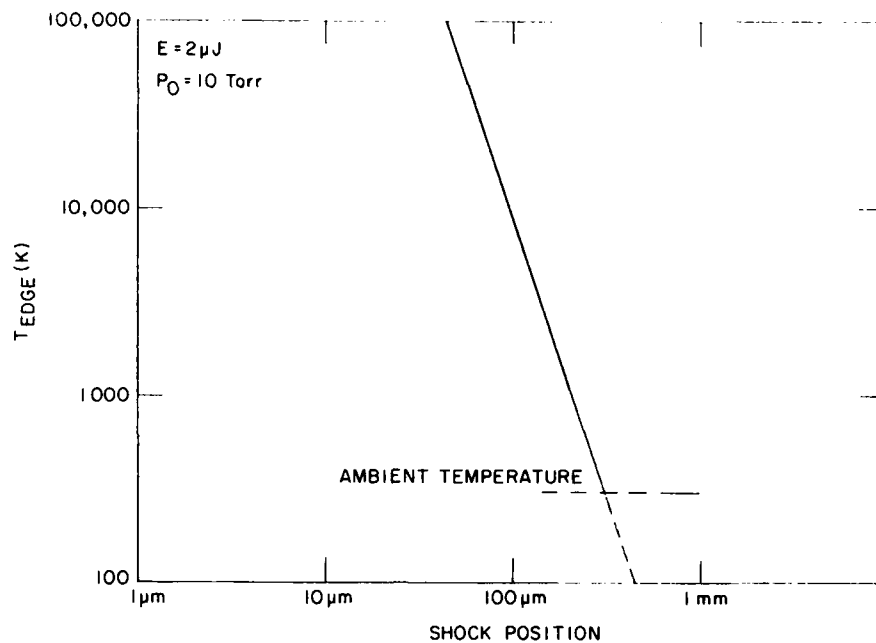
Figure 13. Temperature at Shock Front vs Shock Position
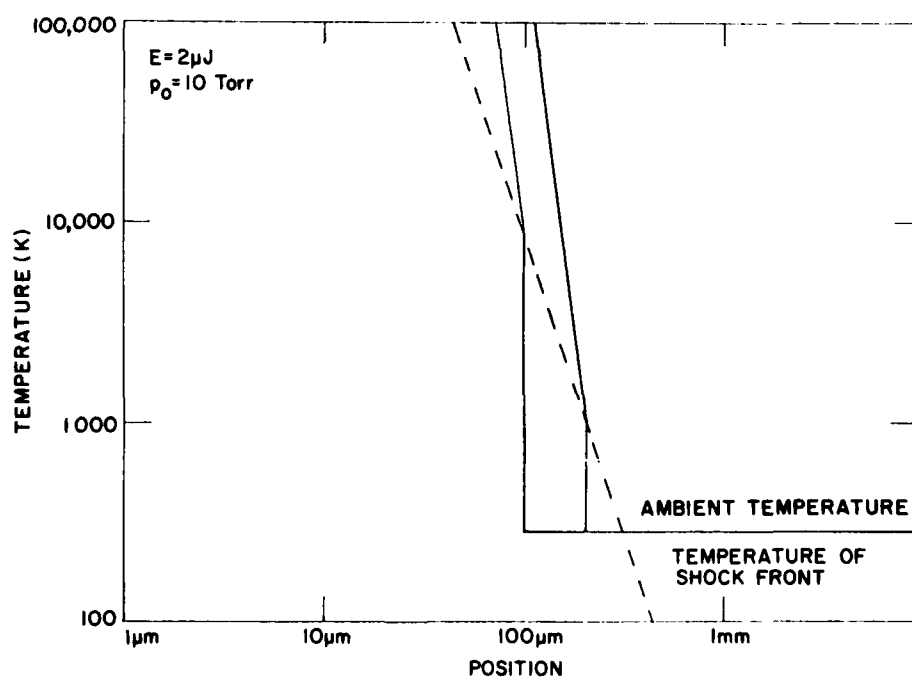
Figure 14. Temperature Profiles Within Shock When Shock is at 100 and 200 μm

165

The last figure provides information about the cooling rate that the gas undergoes. The gas is shock heated and then expands isentropically and therefore cools. Figure 15 shows the cooling rate of gas that is originally at the shock front at the times specified on the ordinate. For example, gas that was shock heated at 10 nsec, (r = 100 μm from Figure 10) was shock heated to 9000 K (Figure 13) and then cooled at 1.5×10^{11} K/sec. If the gas continually cooled at this rate, the gas would cool to ambient temperature in 60 nsec. The cooling rate is fast because expansion velocity is high and the length scale is small.
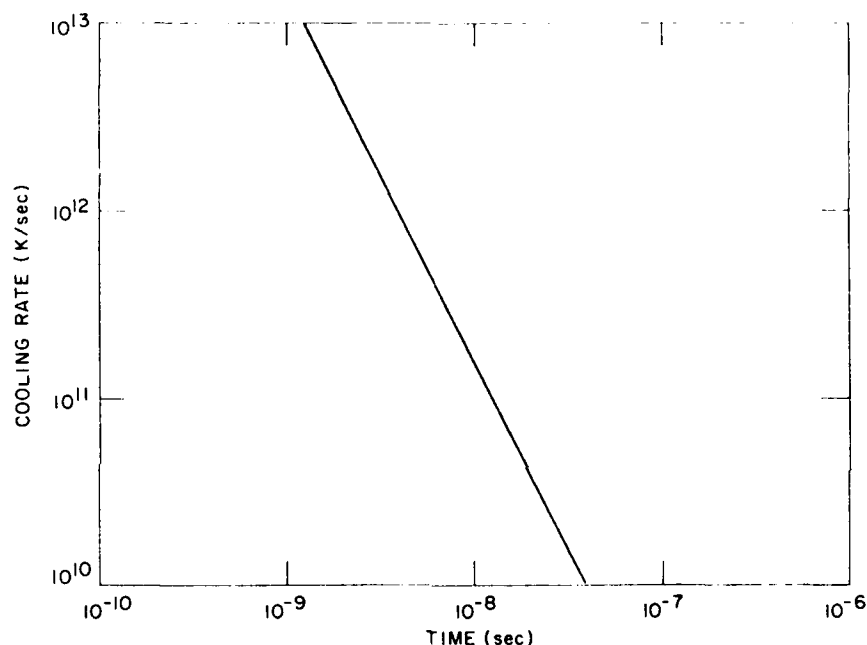
Figure 15. Cooling Rate vs Time

4.2 2-D Expansion

The approximately f/6 laser beam creates a breakdown region longer than it is wide. Hence, it is reasonable to model the breakdown as an expansion from a line. The breakdown is modeled by computing energy deposited per centimeter. In this case it is the 2×10^{-6} J discussed above over the depth of field (580 μm). The following figures are straightforward applications of the formulas given above:

$$r_s = Kt^{1/2} \quad ,$$

where $K = 65 \dfrac{cm}{sec^{1/2}}$ for $E = 2 \times 10^{-6}$ J along 580 μm. This result is plotted in Figure 16.

166
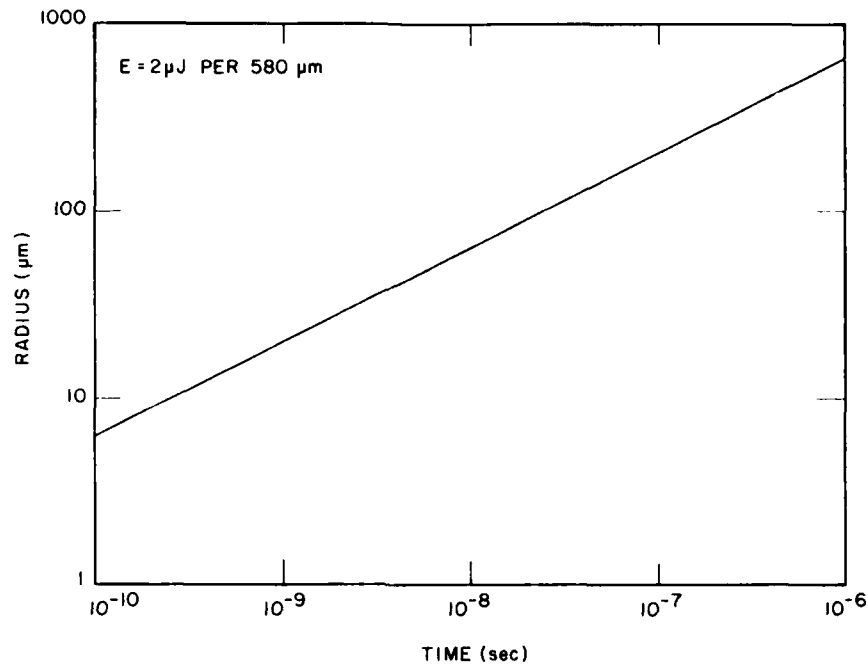
Figure 16. Shock Radius vs Time for 2-D Expansion

The shock front pressure is given by

$$p_s = \frac{2}{\gamma + 1} \rho_o \left(\frac{dr_s}{dt}\right)^2 \quad ,$$

so

$$p_s = 1.5 \times 10^{-2} \frac{1}{t}$$

for $\gamma = 1.4$, and this is plotted in Figure 17.

The temperature is computed using the strong shock approximation, and is plotted in Figure 18 as a function of time and in Figure 19 as a function of shock radius.

The cooling rate of the gas that is originally at the shock front at the specified time on the abscissa is given in Figure 20. For example, at 20 nsec, the gas at the shock front was 2800 K (see Figure 19) and this gas cools at a rate of 4×10^{10} K/sec (see Figure 20 at $t = 20$ nsec). Within a factor of 2, this cooling rate applies to all the shocked gas at each specific time.

167
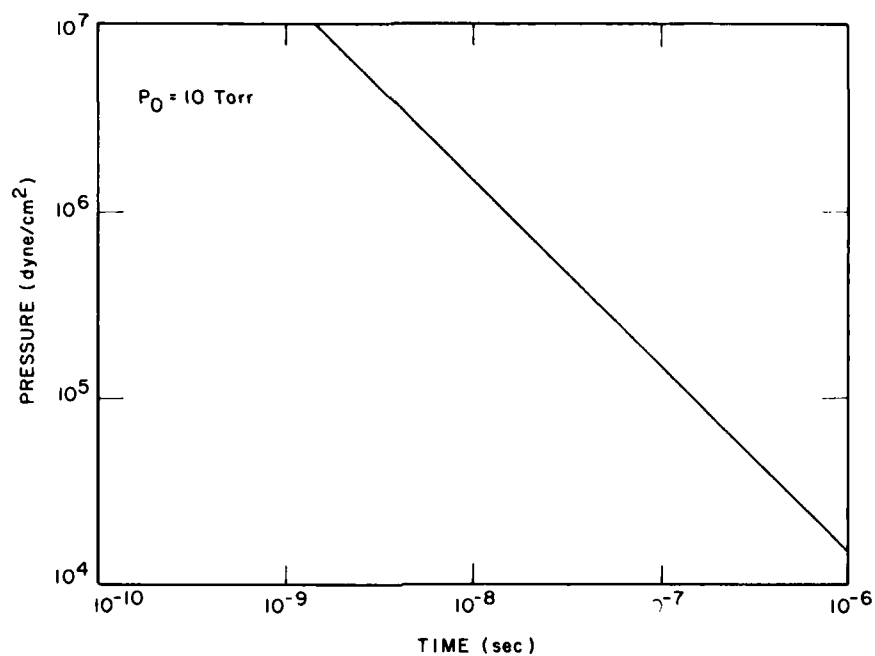
Figure 17.   Shock Pressure vs Time
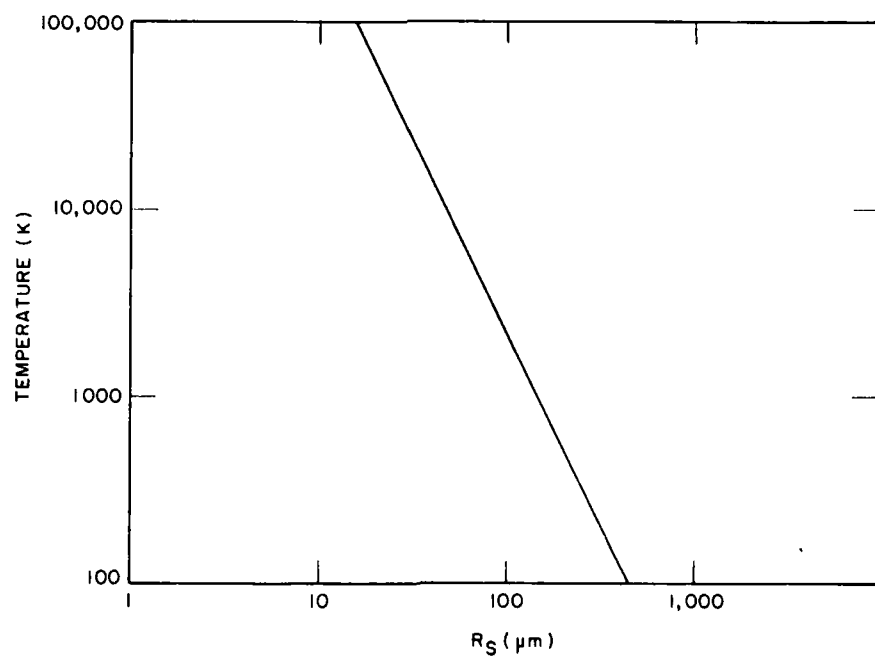
Figure 18.   Temperature at Shock Front vs Shock Radius

168
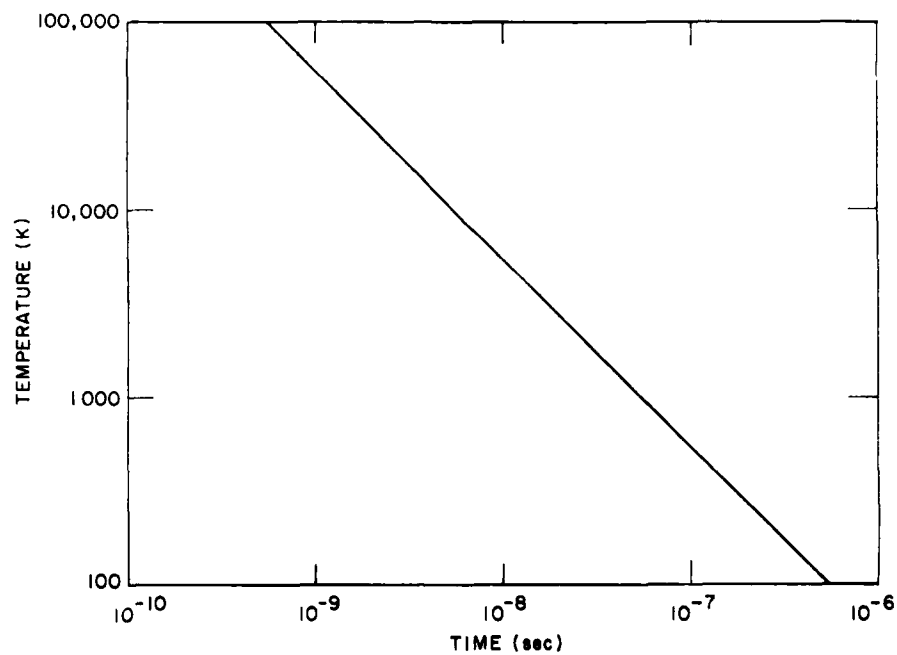
Figure 19.   Temperature at Shock Front vs Time
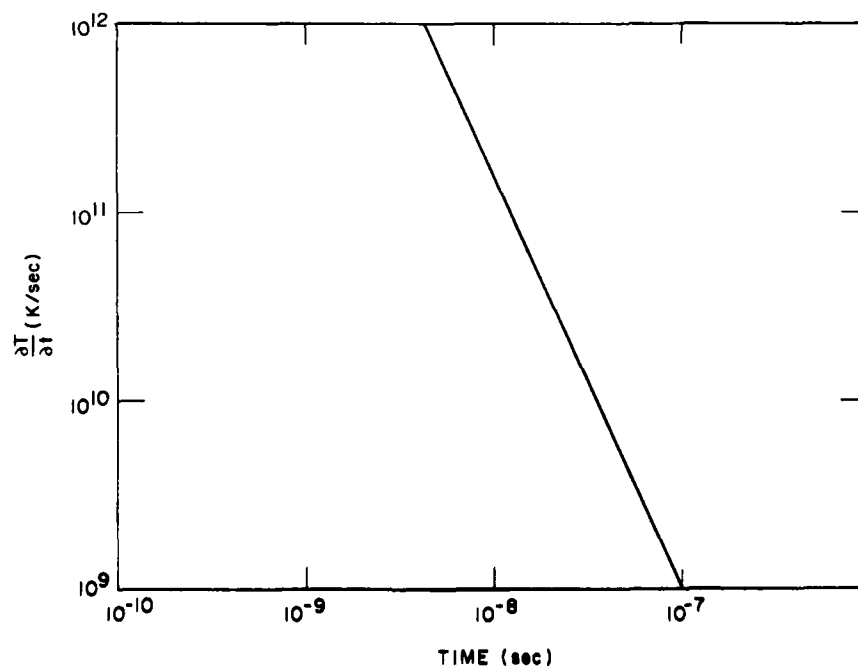
Figure 20.   T vs t for Gas Initially at the Shock Front

4.3 Variable Energy Blast Waves

Equation (10) provides a general formula for the position of the blast wave shock front.[7] We will compare the computed shock front position for an instantaneous release of energy and for a finite release rate. To perform this comparison we will compare the shock position at the time when the same amount of energy has been delivered to the gas over a finite time or instantaneously.

We evaluate r_s for the cases where

$$E_\alpha(\beta = 0) = W_\alpha t^o \qquad ,$$

and

$$E_\alpha(\beta) = W_\alpha t^\beta \qquad .$$

Examining Eq. (10), we will calculate the ratio of shock radii for the case $E_\alpha(\beta = 0) = W_\alpha(\beta) t^\beta$. Using Eq. (10) to compute the ratio, we have

$$\frac{r_s(\beta = 0)}{r_s(\beta)} = \left[\frac{n^2(\beta) J_o(\beta)}{n^2(\beta = 0) J_o(\beta = 0)} \right]^{1/\alpha+3} \qquad . \tag{15}$$

We note the ratio is a constant independent of energy and is close to unity (1.08 for $\alpha = 2$ and $\beta = 1$). Hence, the shock wave will expand to nearly the same location regardless of the rate of energy deposition.

5. DATA ANALYSIS

5.1 Introduction

The data taken by John Swanton to characterize the emission from the spark was analyzed for trends.[2] Data were taken with the Nd^{+++}-YAG laser operating at an output level chosen so that breakdown was consistent at a specific pressure, and also at twice that output energy. Measurements were made to characterize the laser induced sparks in N_2 gas at 3, 5, 10, and 20 Torr.

The 0.5 m Spex spectrometer was operated in zero order, viewing the spark through a sapphire window. The spark was imaged onto the entrance slit using a CaF_2 lens with 1:1 magnification. The photomultiplier tube (RCA C31034) has a

---

7. Dabora, E. K. (1972) Variable energy blast waves, AIAA J. 10:1384.

rather uniform responsivity from 200 to 900 nm. The slit width was 10 μm and the height was 1.2 mm. Scans were made horizontally along the optical axis and vertically perpendicular to the optical axis.

5.2 Horizontal Scans

The scans along the optical axis appear Gaussian. Hence, the 1/e width was used to characterize the lateral extent of the spark. Figure 21 is a sample trace of the variation in signal with horizontal position. The photomultiplier tube was operated using the input impedance of an oscilloscope as the load resistor and the voltage was read off the oscilloscope screen. Because the RC time constant was long compared to the spark duration, the electronic circuit acted as an integrator for the emitted light.
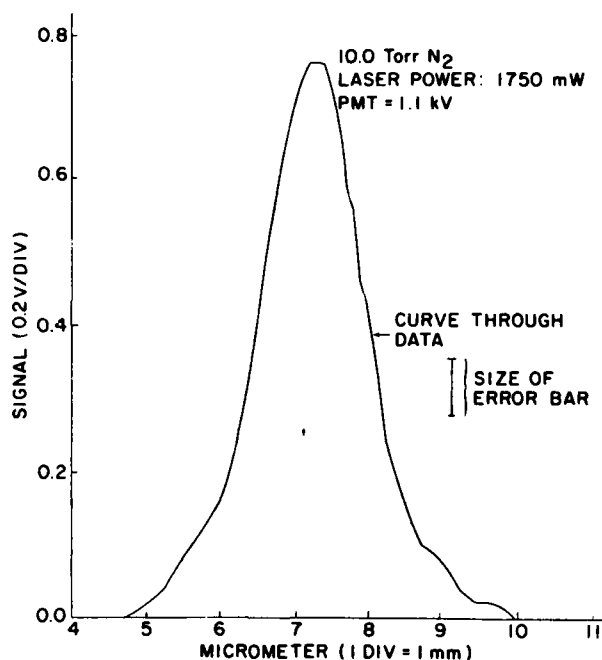
Figure 21. Signal vs Micrometer Setting

Figure 22 shows the reduced data of the full width at 1/e points vs N_2 pressure with the laser operated at a flux level to cause consistent breakdowns and also at an output energy twice that level. The observed size of the luminous zone depends somewhat on the pressure and power level. We note that the luminous zone is always longer than the minimum laser energy deposition length. Because the luminosity peaks approximately tens of nanoseconds after the laser pulse has
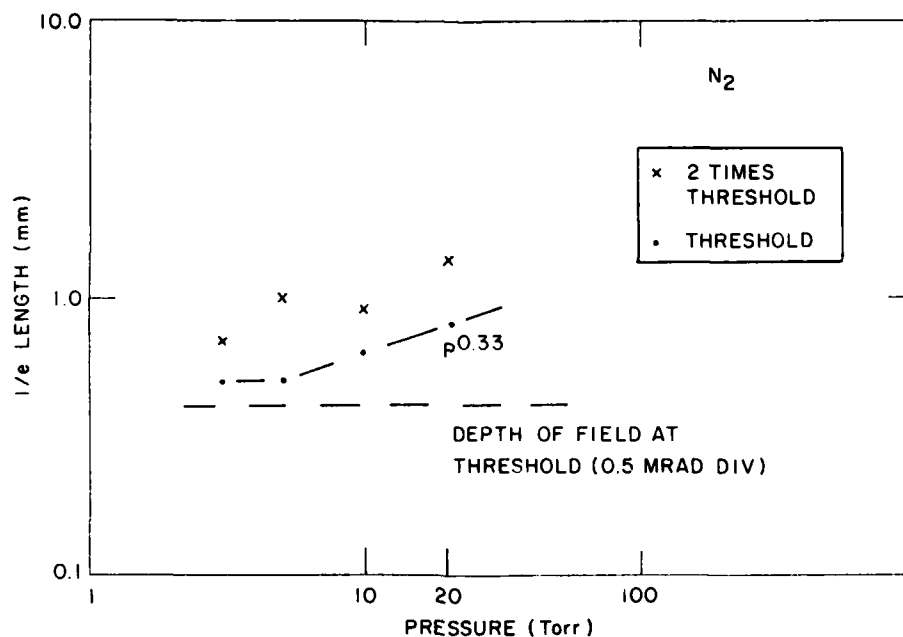
171

Figure 22. Spark 1/e Length vs Pressure

terminated, the plasma has had time to expand and excite molecules that were out of the laser beam.

A nominal line showing the depth of field for the f/6 laser beam has been included in Figure 22. This line is deduced from Figure 9 as the distance along the optical axis where the 50 percent energy contour from geometrical optics matches the minimum laser beam diameter given by the laser beam divergence. A nominal depth of field of 580 μm is calculated. It is expected that the luminous plasma length would be at least this long, and above threshold, even greater than this. Thus, data support our understanding of plasma lengths.

5.3 Vertical Scans

The spark diameter is more difficult to determine precisely because the slit height was comparable to the spark dimension. The lens and cell were vertically translated to obtain the measurements. Figure 23 is a typical trace at the same conditions as Figure 21. We note that the characteristic dimension of the spark height is on the order of 1 mm. Because the translation (1 mm) is much less than the beam size (1 cm) or lens diameter, (~2.5 cm), the laser beam is not expected to be significantly affected by the translation of the lens.

The vertical height of the slit, being 1.2 mm, does not allow an accurate determination of the radius of the luminous spark. However, a comparison of the
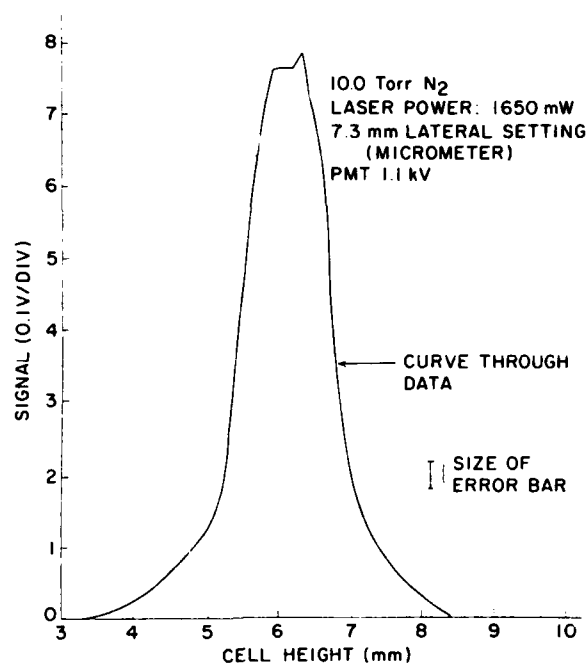
172

Figure 23. Signal vs Cell Height

results compared to what would be observed if the spark had been a Gaussian ir-
radiance distribution indicates that the 1/e width is approximately 0.4 mm ± 0.2
mm. This dimension is much larger than the 14 μm radius of the laser beam di-
vergence. This is undoubtedly because the laser heated gas has expanded and
shock heated additional gas to a radius of hundreds of microns before cooling. As
predicted by blast wave theory (Section 4), an estimate of the volume from which
radiation was measured is 10^{-4} cm^3. This is to be compared to a deposition vol-
ume of 10^{-8} cm^3 for the laser beam.

5.4 Optical Radiation

The measured signals were analyzed to obtain the optical radiation versus
pressure. The measured voltage is proportional to the optical energy radiated by
the spark in the pass band determined by the optical system. The radiated energy
was computed assuming the spark is optically thin and the radiation is isentropic.
Nominal values of 15 percent for the photomultiplier tube quantum efficiency,
10 percent transmission of the spectrometer (grating operated in zero order) and
photomultiplier tube gain of 2.6×10^4 were used. Figure 24 is a plot of the radi-
ated energy vs nitrogen gas pressure in the test cell for the laser operated at an
output energy just sufficient to obtain consistent sparks and at twice that output
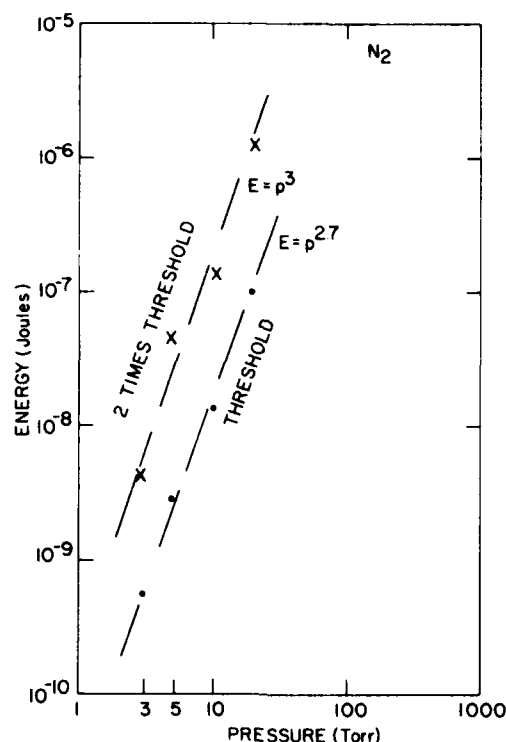
173

Figure 24. Radiated Energy vs Pressure

energy. The data shows a cubic pressure dependence. Because the laser energy
is also changing with pressure, it is also instructive to plot the radiated energy
normalized by the incident laser energy. This behavior is shown in Figure 25.
This ratio is the radiant efficiency of the spark. Because increased laser energy
is needed to obtain a spark as the pressure is reduced, the pressure dependence in
Figure 25 is stronger than in Figure 24. The data to show irradiance vs pressure
is shown in Figure 26. Though the data were taken to characterize the optical ra-
diation rather than measure breakdown thresholds, we have compared these data
with those taken by Roy Lucht. This comparison is shown in Figure 27. We note
the close agreement between the two sets of data at 10 and 20 Torr. John Swanton
undoubtedly used a higher laser energy to obtain consistent breakdowns, compared
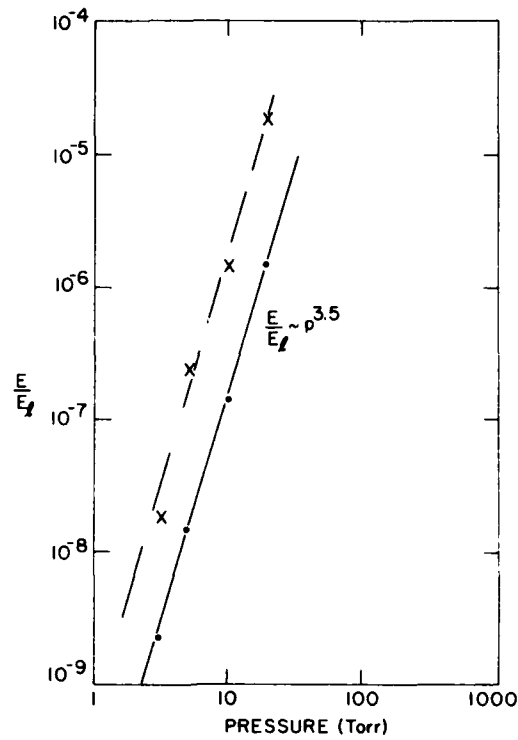to Roy Lucht's breakdown thresholds at 3 and 5 Torr.

174
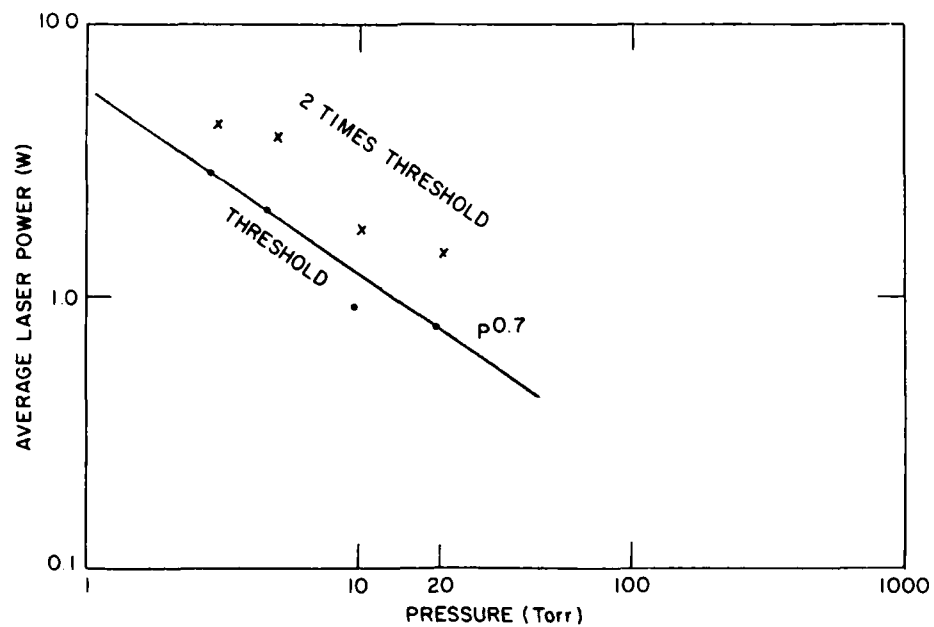
Figure 25. $\frac{E}{E_\ell}$ vs Pressure

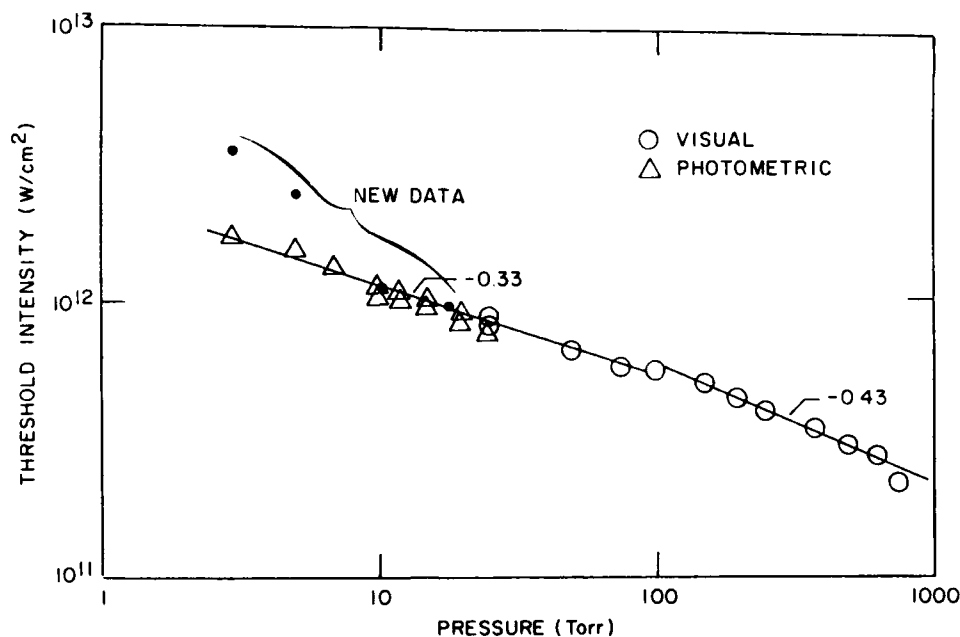Figure 26. Threshold Laser Power vs N_2 Pressure

175

Figure 27. N_2 Breakdown Thresholds

6. CONCLUSIONS

Scoping experiments were done by Roy Lucht to identify breakdown thresholds, radiating species, and time histories of radiating species for low pressure gases. An average color temperature was computed from integrated spectral measurements. The results of these studies indicated that more careful studies of the radiative properties and an analysis of the phenomenon was warranted. Section 3 of this chapter outlined a series of radiometric measurements that could be made to quantify the spark radiation in radiometric units. Spatially, spectrally, and temporally resolved measurements can be analyzed to obtain local color temperatures of radiating species.

Section 4 of this chapter discussed blast wave physics and its application to this problem. Blast wave solutions were calculated for 3-D and 2-D expansions. The shock radius for an instantaneous release of energy was compared to a constant energy input and found to be the same within 8 percent when the input energies are equal. Hence, the time scale over which energy is deposited does little to affect the position of the shock wave. Using the computed energy to obtain a 30,000 K plasma, the blast wave will expand to many laser beam diameters before

176

the laser pulse is over. Blast wave theory provides estimates of the temperature-time history as the gas expands.

The data reduction of the integrated radiometric measurements of the spark radiation shows a strong pressure dependence. The radiometric efficiency (Joules of radiated energy/Joules of laser energy) scaled as the 3.5 power of ambient pressure.

During the next phase of the program, we will model the radiation emitted from the spark. Because the time scale for expansion is short, the plasma may not remain in equilibrium. Calculations will be made of the optical radiation as a loss mechanism as well as cooling due to expansion. The work in the next phase is aimed at providing a physical understanding of the radiation levels and decay time of the laser produced spark.

References

1. Lucht, R., Unpublished.

2. Swanton, J., Unpublished.

3. Nichols, D. B., and Hall, R. B. (1980) Laser-beam attenuation for spatial profiling of small focal spot, Rev. Sci. Instr. 51:1131.

4. Wiese, W., Smith, M., and Glennon, B. (1966) Atomic Transition Probabilities, Vol. 1, National Bureau of Standards, NSROS-NBS4.

5. Griem, H. (1964) Plasma Spectroscopy, McGraw Hill, New York.

6. Zel'dovich, Ya. B., and Raizer, Yu. P. (1966) Physics of Shock Waves and High Temperature Hydrodynamic Phenomena, Academic Press, New York.

7. Dabora, E. K. (1972) Variable energy blast waves, AIAA J. 10:1384.

Contents

6.2 LINUS: Infrared Experiments

by

J. B. Lurie
S. M. Miller
R. A. Armstrong

1. INTRODUCTION

The study of the relaxation of low pressure, highly ionized oxygen plasmas is important to the understanding of the radiation processes and chemistry of the upper atmosphere. The technique of high-powered, pulsed laser-induced breakdown of gases makes possible the convenient generation of such a plasma in the laboratory. Although much effort has been expended towards the understanding of laser-induced breakdown threshold mechanisms, relatively few investigations of ion-electron recombination in laser-produced plasmas have been carried out. Early studies by Baravian et al[1,2] obtained time-resolved electron temperatures and densities in high pressure (1-20 atm) laser-produced helium plasmas, yet did not address the detailed state-to-state spectroscopy and dynamics of the various species playing a role in plasma recombination.

1. Baravian, F., Benattar, R., Bretagne, J., Godart, J. L., and Sultan, G. (1972) Electron-ion recombination in a helium plasma produced by laser, Z. Physik 254:218.

2. Baravian, G., Benattar, R., Bretagne, J., Godart, J. L., and Sultan, G. (1973) Recombination of doubly ionized atoms in the afterglow of a helium plasma produced by laser, Z. Physik 260:121.

Initial studies[3] of the relaxation of laser-produced oxygen and nitrogen plasmas established the presence of many ionic emission lines in the visible spectral region. However, no observations of infrared transitions between high-lying states produced by plasma recombination have been reported. These measurements might make possible the detection of nascent states produced by recombination and the determination of relative populations of states unobservable by visible and ultraviolet transitions. Models predicting infrared emission from the plasma recombination process use the Coulomb approximation to calculate oscillator strengths. Such calculations are taken to be quite reasonable for the oxygen atom, which is strictly L-S coupled. Deviation from assumed recombination and ionization processes and infrared emission oscillator strengths might lead to errors in predictions of atmospheric infrared emission models. These considerations make benchmark measurements of infrared emission from a recombining oxygen plasma extremely useful.

In this paper, we present the first observations of infrared line emission from a laser-produced oxygen plasma. The line emission observed between 1.7 and 3.2 μ originates from the n = 4 manifold of atomic oxygen states generated by ion-electron recombination. We discuss time-resolved visible emission studies that provide additional information on the behavior of the O-atom 4d ^{5}D State. The relative populations of the observed states in the n = 4 manifold are considered in light of theoretical oscillator strengths calculated using the Coulomb approximation.[4]

2. EXPERIMENTAL ARRANGEMENTS

A Quanta-Ray Nd:YAG laser (Model DCR-1A, λ = 1.064 μ, 750 mJ, 10 nsec full width half maximum multi-longitudinal pulse, 10 Hz repetition rate) was focussed with a 56 mm f.1 lens into a gas cell containing oxygen (Matheson, UHP). Laser-induced breakdown produced a visible plasma -2 mm in diameter. Infrared and visible radiation was viewed at right angles through a 0.5 m Spex 1870 spectrometer. Infrared emission was collected using a 300 lines/mm grating blazed at 3.0 μ and a Santa Barbara Research Center photovoltaic InSb detector with

3. Armstrong, R. A., Lucht, R. A., and Rawlins, W. T. (1983) Spectroscopic investigation of laser-initiated low-pressure plasmas in atmospheric gases, Appl. Opt. 22:1573.

4. Biemont, E., and Grevesse, N. (1973) Infrared wavelengths and transition probabilities for atoms, $3 \le Z \le 20$, Atomic Data and Nuclear Data Tables 12:217.

0.5 μsec time response. The relative spectral response of the system was deter-
mined with a blackbody source and lock-in amplifier. The detector output was
averaged with a boxcar (3 μsec delay, 1.5 μsec gate) and recorded on a strip chart
recorder. Overall resolution was 0.02 μ. For time-resolved visible emission
studies, the spectrometer was fitted with a 1200 lines/mm grating blazed at
5000 Å, and a PAR OMA II (optical multi-channel analyzer) in place of the exit
slit, yielding overall resolution of ~2 Å. Use of a high-voltage pulser with micro-
processor control permitted the successive acquisition of nine time-resolved
spectra (300 nsec gate) in a total time period of 15 min. Plotting was carried out
on an x-y recorder.

3. RESULTS

Figure 1 illustrates the 1.7 - 3.2 μ emission spectrum of a 30 Torr laser-
produced oxygen plasma at t = 3 μsec after the laser pulse. In spite of the rela-
tively slow time response of the detector, this setting was sufficiently late in time
to gate out the early-time continuum emission (illustrated in the following OMA
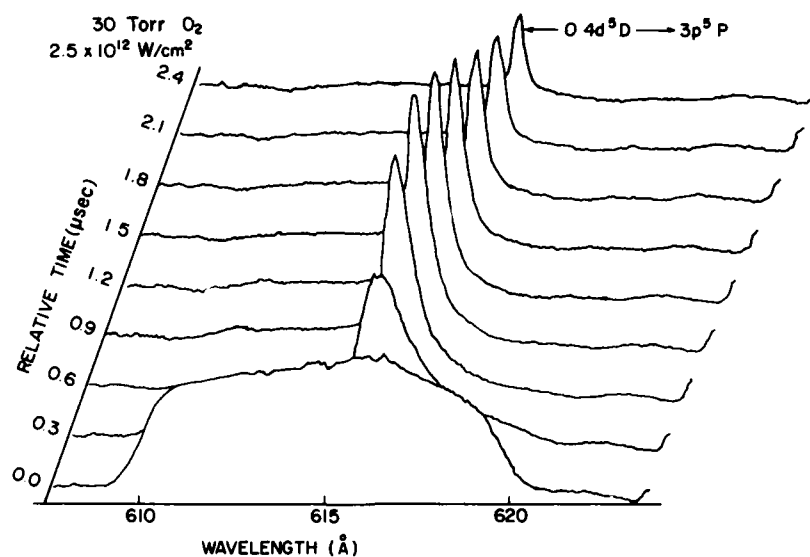data). Line assignments, based on the low-pressure DC discharge results of

Figure 1.   Time-Resolved Emission Spectra of Laser-Produced
Oxygen Plasma From 6100 to 6200 Å

Saum and Benesch,[5] are listed in Table 1. The lines originate in the O-atom levels 4f ^{5}F, 4f ^{3}F, 4d ^{5}D, 4p ^{5}P, 4p ^{3}P, and 4d ^{3}P. Oscillator strengths calculated using the Coulomb approximation by Biemont and Frevesse[4] were used for the determination of relative populations (Table 1), calculated according to

$$N = \frac{I\lambda}{\varepsilon\sigma^2 \Sigma gf} \quad ,$$

where

I is the measured intensity of a spectral line,

σ is the energy of the transition,

ε is the instrument spectral responsivity,

g is the degeneracy of the lower state,

f is the absorption oscillator strength and,

λ is the wavelength of the transition.

Table 1. Line Assignments of Infrared Transitions Observed in a 30 Torr Laser-Produced Oxygen Plasma

$\lambda(\mu)$	Transition	Upper State Energy (cm^{-1})	Lower State Energy (cm^{-1})	Σg (Ref. 5)	Relative Population
1.80	4f ^{5}F → 3d ^{5}D	102968	97420	24.70	1.00 ± 10%
1.82	4f ^{3}F → 3d ^{3}D	102968	97488	15.06	1.00
2.65	4d ^{5}D → 4p ^{5}P	102865	99093	16.62	0.75 ± 20%
2.76	4p ^{5}P → 4s ^{5}S	99093	95476	4.72	2.00
2.89	4p ^{3}P → 4s ^{3}S	99680	96225	4.42	1.53
3.10	4d ^{3}D → 4p ^{3}P	102908	99680	11.00	1.17

No other lines were observed between 1.7 and 5.0 μ under these conditions. We calculate an electron temperature of 4000 K based on the relative population of the 4p ^{5}p and 4d ^{5}D states.

Figure 2 illustrates the temporal evolution of the O-atom 6157 Å line (4d ^{5}D → 3p ^{5}P). The observation of this transition lends further support to the assignment of the 2.65 μ line as 4d ^{5}D → 4p ^{5}P. The OMA provides a temporal history of the entire line, recording wavelength on the x-axis, intensity on the y-axis, and relative time on the z-axis. There exists little or no line emission for the first 300 nsec. Instead, a continuum is present due to radiative recombination and bremsstrahlung events. The apparent reduction of the continuum at

5. Saum, K. A., and Benesch, W. M. (1970) Infrared electronic emission spectrum of oxygen, Appl. Opt. 9:1419.
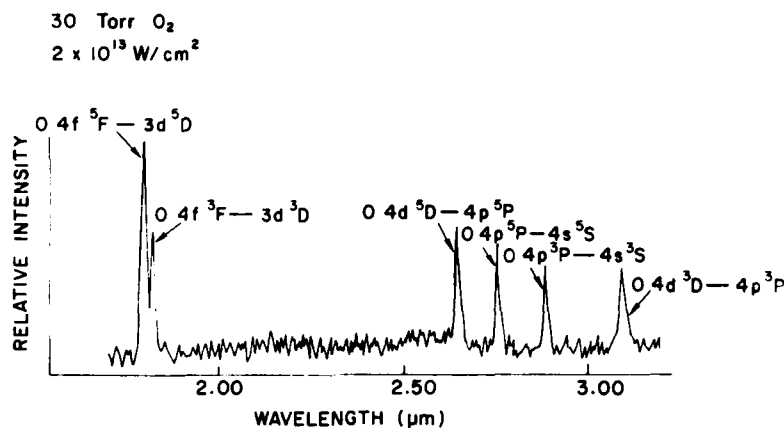
Figure 2. Emission Spectrum of Laser-Produced Oxygen
Plasma From 1.7 to 3.2 μ

the edges of the scan is due to the fall-off of the detector array response at its edges. Similar temporal behavior of the continuum is observed throughout the visible and infrared. The emission line exhibits Stark broadening at early times, which decreases with time as the electron density of the plasma decreases. The relatively low spectral resolution of the OMA when used with a 1200 lines/mm grating ($\sim$2 Å) precludes the accurate determination of electron temperature and density from this measurement. However, a rough estimate of electron density (accurate to within a factor of 2) from the observed linewidth at t = 300 nsec yields $n_e = 10^{17}/cm^3$, using Stark-broadening coefficients calculated by Griem.[6] Although the radiative lifetime of this transition is only 143 nsec,[7] the peak intensity is not reached until $\sim$1 μsec. This is in sharp contrast to the temporal history of the O^+ lines, which show rise times of tens of nanoseconds.[3] In addition, while the decay time of the 6157 Å line is $\sim$2 μsec once the peak intensity is reached, the ionic lines decay in hundreds of nanoseconds.[3]

6. Griem, H. (1974) Spectral Line Broadening by Plasmas, Academic Press, New York, p. 336.
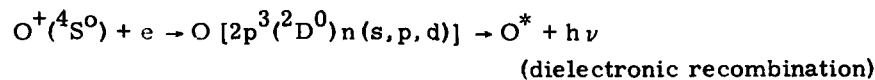
7. Wiese, W. L., Smith, M. W., and Glennon, B. M. (1966) Atomic Transition Probabilities, Volume I, Hydrogen Through Neon, National Standard Reference Data Series NBS-4.

4. DISCUSSION

The long-lived nature of the 6157 Å emission from the 4d ^{5}D state suggests that the observed n = 4 states of atomic oxygen are produced by ion-electron recombination. The dissociative recombination process

$$O_2 + e \rightarrow O^+ + O^*$$
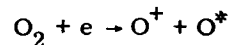
is expected to occur at a rate of $\sim 10^{-7}$ cm^3/sec.[8] Therefore, the expected lifetime of O_2^+ at our estimated electron density of 10^{17}/cm^3 is less than 1 nsec, making this process incompatible with the long-lived production of the O-atom n = 4 states. Hence, recombination of O^+ ions with electrons must account for the observed emission. The two-body recombination processes

$$O^+(^4S^0) + e \rightarrow O^* + h\nu \qquad \text{(radiative recombination)}$$

$$O^+(^4S^0) + e \rightarrow O\,[2p^3(^2D^0)n\,(s,p,d)] \rightarrow O^* + h\nu$$
$$\text{(dielectronic recombination)}$$

might eventually give rise to O(n = 4). Although in some cases dielectronic recombination rates can be much higher than radiative recombination rates, radiative recombination is much faster than dielectronic recombination for $O^+(^4S^0)$.[9] Assessing the relative importance of radiative recombination compared to the three-body process

$$O^+(^4S^0) + e + e \rightarrow O^+ + e$$
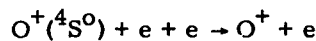
requires an estimate of electron temperature. Radiative recombination dominates over three-body recombination when[10]

$$n_e \geq 1.3 \times 10^{-3}\, T_e^{\,4} \qquad .$$

Even assuming an electron density as low as 10^{16}/cm^3, this would require an electron temperature in excess of 50,000°. Time resolved studies of electron

8. Bardsley, J. N., and Biondi, M. A. (1966) in _Advances in Atomic and Molecular Physics_, D. R. Bates, Ed., Academic Press, New York, p. 405.

9. Bates, D. R. (1962) Dielectronic recombination to normal nitrogen and oxygen ions, _Planet Space Sci._ 9:77.

10. Zel'dovich, Ya., and Raizer, Yu. (1966) _Physics of Shock Waves and High Temperature Hydrodynamic Phenomena_, Academic Press, New York, p. 405.

temperature in a 200 Torr laser-produced helium plasma indicate an electron temperature of 40,000° as late as 1 μsec after the laser pulse.[11] This temperature is probably maintained in the helium plasma due to superelastic collisions of electrons with metastable states of He^+, which lie more than 40 eV above the ground state. Species present in an oxygen plasma have no similar energy storage mechanism. Therefore, on this basis alone we would expect the oxygen plasma to have an electron temperature at late times lower than that of the helium plasma. This is confirmed by the rough temperature estimate (4000°) based on the relative intensities of the infrared lines originating in the 4p ^{5}P and 4d ^{5}D levels. Hence, for our electron densities of 10^{16} - 10^{17} cm^{-3} and electron temperatures less than 10,000°, three-body recombination is expected to dominate over radiative recombination. This implies that, since no atomic line emission is observed in temporal coincidence with the continuum emission, a free-free process probably dominates over a free-bound process for the continuum production.

The ionization potential of atomic oxygen is 109837 cm^{-1}.[7] For the 4d ^{5}D state at 102865 cm^{-1} to be formed directly by three-body recombination, the second electron would have to carry off 0.86 eV in translational energy, an unlikely possibility. The infrared line positions and oscillator strengths calculated by Biemont and Grevesse[4] indicate a series of 5f → 4d transitions in the 3.9 μ region with oscillator strengths similar to those for the 4d → 4p transitions. However, we do not observe any n = 5 → n = 4 transitions between 1.7 and 5.0 μ under our conditions. This argues against the contribution of radiative cascade to the production of the 4d states. Therefore, we favor the process

$$O^+ (^4S) + e + 3 \rightarrow O^{**} + e \qquad ,$$

$$O^{**} + e \rightarrow O (n = 4) + e$$
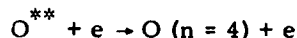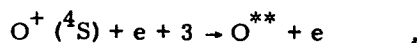
as giving rise to the observed emission.

In addition to the 5f → 4d transitions in the 3.9 μ region, the study by Saum and Benesch in a low-pressure DC discharge[5] identified other transitions originating in n = 4, 5, 6 that we do not observe in this experiment. The calculated oscillator strengths for the missing lines[4] are generally lower than the observed n = 4 lines, perhaps making their observation difficult because the signal-to-noise ratio was low. In addition, since the energy separations between states decrease as n increases, collisional deactivation processes will depopulate the n = 5, 6

11. Lurie, J. B., Armstrong, R. A., and Bashkin, S. (1985) Recombination and expansion in a 200 Torr laser-produced helium plasma, in preparation.

through radiation more difficult, especially under our conditions of high electron density.

The 1.7 - 3.2 μ scan permits observations of both triplet and quintet components of the 4p, 4d and 4f O-atom states. We first discuss the relative population of the 4f ^{5}F and 4f ^{3}F states in light of the oscillator strengths calculated from the Coulomb approximation. The 4f ^{5}F and 4f ^{3}F states lie at the same energy within 1 cm^{-1}. Hence, the two states would be expected to exhibit equal populations. Calculating the relative populations using the Coulomb approximation oscillator strengths, we find that this is indeed the case. Therefore, we believe that the oscillator strength calculation for the quintet is not in error relative to the value calculated for the triplet state. However, the absolute values of the calculated strengths might not be accurate, since the Coulomb approximation calculation is expected to break down for a transition with a lower state as close to the core as the 3d ^{5}D state.

For this reason, the calculation for the 4d ^{5}D → 4p ^{5}P transition is probably more trustworthy. Since we find that N(4f ^{5}F)/N(4d ^{5}D) = 1.3, an apparent population inversion, this constitutes additional evidence that the calculated 4f → 3d oscillator strengths are inaccurate, and in fact ought to be higher. The 4d ^{3}D and 4d ^{5}D states are separated by 43 cm^{-1}, with the 4d ^{3}D state of higher energy, and also ought to exhibit equal relative populations. Instead, another apparent population inversion is in evidence. However, the 4d ^{3}D and 4p ^{3}P levels are known to be perturbed by other close-lying levels.[4] These perturbations cast doubt on the accuracy of the Coulomb approximation calculation for the 4d ^{3}D → 4p ^{3}P and 4p ^{3}P → 4s ^{3}S transitions, with the 4d ^{3}D → 4p ^{3}P transition perhaps being the more severely affected of the two. The 4d ^{5}D and 4p ^{5}p states are not known to be perturbed. Therefore, we believe that the true oscillator strength for the 4d ^{3}D → 4p ^{3}P transition is somewhat higher than the calculated strength, while the true strength for the 4p ^{3}P → 4s ^{3}S transition is somewhat lower than the calculated strength. Such corrections would bring triplet and quintet levels to within reasonably expected relative populations, since we can envision no collisional or radiative processes that might preferentially populate triplet states more than quintet states or vice versa. For the O-atom n = 4 levels, collisional population processes are much faster than radiative population processes for our values of n_e and T_e. Since the calculated Coulomb approximation oscillator strengths for the 4d ^{5}D → 4p ^{5}P and 4p ^{5}P → 4s ^{5}S transitions are expected to be more accurate than those for the other states we observe, we have used the calculated relative population of the 4d ^{5}D and 4p ^{5}P states for our calculation of temperature. These considerations point to the necessity of oscillator strength calculations which take into full account the influence of state-to-state perturbations.

186

5. CONCLUSION

The first observation of infrared line emission from a recombining plasma indicates that three-body recombination of O^+ ($^4S°$) with an electron to form a high-lying Rydberg state followed by collisional deactivation produces atomic oxygen states in the n = 4 manifold. Accompanying time-resolved visible emission studies establish the temporal behavior of the O-atom 4d ^5D state. The relative population of triplet and quintet states in the n = 4 manifold determined using oscillator strengths calculated according to the Coulomb approximation show apparent population inversions, indicating the need for further experimental and theoretical studies which address the question of state-to-state perturbations.

Acknowledgements

References

1. Baravian, F., Benattar, R., Bretagne, J., Godart, J. L., and Sultan, G. (1972) Electron-ion recombination in a helium plasma produced by laser, Z Physik 254:218.

2. Baravian, G., Benattar, R., Bretagne, J., Godart, J. L., and Sultan, G. (1973) Recombination of doubly ionized atoms in the afterglow of a helium plasma produced by laser, Z. Physik 260:121.

3. Armstrong, R. A., Lucht, R. A., and Rawlins, W. T. (1983) Spectroscopic investigation of laser-initiated low-pressure plasmas in atmospheric gases, Appl. Opt. 22:1573.

4. Biemont, E., and Grevesse, N. (1973) Infrared wavelengths and transition probabilities for atoms, $3 \leq Z \leq 20$, Atomic Data and Nuclear Data Tables 12:217.

5. Saum, K. A., and Benesch, W. M. (1970) Infrared electronic emission spectrum of oxygen, Appl. Opt. 9:1419.

6. Griem, H. (1974) Spectral Line Broadening by Plasmas, Academic Press, New York, p. 336.

7. Wiese, W. L., Smith, M. W., and Glennon, B. M. (1966) Atomic Transition Probabilities, Volume I, Hydrogen Through Neon, National Standard Reference Data Series NBS-4.

8. Bardsley, J. N., and Biondi, M. A. (1966) in Advances in Atomic and Molecular Physics, D. R. Bates, Ed., Academic Press, New York, p. 405.

9. Bates, D. R. (1962) Dielectronic recombination to normal nitrogen and oxygen ions, *Planet Space Sci.* 9:77.

10. Zel'dovich, Ya., and Raizer, Yu. (1966) *Physics of Shock Waves and High Temperature Hydrodynamic Phenomena*, Academic Press, New York, p. 405.

11. Lurie, J. B., Armstrong, R. A., and Bashkin, S. (1985) Recombination and expansion in a 200 Torr laser-produced helium plasma, in preparation.

Contents

6.3 LINUS: Plasma Expansion Theory

by

P. Nebolsine
G. Weyl
B. D. Green

1. INTRODUCTION

A series of experiments have been carried out and reported[1] under the LINUS (Laser Induced Nuclear Simulation) program in which visible radiation emitted by a nitrogen plasma in the pressure range 10 to 100 Torr was measured. The plasma was created through laser-induced breakdown in the focus of a $\lambda = 1.06\ \mu$m Nd:

---

1. Armstrong, R., Lucht, R., and Rawlins, W. T. (1973) Spectroscopic investigation of laser-initiated low-pressure plasmas on atmospheric gases, Appl. Opt. 22:1573.

Yag laser beam. The plasma, after expansion to pressure equilibrium, was found to be cigar shaped with length $\cong 0.45$ mm and diameter ≈ 0.2 mm. The purpose of this investigation is to develop a physical model of the plasma that will explain the major features of the radiation data. In particular, time integrated spectra of plasma radiation indicate a continuum in the visible that has a peak at 4500 Å. Such a spectrum is shown in Figure 1. Previous attempts at explaining the features of this continuum as due to electron bremsstrahlung radiation have been unsuccessful. Another series of data involved measurements of the temporal behavior of line radiation, as shown in Figures 2 through 4. The following observations on line radiation were made; they could only be understood for optically thick line radiation.
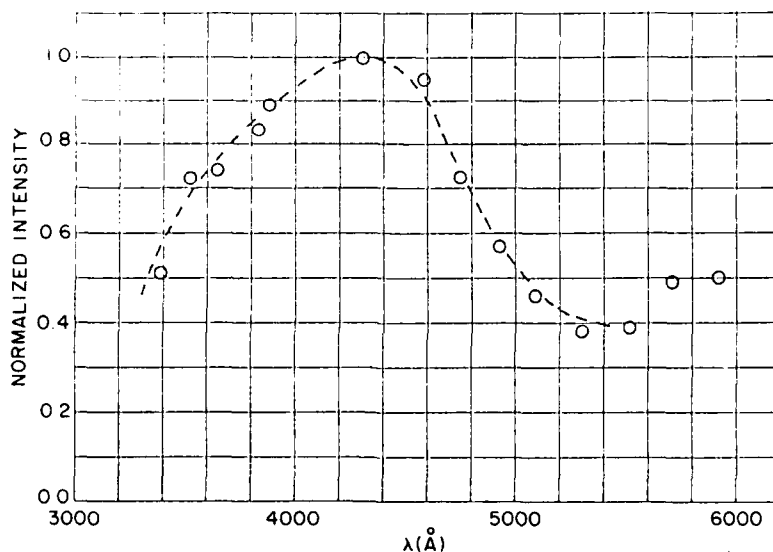

Figure 1. Continuum Spectrum Using 125 Torr N_2 and $I = 9.8 \times 10^{11}$ W/cm^2

(1) All lines originating from the same ionic species have similar profiles, independent of energy level from which they originate.

(2) The decay times increase as one goes from N^{2+} to N^+ and then to N.

(3) The higher the pressure the slower is the decay time.

(4) The decay time increases as the laser intensity is increased above breakdown threshold.

Previous calculations, however, have shown that all lines are optically thin.[1,2]

---

2. Nebolsine, P., and Weyl, G. (1982) LINUS Final Report for the Period Oct. 1, 1981 - Sept. 30, 1982, Physical Sciences Inc., PSI TR-348.
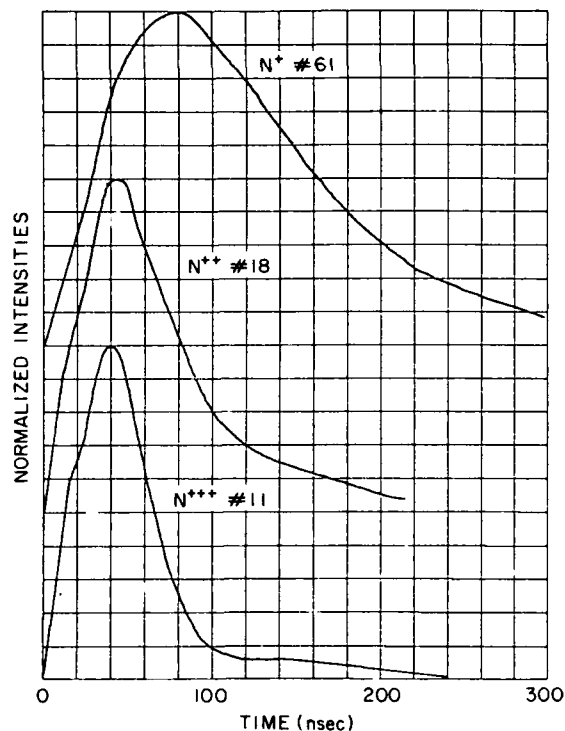
Figure 2. Line Profile Using 10 Torr N_2 and
$I = 2.9 \times 10^{12}$ W/cm^2. Note curves are nor-
malized and displaced with respect to each
other

The temporal behavior of line radiation and decay cannot be obtained under
the assumption of local thermodynamic equilibrium (LTE). The decay times are
1 to 2 orders of magnitude longer than the radiative lifetimes of the excited states.
A possible explanation, as we shall see further on in this study, is that the popu-
lation of excited states and radiation from these states are determined by the rate
of (three body) recombination. This rate varies as $T_e^{-9/2}$ (T_e = electron temper-
ature) so that the rate of cooling of the plasma determines the rate at which ex-
cited states are populated and the level of radiation from those states.

To make a quantitative prediction of the plasma radiation one would have to
evaluate:

(1) The amount and spatial distribution of laser radiation deposited in the gas.
(2) The energy lost to the surrounding gas during the blast wave expansion.
(3) The cooling of the plasma by conduction and radiation.
(4) The chemistry occurring during the cooling.
(5) The absorption of radiation by the surrounding (cold) gas.

193

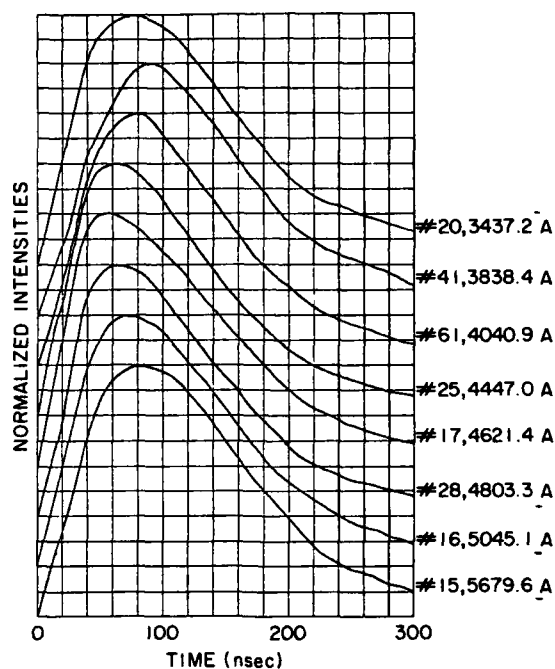MICROCOPY RESOLUTION TEST CHART
NATIONAL BUREAU OF STANDARDS-1963-A

Figure 3. N^+ Line Profiles Using 125 Torr
N_2 and $I = 2.9 \times 10^{12}$ W/cm^2. Curves are
displaced as in Figure 2

Such detailed analysis is beyond the scope of this study. The approach followed is
to survey the many physical processes involved and to determine the most impor-
tant of these. A more quantitative analysis would be reserved for more detailed
further studies.

The various stages in the LINUS experiment are shown in Figure 5. They
are: (a) breakdown, (b) absorption, (c) expansion, and (d) cooling and radiation.
They are analyzed in Sections 2 through 4. Our conclusions are given in Section 5.

2. PHYSICAL PROCESSES OCCURRING DURING THE LASER PULSE

Multi-photon ionization and electron cascade ionization play equally important
roles at $\lambda = 1.06$ μm for the pressures of interest $1 < p < 100$ Torr in the break-
down process. The initial electrons are created by multi-photon ionization of N_2
and impurities having low ionization potential. Buildup of ionization then proceeds
by cascade ionization of the neutrals through collisions with the laser-heated elec-
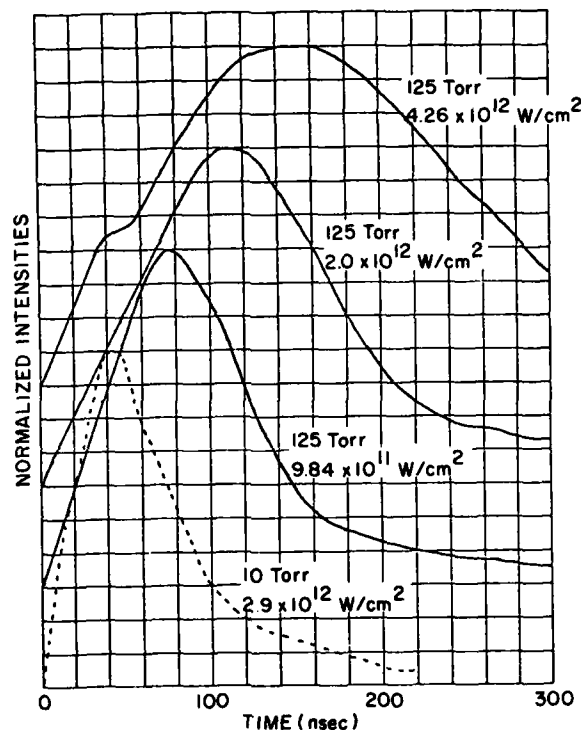trons.

Figure 4. N^{++} Line Profiles. Curves are displaced as in Figure 2

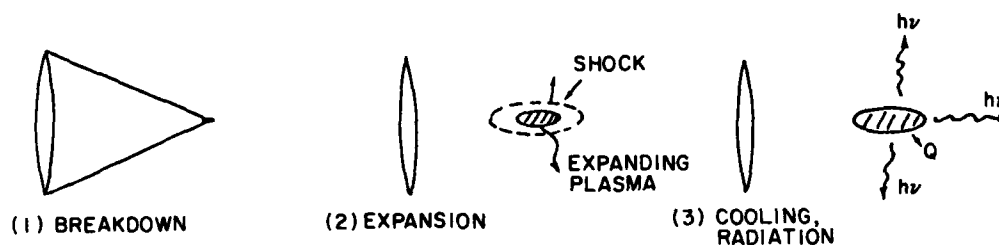(1) BREAKDOWN   (2) EXPANSION   (3) COOLING, RADIATION

Figure 5. Various Stages of Gas/Plasma Behavior in LINUS Experiment

2.1 Time Scales

We have looked at the time scales for various collisional processes and from these time scales we can conclude that:

(1) Electron-electron collisions are sufficiently fast that one can define an electron temperature $T_e \gg T_{gas}$.

(2) Neutral-neutral, neutral-ion and ion-ion collisions occur on a time scale that is comparable to or longer than the pulse time τ_p so that for all practical purposes heavy-heavy collisions are unimportant.

195

(3) The time for electrons to transfer their energy to heavy particles by momentum transfer collisions is so long (due to the factor M/m where M = heavy mass, m = electron mass) that the electrons cannot heat the gas by the time the pulse is over.

(4) The time scale for expansion of the gas is shorter than the pulse time so that the gas has already expanded before the major part of the energy has been deposited.

We have plotted the time scales for various physical processes in Figure 6. These time scales are for a practically totally (singly) ionized plasma before expansion with electron temperature T_e. The pressure of the gas before breakdown for this figure was $p = 10$ Torr and the scaling of all quantities with p is indicated. The formulas used for the derivation of Figure 6 are given below, as well as numerical values for $T_e = 20,000$ K.

Electron neutral momentum transfer,

$$\tau_{en} = (n\,\sigma_M V_e)^{-1} = 3 \times 10^{-11} \left(\frac{10}{p}\right) \text{sec} \qquad ; \qquad (1)$$

Electron-electron equilibration,

$$\tau_{ee} = \frac{0.266\,T_e^{3/2}}{n_e \ell n\Lambda} = 4 \times 10^{-12} \left(\frac{10}{p}\right) \text{sec} \qquad ; \qquad (2)$$

Neutral-neutral collision time,

$$\tau_{nn} = (n\sigma_M V)^{-1} = 10^{-7} \left(\frac{10}{p}\right) \text{sec} \qquad ; \qquad (3)$$

Electron-ion equilibration time,

$$\tau_{ei} = \frac{M}{2m}\,\tau_{ee} = 5 \times 10^{-8} \left(\frac{10}{p}\right) \text{sec} \qquad ; \qquad (4)$$

Pressure equilibration time,

$$\tau_{peq} = \frac{a}{(\gamma k T_e/M)^{1/2}} = 10^{-9} \text{sec} \qquad ; \qquad (5)$$

Thermal diffusion time,

$$\tau_{thd} = \frac{a^2}{K} \cong 10^{-8} \left(\frac{p}{10}\right)^{1/2} \text{sec} \qquad ; \qquad (6)$$
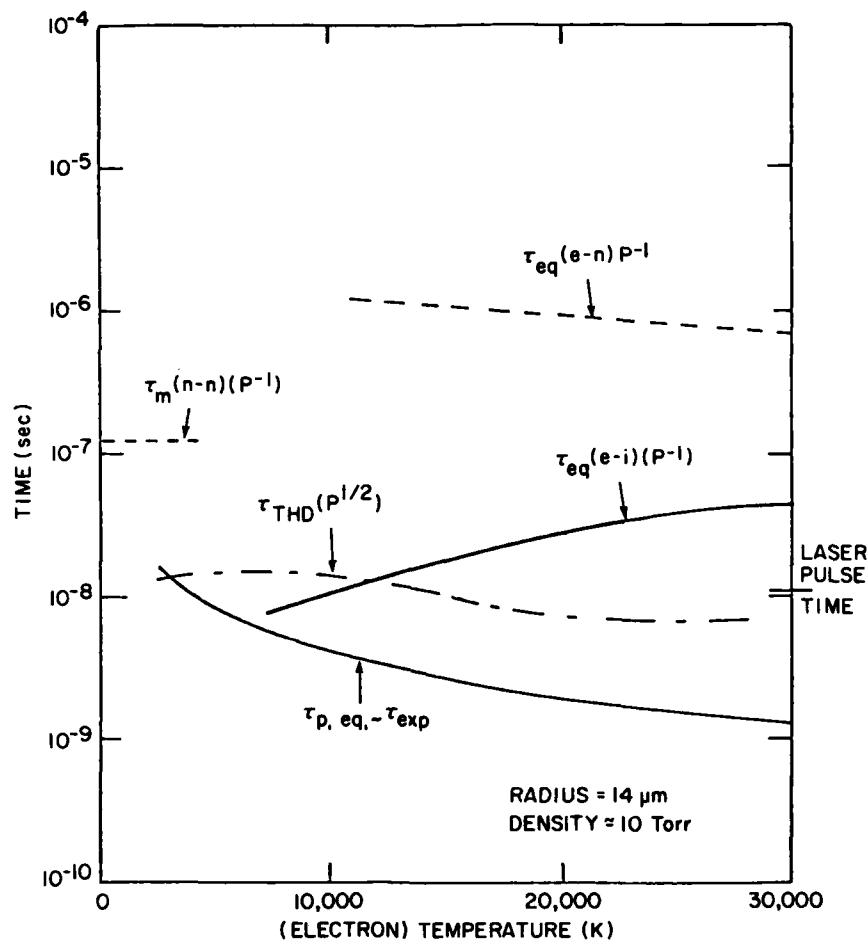
196

Figure 6. Time Scales of Various Physical Processes Before
Plasma Expansion

where we defined $V = (2kT_g/M)^{1/2}$, $V_e = (2kT_e/m)^{1/2}$, $\ell n\Lambda$ = Coulomb logarithm ($\cong 6$), a = beam radius (= 14 μm), and where σ_M is hard sphere cross-section of neutrals ($\approx 10^{-15}$ cm^2). The thermal conductivity used was taken as that of equi-librium high-temperature nitrogen.[2]

Note that the plasma expansion time is estimated to be 10^{-9} sec, which is a factor of 10 shorter than the pulse time. One would expect from such a short time that, if one operates the laser well above threshold, breakdown will occur early in the pulse and that because the plasma is expanding rapidly out of the beam, the latter portion of the laser pulse will be ineffective in depositing much more energy into the plasma.

197

Possible reactions that we have not included but may result in heating of the heavy particles are dissociation and dissociative recombination.
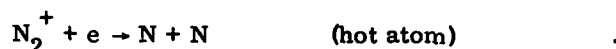
$$N_2 + e \rightarrow N_2^* + e \qquad , \tag{7}$$

followed by

$$N_2^* \rightarrow N + N \qquad \text{(hot atom)} \qquad ,$$

and

$$N_2 + e \rightarrow N_2^+ + e + e \qquad , \tag{8}$$

followed by

$$N_2^+ + e \rightarrow N + N \qquad \text{(hot atom)} \qquad .$$

2.2 Length Scales

To gain better insight into the importance of various physical processes during the breakdown, it is also worthwhile to estimate the various length scales entering into the problem. These are shown in Figure 7. The length scales imposed by the optics are the focal radius $a \cong 14 \ \mu m$ and the depth of focus $\sim 300 \ \mu m$. The *importance of electron diffusion out of the beam during the breakdown is measured* by the diffusion length $l_D \sim \sqrt{\mathcal{D}\tau_p}$ where $\mathcal{D}$ is the electron diffusivity and τ_p the pulse length. The free electron diffusion coefficient $\mathcal{D}$ as a function of 1.06 μm laser intensity at one amagat density is shown in Figure 8. It was obtained by use of a Boltzmann code. l_D, scales as $p^{-1/2}$. This length is so much larger than the beam radius that diffusion of electrons out of the beam will represent a significant loss process for cascade ionization. However, if multi-photon ionization processes can build up the electron concentration to $n_e \geq 10^{11} \ cm^{-3}$, where space charge effects limit diffusion to being ambipolar, then the diffusivity is reduced by the factor $(m/M)^{1/2} \approx 4 \times 10^{-3}$. We show in Figure 9 as a function of focal radius the electron density that has to be exceeded for space charge effects to be important.

The thermal diffusion length is given by

$$l_\theta = \sqrt{k\tau_p} \cong 14 \left(\frac{10}{p} \right)^{1/2} \mu m \qquad . \tag{9}$$

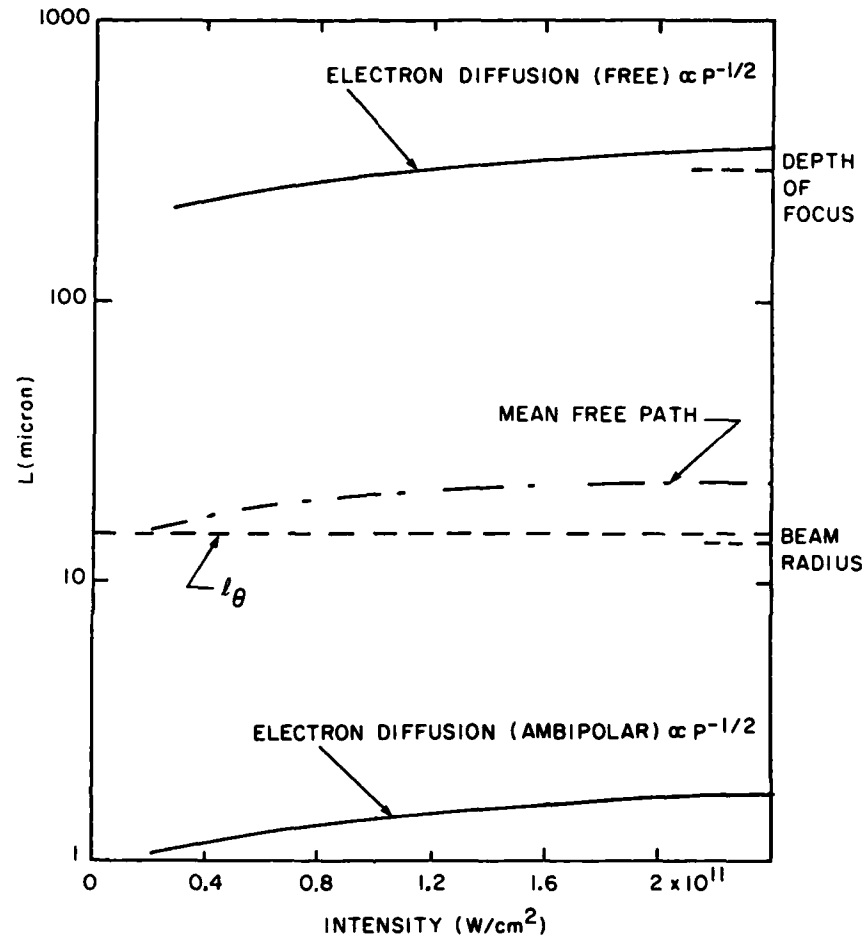For $p < 10$ Torr we will have $l_\theta \geq a$ so that thermal losses during the pulse are important.

198

Figure 7. Length Scales of Interest at p = 10 Torr

Finally, the electron mean free path is $l_e = (N\sigma_M)^{-1} \cong 15\ (10/p)\ \mu m$. The mean free path, therefore, at $p \leq 10$ Torr is of the order or larger than the beam radius. Continuum treatment of the gas will not be a valid approach at the low pressures.

3. EXPANSION OF THE GAS

The absorption of the laser radiation creates a high pressure in the focal volume. The gas expands in a finite time to return the pressure to ambient. Several treatments can be used to estimate the pressures and expansion times. Reference 2 by Nebolsine and Weyl describes two approaches - regular blast wave, and variable energy blast wave theory and the application to this problem.
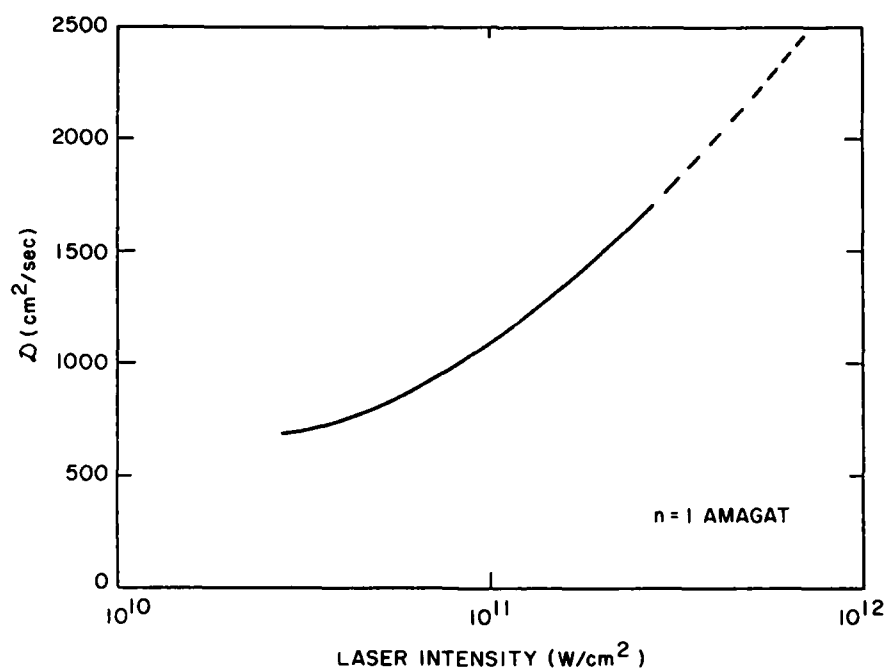
199

Figure 8. Free Electron Diffusivity in N_2 at 1 amagat

A zeroth order estimate of a characteristic expansion time is given by the spot radius divided by the speed of sound of the gas. Using 30,000 K as a temperature, the time scale for a 15 μm spot radius is several nanoseconds. Since the expansion time is shorter than the pulse duration, the gas will already be expanding before the laser pulse is over. With such a short characteristic time, the pressure will drop significantly on a time scale of the order of the laser pulse duration. We will now discuss the time scale for the pressure to return to ambient.

Using an estimate of 30,000 K for a plasma temperature, the peak pressure is expected to be on the order of 1,000 Torr for an initial 10 Torr gas pressure. The plasma will expand predominantly radially because the laser beam diameter is approximately ten times shorter than the depth of field. Two dimensional blast wave theory yields a pressure that scales inversely with time. If at τ = 10 nsec the pressure is 1000 Torr, it will therefore decay to 10 Torr (ambient) after 1 μsec.

The average temperature of the expanded gas can be computed as a function of the ratio of specific heats, γ. Because γ is varying, examples will be given for a range of γ. Using the isentropic expansion relations for p and T, we find that T drops from 30,000 to 4,700 K for a pressure drop of 100 and a γ of 1.67. On the other hand, if γ = 1.2, the average temperature will be 14,000 K for the same
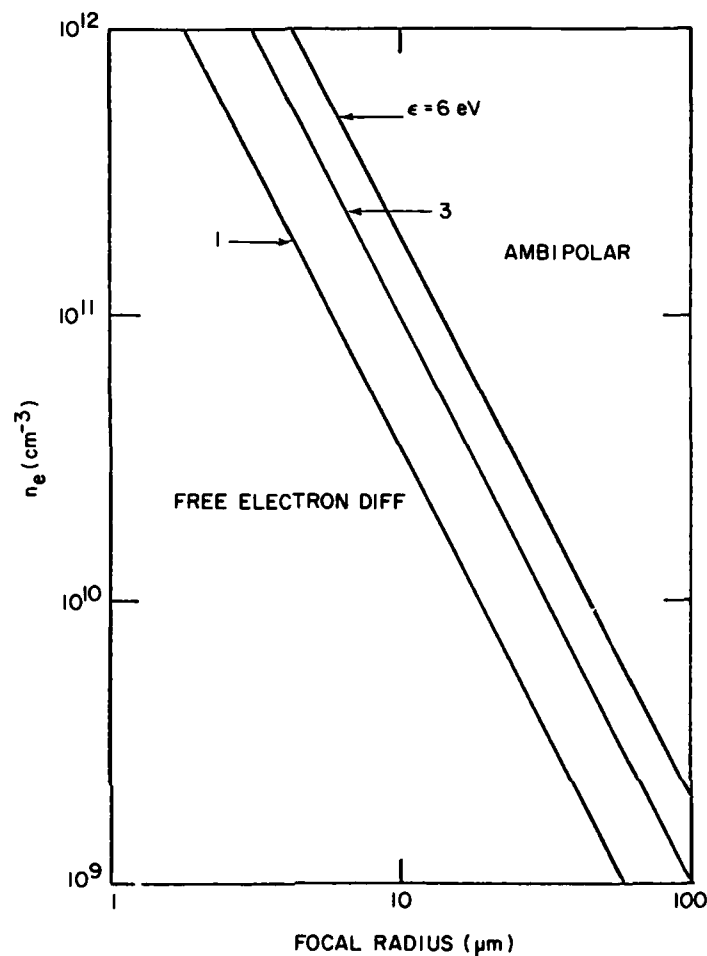
Figure 9. Critical Electron Density for Ambipolar
Diffusion

initial temperature and pressure drop. Thus, we find that the plasma can still be
very hot and continue to radiate after gas dynamic effects are over.

4. RADIATION BY THE NITROGEN PLASMA

4.1 Radiation of Nitrogen Plasma in Thermodynamic Equilibrium

To get an idea of the radiation characteristics of the laser-produced nitrogen
plasma, we have used a radiation code that was developed at PSI under a previous
program to study plasma radiation coupling to metallic surfaces.[3] This code as

Reference 3 will not be listed here. See References, page 227.

201

written takes into account line radiation and continuum radiation (free bound and free free) from a plasma containing electrons, N, and N^+. We have modified the code to include also radiation from excited states of N^{2+}. All lines included are those for which oscillator strengths are known and tabulated, excepting those lines connecting to lower states having two excited electrons. The code uses detailed balance to relate plasma emissivity to plasma absorptivity and is therefore valid only for a plasma in thermodynamic equilibrium at some temperature T. All lines of a same multiplet have been lumped into a single line whose strength is the sum of the line strengths of its constituent lines and having the Stark broadening parameters as given by Griem.[4]

If the plasma is in thermodynamic equilibrium then the concentration of the various ions of nitrogen are related by the following Saha equations.

$$\frac{n_e [N^+]}{N} = \frac{A\, T^{3/2}\, g^+}{g} \exp - (\varepsilon_1/kT) \tag{10}$$

$$\frac{n_e [N^{2+}]}{[N^+]} = \frac{A T^{3/2}\, g^{2+}}{g^+} \exp - (\varepsilon_2/kT) \tag{11}$$

$$\frac{n_e [N^{3+}]}{[N^{2+}]} = A T^{3/2}\, \frac{g^{3+}}{g^{2+}} \exp - (\varepsilon_3/kT) \qquad , \tag{12}$$

where $A = 2\, (2\pi mk/h^2)^{3/2} = 4.83 \times 10^{15}\ cm^{-3}\ deg^{-3/2}$, the g's are partition functions of the heavies, $\varepsilon_1 = 14.54$ eV, $\varepsilon_2 = 29.6$ eV and $\varepsilon_3 = 47.4$ eV. We must add to the above the equation of state

$$([N^+] + [N^{2+}] + [N^{3+}] + [N] + n_e)\, kT = p \tag{13}$$

and the equation of conservation of charge:

$$[N^+] + 2[N^{2+}] + 3[N^{3+}] = n_3 \qquad . \tag{14}$$

It is straightforward to solve Eqs. (10) through (14) for the concentration of species as a function of p and T by noting that at any p, T there will only be two major ionic species and the others may be treated as a perturbation. For example, below 20,000 K we need only consider Eqs. (10) and (11). If B_1 and B_2 are the right-hand sides of Eqs. (10) and (11) and if we write $[N] = n_o(1 - x - y)$, $[N^+] = n_o x$ and $[N^{2+}] = n_o y$, Eqs. (10) and (11) become

---

4. Griem, H. (1964) Plasma Technology, McGraw Hill, New York, Table 4-5.

$$\frac{x(x + 2y)}{1 - x - y} = \frac{B_1}{n_o} \qquad , \tag{15}$$

$$\frac{y(x + 2y)}{x} = \frac{B_2}{n_o} \tag{16}$$

and Eq. (13) yields

$$n_o = \frac{P}{(1 + x + 2y)} \qquad . \tag{17}$$

Equations (15) through (17) were solved on a programmable hand calculator by several iteration schemes. For $x > y$ (low temperature range). We solve for x as a function of y from Eq. (15), given n_o,

$$x = \frac{-(B_1/n_o + 2y) + \sqrt{(B_1/n_o + 2y)^2 - 4(1 - y)}}{2} \qquad , \tag{18}$$

and then calculate y from Eq. (16)

$$y = \frac{(B_2/n_o)\, x}{x + 2y} \qquad .$$

Inserting the value of y and the value of x in Eq. (17) yields an updated n_o. We then solve for x again using Eq. (18). This scheme does not converge for $x < y$, and we proceed as follows. We take the ratio of Eqs. (10) and (11) and solve for y as a function of x.

$$y = \frac{(1 - x) + \sqrt{(1 - x)^2 - (B_2/B_1)x^2}}{2} \qquad .$$

We then solve for x from Eq. (11)

$$x = \frac{y(x + 2y)\, n_o}{B_2} \qquad ,$$

and recalculate n_o by use of Eq. (17).

A similar procedure is used above 20,000 K, where Eqs. (11) and (12) are used rather than Eqs. (10) and (11). The results of these calculations are shown in Figure 10 for the three pressures $p = 1$, 10, and 100 Torr. One sees from this figure that nitrogen becomes significantly ionized above 10,000 K and that N^{2+} becomes a dominant species above 18,000, 22,000, and 25,000 K for $p = 1$, 10, and 100 Torr, respectively.
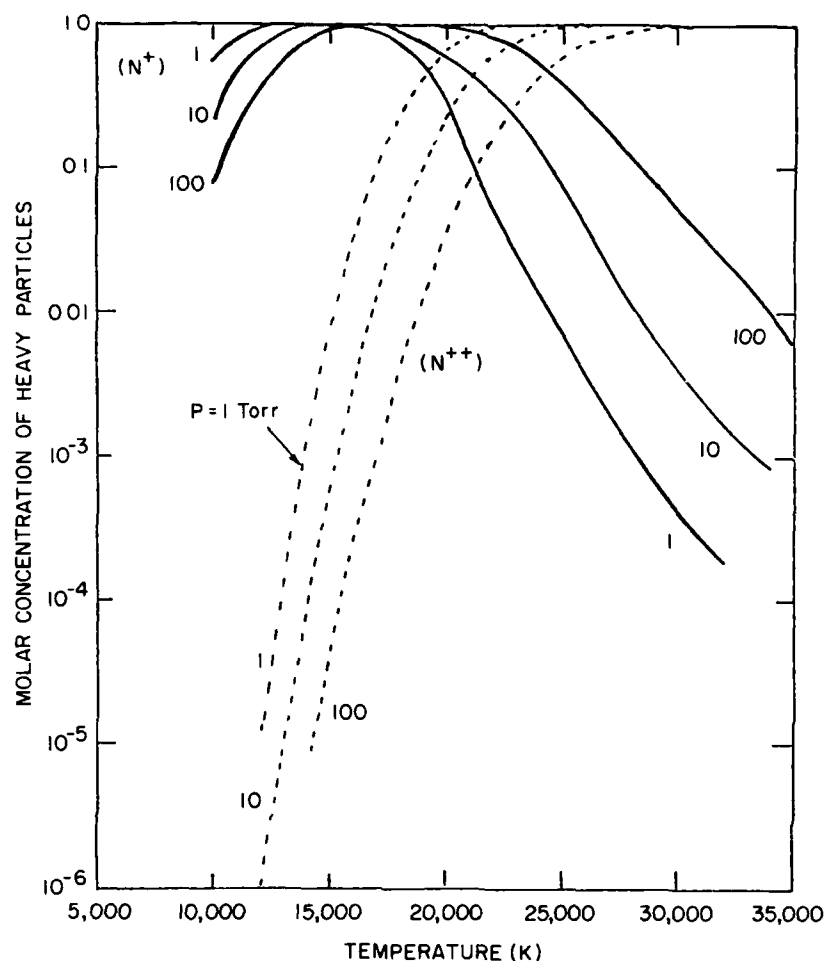
Figure 10. Species Concentrations in Equilibrium Plasma

We show in Figures 11 through 19 computer-generated plots of radiation emitted by a plasma slab of thickness 0.2 mm. These figures also show the black body emission and comparison of the two curves show that the plasma is quite optically thin to its own radiation. Figures 11 through 19 were generated using a grid size of 20 cm^{-1}, which is considerably larger than the Stark broadened line widths. Therefore most lines whose centers fall far from grid points are not apparent. To make the lines more apparent, we have generated special plots, two of which are shown in Figures 20 and 21, that give absorption coefficient at line center in the wavelength interval 0.2 - 0.9 μm. One verifies from Figures 20 and 21 that, indeed, even at line center, a plasma of thickness $\sim$ 0.2 mm is optically thin. A plot such as Figure 20 was expanded so that the wavelength scale was identical to those of the visible spectra taken by R. Lucht.[1] We were able to
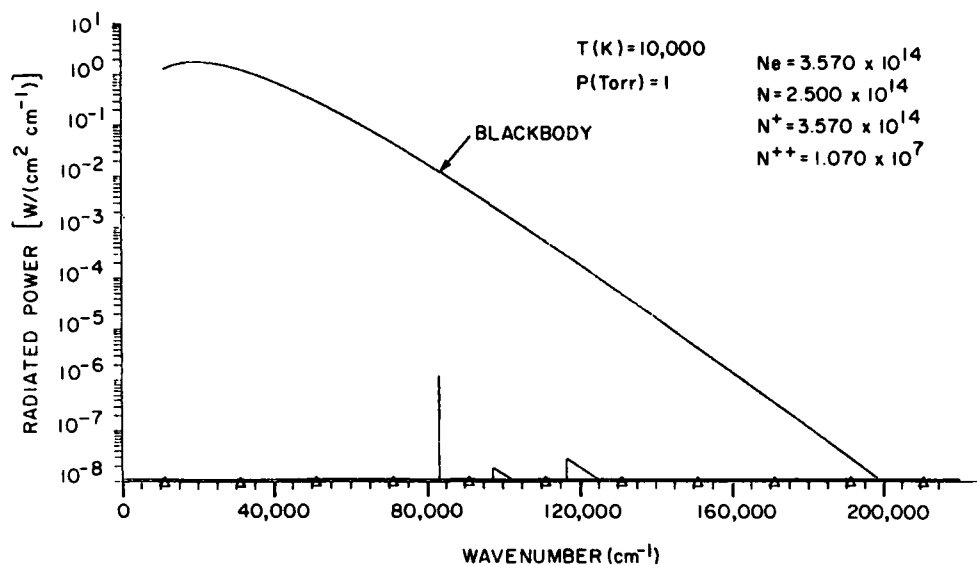
Figure 11. Emission by an Equilibrium Nitrogen Plasma Slab of Thickness
0.2 mm in the 0 to 250,000 cm^{-1} Band, T = 10,000 K, p = 1 Torr

Figure 12. Emission by an Equilibrium Nitrogen Plasma Slab of Thickness
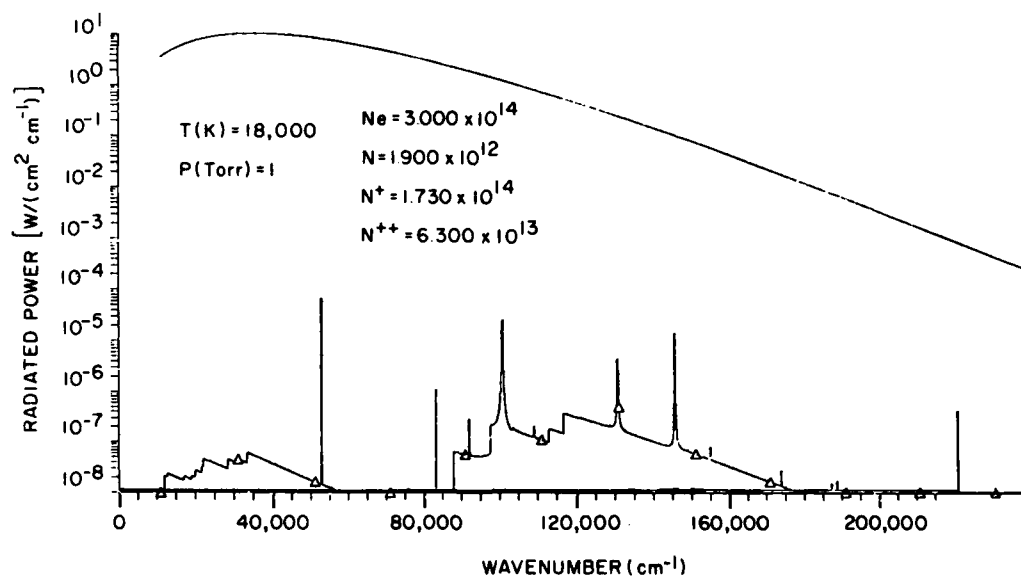0.2 mm in the 0 to 250,000 cm^{-1} Band, T = 18,000 K, p = 1 Torr

Figure 13. Emission by an Equilibrium Nitrogen Plasma Slab of Thickness 0.2 mm in the 0 to 250,000 cm^{-1} Band, T = 32,000 K, p = 1 Torr

Figure 14. Emission by an Equilibrium Nitrogen Plasma Slab of Thickness 0.2 mm in the 0 to 250,000 cm^{-1} Band, T = 10,000 K, p = 10 Torr

Figure 15.   Emission by an Equilibrium Nitrogen Plasma Slab of Thickness
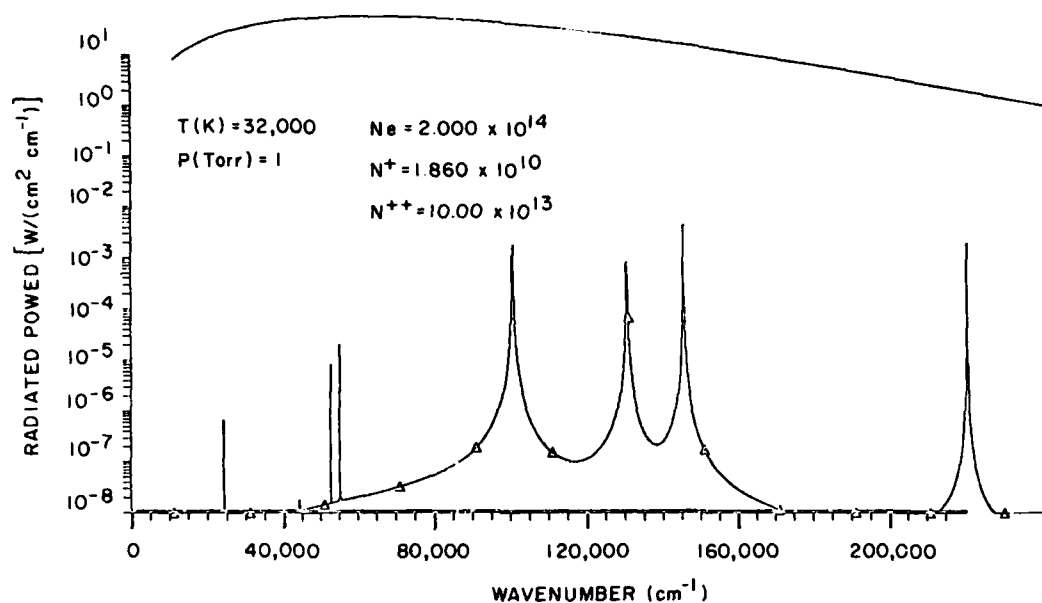0.2 mm in the 0 to 250,000 cm^{-1} Band, T = 22,000 K, p = 10 Torr

Figure 16.   Emission by an Equilibrium Nitrogen Plasma Slab of Thickness
0.2 mm in the 0 to 250,000 cm^{-1} Band, T = 34,000 K, p = 10 Torr

Figure 17. Emission by an Equilibrium Nitrogen Plasma Slab of Thickness
0.2 mm in the 0 to 250,000 cm⁻¹ Band, T = 10,000 K, p = 100 Torr

Figure 18. Emission by an Equilibrium Nitrogen Plasma Slab of Thickness
0.2 mm in the 0 to 250,000 cm⁻¹ Band, T = 22,000 K, p = 100 Torr

Figure 19. Emission by an Equilibrium Nitrogen Plasma Slab of Thickness
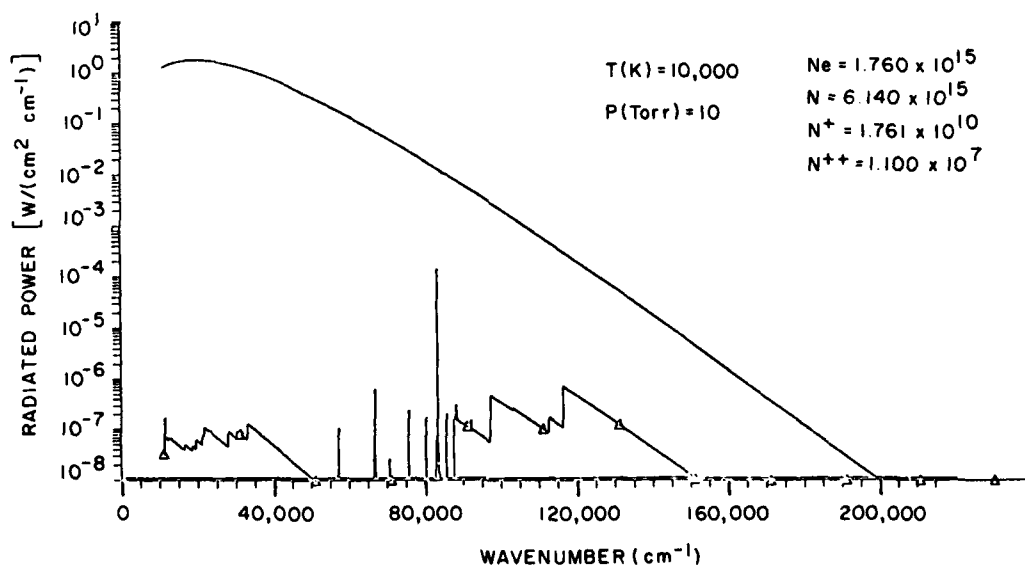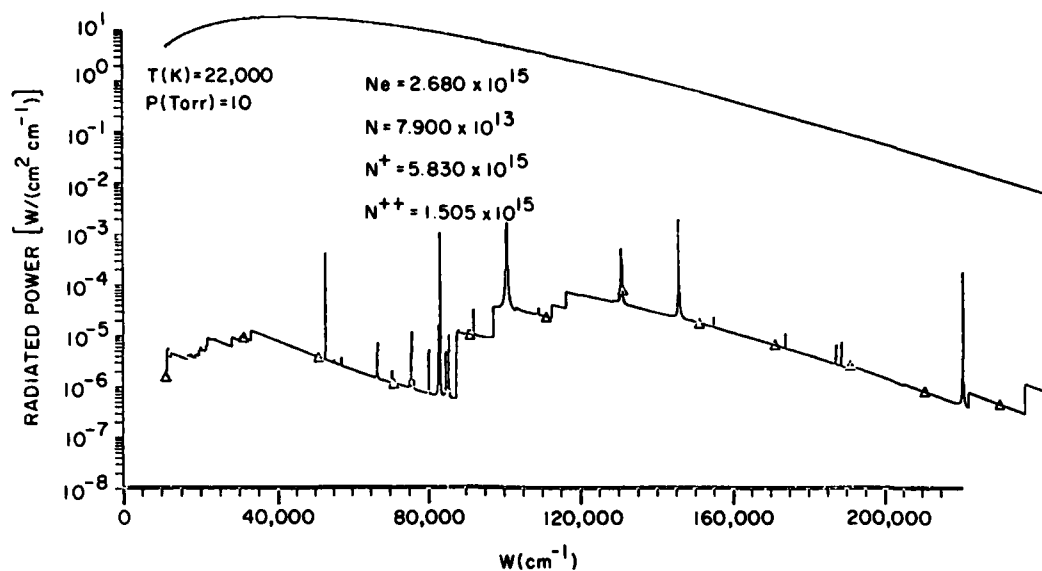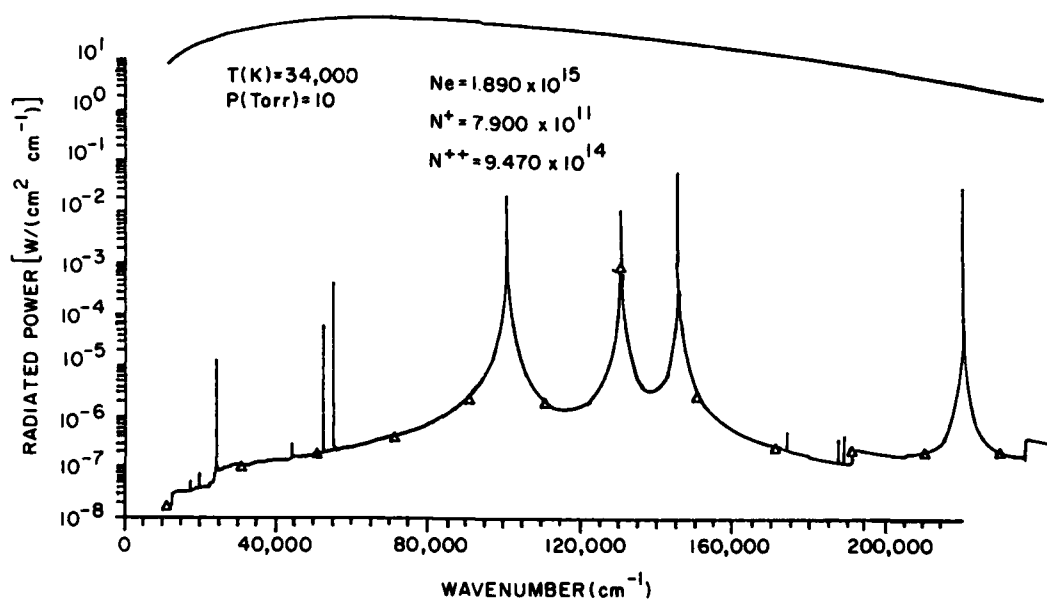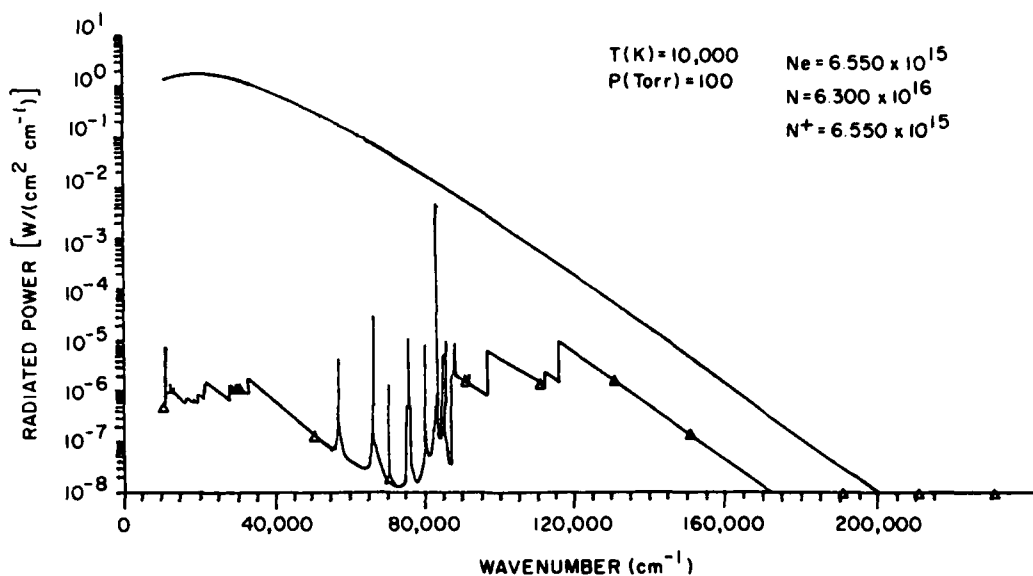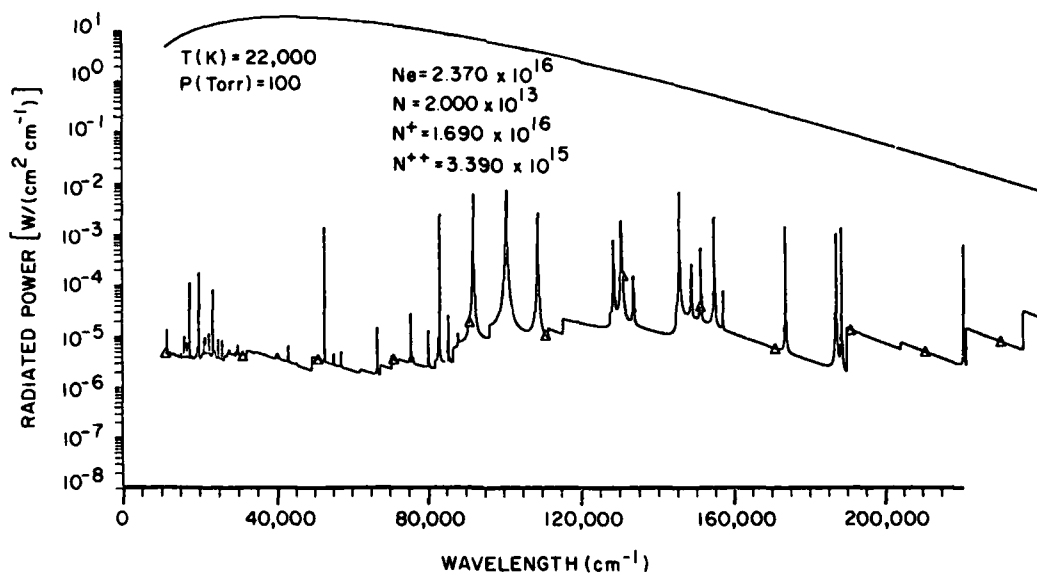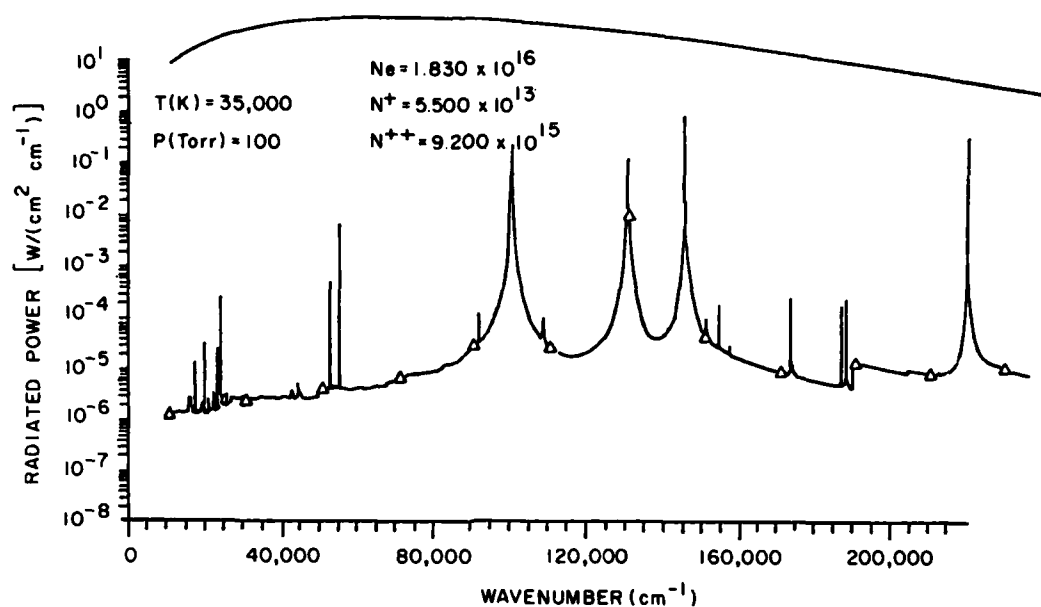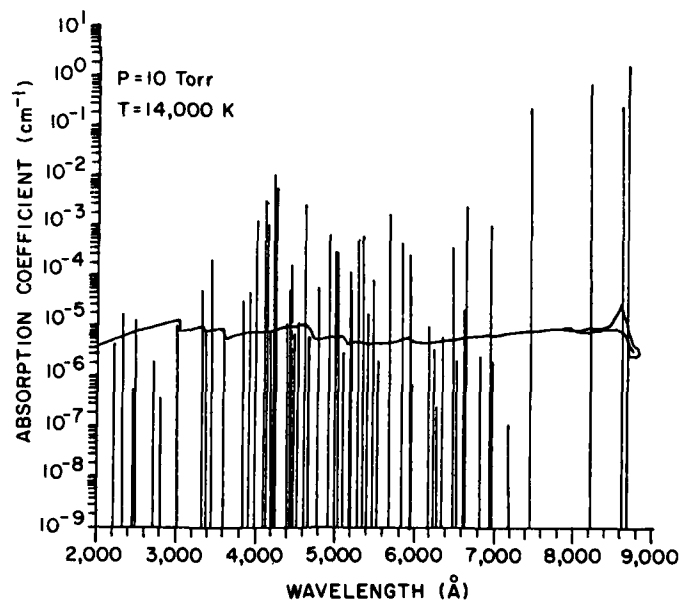0.2 mm in the 0 to 250,000 cm^{-1} Band, T = 35,000 K, p = 100 Torr

Figure 20. Absorption Coefficient at Line Center in
the 0.2 - 0.9 μm Band, Nitrogen, T = 14,000 K,
p = 10 Torr

209
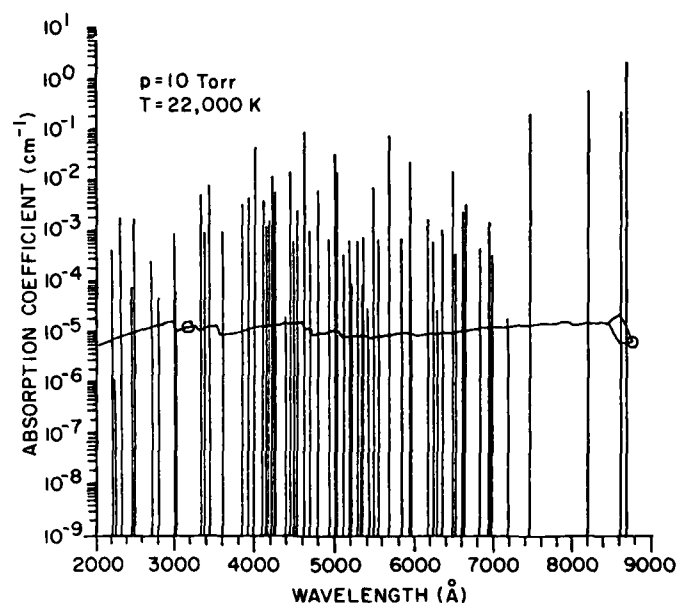
Figure 21. Absorption Coefficient at Line Center in
the 0.2 - 0.9 μm Band, Nitrogen, T = 22,000 K,
p = 10 Torr

verify that practically all experimentally observed lines, excepting the band systems of N_2 and N_2^+, are included in the radiation code. The sudden rise in continuum radiation at wave numbers larger (wavelengths smaller) than some critical wave numbers $\bar{\nu}_c$ (wavelengths λ_c) that are apparent in Figures 11 through 19 are associated with free-bound radiation following the Reaction

$$N^{Z+} + e \rightarrow \left(N^{(Z-1)^+} \right)^* + h\nu \qquad , \qquad (19)$$

where the * represents an excited state of energy ε^* and $\nu = (\varepsilon_I^{Z-1} + \varepsilon - \varepsilon^*)/h$, ε_I^{Z-1} being the ionization energy of the ion of charge $Z - 1$, and ε the free electron energy.

We show in Figure 22 radiation emitted in the wave number band $0 < \bar{\nu} <$ 250,000 cm^{-1} (500 Å $< \lambda < \infty$) and in Figure 23 the integrated emission in the spectral band of the radiometer $0.2 < \lambda < 0.9$ μm. A comparison of Figures 22 and 23 indicates that the radiometer would be measuring less than 1 percent of the radiation emitted by the plasma if it were in thermal equilibrium. Analysis of the validity of LTE for line radiation is presented in Section 4.3.

210
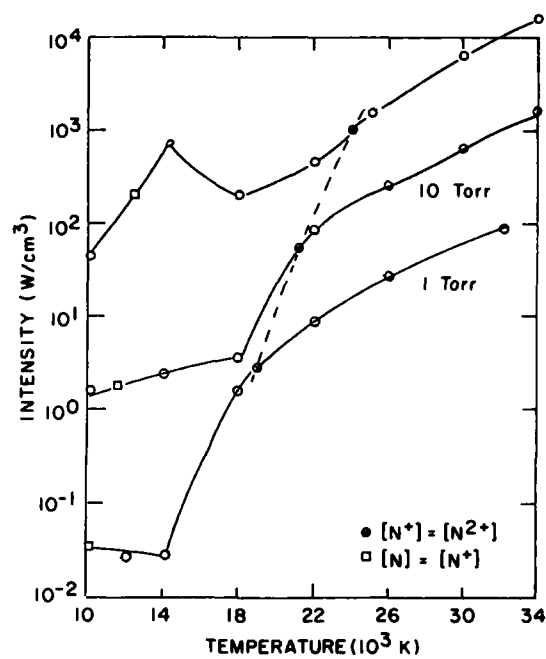
Figure 22. Integrated Emission in the
Wavenumber Band $0 < \bar{\nu} < 250,000$ cm^{-1}
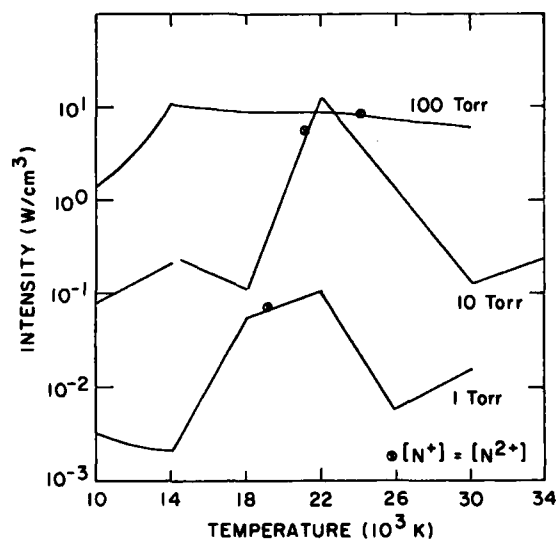
Figure 23. Integrated Emission in the Radiometer
Band $0.2 < \lambda < 0.9$ μm

211

4.2 Free Bound Continuum in the Visible

We show in Figure 24 calculated radiation in the visible (mainly due to bound-bound and free-bound transitions) for p = 100 Torr and T = 10,000 K. Also shown in this figure is time integrated spectrometer data in which line radiation has been eliminated. This curve was reproduced from the normalized spectrum shown in Figure 1. The abscissa at the maximum was chosen in such a way as to superimpose the data and computed radiation. There is a strong indication from a comparison of the two curves that the continuum radiation in the visible is due to free-bound transitions. We examine free-bound radiation in the visible in more detail below, especially with regard to the relaxation of the assumption of LTE. Free-bound radiation can be calculated by detailed balance by looking at the reverse process of Reaction (19), which is photoionization of excited states,

$$N^* + h\nu \rightarrow N^+ + e \qquad . \tag{20}$$

Figure 24. Radiation in the Visible (0.2-mm Slab)

The threshold for Reaction (6) is

$$h\nu_c = \varepsilon_I - \varepsilon^* \qquad ,$$

212

and the cross section, following Zel'dovich and Raizer,[5] is given by

$$\sigma_{phi} = 7.9 \times 10^{-18} \frac{n}{Z^2} \left(\frac{\nu_c}{\nu}\right)^3 \; cm^2 \qquad , \qquad (21)$$

where n is the principal quantum number, Z the charge of the remaining core ($Z = 1$ for N^+) and $\nu > \nu_c$. By detailed balance we must have

$$(1 - e^{-h\nu/kT}) \frac{\rho_{BB}(\nu, T)c}{h\nu} \; d\nu \; \sigma_{phi} [N^*] = n_e [N^+] f_B(\epsilon, T) \; \sigma_{FB}(\epsilon) \sqrt{\frac{2\epsilon}{m}} \; d\epsilon \quad , \qquad (22)$$
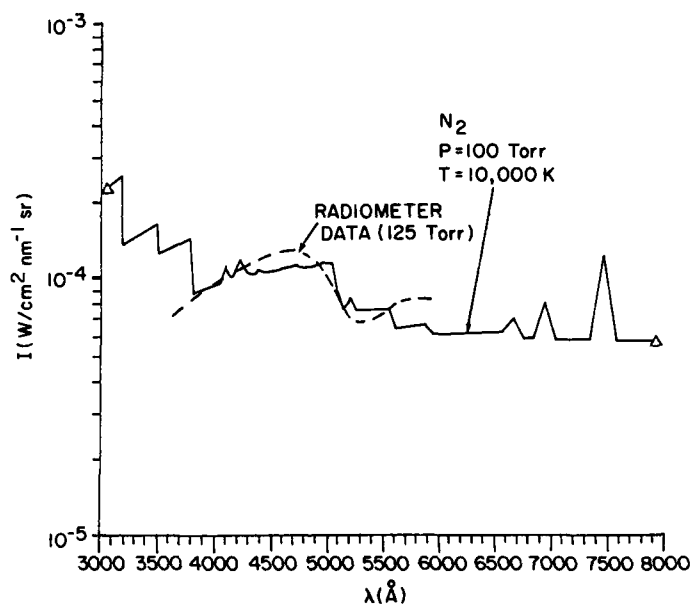
where $d\epsilon = hd\nu$, f_B is a Maxwell Botzmann distribution function for electrons at T and ρ_{BB} is the energy density of black body radiation per unit frequency interval. The concentrations of electrons, $[N^*]$ and $[N^+]$ are related by the equations of LTE,

$$\frac{[N^+][n_e]}{[N^*]} = \frac{[N^+][n_e]}{[N]} \; \frac{[N]}{[N^*]} = \frac{AT^{3/2} g^+}{g^*} e^{-\left(\frac{\epsilon_I - \epsilon^*}{kT}\right)} \quad . \qquad (23)$$

The radiation code that we have used uses the left-hand side of Eq. (22) to calculate the plasma radiation while in reality it is the right-hand side which represents emission. After the rapid expansion, the plasma is far from LTE, as we shall see in Section 4.3, since recombination is slow. The radiation per unit volume is given by

$$\int W(\nu) \, d\nu = \int h\nu \, n_e [N^+] \sqrt{\frac{2\epsilon}{m}} \; f(\epsilon) \; \sigma_{FB} \frac{d\epsilon}{d\nu} \, d\nu$$

$$= \int h^2 \nu \, n_e [N^+] \sqrt{\frac{2\epsilon}{m}} \; f(\epsilon) \; \sigma_{FB}(\epsilon) \, d\nu \qquad ,$$

where $f(\epsilon)$ is the distribution function of electrons in energy space. The free-bound cross section is found to be, from Eqs. (21) through (23),

$$\sigma_{FB}(\epsilon) = \frac{\sigma_{phi}(\nu)}{2} \frac{(h\nu)^2}{mc^2 \epsilon} \frac{g^*}{g^+} \cong \frac{h\nu n^2}{mc^2 \epsilon} \sigma_{phi} \qquad (\nu = \nu_C + \epsilon/h) \quad , \qquad (24)$$

---

5. Zel'dovich, Ya., and Raizer, Yu. (1966) Physics of Shock Waves and High Temperature Hydrodynamic Phenomena, Academic Press, New York, pp. 265 and 405.

where in the last step we used the fact that $g^* \cong 2n^2$ (n = principal quantum number). If we assume that $f(\varepsilon)$ is a Boltzmann distribution at temperature T,

$$f_B(\varepsilon) = \frac{2}{\sqrt{\pi}} \frac{\sqrt{\varepsilon}}{(kT)^{3/2}} e^{-\varepsilon/kT} \quad , \tag{25}$$

we obtain the radiation emitted per unit volume in the bandwidth $\Delta \nu$

$$W(\nu) \Delta \nu = h \nu n_e [N^+] f_B(\varepsilon, T) \sigma_{FB} \sqrt{\frac{2\varepsilon}{m}} \frac{d\varepsilon}{d\nu} \Delta \nu$$

$$= \sqrt{\frac{8}{\pi m}} \frac{1}{(kT)^{3/2}} n_e [N^+] e^{-\varepsilon/kT} \frac{(h\nu)^2}{mc^2} n^2 \sigma_{phi} \quad (\nu = \nu + \varepsilon/h) \Delta \nu$$

$$= B e^{-\varepsilon/kT} \left(\frac{\nu_c}{\nu}\right) \Delta \nu \quad , \tag{26}$$

where in the last step we lumped into the factor B all quantities that do not depend on ν, and note that, by conservation of energy, $\varepsilon = h(\nu - \nu_c)$.

We show in Table 1 the wavelengths $\lambda_j (=c/\nu_j)$ and corresponding energy levels that represent the threshold below which a free-bound radiative transition can occur. The actual radiation at $\lambda(\nu)$ will correspond to the sum of those transitions for which $\lambda_j > \lambda$ (or $\nu_j < \nu$).

$$W(\nu) = \sum_{\nu_j < \nu} B_j e^{-h(\nu - \nu_j)/kT} \left(\frac{\nu_j}{\nu}\right) \quad . \tag{27}$$

We have used Eq. (27) to model free-bound radiation in the visible. Since the spectrometer measured $W(\lambda)$ rather than $W(\nu)$ it is more convenient to rewrite Eq. (27) as

$$W(\lambda) = \sum_{\lambda_j > \lambda} B_j \left(\frac{\lambda}{\lambda_j}\right)^3 e^{-\left[\frac{hc}{kT}\left(\frac{1}{\lambda} - \frac{1}{\lambda_j}\right)\right]} \quad . \tag{28}$$

We have plotted Eq. (28) in Figure 25 assuming B_j was the same for all transitions and with T chosen so that

$$\frac{W(\lambda = 4200\text{Å})}{W(\lambda = 3500\text{Å}} = 2 \quad ,$$

214

Table 1. Energy Levels for Free-Bound Radiation in the Visible

Species	λ_j (Å)	State	ε_j^* (cm^{-1})
N	8180	$2p^2\ 3d\ ^2D$	105030
	7850	$2p^2\ 3d\ ^1P$	104600
	7270	$2p\ 4s\ ^4P$	103600
	5650	$2p^2\ 3s\ ^2D$	99660
	5108	$2p^2\ 3p\ ^2P^o$	97770
	4867	$2p^2\ 3p\ ^2D^o$	96800
	4855	$2p^2\ 3p\ ^4S^o$	96750
	4570	$2p^2\ 3p\ ^4P^o$	95476
	4442	$2p^2\ 3p\ ^4D^o$	94770
	4208	$2p^2\ 3p\ ^2S^o$	93582
	3213	$2p^2\ 3s$	86223
N^+	5680	$2p\ 5f\ ^3G,\ ^1G$	221200
	4067	$2p\ 5s\ ^3P_o$	214250
	3655	$2p\ 4f\ ^3D,\ ^1G$	211490
	3630	$2p\ 4f\ ^3G$	211300
	3590	$2p\ 4f\ ^1F,\ ^3F$	211000
	3550	$2p\ 4d\ ^3P^o$	210705

as was experimentally observed. This yields an electron temperature of 1.4 eV (16,000 K). The resulting free-bound continuum thus obtained has a strikingly similar shape to the experimentally observed continuum. Note, however, that, because the radiation was measured with a relatively long (200 nsec) boxcar integrator, it is likely that the electron temperature varied significantly during the measurement.

We also have plotted, as a dashed line in Figure 25, free-bound radiation due to the reaction
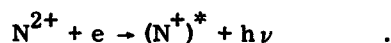
$$N^{2+} + e \rightarrow (N^+)^* + h\nu \qquad .$$

It is clear from the figure that recombinations of N^{2+} cannot explain the radiation peak observed at 4500 Å.

215

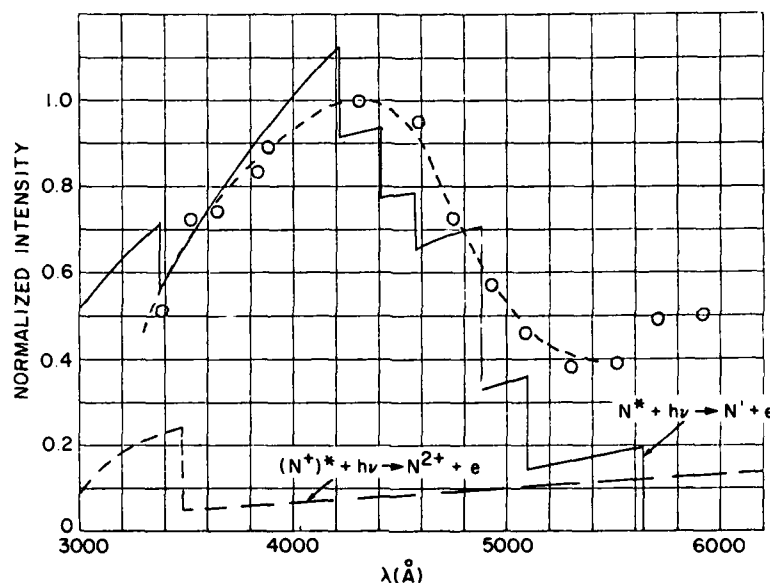Figure 25. Free Bound Continuum Due to the Reactions
$N^+ + e \rightarrow N^* + h\nu$ and $N^{++} + e \rightarrow N^+ + h\nu$

4.3 Temporal Behavior of Line Radiation

We have shown in Figures 2 through 4 some of the data taken that show the temporal behavior of line radius in the LINUS. This behavior can be summarized as follows:

(1) The radiation first increases with time, reaches a maximum, and then decreases.

(2) Peaks in radiation occur first for lines from N^{2+}, then N^+, and finally N.

(3) The decay times increase with increasing pressure, decrease with increasing ionization, and are in the range 20 - 200 nsec.

(4) All lines originating from the same ionic species have roughly the same decay times irrespective of the upper energy level from which they originate.

Since the lifetime for transitions measured in the visible is $\sim 10^{-8}$ sec, that is, much shorter than the observed decay times of the line radiation, one must recognize that the excited states are being replenished. Therefore, observation 3 together with observations 1 and 2 are consistent with the hypothesis that LTE is maintained during and after the expansion. The rise and decay of line radiation would be associated, then, with the shift in dominant ionic species from N^{3+} to N^{2+}, N^+ and, finally, N as the plasma cools by expansion and later by thermal conduction. We must verify, however, that observation 4, obtained from the decay rate of line radiation (see Figure 3) is satisfied. We now analyze decay of N^+

line radiation. If LTE were maintained, the concentration of N^+ ions would be given by the Saha equation, Eq. (10),

$$\frac{n_e[N^+]}{[N]} = A T^{3/2} \frac{g^+}{g} \exp(-\varepsilon_1/kT) \quad . \quad (10)$$

Also, the population of the excited state is proportional to its Boltzmann factor.

$$\frac{[N^+]^*}{[N^+]} = \frac{g^*}{g_+} \exp(-\varepsilon^*/kT) \quad , \quad (29)$$

where ε^* is the energy with respect to the ground state of the ion. When $[N^+]$ $\gg [N]$, we can neglect the variation of n_e and N^+ with temperature and, taking the logarithmic derivative of Eq. (29), we obtain the decay of line intensity S_{ij},

$$\frac{d\ln S_{ij}}{dt} = \frac{d\ln(N^+)}{dt} - \frac{\varepsilon^*}{kT} \frac{d\ln T}{dt} \quad . \quad (30)$$

At lower temperatures, however, when N^+ is rapidly disappearing by recombination, we have $[N^+] \propto T^{3/4} \exp(-\varepsilon_1/2kT)$, so that taking the logarithmic derivative of Eq. (29), we obtain

$$\frac{d\ln S_{ij}}{dt} = \frac{2\varepsilon^* + \varepsilon_1}{2kT} \frac{d\ln T}{dt} \quad . \quad (31)$$

We apply the above to Figure 3. Information on the lines is given in Table 2. We compare line #15 having the lowest energy $\varepsilon^* = 20.63$ eV with line #61 having the highest energy $\varepsilon^* = 26.2$ eV. From Figure 10 we expect the N^+ concentration to become important and that N^+ line radiation peaks when the temperature of the plasma has decreased to ~ 1.6 eV at $p = 10$ Torr. The concentration of the 4 f state of N^+ (upper level of line #61) has decreased by a factor of 10 when the temperature has changed by an amount $-\theta$ such that

$$0.1 = \exp - 26.2 \left(\frac{1}{1.6 + \theta} - \frac{1}{1.6} \right) \quad ,$$

which yields $\theta = 0.2$ eV = 2300 K. The concentration of the 3 p state of N^+ (line #15) using the same change in temperature has decreased by a factor of only 6.1. The data in Figure 1 at $s = 285$ nsec indicate that when line #61 is at 1/10th of its peak, line #15 is at 1/8th of its peak value rather than at 1/6th. There is, therefore, some indication from the relative decay of line radiation that LTE is not maintained. The deviation is not sufficiently large to infer in a conclusive way that LTE is not maintained.

217

Table 2. Energy Levels of Observed Transition

Line Number	Wavelength (Å)	Upper Energy Level (cm^{-1})
20	3437.2	178274
41	3838.4	196712
61	4040.9	211332
25	4447.0	187092
17	4621.4	170573
28	4803.3	187493
16	5045.1	168893
15	5679.6	166679

The line profiles, however, imply a drop of 2300 K in 180 nsec $\times$ (T/θ) = 1.6 μsec. We can readily show that the thermal decay time is much shorter than this. The plasma is cooled by three processes: (1) by expansion during the blast wave, (2) by radiation, and (3) by conduction to the surrounding cooler gas. From Section 3, the rate of cooling of the plasma at time t due to the expansion is

$$\frac{d\ell nT}{dt} = -\left(\frac{\gamma - 1}{\gamma}\right)t^{-1} \qquad , \tag{32}$$

so that for $\gamma = 1.2$, corresponding to LTE being maintained and $t \sim 10^{-7}$ sec, we find $d\ell nT/dt \sim 16 \times 10^6$ sec^{-1}, which is a factor of three larger than the decay rate inferred from line radiation.

The plasma cooling rate due to conduction and radiative losses can be estimated from the enthalpy equation for the plasma

$$\rho \frac{dh}{dt} = \frac{1}{r}\frac{\partial}{\partial r}\left(rK \frac{\partial T}{\partial r}\right) + \phi_R \qquad , \tag{33}$$

where K = heat conductivity, h = enthalpy and ρ = density. The second term on the right-hand side of Eq. (33) represents radiation losses. The decay rates due to thermal conduction and radiative losses are, respectively

$$\tau_C^{-1} = \frac{1}{h}\frac{d_C h}{dt} = \frac{KT}{\rho hL^2} \qquad , \tag{34a}$$

and

$$\tau_R^{-1} = \frac{1}{h} \frac{d_R h}{dt} = \frac{\phi_R}{\rho h}$$ (34b)

We use the equilibrium high temperature air properties of Yos to obtain ρ, h and K as a function of T for various pressures. These are shown in Figures 26 through 28. Open shutter photographs of the plasma indicate a plasma diameter after expansion of 0.2 mm, so that we may take L = 0.1 mm as an upper bound on plasma radius during the expansion. Using the above values, we obtain the times τ_L and τ_R shown in Figures 29 and 30. We see that thermal conduction losses will dominate the cooling process. At T ≈ 20,000 K and p = 10 Torr the cooling rate is 5×10^8 sec^{-1}, which would lead to a line decay rate (ϵ^*/kT) $\times 5 \times 10^8 = 5 \times 10^9$ to 3×10^{10} sec^{-1}, a rate faster than the decay rate of the highly excited states (10^8 sec^{-1}). We, therefore, can conclude that the plasma cooling rate by conduction is inconsistent with the observation of decay of line radiation and with the assumption of LTE. Some mechanism must play a role in limiting the population of the excited states from following LTE. We believe that the bottleneck is three-body recombination, as discussed in the next subsection.

We close the subsection by noting that the pressure dependence of the decay of line radiation is more consistent with the conclusion that thermal conduction rather than blast wave expansion determines the cooling rate of the plasma at t ≥ 100 nsec. The blast wave formulas do not have a pressure dependence in the decay rate of
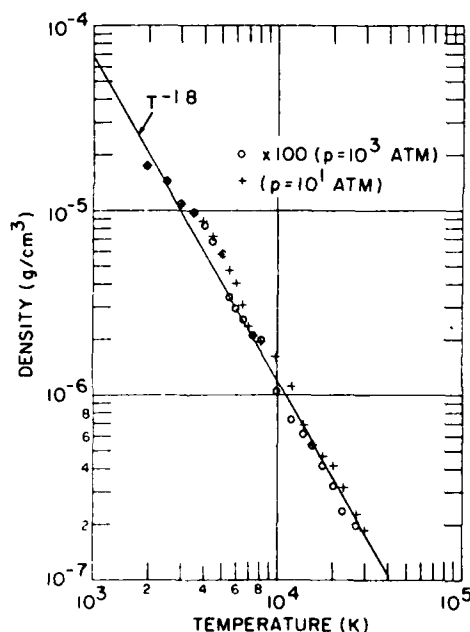
Figure 26. Density of Nitrogen

219
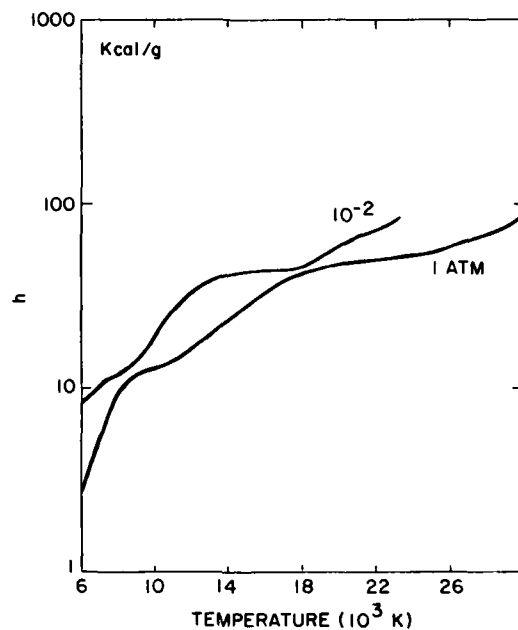
Figure 27. Enthalpy of Nitrogen
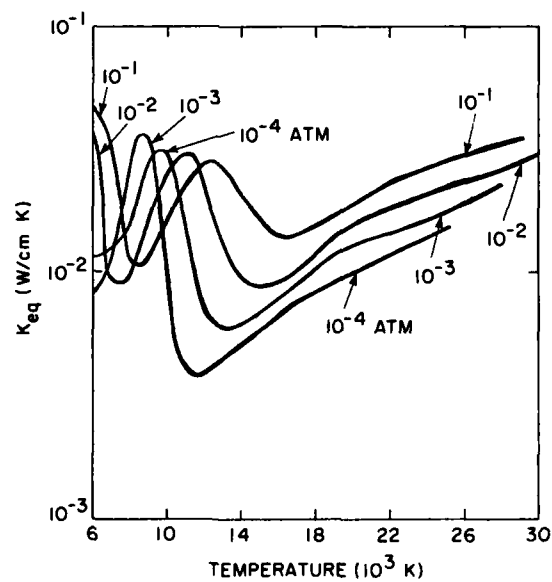
Figure 28. Thermal Conductivity of Nitrogen

220
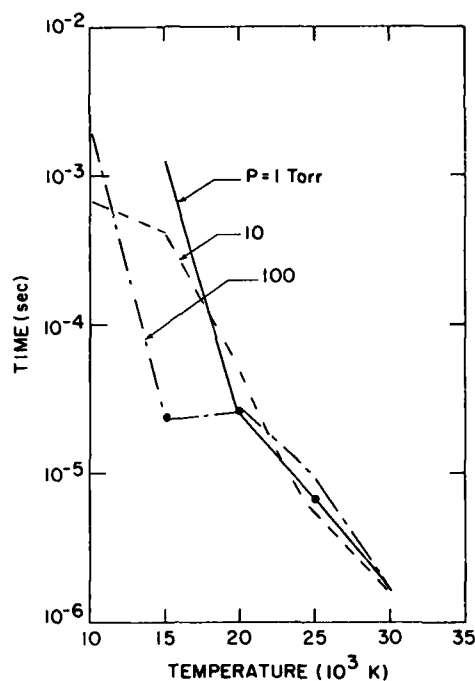
Figure 29. Thermal Decay Time Due
to Radiation - τ_R

temperature. We note from Figure 30 that the thermal decay time τ_C scales roughly as p. Figure 2 shows the decay time of line radiation increases as some positive power of p.

4.4 Recombination of Plasma During and After Expansion

There are two mechanisms through which the fully ionized nitrogen plasma may recombine:

(a) Radiative recombination

$$N^{Z+} + e^- \overset{b_\nu}{\rightarrow} N^{(Z-1)^+} + h\nu \qquad ; \qquad (35)$$
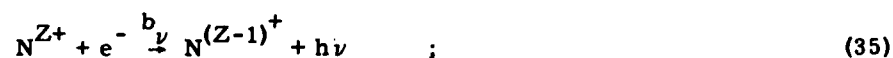
(b) Three-body recombination

$$N^{Z+} + e^- + M \overset{k_R}{\rightarrow} N^{(Z-1)^+} + M \qquad . \qquad (36)$$

Following Zel'dovich and Raizer[5] the radiative recombination rate is given by

221
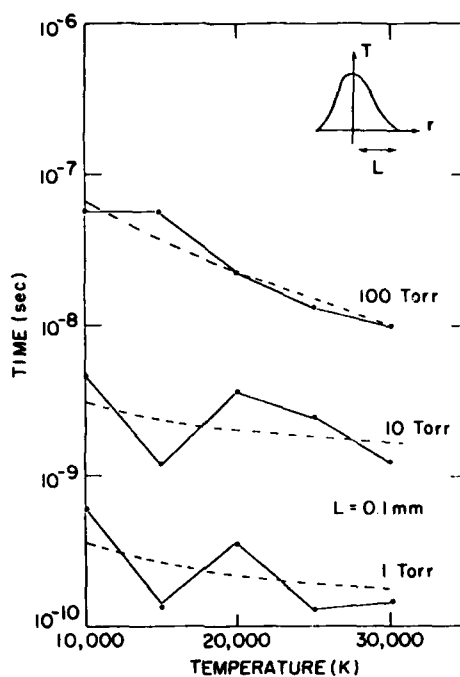
Figure 30. Thermal Decay Time Due
to Thermal Conduction. Plasma radi-
us = 0.1 mm

$$b_\nu \cong \frac{2 \times 10^{-11} Z^2}{T^{1/2}} \text{ cm}^3/\text{sec} \qquad , \qquad (37)$$

while the three-body recombination rate is given by

$$k_R = \frac{1.65 \times 10^{-8} Z^2 n_e}{T^{9/2}} \text{ cm}^3/\text{sec} \qquad , \qquad (38)$$

where we chose the third body in reaction b to be an electron. Three-body re-
combination is found to dominate two-body recombination when

$$n_e > 1.3 \times 10^{-3} \, T^4 \qquad .$$

The above inequality is expected to be satisfied under the conditions of the LINUS
experiment so that we need only consider three-body recombination.

222

Following the analysis of Pitaevskii[6] and others,[7] electron three-body re-combination is a process whereby a third body (an electron for the problem at hand) carries away the energy that is lost when a free electron gets captured into a highly excited state. The radiative lifetime of the excited state then formed is sufficiently long that many more collisions occur with free electrons exciting and deexciting the excited states till finally a sufficiently strongly bound state is formed that can radiate (in the UV and deep UV) to the ground state of the ion (atom). Pitaevskii treats the problem of recombination as a diffusion of electrons in energy space subject to the boundary condition $f(\varepsilon) = 0$ for $\varepsilon < \varepsilon^*$, where $f(\varepsilon)$ is the electron distribution function and ε^* is the lowest lying excited state above which radiation by a transition to the ground (or low lying) state can be neglected.

To ascertain the importance of two and three body recombination reactions in the LINUS, we have developed a map, Figure 31, which shows rates as a function of n_e and T. We show in Figure 31 n_e versus T for a plasma in LTE at 1, 10, and 100 Torr. The dashed line corresponds to equality of the two recombination rates. The region of the map to the left of this dashed line is the region where three-body recombination dominates. The dash-dotted line in Figure 31 represents the lines of constant recombination rate for the reactions

$$N^+ + 2e \rightarrow N + e \qquad , \qquad (39)$$

and

$$N^{++} + 2e \rightarrow N^+ + e \qquad . \qquad (40)$$

Since the rate scales as Z^2, the lines to right of the graph representing Reaction (40) are displaced downward by a factor of $\sqrt{Z^2} = 2$ as compared to those representing Reaction (39). Recombination is seen to be fast at p = 100 Torr but slow when p ≤ 10 Torr. The recombination rate, however, following Eq. (4) depends strongly on the electron temperature. During the recombination process there will be a tendency for T_e to increase. Cooling of the electrons will occur due to collisions with the heavies. We showed in Figure 6 the electron-ion equilibration time (τ_{ei}) before expansion. After expansion, when the pressure has decreased by a factor of 100 to 1000 and the density by a somewhat smaller amount, the electron-ion equilibration time is expected to be ~ 100 times longer than that

6. Pitaevskii, L. (1962) Electron recombination in a monatomic gas, Sov. Phys. JETP 15:919.

7. Bates, D., Kingston, R., and McWhirter, R. (1962) Recombination between electrons and atomic ions in optically thick plasmas, Proc. Roy. Soc. (London) A270:155.
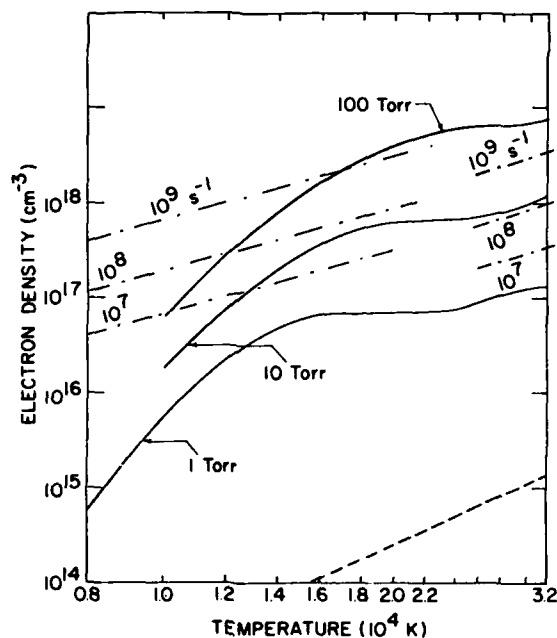
223

Figure 31. Equilibrium Electron Density
in a Nitrogen Plasma

shown on Figure 6. We believe that the electron cooling time will be sufficiently lengthened as recombination occurs as to significantly slow down this recombination process.

4.5 Validity of Assumption of LTE for Line Radiation

The line radiation that has been monitored in the LINUS experiment originates from highly excited states of N, N^+, and N^{++} that are being populated by the three-body recombination process. Depending on how high these states are the relative population of the states with respect to each other will be related through a Boltzmann relation with some effective temperature T_e or will only be related by the branching ratios for radiative decay from excited states above the state of interest. Following Griem[4] the validity of LTE for a given state depends on the electron density exceeding the critical value.

$$N_e = 7 \times 10^{18} \frac{Z^7}{n^{17/2}} \left(\frac{kT}{\varepsilon_H Z^2}\right)^{1/2} cm^{-3} \qquad ,$$

where Z = ionic charge as seen by the outer electron, n = principal quantum number of the state considered, and ε_H = 13.6 eV. The validity of LTE has to be determined on a line-by-line basis. As an example consider the 4040 Å line of N^+

224

for which $n = 4$, $Z = 2$. If we choose $T = 20,000$ K we obtain $n_e > 1.2 \times 10^{15}$ cm^{-3} for LTE to be maintained for the line. If, on the other hand, we had considered the 4059 Å line of N^{++} ($n_{eff} = 2.5$, $Z = 3$, $T = 25,000$ K) we would have the much more stringent condition $n_e > 7 \times 10^{17}$ cm^{-3}. These densities are to be compared with the calculated n_e for LINUS: $n_e = 2.4 \times 10^{16}$, 2.7×10^{15}, and 3×10^{14} at pressures of 100, 10, and 1 Torr, respectively. One will, therefore not expect to obtain an LTE population of the upper state corresponding to the 4059 Å transition of N^{++}; LTE for the 4040 Å transition of N^{+} may, however, hold at the highest pressure considered.

5. CONCLUSIONS

From the discussion of the previous sections we can draw the following conclusions with respect to visible radiation in the LINUS experiment:

(1) Continuum radiation observed in the 3500 - 7000 Å band is very probably due to the two-body radiative recombination reaction

$$N^{+} + e \rightarrow N^{*} + h\nu \qquad .$$
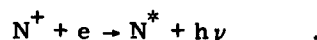
The spectral characteristics of the continuum indicate an electron temperature $T_e \cong 14,000$ K. Since spectral measurements were obtained with an open shutter camera over a period of time which is long as compared to the plasma expansion time and cooling time, the measured electron temperature can only be considered as a time averaged one.

(2) The line radiation observed cannot be analyzed on the basis of LTE since (a) the electron density is too low to maintain a temperature equilibrium between free and most bound electronic states, and (b) the decay of line radiation is much longer than the calculated cooling times (multiplied by kT/ϵ_I) based on thermal conduction losses.

(3) The temporal behavior of line radiation is dominated by three-body recombination which populates highly excited states of the ions and atoms. These excited states then radiate by bound-bound transitions, a fraction of which spans the visible spectrum. The rise and decay of N^{2+}, N^{+} and N* radiation is associated with the population growth and decay of these ions and atoms by successive recombination. The recombination rate scales as $n_e^2/T_e^{9/2}$. As the plasma cools down (by conduction losses) it contracts so that n_e increases. The increase in n_e and decrease in T_e make the recombination rate, and thus radiation, increase with time. The ultimate decay of line radiation will then be associated with disappearance of the particular species considered.

225

(4) The pressure dependence of the time scales for line radiation is due to heat conduction losses that scale as $1/p$. The radial diffusion of charged species, which increases as the pressure is decreased, should, however, slow down the recombination and may counterbalance somewhat the effect of more rapid heat losses at the lower pressures.

Finally, one must consider radiation and cooling during the blast wave expansion. The time for pressure equilibrium is of the order of 100 nsec, that is, of the same order as the duration of line radiation. Though blast wave expansion times should be independent of pressure for a constant energy per unit mass deposited, the breakdown mechanisms should be somewhat dependent on pressure, that is, the efficiency of laser coupling to the nitrogen would depend on p. If we assume that recombination is slow during the expansion, then n_e is proportional to density ρ and we obtain a radiation per unit volume that scales as $n_e^2/T_e^{9/2} = \rho^2/T^{9/2}$. Since the spectrometer is looking at a slice of the plasma, the radiation will be proportional to $R^2\rho$, but, by conservation of mass for the laser heated gas, $R^2\rho$ = constant. Radiation will therefore scale as $R^2\rho^2/T^{9/2} \propto \rho/T^{9/2} \propto (t/t_o)^{9\gamma-11/2\gamma}$, where in the last step we used cylindrical blast wave results for a gas of constant γ. For frozen gas chemistry (that is, slow recombination), $\gamma = 5/3$ and the radiation will scale as $t^{6/5}$, or almost linearly with time. However, as the recombination rate increases and recombination becomes important, the value of γ should decrease. Indeed when $\gamma \leq 11/9$ (which should occur under equilibrium conditions) blast wave scaling will yield a decrease in line radiation with time. Thus, blast wave effects could also explain the rise and fall of line radiation.

References

1. Armstrong, R., Lucht, R., and Rawlins, W. T. (1973) Spectroscopic investigation of laser-initiated low-pressure plasmas on atmospheric gases, Appl. Opt. 22:1573.

2. Nebolsine, P., and Weyl, G. (1982) LINUS Final Report for the Period Oct. 1, 1981 - Sept. 30, 1982, Physical Sciences Inc., PSI TR-348.

3. Pirri, A., Root, R., and Wu, P. (198) Analytical Laser/Material Interaction Investigation -- Part I, Theory, Final Report, Physical Sciences Inc, PSI TR-104.

4. Griem, H. (1964) Plasma Technology, McGraw Hill, New York, Table 4-5.

5. Zel'dovich, Ya., and Raizer, Yu. (1966) Physics of Shock Waves and High Temperature Hydrodynamic Phenomena, Academic Press, New York, pp. 265 and 405.

6. Pitaevskii, L. (1962) Electron recombination in a monatomic gas, Sov. Phys. JETP 15:919.

7. Bates, D., Kingston, R., and McWhirter, R. (1962) Recombination between electrons and atomic ions in optically thick plasmas, Proc. Roy. Soc. (London) A270:155.

Appendix A

COCHISE: Laboratory Studies of Atmospheric IR
Chemiluminescence in a Cryogenic Environment

by

W. T. Rawlins
H. C. Murphy
G. E. Caledonia
J. P. Kennealy
F. X. Robert
A. Corman
R. A. Armstrong

229

COCHISE: laboratory studies of atmospheric IR chemiluminescence in a cryogenic environment

W. T. Rawlins, H. C. Murphy, G. E. Caledonia, J. P. Kennealy, F. X. Robert, A. Corman, and R. A. Armstrong

The design of the Cold Chemiexcitation Infrared Stimulation Experiment (COCHISE) facility, a cryogenic apparatus used for laboratory studies of high-altitude infrared excitation phenomena, is presented. The basic design concept is the extensive reduction of thermal background radiation through cryogenic (20 K) cooling of the entire reaction volume and detection system. Vibrationally excited molecules (e.g., NO, O_3, CO) are formed in a low-pressure environment by interaction of a flowing reactant gas with discharge-produced radical and/or metastable species; the resulting IR radiation is detected with minimal interference from relaxation and surface effects. A long-path optical system and cryogenic monochromator permit high sensitivity for vibrationally excited species ($\sim 10^5$ molecules cm^{-3}) and excellent spectral resolution (~ 2 cm^{-1}) over the 2-16-μm spectral range. The design and operation of the facility are described in detail. Specific applications of the facility to investigations of IR atmospheric phenomena are also discussed.

I. Introduction

Chemical excitation processes, in which some of the energy released by the reactants appear as internal energy in the product molecules, can provide important mechanisms for molecular IR radiation and nonequilibrium energy disposal in the quiescent and disturbed upper atmosphere. There are two generic types of such processes: chemiexcitation,

$$A + BC \rightarrow AB^\dagger + C, \qquad (1)$$
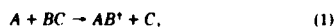
where chemical bonds are broken and/or formed; and energy transfer,

$$AB + C^\dagger \rightarrow AB^\dagger + C, \qquad (2)$$
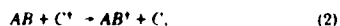
in which the chemical identities of the collision partners are unchanged, but excitation energy is transferred from species C to species AB. The predominant IR-active mode of excitation of $AB^\dagger$ is vibrational; however, some atmospheric species (most notably N_2 and O_2) possess electronic states which can radiate in the IR. It is often

difficult to deduce detailed information about these processes from in situ atmospheric measurements of IR emission; such data often have low spectral resolution and contain contributions from competing thermal and scattering mechanisms. However, laboratory investigations of individual chemical processes under carefully controlled conditions can provide detailed mechanistic and spectroscopic information; this information can, in turn, be used in conjunction with atmospheric models to both interpret in situ data and define further measurements.

Infrared emission spectroscopic experiments designed to investigate gas phase chemiexcitation reactions require (1) high sensitivity to the relatively weak molecular radiation from the products of reactions (1) and (2); (2) adequate resolution to allow conclusive spectral analysis; and (3) specificity to the chemiexcitation process under investigation, i.e., negligible interference from radiative, collisional, and surface relaxation processes. These conditions work against each other; the achievement of condition (3) necessitates the use of small pressures and/or product yields, which results in low radiation levels and increases the difficulty of achieving conditions (1) and (2). Furthermore, the limitation of IR detection sensitivity by thermal background radiation in the field of view severely inhibits spectrally resolved observations of long-wavelength radiation from important atmospheric species such as CO_2 (15 μm) and O_3 (10 μm). Previous IR chemiluminescence methods, such as arrested relaxation[1-3] and

W. T. Rawlins, H. C. Murphy, and G. E. Caledonia are with Physical Sciences, Inc., Research Park, P.O. Box 3100, Andover, Massachusetts 01810; when this work was done all the other authors were with U.S Air Force Geophysics Laboratory, Infrared Technology Division. Hanscom Air Force Base, Massachusetts 01731; J. P. Kennealy is now with Eikonix Corporation, 23 Crosby Drive, Bedford, Massachusetts 01731.
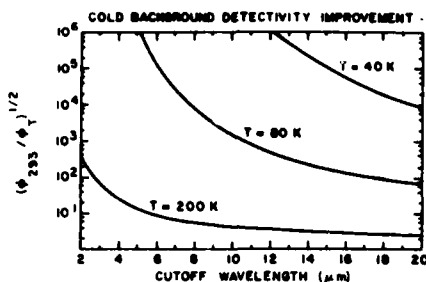
Fig. 1. Reduction in background photon flux by cryogenic operation.

discharge flow[4,5] coupled with the use of circular-variable-filter spectrometers,[5] grating monochromators,[2] and Fourier transform spectrometers,[1-4] have been highly successful in studies of chemiexcitation at wavelengths less than ~5 μm.[6] In general, however, these methods suffer from thermal background limitations; for example, at 10 μm, the spectral radiance from a typical $AB^\dagger$ species at a column density of ~10^8 cm^{-2} (often representative of such experiments) would be ~9 orders of magnitude less than that from a room temperature blackbody.

Infrared detectivity can be dramatically improved by resorting to a cryogenic background, as shown in Fig. 1. Since the limiting noise mechanism is the statistical fluctuation in the photon flux associated with the detector's environment, the detectivity of the system is inversely proportional to the square root of that flux. The results plotted in Fig. 1 are normalized to the detectivity at 293 K. Although considerable enhancement in detectivity is obtained with an 80 K background, the effects of background radiation can be virtually eliminated by cooling the entire reaction chamber/detection system to temperatures below 40 K. As a further benefit of cryogenic temperatures, rapid cryopumping of reagent gases can be attained near 20 K, and radiation leakage from the external vacuum system can then be eliminated by isolating the reaction/detection system during the experiments.

The COCHISE facility at the Air Force Geophysics Laboratory is a cryogenic apparatus designed for partial simulations and detailed experimental studies of high-altitude IR excitation phenomena, particularly chemiexcitation and excitation transfer processes. The primary design objective for the apparatus was to eliminate the limitations to IR detectivity outlined above. The experimental direction taken in the development of Cold Chemiexcitation Infrared Stimulation Experiment (COCHISE) has been to reduce the temperatures of both the reaction chamber and the detection system to ~20 K to optimize the benefits of cold background and cryopumping. A state-of-the-art IR detector and a cryogenic scanning monochromator are coupled to a long-path reaction cell to allow spectrally resolved detection of IR radiation (2–20 μm) from emitting species at concentrations below 10^6 molecules cm^{-3}. The techniques of discharge flow and arrested

relaxation are combined to allow mixing of the reacting species in the field of view at steady-state pressures near 3 mTorr, so that, in most cases, the chemiexcited products can be formed and observed under nearly single-collision conditions. The high-speed cryopumping of the reaction vessel removes the excited species from the field of view of the detection system before radiative or collisional relaxation can occur and eliminates contamination by back-diffusion from the chamber walls.

The purpose of this paper is to describe the detailed design and operation of the COCHISE apparatus. In the following section, an overall description of the apparatus will be given followed by more detailed descriptions of the various components. In the final section, some specific applications of the facility to relevant atmospheric problems will be discussed.

II. Apparatus Description

A schematic of the entire COCHISE apparatus is given in Fig. 2. The reaction cell and detection system are enclosed within a cryogenic thermal shroud, which is, in turn, enclosed by a main vacuum chamber to minimize conductive losses. All surfaces within the shroud, with the exception of selected optical components and reagent gas lines, are held at temperatures as low as ~20 K; this allows rapid cryopumping of all reagent and background gases except He and H$_2$. The reagent gases enter the reaction cell through four sets of opposing jets (see also Fig. 3) and interact along the center line of the cell; the resulting radiation is viewed along the center line through a lens by a grating monochromator detection system. The data processing, temperature control, and system housekeeping are performed by an external computer. The various components of the system are described in more detail below.

A. Thermal Isolation and Control System

The cryogenic portion of the apparatus is thermally isolated inside a cylindrical main vacuum chamber ~3 m long and ~1.5 m in diameter (Fig. 2). The thermally insulating vacuum enclosure is maintained at ~10^{-10} atm by a 50-cm (20-in.) cold-baffled diffusion pump (Consolidated Vacuum Corp.) backed by a large two-stage mechanical pump (Leybold-Heraeus DK-180). The light-tight aluminum shroud, ~2.5 m long and 1.25 m in diameter, is supported on stainless steel and phenolic standoffs and is completely surrounded by a multilayer thermal shield to provide insulation from the 300 K thermal radiation of the outer wall. This shield consists of 19 alternating layers of aluminized Mylar, Dacron bridal veil, and 0.76-mm (0.030-in.) Scott Industrial Foam and admits a total radiative load of <50 W from the 300 K outer wall to the 20 K shroud. This corresponds to a net reduction of over 2 orders of magnitude in the radiative heat flux, allowing a huge increase in the efficiency and load-carrying capacity of the cooling system. The shroud, reaction cell, and detection system are cooled to ~20 K by a 600-W closed-cycle helium refrigeration system (Cryogenic Technology,
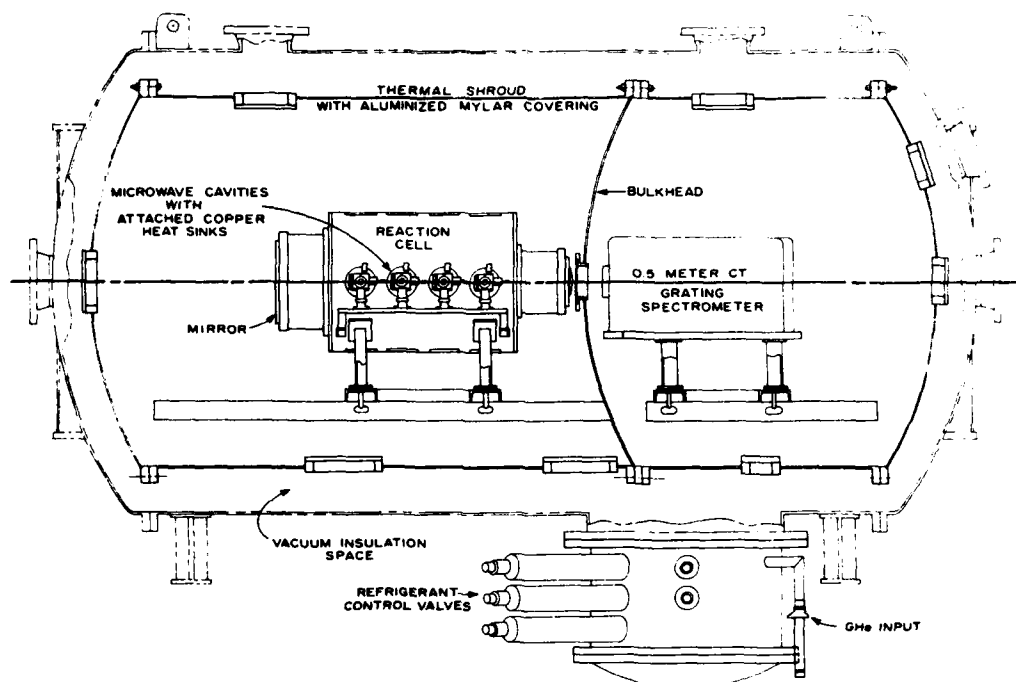
231

Fig. 2. Schematic of COCHISE facility.

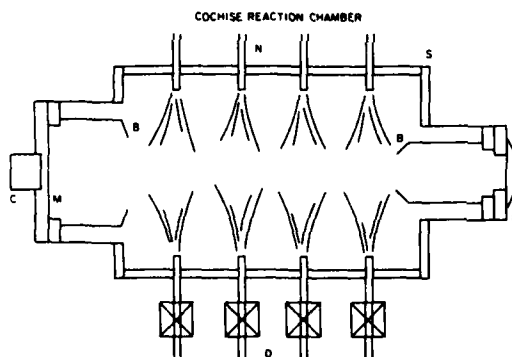COCHISE REACTION CHAMBER

Fig. 3. Scale drawing of chemiluminescence reaction cell. Ar/N$_2$/O$_2$ mixtures are excited by microwave discharges D and mix with the counterflow from nozzles N in an axisymmetric reaction zone at the chamber center. Baffles B restrict detection system field of view to the on-axis reaction volume. M is a plane mirror which increases the intensity of the radiation collected by lens L. Spectral response calibration is performed using blackbody source C embedded behind a small hole in the end mirror.

Inc.). Extended-stem valves permit control of coolant flow in three independent loops supplying the shroud, reaction cell, and microwave discharge heat sink (see below).

Component temperatures are monitored at roughly 25 locations by calibrated platinum resistance thermometers. Direct current voltage is supplied from an external source; the resulting voltage drop across each sensor is amplified, processed by analog–digital conversion in a PDP-8E (Digital Equipment Corp.) computer, converted to absolute temperature, and displayed on various storage oscilloscopes or hard copy devices. Temperatures of gas flow lines and optical components are controlled in 13 different areas by resistive heaters mounted on the appropriate hardware. Temperature-controlled portions are isolated from surrounding areas by stainless steel or phenolic standoffs. Power to the heaters is percentage-controlled by the computer via solid-state switches so that the temperature of each heat station is independently sampled and regulated to within ±0.5 K.

Because the internal cryogenic chambers are rapidly cryopumped, they may be vacuum-isolated from each other and from the external vacuum system during the measurements to seal off external light leaks. This is accomplished by means of specially modified, cryogenic, latching solenoid valves of a type not commercially available. These valves, which are operated from an external control panel, can be opened and closed by separate solenoids and will remain in either position in the absence of applied power; microswitches mounted

232

on the valve shafts provide positive readouts of the valve positions.

The physical arrangement shown in Fig. 2 emphasizes flexibility in use of the apparatus. The main vacuum chamber and cryogenic shroud have full-opening end doors and a number of access ports through which all the services for the experiments, e.g., cryogenic coolant, microwave power, reagent gases, and instrumentation, are introduced. All diagnostic and control devices are mounted externally. The ready availability of extra access ports and vacuum feedthroughs allows a high degree of adaptability to future diagnostic concepts, such as use of lasers or atomic resonance line sources.

B. Reaction Cell and Reagent Gas Lines

A schematic of the chemiluminescence reaction chamber is given in Fig. 3. The copper reaction cell is cylindrically symmetric, 60 cm in length, 40 cm in diameter. To control the cryopumping speed (and thus the reagent gas residence time—see below), the reaction cell temperature can be independently varied; temperature uniformity to ±0.1 K over the entire surface is achieved through proper positioning of coolant flow lines and heater elements.

The reagent gases are metered into the system by motorized Granville-Phillips leak valves; flow rates are monitored by calibrated mass flowmeters (Brooks). One gas mixture flows through four sapphire microwave discharge sidearms on one side of the cell; another gas mixture flows through four counterflow sidearms on the opposite side of the cell. Up to three gases can be mixed prior to introduction into the discharge cavities; two gases can be separately mixed for the counterflow. Upon penetration of the outer vacuum chamber, the room-temperature gases undergo a two-stage heat exchange process. The first stage, outside the shroud, is a copper plate cooled with liquid nitrogen; the second stage, inside the cryogenic shroud, permits variable temperature selection over the 30–500 K range. The gases then pass through temperature-controlled copper lines to the appropriate inlet sidearms and into the reaction volume. Just prior to entering the reaction cell, gases in the sapphire discharge tubes are ionized and excited by four modified McCarroll-Evenson[7] microwave discharge cavities (Opthos Instruments) powered by Raytheon PGM 10 power supplies (2450 MHz, 100 W) with a variable duty cycle. Typical operation is at 50–90% of maximum power with duty cycles of either 100 or 50% at 23 Hz, creating steady-state conditions while the discharges are on; all four discharges are driven by a single pulse generator to insure synchronous operation to within a few microseconds. Excess heat generated by the discharge plasmas is transmitted to a copper heat sink plate where it is removed by the helium coolant; the heat transfer rate is controlled via an extended-stem valve on the coolant as described above. In normal operation, the discharges are held at the desired gas temperature (typically 80–100 K in experiments to date) to within 1 or 2 K.

As shown in Fig. 3, the reagent gases are expanded into the interaction volume, with equal mass flow rates,

through four sets of diametrically opposed inlet jets which are equally spaced along the cylindrical cell. Flow conditions in the reaction cell have been modeled[8] for a range of experimental conditions; free expansion occurs in the reaction cell, and the gas reaches a limiting velocity in which nearly all the thermal energy in the inlet tube is converted into kinetic energy. Near the cylinder axis, an axisymmetric stagnation point occurs, and the thermal energy of the gas molecules returns to that of the gas in the inlet tubes. Gas density variations along the cylinder axis (reaction volume) are predicted to be ≤10%. The pressures in the reaction zone and in the sidearms are monitored by MKS Baratron capacitance manometers.

At typical flow rates used in the past, ~4 standard liter/min of various $Ar/N_2/O_2$ combinations on each side, the resulting pressures are ~1 Torr in each sidearm and ~3 mTorr in the reaction zone; the corresponding gas residence times are ~2 msec from the discharge to the expansion region, ~0.5 msec from the expansion region to the field of view, and ~0.3 msec in the field of view (see below).[9]

The chemiluminescent reactions occur primarily in the stagnation region where the opposing flows meet. The IR radiation is viewed by the detection system through a 7.6-cm (3-in.) $f/5$ antireflection (AR)-coated germanium lens; the resulting observed volume is roughly cylindrical along the optical axis so that only radiation occurring within ~4 cm of the axis is observed. A polished gold mirror at the far end of the cell enhances the collection efficiency of the system. Internal baffles on the mirror and lens discriminate against scattered light from the discharges. The walls of the reaction cell are not in the field of view. The spectral response of the optical system is routinely calibrated with a variable-temperature blackbody source imbedded in the center of the mirror.

C. Spectral Detection System

The detection system is isolated from the reaction system by an aluminum bulkhead which both blocks scattered radiation from the cell and prevents the passage of reagent gases into the detection system. Infrared radiation emanating from a cylinder ~8 cm in diameter centered along the axis of the reaction cell (or from the blackbody source in the center of the end mirror, in the case of calibration measurements) passes through the reaction cell lens into the detection system via a 7.6-cm AR-coated germanium window in the center of the bulkhead. The radiation then passes through an order-sorting filter and an optional tuning fork chopper into a cryogenic grating monochromator, where it is dispersed and focused onto a liquid-helium cooled detector.

D. Foreoptics

A series of long-wavelength-pass and/or bandpass filters is deployed by a specially constructed, solenoid-driven, rotating filter wheel. For most applications to date, long-wavelength-pass filters with sharp short-wavelength cutoffs at nominally 2, 4, and 8 μm

have been used to isolate the corresponding first-order spectral regions of 2–4, 4–8, and 8–16 μm.

A 23-Hz tuning fork chopper (American Time Products type L40 or Philamon type TFLC 34CH-7178) positioned in front of the monochromator entrance slit can be used to modulate the incoming radiation. This chopper is used in all blackbody measurements and is optional in the chemiluminescence measurements, as will be described below.

E. Cryogenic Monochromator

In the development of a cryogenic spectrometer system for the COCHISE facility, a scanning grating monochromator proved to be the most straightforward, reliable, and economical approach. The instrument chosen was a 0.5-m asymmetric Czerny-Turner system (Minuteman 305 CM), which is mounted on an Invar frame to minimize distortion at low temperatures. The spherical collecting and focusing mirrors and the grating are mounted in Invar supports, which are in turn mounted directly to the basic frame. The entire assembly is covered with a light-tight aluminum housing and is held at ~20 K during normal operation.

Two interchangeable replica gratings are employed, their selection depending on the wavelength region of interest. Both gratings are 6.4 cm square, which gives the instrument an aperture ratio of $f/6.9$. For wavelengths below 8 μm, a grating blazed at 3 μm with 150 lines/mm (at room temperature) allows a nominal first-order reciprocal dispersion of 0.013 μm/mm in the exit slit plane; for longer wavelengths, a grating blazed at 10 μm with 75 lines/mm gives 0.027 μm/mm. Thus, for a slit width of 0.5 mm, the resolution element is ~2.6 cm^{-1} at 5 μm and ~1.4 cm^{-1} at 10 μm. Such resolution permits not only determination of detailed vibrational structure for most small atmospheric molecules (typical vibrational spacings of ~10 cm^{-1}) but also the observation of some rotational structure in many cases.

The entrance and exit slit assemblies consist of rotatable disks containing a series of fixed 2-cm high slits ranging in width from 0.1 to 3.0 mm; the slits can be independently indexed by manual controls outside the vacuum chamber. The grating is rotated by a conventional sine-drive mechanism using a precision ball screw designed specifically for cryogenic service; the scan drive controls are located outside the vacuum system. Three shafts penetrate the outer and inner walls of the system and are coupled to the slit assemblies and grating drive screw via stainless steel bellows.

F. Cryogenic Infrared Detector

The IR preamplifier detector module was designed and fabricated at the Electrodynamics Laboratory of Utah State University. The photovoltaic detector element is an arsenic-doped silicon cube, 3.0 mm on an edge (Santa Barbara Research Center); an $f/0.25$ parabolic reflector images the monochromator exit slit onto the detector and thus permits collection of virtually all radiation passing through the slit. A contiguous preamplifier unit utilizes an integrated JFET operational amplifier (Burr-Brown 3521R) in a direct-coupled

negative-feedback operational scheme that previously has been applied successfully to ultrahigh impedance cryogenic detectors.[10] The module also contains an IR emitting diode, temperature monitors, and associated electronic elements and devices. The preamplifier and detector are maintained at temperatures of ~220 and 9 K, respectively, by proportional control systems. An external console provides system control functions, detector bias, signal conditioning circuitry, and output indicators and terminals. This detector, when operated at ~9 K, is sensitive to 1.2–22-μm radiation and has a peak noise equivalent power of ~10^{-16} W/Hz$^{1/2}$.

Liquid helium cooling of the detector package is provided by a 20-liter liquid helium vessel suspended from a port in the top of the vacuum chamber. The neck of the vessel, which serves as a fill-and-vent line, is flexibly connected by a bellows to a port in the 20 K shroud to effect a light-tight penetration. Thermal coupling between the detector and the liquid helium vessel is accomplished by a copper bar and thermal strap, with sapphire electrical standoffs to isolate the detector–preamplifier case.

G. Signal Processing

The detector output is processed by phase-sensitive detection to discriminate against random-phase background noise. The radiation reaching the detector is modulated in one of two ways. In most chemiluminescence observations, the microwave discharges are pulsed at ~23 Hz with a square wave, 50% duty cycle; since chemical reaction does not occur in the absence of the reactive species formed in the discharge plasma, this results in a square wave oscillation in the chemiluminescence signal (provided the chopping frequency is slow enough relative to the flow speed so that diffusional blurring of the waveform does not occur). An alternate method of data collection is to operate the discharge continuously and modulate the radiation with the chopper. However, the pulsed discharge method has the advantage of discrimination against stray radiation, which is not directly linked to species produced in the discharge plasma. The chopper is also used to modulate the radiation from the internal blackbody source during calibration measurements.

The ac detector output passes through an optional bandpass amplifier (PARC model 113) and into a lock-in amplifier (PARC model 124) which is synchronized either to the frequency of the chopper pickup coil or to the external pulse generator used to pulse the microwave discharges. The final demodulated signal is digitally filtered, displayed, and stored in real time by the PDP-8/E computer. The combination of grating scan rate, electronic time constant, and digital filtering rate for a given spectral scan is carefully chosen so that there are at least seven averaged data points and three time constants per spectral resolution element; these criteria insure that the apparent spectral detail is indeed limited by the instrument resolution. The data are initially stored on disk by the PDP-8/E computer and are subsequently transferred via magnetic tape to a Prime 400 computer for detailed analysis.
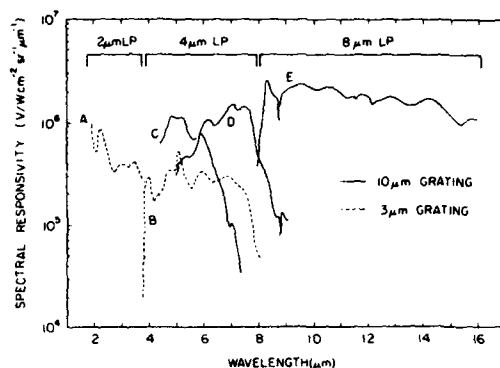
Fig. 4. Approximate spectral responsivity of COCHISE optical system for two grating blaze wavelengths and three order-sorting long-pass filters as indicated. Curves A,B,D,E were obtained in first order; curve C was obtained in second order using a sapphire long-wavelength cutoff filter.

III. Applications

The spectral responsivity of the COCHISE optical/detection system, as determined from calibrations with the internal blackbody source, is plotted as a function of wavelength in Fig. 4. The 2–16-μm spectral region was traversed by means of two gratings and three long-wavelength-pass filters. The solid curves were obtained using a 10-μm blazed grating. First-order measurements employ a 4-μm long-pass filter (5–9 μm) and an 8-μm long-pass filter (8–16 μm), while second-order measurements can be made using a 4-μm long-pass filter together with a sapphire window (4–8 μm). The dashed curves were obtained in first order using a 3-μm blazed grating with 2- and 4-μm long-pass filters. Since the noise level of the instrumentation is ~10^{-6} V, the maximum responsivity, at ~10 μm, corresponds to an optimum NESR near 10^{-12} W cm^{-2} sr^{-1} μm^{-1} or ~10^6 photons cm^{-3} sec^{-1} μm^{-1} for the effective optical path length of 100 cm. For typical species of interest (e.g., O_3—see discussion below), the transition probability is ~10 sec^{-1}, and the bandwidth is ~1 μm; thus the minimum detectable concentration of such vibrationally excited species is of the order of 10^5 molecules cm^{-3}. This unusually high sensitivity at such long wavelengths is due to the absence of noise from thermal background radiation and to the long optical path which is available for the measurements.

The versatility of the apparatus is illustrated by the spectra of Figs. 5 and 6. In Fig. 5 is shown a CO($\Delta v = 1$) fluorescence spectrum observed when a discharged N_2/Ar mixture interacts in the viewing region with a counterflowing CO/Ar mixture. The spectral resolution of 0.007 μm (~3 cm^{-1}) was attained using 0.5-mm slits. The vibrational structure ($\omega_e \chi_e$ ~13.5 cm^{-1}) is well resolved, with contributions evident from at least the first eight vibrational levels; furthermore, even the rotational structure (B_e ~1.9 cm^{-1}) is partially resolved. Since the band center of the ($v' \rightarrow v''$) = (1 → 0) tran-
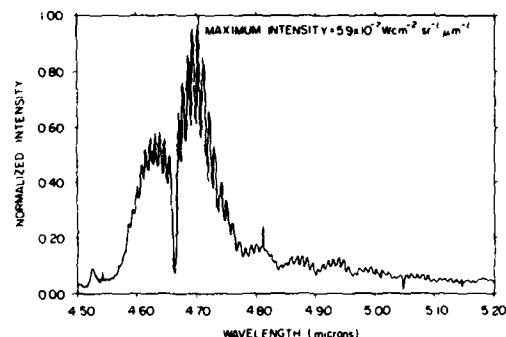

Fig. 5. Partial spectrum of CO ($\Delta v = 1$) vibraluminescence observed in the interaction of discharged N_2/Ar with counterflowing CO/Ar at ~80 K, ~3 mTorr. The spectral resolution is 0.0067 μm.

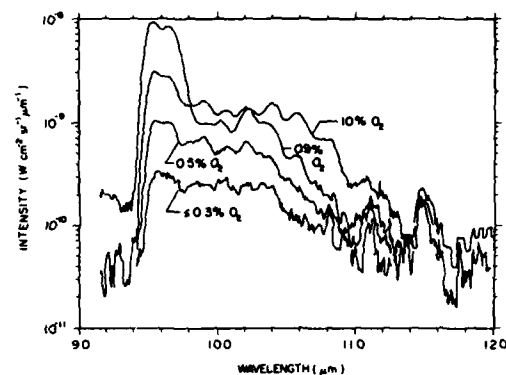Fig. 6. O_3 (ν_3) chemiexcitation spectra from microwave discharge of O_2/Ar mixtures at 1 Torr. The sidearm temperature is 80 K, and the spectral resolution is 0.08 μm. The features near 11.1 and 11.5 μm are Ar emission lines scattered from the discharges.

sition is well-known to be 4.667 μm,[11] high-resolution spectra as in Fig. 5 provide convenient internal wavelength calibration standards for the system. The mechanism for excitation of CO(v) in these preliminary measurements appears to involve energy transfer from components of active nitrogen in processes similar to reaction (2); a systematic investigation is planned for future experiments.

In other experiments, we have observed fluorescence from NO($\Delta v = 1,2$) near 5.4 and 2.7 μm arising from the interaction of active nitrogen and O_2. The fluorescence spectra are quite broad, showing evidence of excitation of up to 13 vibrational levels. A detailed COCHISE investigation of NO($\Delta v = 1$) chemiluminescence near 5.4 μm has been published[9]; the observed fundamental and overtone band radiation is due to a chemiexcitation reaction similar to reaction (1):

$$N(^2D) + O_2 \rightarrow NO(v) + O. \qquad (3)$$
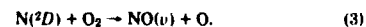
A parallel investigation of the overtone band is now in

progress, with the objective of determining the ratio of fundamental and overtone band Einstein transition probabilities as a function of vibrational level. Reaction (3) is known to be an important source of NO infrared radiation in the disturbed upper atmosphere. The COCHISE results[9] on this process have provided input for atmospheric modeling calculations[12] directed toward interpretation of *in situ* measurements of IR radiation in quiescent[13] and auroral[14] atmospheres. It is now clear from this body of work that atmospheric $NO(v)$ fluorescence is extensively excited in auroras by reaction (3), and that the photon yield scales directly with the auroral strength through the formation of $N(^2D)$.

A series of O_3 ν_3-band spectra, observed near 10 μm in the interaction of discharged O_2/Ar mixtures with counterflowing O_2, is shown in Fig. 6. In contrast to the CO and NO observations, this fluorescence arises primarily from $O_3(v)$ formed in the discharge sidearms via the recombination reaction[15]:

$$O + O_2 + Ar \rightarrow O_3(v) + Ar. \tag{4}$$

Hence the vibrational distribution responsible for the observed spectrum is collisionally relaxed to some extent. The spectral resolution exhibited here is 0.08 μm (8 cm^{-1}), which is sufficient to resolve vibrational structure in O_3 ($\omega_e\chi_e \sim 12$–15 cm^{-1}); resolutions of 1–2 cm^{-1} have been obtained in other scans. Although emission from the (001) vibrational level is the dominant feature in the observed spectrum, contributions from higher levels up to $v_3 = 5$ are evident at longer wavelengths. The fluorescence observed in these experiments represents the first spectrally resolved observations of emission from the higher vibrational levels of ozone. The series of spectra in Fig. 6 illustrates the evolution of the $O_3(v)$ spectral distribution as the O_2 flow into the discharges is varied at constant pressure. As the level of O_2 is reduced, the overall spectral intensity decreases due to the concomitant reduction of the rate of reaction (4), but the relative contributions from the higher vibrational levels increase owing to a reduction in the effects of collisional deactivation of $O_3(v)$ by O and O_2. Furthermore, for the higher O_2 levels, a bimodal spectral distribution is observed, indicating the presence of another excitation mechanism in addition to reaction (4). By examining spectral sequences such as that in Fig. 6, COCHISE can be used in an arrested relaxation mode to study the kinetics of reactions occurring in the discharge tubes.

COCHISE studies of O_3 chemiluminescence have had substantial impact on the analysis and interpretation of high-altitude IR fluorescence observations near 10 μm.[16] Recent rocketborne spectral measurements show marked diurnal[17] and auroral[18,19] effects on the atmospheric production of $O_3(v)$. The chemical and radiative processes responsible for the formation and deactivation of $O_3(v)$ in the upper atmosphere[20] are largely the same as those encountered in the COCHISE experiments; thus the field and laboratory measurements are closely related. In particular, reaction (4) (with N_2 and O_2 instead of Ar as third bodies) is primarily responsible for daytime $O_3(\nu_3)$ fluorescence near

the mesopause, and auroral enhancements of $O_3(v)$ may occur through electron-initiated processes similar to that observed in the COCHISE discharges at high O_2 levels.[20]

Spectra such as those of Figs. 5 and 6 contain information on the populations of the vibrational states which give rise to the observed emission; these populations are related in turn to fundamental kinetic processes in the interaction region and/or in the discharge tubes. In the COCHISE studies, the vibrational populations are determined by a least-squares spectral fitting analysis similar to that used by other investigators.[1-6,11] In general, the emission intensity of the ith spectral line is given by[21]

$$I_i = hc\nu_i A_i N_i, \tag{5}$$

where ν_i and A_i are the frequency and probability of the transition, and N_i is the number density of the species of interest in the upper (emitting) vibration–rotation state. If rotations are assumed to be thermalized in our experiments, N_i is given by $N_i = F_{J'}(v')N_{v'}$, where the relative rotational population for each vibrational level $F_{J'}(v')$ is given by a Boltzmann factor:

$$F_{J'}(v') = \frac{g_{J'}\exp[-E_{J'}(v')/kT]}{Q_R(v')}. \tag{6}$$

and $N_{v'}$ is unknown. In Eq. (6), $E_{J'}(v')$ and $g_{J'}$ are the rotational energy and degeneracy of the emitting state, and $Q_R(v')$ is the rotational partition function for vibrational level v'. The total spectral intensity at each point then has the form

$$\sum_{v'} I_i(v'),$$

where the vibrational basis functions $I_i(v')$ are computed from Eqs. (5) and (6) and are convolved over the band with the instrument resolution function. In practice, the convolved basis functions for unit vibrational populations are computed from fundamental spectroscopic constants or from line-by-line compilations such as that of McClatchey *et al.*[22] The vibrational populations are then determined by a least-squares method in which the quantities $\{N_{v'}\}$ are the solutions which minimize the sum of the squares of the intensity differences between experimental and computed spectra. In this way, vibrational populations are uniquely determined for each experiment, with no inherent assumptions of a functional form such as a Boltzmann distribution.

A computed $CO(\Delta v = 1)$ spectrum, the least-squares fit to the experimental spectrum of Fig. 5, is shown in Fig. 7. Also shown are the individual vibrational basis functions which sum together to give the total spectrum. As illustrated by the relationship between the vibrational basis functions and the total spectrum, the vibrational distribution is a property of the coarse envelope of the band, and its determination requires only moderate spectral resolution (of the order of the vibrational anharmonicity of the species of interest). However, higher resolution measurements are occasionally useful to check spectroscopic constants, conclusively identify the radiating species, and separate
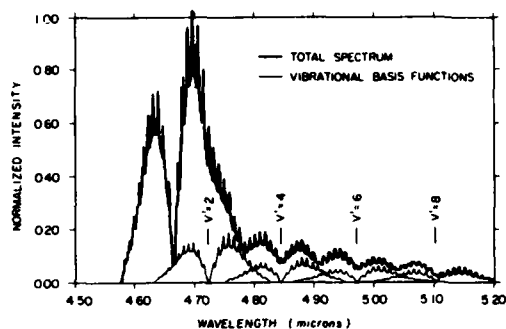
Fig. 7. Computed spectral least-squares fit to the experimental CO spectrum of Fig. 5. The assumed rotational temperature is 80 K. For the portion of the spectrum shown here, the vibrational state number densities range from 4.3×10^7 cm^{-3} for CO ($v = 1$) to 4.5×10^5 cm^{-3} for CO ($v = 8$). Only the vibrational basis functions for $v' = 2,4,6,8$ are shown with the band centers as designated.

overlapping contributions from other radiators. In addition, higher resolution spectra can be used to examine rotational nonequilibrium effects, which have been observed under some conditions.[9] The utility of the spectral fitting analysis is diminished when there is extensive overlap between adjacent vibrational basis functions. Thus cryogenic capability offers yet another advantage, since the reagent temperatures are usually near 80 K, and the resulting product rotational temperatures are low enough that the band overlap is not a significant limitation.

The example measurements discussed here demonstrate how, by judicious choices of the experimental conditions and application of spectral fitting techniques, the IR spectral signatures observed in CO-CHISE can be transformed into quantitative kinetic data for a variety of chemical energy-transfer processes. Much of the work referred to here is still in progress and will be presented in detail elsewhere.

IV. Conclusions

To simulate atmospheric IR radiative processes in the laboratory, one requires high sensitivity at long wavelengths and low pressures. The COCHISE facility satisfies these criteria by means of cryogenic (20 K) operation of the entire reaction vessel and detection system. This provides minimal thermal background and rapid cryopumping of reagents, which in turn permit operation with low pressure and large optical paths. The ultimate detection sensitivity of the system is of the order of 10^5 molecules cm^{-3} for vibrationally excited species.

The achievement of total cryogenic operation of such a large and complex apparatus requires careful design and testing of each component; we have documented here the end results of this development effort. The facility has already been successfully applied to several fundamental problems of interest to the atmospheric community; we anticipate that further research in this direction will improve significantly our understanding of these and other basic processes.

References

1. Carrington and J. C. Polanyi, *MTP International Review of Science, Physical Chemistry, Ser. 1, Vol. 9,* J. C. Polanyi, Ed. (Butterworth, London, 1972), p. 135.
2. B. E. Holmes and D. W. Setser, "Energy Disposal in Unimolecular and Bimolecular Reactions," in *Physical Chemistry of Fast Reactions, Vol. 3,* I. W. M. Smith, Ed. (Plenum, London, 1977).
3. J. G. Moehlmann, J. T. Gleaves, J. W. Hudgens, and J. D. McDonald, "Infrared Chemiluminescence Studies of the Reactions of Fluorine Atoms with Monosubstituted Ethylene Compounds," J. Chem. Phys. **60,** 4790 (1974).
4. J. P. Sung, R. J. Malins, and D. W. Setser, "Comparison of Rate Constants for Reactions of Hydrogen Atoms with Chlorine, Fluorine, Iodine Chloride, and Chlorine Fluoride," *J. Phys. Chem.* **83,** 1007 (1979).
5. B. M. Berquist, J. W. Bozzelli, L. S. Dzelzkalns, L. G. Piper, and F. Kaufman, "Vibrational Relaxation of Highly Excited Diatomics. I. Method, Analysis and Application to HCl($v \leq 7$) + CO$_2$ and N$_2$O," J. Chem. Phys. **76,** 2972 (1982).
6. D. Bogan and D. W. Setser, "Fluorine Containing Free Radicals, Kinetics and Dynamics of Reactions," ACS Symp. Ser. **66** (1977).
7. B. McCarroll, "An Improved Microwave Discharge Cavity for 2450 MHz," Rev. Sci. Instrum. **41,** 279 (1970); F. C. Fehsenfeld, K. M. Evenson, and H. P. Broida, "Microwave Discharge Cavities Operating at 2450 MHz," Rev. Sci. Instrum. **36,** 294 (1965).
8. G. E. Caledonia, B. D. Green, G. A. Simons, J. P. Kennealy, F. X. Robert, A. Corman, and F. P. Del Greco, "COCHISE Studies I; Fluid Dynamical and Infrared Spectral Analysis," AFGL-TR-77-0281, Air Force Geophysics Laboratory, Hanscom AFB, Mass. (1977), NTIS ADA-053218.
9. J. P. Kennealy, F. P. Del Greco, G. E. Caledonia, and B. D. Green, "Nitric Oxide Chemiexcitation Occurring in the Reaction between Metastable Nitrogen Atoms and Oxygen Molecules," J. Chem. Phys. **69,** 1574 (1978).
10. C. L. Wyatt, "Infrared Helium-Cooled Circular-Variable Spectrometer, Model HS-1," Final Report AFCRL-71-0340 contract F19628-67-C-0322, Electro-Dynamics Labs., Utah State U, Logan (15 Sept. 1971); C. L. Wyatt and D. J. Baker, "Rocket Launch of an LWIR Spectrometer Into an Aurora," Internal Report, Electro-Dynamics Labs., Utah State U. (30 June 1973).

237

11. G. E. Caledonia, B. D. Green, and R. E. Murphy, "A Study of the Vibrational Level Dependent Quenching of CO(v = 1–16) by CO_2," J. Chem. Phys. 71, 4369 (1979); G. Hancock and I. W. M. Smith, "Quenching of Infrared Chemiluminescence 1: The Rates of Deexcitation of CO($4 \leq v \leq 13$) by He, CO, NO, N_2, O_2, OCS, N_2O, and CO_2," Appl. Opt. 10, 1827 (1971).

12. G. E. Caledonia and J. P. Kennealy, "NO Infrared Radiation in the Upper Atmosphere," Planet. Space. Sci. 30, 1043 (1982).

13. R. M. Nadile, A. T. Stair, Jr., N. B. Wheeler, D. G. Frodsham, C. L. Wyatt, B. J. Baker, and W. F. Grieder, "SPIRE—Spectral Infrared Rocket Experiment (Preliminary Results)," AFGL-TR-78-0107, Air Force Geophysics Laboratory, Hanscom AFB, Mass (1978), NTIS ADA-058504.

14. W. T. Rawlins, G. E. Caledonia, J. J. Gibson, and A. T. Stair, Jr., "Infrared Emission from NO(Δv = 1) in an Aurora: Spectral Analysis and Kinetic Interpretation of HIRIS Measurements," J. Geophys. Res. 86, 1313 (1981).

15. W. T. Rawlins, G. E. Caledonia, and J. P. Kennealy, "Observation of Spectrally Resolved Infrared Chemiluminescence from Vibrationally Excited $O_3(\nu_3)$," J. Geophys. Res. 86, 5247 (1981).

16. W.T. Rawlins and R. A. Amstrong, "COCHISE Observations of O_3 Formed by Three-Body Recombination of O and O_2," AFGL-TR-82-0273, Air Force Geophysics Laboratory, Hanscom AFB, Mass. (1982), NTIS ADA-123653.

17. B. D. Green, W. T. Rawlins, and R. M. Nadile, "Diurnal Variability of Vibrationally Excited Mesospheric Ozone as Observed During the SPIRE Mission," J. Geophys. Res., submitted, 1984.

18. A. T. Stair, Jr., J. Pritchard, I. Coleman, C. Bohne, W. Williamson, J. Rogers, and W. T. Rawlins, "Rocketborne Cryogenic (10 K) High-Resolution Interferometer Spectrometer Flight HIRIS: Auroral and Atmospheric IR Emission Spectra," Appl. Opt. 22, 1056 (1983).

19. W. T. Rawlins, G. E. Caledonia, J. J. Gibson, and A. T. Stair, Jr., "HIRIS Rocketborne Spectra of Infrared Fluorescence in the $O_3(\nu_3)$ Band Near 100 km," submitted to J. Geophys. Res. (1984).

20. W. T. Rawlins, "Chemistry of Vibrationally Excited Ozone in the Upper Atmosphere," to be submitted, J. Geophys. Res. 1984.

21. G. Herzberg, *Molecular Spectra and Molecular Structure 1, Spectra of Diatomic Molecules* (Van Nostrand, New York, 1951).

22. R. A. McClatchey, W. S. Benedict, S. A. Clough, D. E. Burch, R. F. Calfee, K. Fox, L. S. Rothman, and J. S. Garing, "AFCRL Atmospheric Absorption Line Parameters Compilation," AFCRL-TR-73-0096, Air Force Geophysics Laboratory, Hanscom AFB, Miss. (1973), NTIS AD-762904.

238

Appendix B

**Spectroscopic Investigation of Laser-Initiated
Low-Pressure Plasmas in Atmospheric Gases**

by

R. A. Armstrong
R. A. Lucht
W. T. Rawlins

Spectroscopic investigation of laser-initiated low-pressure plasmas in atmospheric gases

R. A. Armstrong, R. A. Lucht, and W. T. Rawlins

Laser-initiated breakdown of N_2, O_2, and Ar has been investigated at sub-atmospheric pressures using a pulsed (10-nsec) Nd:yttrium aluminum garnet (Nd:YAG) laser at 1.06 μm. Breakdown thresholds have been determined from 3 to 760 Torr, and spectral analysis of the plasma emission has been carried out at 10 and 125 Torr over the 300–600-nm range. Sharp spectral features arising from highly excited singly and multiply charged ions are reported as well as an underlying continuum at intermediate pressure. Time-resolved measurements indicate a complex kinetic dynamic optical behavior.

I. Introduction

The subject of laser-initiated breakdown of gases has been of interest since the early application of lasers. Excellent articles have been published on some phases of this subject, and Morgan[1] has reviewed the important results of the early work. The vast majority of the work has involved investigation of the energy coupling and breakdown threshold mechanisms and resulting electron densities and temperatures. More recently, interest has increased in energy coupling at or near surfaces in support of laser fusion and laser damage studies. Relatively little attention, however, has been focused on understanding the time-resolved spectroscopy of the relaxing plasma after the breakdown. Stricker and Parker[2] have initiated some limited work in this area, and Radziemski et al.[3,4] have applied the technique to spectroscopic analysis of trace species. These investigations, however, are at relatively high pressures. Detailed knowledge of the spectroscopy and dynamics of plasmas of low-pressure atmospheric gases is important for understanding the behavior of upper atmospheric disturbances. The technique of laser-initiated breakdown can be used to simulate strong electron disturbances in the laboratory. We report here the results of initial investigations of the plasma spectroscopy at 10 and 125 Torr and additional information on

breakdown thresholds for Ar, N_2, and O_2 over the 3–760-Torr pressure range using focused laser radiation at 1.06 μm.

II. Experimental

A schematic of the experimental apparatus is shown in Fig. 1. The experiments employed a Quanta-Ray DCR-1A Nd:yttrium aluminum garnet (Nd:YAG) laser, which can produce up to 750 mJ/pulse at 1.06 μm with a measured pulse width of <10-nsec full width at half-maximum (FWHM). The pulse shape is typically spikey in normal operation without an etalon in the oscillator cavity. However, the pulses were not mode locked, so the breakdown threshold data could be interpreted in a straightforward manner. No discernible difference was found with a single-mode-generating etalon inserted into the cavity. The unstable resonator cavity produced a 0.65-cm (diam) annular beam in the near field with a divergence $\theta < 0.5$-mrad (FWHM). The beam was focused into the gas chamber by a short focal length lens ($f = 5.8$ cm) with less than one wavelength of spherical aberration. The laser was pulsed typically at 10 Hz; the results were not affected significantly by reducing the frequency to 2 Hz. Ultrahigh purity argon, oxygen, and nitrogen gases were used directly from the bottles. Experiments were performed with static pressures measured with an MKS baratron capacitance manometer.

Apparent breakdown thresholds were determined by observing broadband (300–700-nm) emission from the focal volume without the monochromator. For pressures above 25 Torr, the onset of breakdown was defined by the sudden appearance to the eye of visible emission from the focal volume. However, this method proved to be unreliable at pressures below 25 Torr, so an RCA 1P28 photomultiplier tube was used to observe the

Russell Armstrong is with U.S. Air Force Geophysics Laboratory, Optical Physics Division, Hanscom Air Force Base, Massachusetts 01731; R. A. Lucht is with University of California, Los Alamos National Laboratory, Los Alamos, New Mexico 87545; and W. T. Rawlins is with Physical Sciences, Inc., Research Park, Andover, Massachusetts 01810.
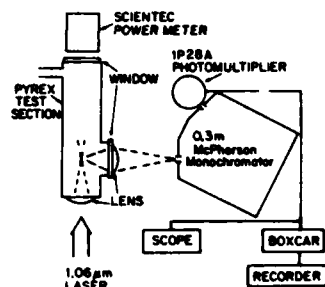
Fig. 1. Schematic diagram of the experimental apparatus. The monochromator was not used in the breakdown threshold measurements (see text).

plasma emission at lower pressures. Spectral and temporal information was obtained with a McPherson 218 scanning monochromator and PARC 162/165 boxcar integrator.

III. Results and Discussion

The results of the visual and photometric breakdown threshold measurements for Ar, N_2, and O_2 are plotted in Fig. 2. The data were fit to the function $I_p = aP^b$, where I_p is peak intensity obtained from measured laser power divided by calculated focal radius (see below), and P is the pressure in Torr. The observed breakdown curves for all three gases are remarkably similar, with pressure exponents b of from -0.3 to -0.5. An obvious change in slope occurs near 100 Torr for argon and nitrogen but not for oxygen. While the argon data are similar to Ireland's[5] for similar pulse widths, the break in slope was not evident from previous investigations using a Nd:YAG laser source.

The pressure dependence above 100 Torr is weaker than the P^{-1} behavior predicted by the theory of inverse bremsstrahlung cascade,[1,6-8] in marked contrast to measurements for argon gas breakdown at 0.69 μm[9] which show an $\sim P^{-0.8}$ dependence. The weak pressure dependence in the present case may result from other effects such as multiple-photon inverse bremsstrahlung ionization[10] or self-focusing, which have not been included in theoretical treatments.

At sufficiently low pressure, direct multiphoton ionization should dominate over the cascade mechanism,[1] resulting in a change of slope of the pressure-dependent plots to $\sim P^{-1/n}$, where n is the number of photons required for multistep ionization. The previously unreported break in the slope of I_p vs P occurs at nearly an order of magnitude higher pressure than the theoretically predicted $P < 10^{-7}/\tau$, where τ is the laser pulse width in seconds. However, we do not observe an approach to $P^{-1/n}$ behavior as seen in cases of visible, picosecond time-scale generated breakdown,[11] a result consistent with findings of other investigations.[1,5] This observation is difficult to understand for several reasons. First, below 10 Torr, the electron mean-free path is long relative to the spark dimensions. We calculate our focal radius and length to be $r = f(\theta/2) = 14.5 \, \mu m$ and $l = (\sqrt{2} - 1)\theta f^2/d = 107 \, \mu m$, respectively, from which we derive an effective cylindrical

electron diffusion length of 6 μm. Since the electron mean-free path in air is $\sim 10 \, \mu m$ at 1 Torr and ~ 10 inverse bremsstrahlung events are required per electron to achieve ionization, collisional processes should not dominate at pressures below 10 Torr. Second, our photometric results below 25 Torr show a significant range of laser intensities near threshold over which plasma emission can be observed, similar to picosecond pulse-width observations[11] which exhibited optical behavior consistent with multiphoton breakdown ($\sim 10^{-3}$ Torr). Third, using ion counting, Baravian et $al.$[12] showed that the multiphoton process dominates up to at least a few Torr. Thus, although our low-pressure data should reflect multiphoton-controlled ionization, the optical behavior of the pressure dependence of breakdown intensity I_p is more consistent with cascade breakdown.

Time-integrated spectra of the plasma emission following the laser pulse were obtained for the three gases from 300 to 600 nm. A sample of a typical spectrum is

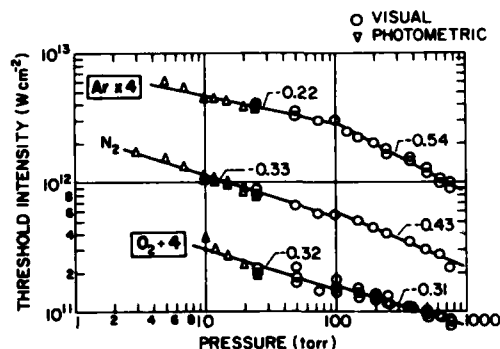Fig. 2. Apparent breakdown thresholds for Ar, N_2, and O_2. Pressure exponents b obtained from least-squares fits (solid lines) for $P > 100$ Torr and $P < 100$ Torr are indicated. For clarity, the argon and oxygen curves have been offset by a factor of 4 from their actual position.
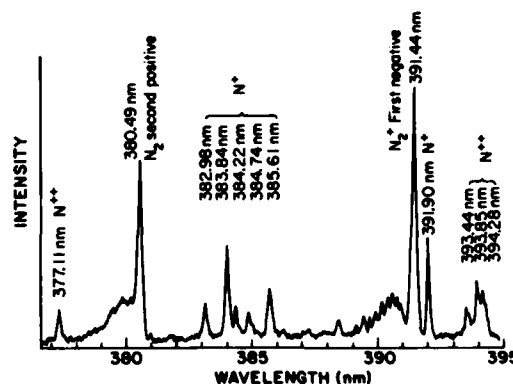

Fig. 3. Portion of the laser-initiated spectrum obtained for N_2 at 10 Torr and $I_p = 2 \times$ threshold.

shown in Fig. 3. Gas pressures of 10 and 125 Torr were used, and the laser intensity was held at twice the apparent threshold value in each case. The spectra were obtained with the scanning monochromator and a boxcar integrator with an undelayed 200-nsec wide gate, averaging over several laser pulses for each element of spectral resolution. The electronically excited species identified[13,14] from the spectra are N_2, N_2^+, N^+, N^{2+}, and N^{3+}, O^+ and O^{2+}, Ar^+ and Ar^{2+}, for breakdown in N_2, O_2, and Ar, respectively. The atomic states observed include high-lying Rydberg levels. Conspicuous by their absence are transitions of O_2, O_2^+, and O^{3+}. In similar experiments performed at pressures at and above 1 atm,[2] the multiply charged species found here were not observed, indicating very strong quenching at higher pressures.

Table I. Spectral and Temporal Results Obtained for N_2 and O_2 at 10 and 125 Torr.[a]

Species	λ (A)	P (Torr)	E_u (cm^{-1})	g_e	g_u	τ_{life} (nsec)	τ_{exptl} (nsec)	I_p (W/cm²)
N_2 second pos.	3536.7	10	90,580	—	—	40.6	58	2.9 × 10¹²
N_2 second pos.	3536.7	10	90,580	—	—	40.6	56.6	2.9 × 10¹²
N_2 second pos.	3576.9	10	88,980	—	—	40.4	62.0	2.9 × 10¹²
N_2 second pos.	3804.9	10	88,980	—	—	40.4	64.8	2.9 × 10¹²
N_2 second pos.	3804.9	125	88,980	—	—	40.4	46.8	9.84 × 10¹¹
N_2 second pos.	3804.9	125	88,980	—	—	40.4	51.6	2.00 × 10¹²
N_2 second pos.	3804.9	125	88,980	—	—	40.4	79.2	4.26 × 10¹²
N_2^+ first neg.	3914.1	10	151,233	—	—	10.4	34	2.9 × 10¹²
N_2^+ first neg.	3914.4	125	151,233	—	—	40.4	42.2	9.48 × 10¹¹
N^+	3437.2	10	178.274	3	1	4.17	77	2.9 × 10¹²
N^+	3437.2	10	178.274	3	1	4.17	81	2.9 × 10¹²
N^+	3437.2	125	178.274	3	1	4.17	169	9.84 × 10¹¹
N^+	3838.4	10	196.712	5	5	19.2	82	2.9 × 10¹²
N^+	4040.9	10	211.332	21	27	3.79	77	2.9 × 10¹²
N^+	4447.0	10	187,092	3	5	7.69	72	2.9 × 10¹²
N^+	4447.0	125	187,092	3	5	7.69	168	9.84 × 10¹¹
N^+	4447.0	125	187,092	3	5	7.69	202	2.00 × 10¹²
N^+	4447.0	125	187,092	3	5	7.69	341	4.26 × 10¹²
N^+	4621.4	10	170,573	3	1	11.1	74.0	2.9 × 10¹²
N^+	4621.4	125	170,573	3	1	11.1	168	9.84 × 10¹¹
N^+	4803.3	10	187,493	7	7	32.0	74	2.9 × 10¹²
N^+	4803.3	125	187,493	7	7	32.0	175	9.84 × 10¹¹
N^+	5045.1	10	168,893	5	3	24.4	78	2.9 × 10¹²
N^+	5679.6	10	166,893	5	7	17.9	73	2.9 × 10¹²
N^+	5679.6	125	166,893	5	7	17.9	217	9.84 × 10¹¹
N^{++}	3938.5	10	334,569	4	6	10.4	37.2	2.9 × 10¹²
N^{++}	4097.3	10	245,702	2	4	10.4	33	2.9 × 10¹²
N^{++}	4097.3	125	245,702	2	4	10.4	41.1	9.84 × 10¹¹
N^{++}	4097.3	125	245,702	2	4	10.4	53.4	2.00 × 10¹²
N^{++}	4097.3	125	245,702	2	4	10.4	88.8	4.26 × 10¹²
N^{++}	4514.9	10	309,857	6	8	14.3	30.7	2.9 × 10¹²
N^{++}	4867.2	10	330,397	8	10	15.9	34.8	2.9 × 10¹²
N^{+++}	3478.7	10	405,944	3	5	8.62	21	2.9 × 10¹²
N^{+++}	3478.7	125	405,944	3	5	8.62	22.0	9.84 × 10¹¹
N^{+++}	3478.7	125	405,944	3	5	8.62	28.2	2.00 × 10¹²
N^{+++}	3478.7	125	405,944	3	5	8.62	34.4	4.26 × 10¹²
O^+	3973.3	10	214,229	4	4	7.87	92.4	2.9 × 10¹²
O^+	3973.3	125	214,229	4	4	7.87	202	1.12 × 10¹²
O^+	4414.9	10	211,713	4	6	8.70	88.8	2.9 × 10¹²
O^+	4414.9	125	211,713	4	6	8.70	180	1.12 × 10¹²
O^+	4591.0	10	228,747	6	8	9.01	81.6	2.9 × 10¹²
O^+	4591.0	125	228.747	6	8	9.01	173	1.12 × 10¹²
O^+	4649.1	10	207,003	6	8	9.62	92.9	2.9 × 10¹²
O^+	4649.1	125	207,003	6	8	9.62	209	1.12 × 10¹²
O^+	4649.1	125	207,003	6	8	9.62	274	2.26 × 10¹²
O^+	4649.1	125	207,003	6	8	9.62	276	4.66 × 10¹²
O^{++}	3759.9	10	294,222	5	7	9.35	31.7	2.9 × 10¹²
O^{++}	3759.9	125	294,222	5	7	9.35	39.8	1.12 × 10¹²
O^{++}	3759.9	125	294,222	5	7	9.35	50.0	2.26 × 10¹²
O^{++}	3759.9	125	294,222	5	7	9.35	65.4	4.66 × 10¹²
O^{++}	3961.6	125	306,585	5	7	7.81	42.0	1.12 × 10¹²

[a] Symbols λ, P, E_u, g_e, g_n, and I_p are defined in the text, τ_{life} is the given radiative lifetime from Refs. 13 and 14, and τ_{exptl} is the decay time obtained in this experiment.

The nominal spectral resolution in our measurements is ~0.05 nm. The observed linewidths are 2–3 times broader, likely due to Stark broadening. Estimates of the electron density from the observed linewidths give ~10^{18} cm^{-3} at optically thin conditions at 10 Torr, indicating the gas is essentially fully ionized. The prevalence of atomic transitions in the spectral data further indicates that the molecular gases are highly dissociated. In addition to the line spectra, a broad continuum was observed at 125 Torr but was absent at 10 Torr. This time-integrated continuum, which is identical for O_2 and N_2, has a peak near 420 mm, a FWHM of ~150 nm, and is skewed to the red. The spectral distribution does not fit that of blackbody radiation, and we conclude that it is due to bremsstrahlung emission.

A measure of the excitation of N$^+$ and O$^+$ at a laser intensity of twice breakdown threshold was obtained from the time-integrated spectra by plotting the observed relative emitting-state populations N_u vs energy. Table I summarizes the spectral assignments and energy parameters. Relative populations of N_u were determined from the observed peak intensities I of isolated atomic lines by $N_u \propto I\lambda/(A_{ul}g_u\epsilon_\lambda)$, where λ is the wavelength, ϵ_λ is the instrument spectral efficiency (as determined from separate calibrations), and A_{ul} and g_u are the upper-level transition probability and degeneracy as obtained from compilations.[14] Apparent electronic temperatures were then determined by fitting the data to the Boltzmann formula $N_u \propto \exp(-E_u/kT)$, where E_u is the upper energy level of the emitting species. These electronic temperatures, which should not be assumed to indicate equilibrium conditions, are accuracy limited by the uncertainty of the transition probabilities given in Ref. 14. The results at 10 Torr ($\pm 1\sigma$) give (17,900 $\pm$ 1,400) K for N$^+$ and (26,700 $\pm$ 1,600) K for O$^+$; at 125 Torr, the apparent temperatures are (24,400 $\pm$ 2700) K for N$^+$ and (24,300 $\pm$ 2700) K for O$^+$. Figure 4 shows the results for N$^+$ at 10 Torr. The significant difference between the N$^+$ and O$^+$ temperatures at 10 Torr reflects the larger energy required to excite high levels of N$^+$ from N_2 by the multiphoton process. The similarity of the O$^+$ and N$^+$ temperatures at 125 Torr may be accounted for if the plasma formation is totally in the collision-dominated cascade regime, which is expected at this pressure. In this case, the effective temperature is primarily determined by the electron density-dependent cascade plasma production term, not by the molecular properties. Further analysis of absorption coefficients using a Stark broadening line-shape function indicates that at neither pressure are the emission lines optically thick.

Time-resolved measurements summarized in Table I, columns 7 and 8, were made of several emitting species with a 5-nsec boxcar gate width. Nearly all visible emission occurs after the laser pulse. Measured species exhibited varied rise times of <100 nsec at laser intensity of twice breakdown threshold for a given pressure, but in no case was peak emission reached within the laser pulse width. Emission decay rates of molecular nitrogen second-positive and first-negative systems were close to radiative decay rates. All atomic species,

however, including those excited to high-lying energy levels, exhibited decay rates much longer than radiative. Species for which electronic temperatures were obtained exhibited constant relative population distribution throughout the decay. These results may be explained by a combination of spatial variations of source emitters and local thermodynamic equilibrium as presented by Radziemski et al.[4] However, increasing laser intensity results in nonuniform temporal relaxation as shown in Fig. 5, a plot of the temporal profile of the 444.7-nm line of N$^+$. The upper curve exhibits a very complex kinetic and dynamic behavior which is not consistent with a thermodynamic equilibrium model. Furthermore, the
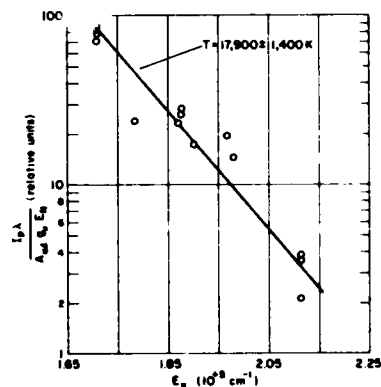

Fig. 4. Determination of apparent electronic temperature of N$^+$ at 10 Torr. The solid line is a least-squares fit to the data and has a slope proportional to T^{-1}.
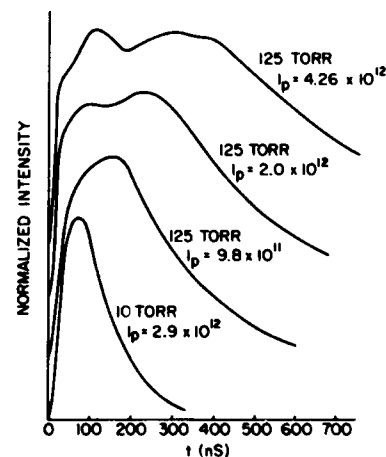

Fig. 5. Temporal profile of the 444.7-nm line of N$^+$. I_p is peak laser intensity in W cm^{-2} at the pressures indicated. The 10-Torr and first 125-Torr curves are generated at I_p of twice threshold for breakdown.

fact that N_2 and N_2^+ show decay rates close to radiative, but the atomic species do not, fails to support thermal equilibrium arguments.

In conclusion, although several articles on laser-induced gas breakdown have appeared in the literature, an adequate explanation of the failure of nanosecond pulse-width 1.06-μm laser breakdown to show clear crossover to multiphoton behavior at low pressure has never emerged. A recent article[8] purports to explain the behavior, but their analysis fails to fit the data and cannot be generally applied to all laser breakdown conditions. We have used a photometric scheme to determine the low-pressure breakdown thresholds and, by so doing, identified a heretofore unreported break in the slope of breakdown threshold vs pressure for a 10-nsec pulse-width Nd:YAG laser. We have also reported new data on O_2 and N_2 as well as time behavior not explainable by a thermal equilibrium model.

While we do not yet have a full explanation of the optical behavior of the laser-produced plasma, it is clear that simple models of multiphoton vs cascade processes are not adequate. We also caution that it is difficult and somewhat arbitrary to assign breakdown threshold at reduced pressures, and the onset of detectable emission from the focal volume may be an insufficient criterion for the attainment of breakdown threshold. The issues cannot be resolved without a detailed experimental and theoretical investigation of the coupled gas dynamics, optics, and kinetics of the laser-initiated plasma. We are continuing to investigate these processes.

References
1. C. G. Morgan, Sci. Prog. 65, 31 (1978) and references therein.
2. J. Stricker and J. G. Parker, J. Appl. Phys. 53, 851 (1982).
3. L. J. Radziemski and T. R. Loree, Plasma Chem. Plasma Process. 1, 281 (1981).
4. L. J. Radziemski, T. R. Loree, D. A. Cremers, and N. M. Hoffman, unpublished.
5. C. L. M. Ireland, J. Phys. D 7, L179 (1974).
6. C. L. M. Ireland and C. G. Morgan, J. Phys. D 6, 720 (1973).
7. F. Morgan, L. R. Evans, and C. G. Morgan, J. Phys. D 4, 225 (1971).
8. Y. Gamal and M. Harith, J. Phys D 14, 2209 (1981).
9. R. J. Dewhurst, J. Phys. D 10, 283 (1977).
10. R. J. Dewhurst, J. Phys. D 11, L191 (1978).
11. P. Agostini, G. Barjot, G. Mainfray, C. Manus, and J. Thebault, IEEE J. Quantum Electron. QE-6, 782 (1970).
12. G. Baravian, J. Godart, and G. Sultan, Appl. Phys. Lett. 36, 415 (1980).
13. R. W. B. Pearse and A. G. Gaydon, *The Identification of Molecular Spectra* (Wiley, New York, 1976).
14. W. L. Wiese, M. W. Smith, and B. M. Glennon, "Atomic Transition Probabilities," Natl. Stand. Ref. Data Ser. Natl. Bur. Stand. 4 (1966).

244

END

FILMED

1-86

DTIC